

**ELECTROCHEMICAL RESPONSES OF NOVEL PREFERENTIALLY  
ORIENTED PLATINUM (100) NANOALLOYS FOR AMMONIA AND  
HYDRAZINE CATALYSIS**



By

**STEPHEN NZIOKI MAILU**

*B.Ed. (Sc.) First class Honours (Kenya University), MSc. (Cum Laude) (UWC)*

UNIVERSITY of the  
WESTERN CAPE

A thesis submitted in fulfilment of the requirement for the Degree of Philosophiae Doctor in  
the Department of Chemistry, University of the Western Cape, South Africa.

Supervisor

Professor Emmanuel I. Iwuoha

Co-supervisor

Professor Priscilla GL. Baker

May, 2013.



UNIVERSITY *of the*  
WESTERN CAPE

UNIVERSITEIT VAN WES-KAAPLAND  
BIBLIOTHEEK

*.tz, .? 12t2 vi,*

LIBRARY  
UNIVERSITY OF THE WESTERN CAPE

## KEYWORDS

### Electrochemical Responses of Novel Preferentially Oriented Platinum (100) Nanoalloys for Ammonia and Hydrazine Catalysis

Stephen Nzioki Mailo

#### Keywords

Adatoms

Ammonia oxidation

Catalysts

Current density

Cyclic voltammetry

Electrocatalyst

Electrochemical impedance spectroscopy

Hydrazine

Hydrogen

Metal nanoparticles

Nanoalloys

Nanoclusters

Overpotential

Preferentially oriented Pt(100) nanoparticles



## ABSTRACT

### **Electrochemical Responses of Novel Preferentially Oriented Platinum (100) Nanoalloys for Ammonia and Hydrazine Catalysis**

S.N. Mailu

PhD Thesis, Department of Chemistry, University of the Western Cape, May 2013.

Ammonia has attracted attention as a possible fuel for direct fuel cells since it is easy to handle under low pressure, costs only slightly higher than methanol and can easily be cracked down into hydrogen and nitrogen. At low temperature, ammonia oxidation on noble metal electrodes is a sluggish reaction and efficient catalysts are required to convert ammonia to nitrogen and hydrogen at reasonable reaction rates. In this thesis, I present polycrystalline and oriented nanoalloys synthesised at room temperature in aqueous media and their catalytic effects on the oxidation of ammonia. The electro-oxidation of ammonia on palladium-gold-silver (PdAuAgNPs) ternary nanoalloys was systematically studied in alkaline solution of potassium hydroxide (KOH) by cyclic voltammetry (CV). The PdAuAg nanoalloys were prepared through a facile synthesis with ascorbic acid as a reductant and polyvinylpyrrolidone (PVP) as a stabilising agent from aqueous solutions of PdCl<sub>2</sub>/HAuCl<sub>4</sub>.3H<sub>2</sub>O/AgNO<sub>3</sub> mixtures. UV-visible spectroscopy was used to confirm the complete reduction of the metal ions; absorption peaks observed at 260 nm, 285 nm and 420 nm for Ag<sup>+</sup>, Au<sup>3+</sup> and Pd<sup>2+</sup> ions respectively, disappeared after reduction indicating a complete reduction of the metal ions to zero-valent nanoparticles. High resolution transmission electron microscopy (HRTEM) revealed the formation of crystalline non-aggregated 25-35 nm sized nanoalloys. The elemental composition of the nanoalloys

measured using energy dispersive X-ray spectroscopy (EDX) showed the presence of the three elements; Pd, Au and Ag. The well-dispersed non-agglomerated PdAuAg nanoalloys exhibited a reduced overpotential and a 33%, 400%, 82% and 54% increase in current density for ammonia electro-oxidation compared to Pd, PdAg, PdAu nanoparticles and bare Pt electrode, respectively. The much improved current density of the well-dispersed PdAuAg nanoalloys is attributed to the increased electrochemically active surface area of the nanoalloys. This electrocatalytic behaviour of the PdAuAg nanoalloys for ammonia oxidation in KOH solutions provides a promising route for development of low-cost and high-performance electrocatalyst for electro-oxidation of ammonia.

Moreover, ammonia oxidation on platinum surfaces has been found to be a very structure-sensitive reaction which takes place almost exclusively on Pt(100) surfaces. I report for the first time the preparation of sodium polyacrylate-capped Pt(100)Pd, Pt(100)Au, Pt(100)Ir, Pt(100)Rh, Pt(100)PdAu, Pt(100)IrAu, Pt(100)PdIr and Pt(100)RhAu nanoalloys. The reduction of the metal ions to nanoparticles was confirmed by UV-visible spectroscopy while the shapes and the structures of the nanoparticles were studied using HRTEM and CV. HRTEM analysis showed well distributed non-agglomerated 5-20 nm semi-spherical and cubic nanoalloys with lattice fringes on their surfaces indicating the crystalline nature of the nanoalloys. Pt(100) nanoalloy systems showed particles with triangular and cubic shapes. The existence of the preferentially cubic shaped nanoparticles in the samples indicated that the nanoalloys had some (100) sites orientation/a significant amount of (100) sites at their surfaces. The CV of the nanoparticles in the hydrogen adsorption/desorption region (-200 mV to 100 mV vs. Ag/AgCl) was used to obtain qualitative information about the surface structure of the nanoparticles. The voltammogram of oriented Pt(100) nanoparticles showed very clearly the presence of adsorption states associated with (110) sites, (100) domains and

(100) sites at -131 mV, -34 mV and 29 mV, respectively. The comparison of this voltammetric profile with that obtained for a Pt(100) single crystal electrode clearly points out that the synthesised Pt nanoparticles have a high density of (100) sites. However, the peak that was observed at 29 mV in the CV of Pt(100) nanoparticles was not present in the voltammograms of the Pt(100) nanoalloy systems confirming the formation of the nanoalloys. The results reported in this work demonstrate the importance of controlling the intrinsic structural properties of Pt nanoparticles; in terms of nature of the active sites and the effect of adding adatoms (such as Au, Pd, Rh, Ir) in order to understand their catalytic properties. The electrochemical activities of these nanoparticles for ammonia oxidation in basic medium showed an increase of over 100% current density compared to Pt electrode. Pt(100)RhAu nanoalloys showed the highest catalytic properties while Pt(100)PdAu had the lowest as shown in the trend: Pt(100)RhAu > Pt(100)PdIr > Pt(100) > Pt(100)IrAu > Pt(100)Pd > Pt(100)Rh > Pt(100)Au > Pt(100)Ir > Pt(100)PdAu.

The synthesised oriented nanoalloys were further interrogated towards the oxidation of hydrazine as a fuel for hydrazine fuel cells. The oriented Pt(100) nanoparticles and Pt(100) nanoalloy systems exhibited over 1000% increase in current density and reduced oxidation overpotential compared to bare glassy carbon electrode. These excellent catalytic properties are attributed to the increased surface area and the presence of (100) sites which favour the oxidation of hydrazine.

## DECLARATION

I declare that *Electrochemical responses of novel preferentially oriented platinum (100) nanoalloys for ammonia and hydrazine catalysis* is my own work, that it has not been submitted for any degree or examination in any other university, and that all sources I have used or quoted have been indicated and acknowledged by means of complete references.



UNIVERSITY of the  
WESTERN CAPE

Stephen Nzioki Mailu

May, 2013

Signed:

A handwritten signature in black ink, appearing to read "S. Nzioki Mailu".

## ACKNOWLEDGEMENT

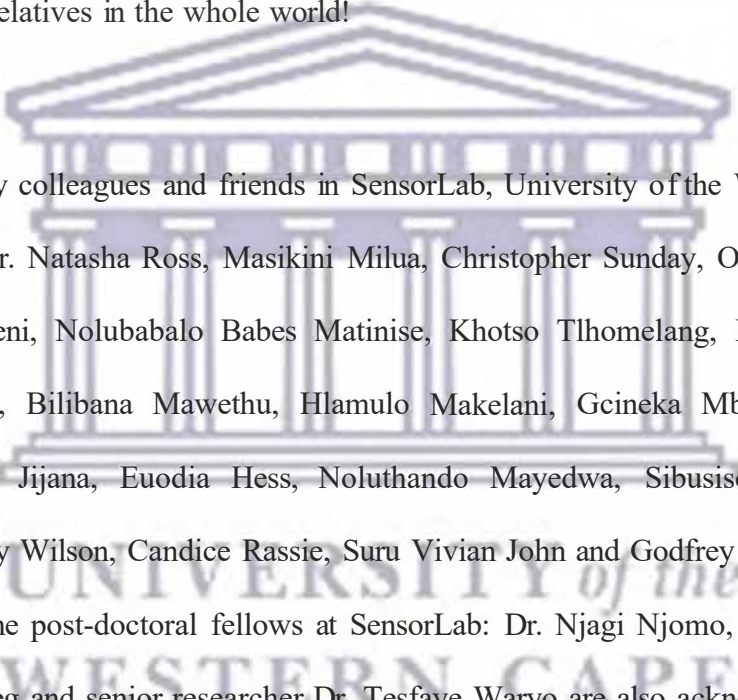
It is my pleasure to say thank you to the wonderful people God brought my way and on whose shoulders I stood to get to where I am today. Firstly, I would like to give the Almighty God, all the glory, honour and adoration for giving me the strength and wisdom through the Holy Spirit to complete my studies.

Many thanks to my supervisors: Professor Emmanuel I. Iwuoha and Professor Priscilla GL. Baker. I am intellectually indebted to you; thank you for your excellent supervision, support and encouragement as well as granting me the great chances to interact, learn and share knowledge at national and international conferences and workshops. Dr. Nazeem Jahed is highly appreciated for his continuous support and encouragement throughout the research period.

I would like to say a big thank you to Dr. Peter Munyao Ndongili; knowing you my "bhuti" is an encounter of a lifetime; you were more than a brother to me and an encouragement during the hard and stressful moments of my research work. Your contribution in making my dreams of pursuing post-graduate studies come true is wholeheartedly appreciated. The outstanding assistance accorded by Dr. Faiza 'Sister Boss' is highly appreciated. Special thanks are extended to my friends, Mr. & Mrs. Jones M. Mutua (my pastor), Mr. & Mrs. James Muthiani (my pastor), Mr. & Mrs. Jackson M. Nthuka, Mr. & Mrs. Benson Mutua, Mr. & Mrs. Thaddeus M. Mwololo, Mr. & Mrs. Chris K. Muindi, Mr. & Mrs. Mutua Mutunga, Mr. & Mrs. James N. Muinde and Mr. Samson N. Kimeu. To my great friend; Susan Mbithe Maingi, I deeply thank you for your unwavering moral support. I do also thank the students, staff and alumni of Clay international secondary school-Kenya for their moral support.



Much appreciation goes to all my family members especially my mother Mrs Rhodah Mumbi Mailu. Your love, care, encouragement and constant prayers are highly appreciated. You are a real gem and my inspiration in life! I am equally grateful to my late great dad Mr. Bredan Mailu Kituku (sweet father, I will always remember you) for my education and upbringing. A very big thank you to my sisters and brothers: Rabeca Mbula, Mary Kamene, Damaris Ngina, Irene Katunge, Nicholas Loki, Richard Kituku and Peter Kinyae; your love, care, support and encouragement all through the years has made me climb up the ladder to this far! You are the best relatives in the whole world!



The support of my colleagues and friends in SensorLab, University of the Western Cape; Dr. Fanelwa Ajayi, Dr. Natasha Ross, Masikini Milua, Christopher Sunday, Oluwakemi Tovide, Olubunmi Omoyeni, Nolubabalo Babes Matinise, Khotso Tlhomelang, Lundi Ngqongwa, Abebaw Tsegaye, Bilibana Mawethu, Hlamulo Makelani, Gcineka Mbambisa, Kerileng Molapo, Abogile Jijana, Euodia Hess, Noluthando Mayedwa, Sibusiso Qwasha, Carlo Baugaard, Lindsay Wilson, Candice Rassie, Suru Vivian John and Godfrey Fuku is gratefully acknowledged. The post-doctoral fellows at SensorLab: Dr. Njagi Njomo, Dr. Chinwe Ikpo, Dr. Abdul A. Baleg and senior researcher Dr. Tesfaye Waryo are also acknowledged. Special thanks to my great friend Tshifhiwa Mamphogoro "Chif"; you made it a lot easier for me during those critical times!

To the members of the Department of Chemistry, University of the Western Cape, South Africa and many other good people at UWC, I say thank you for the good and cordial working relationship that I enjoyed during my studies. Many thanks to the members of electron microscope unit (EMU), physics department, UWC: Prof. Basil, Dr. Subelia and Mr.

Adrian for the training they offered to me on how to operate the TEM and HRTEM and helping me analyse my samples using the HRTEM.

I gratefully acknowledge the National Research Foundation (NRF) of South Africa for funding my research programme. Finally, to Him who was, and is and is to come, my Lord Jesus, I remain forever grateful.



UNIVERSITY *of the*  
WESTERN CAPE

## DEDICATION

I dedicate this thesis to

My mother

Mrs. Rhodah Mumbi Mailu

&

To the memory of my beloved father Mr. Bredan Mailu Kituku.



UNIVERSITY *of the*  
WESTERN CAPE

## ACADEMIC OUTPUT

### List of publications

1. **Stephen N. Mailu**, Tesfaye Waryo, Peter M. Ndangili, Fanelwa R. Ngece, Abd A. Baleg, Priscilla G. Baker, Emmanuel I. Iwuoha, Determination of Anthracene on Ag-Au Alloy Nanoparticles/Overoxidized-Polypyrrole Composite Modified Glassy Carbon Electrodes, *Sensors*, 2010, 10, 9449-9465.
2. Rasaan A. Olowu, Omotayo Arotiba, **Stephen N. Mailu**, Tesfaye T. Waryo, Priscilla Baker, Emmanuel Iwuoha, Electrochemical Aptasensor for Endocrine Disrupting 17-Estradiol Based on a Poly(3,4-ethylenedioxythiophene)-Gold Nanocomposite Platform, *Sensors*, 2010, 10, 9872-9890.
3. Abd Almonam A. Baleg, Nazeem M. Jahed, Omotayo A. Arotiba, **Stephen N. Mailu**, Nicolette R. Hendricks, Priscilla G. Baker, Emmanuel I. Iwuoha, Synthesis and Characterization of Poly(propylene imine) Dendrimer - Polypyrrole Conducting Star Copolymer, *Journal of Electroanalytical Chemistry*, 2011, 652, 18-20.
4. Peter M. Ndangili, Abongile N. Jijana, Rasaan A. Olowu, **Stephen N. Mailu**, Fanelwa R. Ngece, Avril Williams, Tesfaye T. Waryo, Priscilla G.L. Baker, Emmanuel I. Iwuoha, Impedimetric Response of a Label-Free Genosensor Prepared on a 3-Mercaptopropionic Acid Capped Gallium Selenide Nanocrystal Modified Gold Electrode, *International Journal of Electrochemical Science*, 2011, 6, 1438-1453.
5. Faiza J. Iftikhar, Priscilla G.L. Baker, Abdul M. Baleg, Peter M. Ndangili, **Stephen N. Mailu**, Emmanuel I. Iwuoha, Modulation of the interfacial electrochemistry of surfactant-functionalised polypyrrole chemical sensor systems, *Electrochemical Acta*, 2011, 56, 5214-5221.

6. Rachel F. Ngece, Natasha West, Peter M. Ndangili,, Rasaan A Olowu, Avril Williams, Nicolette Hendricks, **Stephen Mailo**, Priscilla Baker, Emmanuel Iwuoha, A silver Nanoparticle/Poly (8-Anilino-1-Naphthalene Sulphonic Acid) Bioelectrochemical Biosensor System for the Analytical Determination of Ethambutol, *International Journal of Electrochemical Science*, 6 ,2011, 1820-1834.
7. Rasaan A Olowu, Avril Williams, Peter M. Ndangili, Rachel F Ngece, **Stephen N Mailo**, Priscilla Baker, Emmanuel Iwuoha, Impedimetry and microscopy of electrosynthetic poly(propylene thiophenoimine)-co-poly(3,4 ethylene dioxythiophene) dendritic star copolymer, *International Journal of Electrochemical Science*, 2011, 6, 1855-1870.
8. Kerileng M. Molapo, Peter M. Ndangili, Rachel F. Ajayi, Gcineka Mbambisa, **Stephen N. Mailo**, Njagi Njomo, Milua Masikini, Priscilla Baker, Emmanuel I. Iwuoha, Electronics of Conjugated Polymers (I): Polyaniline, *International Journal of Electrochemical Science*, 2012, 7, 11859-11875.
9. Rachel Ngece, Nicolette Hendricks, Natasha West, Peter M. Ndangili, Abongile Jijana, **Stephen Mailo**, Tesfaye Waryo, Priscilla Baker, Emmanuel Iwuoha, A silver nanoparticles-poly (8-anilino-1-naphthalene sulphonic acid) bioelectrochemical sensor system for the analytical determination of ethambutol, In V. Rajendra, B. Hillbrands, P. Prabu and K.E. Geckeler (eds.): *Biomedical Applications of Nanostructured Materials*, Macmillan Publishers India Limited, 2010, Pages 269-274.
10. **Stephen N. Mailo**, Tesfaye Waryo, Rasaan A. Olowu, Priscilla G. Baker, Emmanuel I. Iwuoha, Simultaneous amperometric detection of anthracene and phenanthrene on Ag-Au alloy nanoparticles/overoxidized-polypyrrole composite modified carbon electrode (*Submitted to Advanced Material Letters*).

11. **Stephen N. Mailu**, Tesfaye Waryo, Rasaan A. Olowu, Priscilla G. Baker, Emmanuel I. Iwuoha, Recent advances in synthesis, characterization and application of bimetallic alloy nanoparticles as novel materials in electrochemical sensors and enzyme biosensors (*Submitted to Electrochimica Acta*).
12. **Stephen N. Mailu**, Masikini Milua, Chinwe Ikpo, Tesfaye Waryo, Njagi Njomo, Faiza Iftkhar, Priscilla G. Baker, Emmanuel I. Iwuoha, Novel high-performance electrocatalytic Pd-Au-Ag clusters for ammonia oxidation 2013 (*Submitted to Advanced material letters*).
13. **Stephen N. Mailu**, Masikini Milua, Njagi Njomo, Chinwe Ikpo, Tesfaye Waryo, Priscilla G. Baker, Emmanuel I. Iwuoha, Reactivities of novel ultrasensitive symmetrical Pt(100) nanoalloy systems in ammonia oxidation 2013 (*Submitted to electrochemistry communication*).
14. **Stephen N. Mailu**, Masikini Milua, Tesfaye Waryo, Priscilla G. Baker, Emmanuel I. Iwuoha, Screening of electro-catalysts for direct ammonia fuel cell: Ammonia oxidation on Pt(100)M (M: Ir, Rh, IrAu, PdIr, PdRh and RhAu) nanoalloy systems 2013 (*in preparation for Chemical Communication*).
15. **Stephen N. Mailu**, Masikini Milua, Tesfaye Waryo, Priscilla G. Baker, Emmanuel I. Iwuoha, Highly Sensitive Hydrazine Electrochemical Sensor Based on Pt(100)Rh Nanoalloys Modified Carbon Electrode 2013 (*in preparation for International Journal of Electrochemical Science*).

## Oral Presentations

1. **Stephen N. Mailu**, Priscilla G. Baker and Emmanuel I. Iwuoha, Production of Hydrogen in Alkaline Media Via Ammonia Electrolysis, Young SACI Symposium, University of the Western Cape (UWC), South Africa, 24<sup>th</sup> -25<sup>th</sup> November, 2011.
2. **Stephen N. Mailu**, Priscilla G. Baker and Emmanuel I. Iwuoha, Synthesis, Characterisation and Application of Novel (100) Preferentially Oriented Platinum Nanoalloys for Direct Ammonia Fuel Cells, 2<sup>nd</sup> International symposium on Electrochemistry, Electrochemistry for energy, African Routes Conference Centre, University of the Western Cape (UWC), South Africa; 19-20<sup>th</sup> July, 2012.
3. **Stephen N. Mailu**, Priscilla G. Baker and Emmanuel I. Iwuoha, Facile Synthesis and Characterisation of Novel Pd-Au-Ag Nanoclusters and their Application as Electrocatalysts for Ammonia Oxidation, 63<sup>rd</sup> Annual Meeting of the International Society of Electrochemistry (ISE), Prague, Czech Republic, 19-24<sup>th</sup> August, 2012.
4. **Stephen N. Mailu**, Priscilla G. Baker and Emmanuel I. Iwuoha, Reactivities of novel ultrasensitive symmetrical Pt(100) nanoalloy systems in ammonia oxidation, Faculty of Science Postgraduate Research Open Day, University of the Western Cape (UWC), South Africa, 31<sup>st</sup> October, 2012.

## TABLE OF CONTENTS

<i>Title page</i> .....	<i>i</i>
<i>Keywords</i> .....	<i>ii</i>
<i>Abstract</i> .....	<i>iii</i>
<i>Declaration</i> .....	<i>vi</i>
<i>Acknowledgement</i> .....	<i>vii</i>
<i>Dedication</i> .....	<i>x</i>
<i>Academic output</i> .....	<i>xi</i>
<i>Table of contents</i> .....	<i>xv</i>
<i>List of figures</i> .....	<i>xxiv</i>
<i>List of tables</i> .....	<i>xxxiv</i>
<i>List of schemes</i> .....	<i>xxxv</i>
<i>List of abbreviations</i> .....	<i>xxxv</i>
CHAPTER ONE.....	1
INTRODUCTION .....	1
1.1 Background information .....	2
1.2 Problem statement .....	7
1.3 Rationale and motivation .....	8
1.4 Research aim and objectives .....	9
1.4.1 Aim .....	9
1.4.2 Objectives .....	9



1.5 Research framework.....	10
1.6 Thesis statement .....	11
1.7 Thesis outline .....	11
CHAPTER TWO .....	13
LITERATURE REVIEW .....	13
2.1 Fuel cells .....	14
2.1.1 Introduction .....	14
2.1.2 Fuel cells technology.....	15
2.1.3 Operating principle of fuel cells .....	16
2.1.4 Classification of fuel cells .....	17
2.1.4.1 Proton exchange membrane fuel cell (PEMFC) .....	18
2.1.4.1.1 Direct formic acid fuel cell (DFAFC) .....	19
2.1.4.1.2 Direct ethanol fuel cell (DEFC) .....	19
2.1.4.2 Alkaline fuel cell (AFC) .....	19
2.1.4.2.1 Proton ceramic fuel cell (PCFC) .....	20
2.1.4.2.2 Direct borohydride fuel cell (DBFC) .....	20
2.1.4.3 Phosphoric acid fuel cell (PAFC) .....	21
2.1.4.4 Molten carbonate fuel cell (MCFC) .....	21
2.1.4.5 Solid oxide fuel cell (SOFC).....	21
2.1.4.6 Direct methanol fuel cell (DMFC) .....	22
2.1.5 Sources of fuel for fuel cells .....	22
2.1.5.1 Hydrogen gas .....	23
2.1.5.1.1 Oxidation of ammonia for hydrogen production.....	23
2.1.5.1.2 Ammonia as a hydrogen carrier/hydrogen storage medium .....	24

2.1.5.1.3 Electro-oxidation of ammonia: thermodynamics .....	25
2.1.5.1.4 Technological challenges faced during hydrogen production .....	26
2.1.5.2 Hydrazine .....	27
2.1.5.2.1 Effects of exposure of hydrazine on humans .....	27
2.1.5.2.2 Uses of hydrazine .....	27
2.1.5.2.3 Hydrazine as a fuel for fuel cells .....	28
2.1.5.2.4 Oxidation of hydrazine .....	29
2.2 Nanotechnology .....	30
2.2.1 Introduction .....	30
2.2.2 Definitions and scope in nanotechnology .....	30
2.2.3 Nanoparticles .....	31
2.2.3.1 Prehistory of metal nanoparticles .....	33
2.2.3.2 Passivated (capped) metal nanoparticles .....	34
2.2.4 Nanoalloys .....	34
2.2.4.1 Reasons for studying nanoalloys .....	35
2.2.4.2 Isomerism in nanoalloys .....	35
2.2.4.2.1 Homotops .....	36
2.2.4.3 Types and structures of nanoalloys .....	37
2.2.4.3.1 Factors influencing the chemical ordering of nanoalloys .....	39
2.2.4.4 Application of nanoalloys .....	40
2.2.4.5 Platinum group metal (PGM) nanoalloys .....	43
2.2.4.6 Single crystal Pt(111) and Pt(100) materials .....	45
2.2.4.6.1 Preferentially oriented Pt(100) and (111) nanoparticles .....	47
2.2.4.7 Methods of synthesising nanoalloys .....	48
2.2.5 Characterisation techniques for the nanoalloys .....	52

2.2.5.1 Electrochemistry .....	52
2.2.5.1.1 Cyclic voltammetry (CV) .....	53
2.2.5.1.1.1 Data interpretation .....	56
2.2.5.1.2 Electrochemical impedance spectroscopy (EIS) .....	63
2.2.5.2 Microscopy .....	70
2.2.5.2.1 Electron microscopy .....	70
2.2.5.2.1.1 Transmission electron microscopy (TEM) .....	70
2.2.5.2.1.2 High resolution transmission electron microscopy (HRTEM) .....	71
2.2.5.2.1.3 Scanning transmission electron microscopy (STEM) .....	72
2.2.5.2.1.4 Scanning electron microscopy (SEM) .....	72
2.2.5.2.2 Scanning probe microscopy .....	73
2.2.5.2.2.1 Scanning tunneling microscopy (STM) .....	74
2.2.5.2.2.2 Atomic force microscopy (AFM) .....	75
2.2.5.3 Mass spectrometry .....	76
2.2.5.4 Diffraction .....	77
2.2.5.4.1 X-ray Diffraction (XRD) .....	77
2.2.5.4.2 Electron diffraction .....	77
2.2.5.5 X-ray spectroscopy .....	77
2.2.5.5.1 X-ray absorption spectroscopy (XAS) .....	77
2.2.5.5.2 X-ray photoelectron spectroscopy (XPS) .....	79
2.2.5.6 Energy disperse X-ray microanalysis (EDX) .....	79
2.2.5.7 Other spectroscopic techniques .....	80
2.2.5.7.1 UV-visible spectroscopy .....	80
2.2.5.7.2 Infrared (IR) spectroscopy .....	82
2.2.5.7.3 Photoelectron spectroscopy .....	83

2.2.5.7.4 Surface-enhanced Raman spectroscopy .....	83
2.2.5.7.5 Nuclear Magnetic Resonance (NMR) .....	83
2.2.5.7.6 Electrochemical NMR spectroscopy (EC-NMR) .....	84
2.2.5.8 Ion Spectroscopy/Scattering (IS) .....	84
CHAPTER THREE .....	85
EXPERIMENTAL SECTION .....	85
3.1 Reagents and materials .....	86
3.2. Measurements and instrumentations .....	86
3.3 Preparation of the nanoalloys .....	87
3.3.1. Synthesis of PdAu, PdAg and PdAuAg nanoalloys .....	87
3.3.2. Synthesis of polycrystalline Pt nanoparticles .....	88
3.3.3 Synthesis of preferentially oriented Pt(100) nanoparticles .....	88
3.3.4 Synthesis of Pt(100)M (M: Au, Pd, Ir, Rh, PdAu, IrAu, PdIr, RhAu) nanoalloys ..	89
3.4. Fabrication of Pt electrode with nanoalloys .....	90
3.5 Characterisation of the nanoalloys .....	91
3.5.1 Electrochemical characterisation .....	91
3.5.1.1 Cyclic voltammetry (CV) .....	91
3.5.1.2 Electrochemical impedance spectroscopy (EIS) .....	91
3.5.2 Morphological characterisation .....	92
3.5.2.1 High resolution transmission electron microscopy (HRTEM) .....	92
3.5.2.2 Atomic force microscopy (AFM) .....	92
3.5.3 UV-visible spectroscopy .....	92
3.6 Electrochemical oxidation of ammonia .....	93

3.7 Electrochemical oxidation of hydrazine .....	93
CHAPTER FOUR.....	94
RESULTS AND DISCUSSION: Part 1 .....	94
NOVEL HIGH-PERFORMANCE ELECTROCATALYTIC PdAuAg NANOALLOYS FOR AMMONIA OXIDATION .....	94
4.1 Introduction .....	95
4.2 Spectroscopic and microscopic characteristics of the nanoalloys .....	96
4.2.1 UV-visible spectroscopy .....	96
4.2.2 High resolution transmission electron microscopy .....	98
4.2.3 Energy dispersive X-ray spectroscopy (EDX) analysis .....	100
4.2.4 Atomic force microscopy (AFM) analysis .....	102
4.3 Electrochemistry of PdCh, AgNO <sub>3</sub> and HAuCl <sub>4</sub> ·3H <sub>2</sub> O .....	106
4.3.1. Redox behaviour of palladium chloride (PdCh) in solution .....	106
4.3.2 Redox behaviour of silver nitrate (AgNO <sub>3</sub> ) in solution .....	108
4.3.3 Behaviour of hydrogen tetrachloroaurate (III) trihydrate in solution .....	109
4.3.4 Behaviour of a mixture of PdCh, AgNO <sub>3</sub> and HAuCl <sub>4</sub> ·3H <sub>2</sub> O solutions .....	110
4.4 Electrochemical characteristics of PdAu, PdAg and PdAuAg nanoalloys .....	111
4.4.1 Electrochemistry of the nanoalloys in 0.1 M LiClO <sub>4</sub> .....	111
4.4.1.1 Effect of potential scan rates .....	114
4.4.2 Electrochemistry of the nanoalloys in 1 M KOH .....	116
4.4.3 Electrochemistry of PdAuAg nanoalloys in solution .....	118
4.5 The catalytic performance of PdAg, PdAu and PdAuAg nanoalloys .....	120
4.5.1 Catalytic oxidation of ammonia .....	120
4.5.1.1 Choice of potential window .....	120

4.5.1.2 Choice of supporting electrolyte .....	123
4.5.2 Effects of ammonia concentration .....	128
4.5.3 Effects of KOH concentration .....	129
4.5.4 Effects of scan rate .....	130
4.6 Sub conclusion .....	120
CHAPTER FIVE .....	134
RESULTS AND DISCUSSION: Part 2 .....	134
REACTIVITIES OF NOVEL ULTRASENSITIVE SYMMETRICAL Pt(100) NANOALLOY SYSTEMS IN AMMONIA OXIDATION .....	134
5.1 Introduction .....	135
5.2 Spectroscopic and morphological characterisation of preferentially oriented Pt(100) nanoparticles, Pt(100)Pd, Pt(100)Au and Pt(100)PdAu nanoalloy systems .....	136
5.2.1 UV-visible spectroscopy .....	136
5.2.2 High resolution transmission electron microscopy (HRTEM) .....	137
5.2.3 Energy dispersive X-ray spectroscopy (EDX) analysis .....	140
5.2.4 Atomic force microscopy (AFM) .....	143
5.3 Electrochemistry of the starting materials .....	145
5.3.1 Electrochemistry of K <sub>2</sub> PtCl <sub>6</sub> in solution .....	145
5.4 Electrochemistry of Pt(100)Au, Pt(100)Pd and Pt(100)PdAu nanoalloys .....	147
5.4.1 Cyclic voltammetric behaviour of the oriented nanoalloys .....	147
5.4.1.1 Electrochemistry of the nanoalloys in 0.5 M H <sub>2</sub> SO <sub>4</sub> solution .....	147
5.4.1.1.1 Determination of the electrochemical active surface area (ESA) .....	154
5.4.1.2 Electrochemistry of the nanoalloys in 1 M KOH solution .....	155
5.4.2 Impedimetric characteristics of the oriented nanoalloys in 1 M KOH solution ....	157

5.4.3 Electrochemistry of the oriented nanoalloys in $[\text{Fe}(\text{CN})_6]^{3-}$ .....	159
5.5 Catalytic performance of Pt(100)Au, Pt(100)Pd and Pt(100)PdAu nanoalloys .....	164
5.5.1 Electrocatalytic oxidation of ammonia .....	164
5.5.2 Effect of potential scan rates .....	168
5.5.3 Effect of ammonia concentration .....	169
5.6 Sub conclusion .....	164
CHAPTER SIX .....	172
RESULTS AND DISCUSSION: Part 3 .....	172
AMMONIA OXIDATION ON Pt(100)Ir, Pt(100)Rh, Pt(100)IrAu, Pt(100)PdIr and Pt(100)RhAu NANOALLOY SYSTEMS .....	172
6.1 Introduction .....	173
6.2 Spectroscopic and morphological characterisation of the oriented nanoalloys .....	173
6.2.1 UV-visible spectroscopy .....	173
6.2.2 High resolution transmission electron microscopy (HRTEM) .....	175
6.2.3 Energy dispersive X-ray spectroscopy (EDX analysis) .....	176
6.3 Electrochemical characteristics of the nanoalloys .....	179
6.3.1 Electrochemistry of the nanoalloys in 0.5 M $\text{H}_2\text{SO}_4$ test solution.....	179
6.3.2 Electrochemistry of the nanoalloys in 1 M KOH solution .....	180
6.4 Catalytic performance of the nanoalloys .....	182
6.4.1 Electrocatalytic oxidation of ammonia .....	182
6.5 Sub conclusion .....	185
CHAPTER SEVEN .....	186
RESULTS AND DISCUSSION: Part 4 .....	186

Pt(100) NANOALLOY SYSTEMS AS ELECTROCATALYSTS FOR HYDRAZINE OXIDATION .....	186
7.1 Introduction .....	187
7.2 Catalytic performance of Pt(100) nanoparticles and oriented Pt(100) nanoalloys .....	187
7.2.1 Electro-oxidation of hydrazine on Pt(100) nanoparticles modified GCE .....	187
7.2.1.1 Effect of scan rates .....	189
7.2.2 Electro-oxidation of hydrazine on Pt(100)Pd nanoalloy modified GCE .....	192
7.2.2.1 Effect of scan rates .....	193
7.2.3 Electro-oxidation of hydrazine on Pt(100)Au nanoalloy modified GCE .....	197
7.2.3.1 Effect of scan rates .....	198
7.2.4 Electro-oxidation of hydrazine on Pt(100)Ir, Pt(100)IrAu and Pt(100)PdIr nanoalloys modified GCE .....	200
7.2.4.1 Effect of scan rates.....	201
7.2.5 Electrocatalytic oxidation of hydrazine on Pt(100)Rh and Pt(100)RhAu nanoalloys modified GCE.....	204
7.2.5.1 Effect of scan rates .....	205
7.2.6 Comparison of the catalytic effects of the nanoalloys on hydrazine oxidation .....	207
7.3 Sub conclusion .....	208
CHAPTER EIGHT .....	209
GENERAL CONCLUSION AND RECOMENDATIONS .....	209
8.1 General conclusion .....	210
8.1.1 Summary of findings and contributions .....	210
8.2 Recommendations .....	213
References: .....	214



## LIST OF FIGURES

FIGURE	TITLE	PAGE
Figure 1:	Fuel cell operation diagram	17
Figure 2:	Examples of types of nanoparticles	33
Figure 3:	Examples of homotops in small nanoalloys	37
Figure 4:	Schematic representation of some nanoalloy mixing patterns	38
Figure 5:	The periodic table showing platinum group metals	44
Figure 6:	Top view of (a) Pt(100) and (b) Pt(1 11) surfaces	46
Figure 7:	Cyclic voltammograms of (a) Pt(100) nanoparticles and (b) Pt(1 11) nanoparticles modified Pt electrode in 0.5 M H <sub>2</sub> SO <sub>4</sub>	48
Figure 8:	Set-up for electrochemical synthesis of nanoalloys	49
Figure 9:	Schematic representation of an electrochemical cell	53
Figure 10:	A typical cyclic voltammogram showing the basic peak parameters	55
Figure 11:	The Randles-Sevcik plot ( $I_p$ against $v^{1/2}$ )	58
Figure 12:	Typical cyclic voltammograms for an irreversible electrochemistry process (curve A) and for quasi-reversible process (curve B)	61
Figure 13:	A typical impedance diagram	65
Figure 14:	A typical Nyquist plot	66
Figure 15:	A typical Nyquist plot showing some kinetic parameters	67
Figure 16:	A typical bode plot showing variation of impedance and phase angle with changes in frequency	68
Figure 17:	A bode plot showing some kinetic parameters	69
Figure 18:	Randles equivalent circuit for a simple electrochemical cell	69
Figure 19:	Schematic presentation of HRTEM (A) and an example of HRTEM image (B)	72

Figure 20:	An illustration of AFM probing a sample surface with a sharp tip (A) and an example of AFM image (B)	76
Figure 21:	Illustration of how a UV-vis spectrometer functions	82
Figure 22:	UV-vis spectra of palladium chloride, silver nitrate and Hydrogen tetrachloroaurate (III) trihydrate solutions	97
Figure 23:	UV-vis spectra of Pd nanoparticles, PdAg, PdAu and PdAgAu nanoalloys	97
Figure 24:	HRTEM images of Pd nanoparticles (A), PdAg nanoalloys (B) PdAu nanoalloys (C) and PdAuAg nanoalloys (D)	99
Figure 25a:	Energy dispersive X-ray spectrum of Pd nanoparticles	100
Figure 25b:	Energy dispersive X-ray spectrum of PdAg nanoalloys	101
Figure 25c:	Energy dispersive X-ray spectrum of PdAu nanoalloys	101
Figure 25d:	Energy dispersive X-ray spectrum of PdAuAg nanoalloys	102
Figure 26A:	(i) 2D and (ii) 3D AFM images of silicon substrates	103
Figure 26B:	(i) 2D and (ii) 3D AFM images of Pd nanoparticles	104
Figure 26C:	(i) 2D and (ii) 3D AFM images of PdAg nanoalloys	104
Figure 26D:	(i) 2D and (i) 3D AFM images of PdAu nanoalloys	105
Figure 26E:	(i) 2D and (ii) 3D AFM images of PdAuAg nanoalloys	105
Figure 27:	Cyclic voltammograms of Pt electrode in 0.1 M LiClO <sub>4</sub> (black curve) and 5 mM PdCh in 0.1 M LiClO <sub>4</sub> (red curve), (-500 to 1000 mV): Scan rate, 100 mV s <sup>-1</sup>	107
Figure 28:	Cyclic voltammograms of Pt electrode in 0.1 M LiClO <sub>4</sub> (black curve) and 5 mM PdCh in 0.1 M LiClO <sub>4</sub> (red curve), (-700 to 1000 mV): Scan rate, 100 mV s <sup>-1</sup>	107
Figure 29:	Cyclic voltammograms of Pt electrode in 0.1 M LiClO <sub>4</sub> (black curve)	

- and 5 mM AgNO<sub>3</sub> in 0.1 M LiClO<sub>4</sub> (red curve): Scan rate, 100 mV s<sup>-1</sup>. 108
- Figure 30: Cyclic voltammograms of Pt electrode in 0.1 M LiClO<sub>4</sub> (red curve) and 5 mM HAuCl<sub>4</sub>.3H<sub>2</sub>O in 0.1 M LiClO<sub>4</sub> (black curve): Scan rate, 100 mV s<sup>-1</sup>. 109
- Figure 31: Cyclic voltammograms of Pt electrode in a mixture of 5 mM solutions of PdCb, AgNO<sub>3</sub> and HAuCl<sub>4</sub>.3H<sub>2</sub>O in 0.1 M LiClO<sub>4</sub> at different scan rates 110
- Figure 32: Cyclic voltammograms of (A) PtPdNPs, (B) PtPdAuNPs, (C) PtPdAgNPs and (D) PtPdAuAgNPs electrodes in 0.1 M LiClO<sub>4</sub>: Scan rate, 100 mV s<sup>-1</sup>. 113
- Figure 33: Cyclic voltammograms of (A) PtPdNPs, (B) PtPdAuNPs, (C) PtPdAgNPs and (D) PtPdAuAgNPs in 0.1 M LiClO<sub>4</sub> at different scan rates 114
- Figure 34: Relationship between the peak currents and scan rates for PtPdAuAgNPs (peak b/b'). 115
- Figure 35: Cyclic voltammograms of (A) PtPdNPs, (B) PtPdAuNPs, (C) PtPdAgNPs and (D) PtPdAuAgNPs electrodes in 1 M KOH: Scan rate, 100 mV s<sup>-1</sup>. 117
- Figure 36: Cyclic voltammograms of PdAuAg nanoalloys in solution 119
- Figure 37: Relationship between the peak currents and scan rates for PdAuAg nanoalloys. 120
- Figure 38: Cyclic voltammograms measured on bare Pt electrode (a) with and (b) without 0.1 M ammonia in 1 M KOH: Scan rate, 50 mV s<sup>-1</sup>. 121
- Figure 39: Cyclic voltammograms of bare Pt electrode in 0.1 M ammonia and 1

	M KOH aqueous solution with various upper sweep limits; (600,400, 100, 0, -200, -400, -600 mV): Scan rate, 50 mVs <sup>-1</sup>	122
Figure 40:	Cyclic voltammograms measured on bare Pt electrode (a) with and (b) without 0.1 M ammonia (-1000 mV to 100 mV)	122
Figure 41:	Cyclic voltammograms measured on bare Pt electrode with and without 0.1 M LiClO <sub>4</sub> .	124
Figure 42:	Cyclic voltammograms measured on bare Pt electrode with and without 1 M KOH	124
Figure 43:	Cyclic voltammograms of PtPdAgNPs (A), PtPdAuNPs (B), PtPdNPs (C) and PtPdAuAgNPs (D) electrodes in 0.1 M ammonia and 1 M KOH aqueous solution: Scan rate, 50 mV s <sup>-1</sup>	126
Figure 44:	Overlay CVs of bare Pt, PtPdNPs, PtPdAgNPs, PtPdAuNPs and PtPdAuAgNPs electrodes in 0.1 M ammonia and 1 M KOH aqueous solution: Scan rate, 50 mV s <sup>-1</sup>	127
Figure 45:	Cyclic voltammograms of PtPdAuAgNPs in 1 M KOH solutions with various concentrations of ammonia (0.05-2 M ammonia)	129
Figure 46:	Cyclic voltammograms of PtPdAuAgNPs in 0.1 M ammonia solutions with various KOH concentrations	130
Figure 47:	Cyclic voltammogram of PtPdAuAgNPs electrode in the presence of 0.1 M ammonia and 1 M KOH aqueous solution at different scan rates	131
Figure 48:	Randles-Sevcik plot of PtPdAuAgNPs electrode in 0.1 M ammonia and 1 M KOH aqueous solution.	131
Figure 49:	Relationship between the oxidation peak potential (E <sub>p</sub> ) and log of scan rate	132

Figure 50:	UV-visible spectra of $K_2PtCl_6$ , $H AuCl_4 \cdot 3H_2O$ and PdCh salts	136
Figure 51:	UV-visible spectra of Pt(100), Pt(100)Pd, Pt(100)Au and Pt(100)PdAu nanoparticles	137
Figure 52:	HRTEM images of Pt nanoparticles	138
Figure 53:	HRTEM images of Pt(100) nanoparticles (A), Pt(100)Pd nanoalloys (B), Pt(100)Au nanoalloys (C) and Pt(100)PdAu nanoalloys (D)	139
Figure 54:	Schematic illustration of (a) sodium polyacrylate and (b) sodium polyacrylate-capped nanoparticle/nanoalloy	140
Figure 55a:	Energy dispersive X-ray spectrum of Pt(100) nanoparticles	141
Figure 55b:	Energy dispersive X-ray spectrum of Pt(100)Pd nanoalloys	141
Figure 55c:	Energy dispersive X-ray spectrum of Pt(100)Au nanoalloys	142
Figure 55d:	Energy dispersive X-ray spectrum of Pt(100)PdAu nanoalloys	142
Figure 56a:	(i) 2D and (ii) 3D AFM images of Pt(100) nanoparticles	143
Figure 56b:	(i) 2D and (ii) 3D AFM images of Pt(100)Pd nanoalloys	143
Figure 56c:	(i) 2D and (ii) 3D AFM images of Pt(100)Au nanoalloys	144
Figure 56d:	(i) 2D and (ii) 3D AFM images of Pt(100)PdAu nanoalloys	144
Figure 57:	Cyclic voltammogram of Pt electrode in 5 mM $K_2PtCl_6$ salt and 0.1 M $LiClO_4$ ; Scan rate, $50 \text{ mV s}^{-1}$	146
Figure 58:	Cyclic voltammograms of Pt electrode in 5 mM $K_2PtCl_6$ and 0.1 M $LiClO_4$ solution at different scan rates	146
Figure 59:	Cyclic voltammograms of (a) polycrystalline Pt nanoparticles and (b) Pt(100) nanoparticles modified Pt electrode; Test solution: 0.5 M $H_2SO_4$ ; Scan rate, $20 \text{ mV s}^{-1}$	149
Figure 60:	Cyclic voltammograms of Pt(100) nanoparticles modified Pt electrode at different scan rates; Test solution: 0.5 M $H_2SO_4$	151

Figure 61:	Relationship between the peak currents and scan rates for Pt(100) nanoparticles modified Pt electrode (peak b/b')	151
Figure 62:	Cyclic voltammograms of (a) Pt(100)Au nanoalloys and (b) Pt(100)Pd nanoalloys modified Pt electrode at different scan rates; Test solution: 0.5 M H <sub>2</sub> SO <sub>4</sub>	153
Figure 63:	Cyclic voltammograms of Pt(100)PdAu nanoalloys modified Pt electrode at different scan rates; Test solution: 0.5 M H <sub>2</sub> SO <sub>4</sub>	153
Figure 64:	Cyclic voltammograms of Pt/Pt(100)NPs (A), Pt/Pt(100)AuNPs (B), Pt/Pt(100)PdNPs (C), Pt/Pt(100)PdAuNPs (D) in 1 M KOH: Scan rate, 100 mV s <sup>-1</sup>	156
Figure 65:	Nyquist plots of bare Pt electrode, Pt/Pt(100)NPs, Pt/Pt(100)PdNPs, Pt/Pt(100)AuNPs and Pt/Pt(100)PdAuNPs in 1 M KOH	157
Figure 66:	Equivalent circuit	158
Figure 67:	Cyclic voltammograms of Pt/Pt(100)PdAuNPs (curve a), Pt/Pt(100)AuNPs (curve b), Pt/Pt(100)PdNPs (curve c), Pt/Pt(100)NPs (curve d) and bare Pt electrode (curve e) in 5 mM K <sub>3</sub> Fe(CN) <sub>6</sub> /Fe(CN) <sub>6</sub> solution: Scan rate, 100 mV s <sup>-1</sup> .	160
Figure 68:	Nyquist plots of Pt electrode (curve a), Pt/Pt(100)NPs (curve b) Pt/Pt(100)AuNPs (curve c), Pt/Pt(100)PdNPs (curve d), and Pt/Pt(100)PdAuNPs (curve e) in the presence of [Fe(CN) <sub>6</sub> ] <sup>3-/4-</sup> .	161
Figure 69:	Cyclic voltammograms of (a) bare Pt electrode, (b) Pt/Pt(100)PdAuNPs, (c) Pt/Pt(100)AuNPs and (d) Pt/Pt(100)PdNPs electrodes in 1 M KOH and 0.1 M ammonia: Scan rate, 100 mV s <sup>-1</sup>	165
Figure 70:	Cyclic voltammograms of a) Pt/PtNPs electrode and b)	

	Pt/Pt(100)NPs electrode in 1 M KOH and 0.1 M ammonia: Scan rate, 100 mV s <sup>-1</sup>	166
Figure 71:	Cyclic voltammograms of Pt/PtNPs electrode and Pt/Pt(100)NPs electrode in 1 M KOH and 0.1 M ammonia: Scan rate, 100 mV s <sup>-1</sup>	166
Figure 72:	Cyclic voltammograms of bare Pt electrode, Pt/Pt(100)PdAuNPs, Pt/Pt(100)PdNPs, Pt/Pt(100)AuNPs and Pt/Pt(100)NPs electrodes 1 M KOH and 0.1 M ammonia: Scan rate, 100 mV s <sup>-1</sup>	167
Figure 73:	Cyclic voltammograms of Pt/Pt(100)NPs electrode in the presence of 0.1 M ammonia in 1 M KOH aqueous solution at different scan rates	168
Figure 74:	Randles-Sevcik plot of Pt/Pt(100)NPs electrode in the presence of 0.1 M ammonia and 1 M KOH aqueous solution.	169
Figure 75:	Cyclic voltammograms of Pt/Pt(100)NPs in 1 M KOH solutions with various concentrations of ammonia (0-0.0125 M)	170
Figure 76:	UV-visible spectra of H <sub>2</sub> IrCl <sub>6</sub> ·H <sub>2</sub> O and Na <sub>3</sub> RhCl <sub>6</sub> salts	174
Figure 77:	UV-visible spectra of Pt(100)Ir, Pt(100)Rh, Pt(100)IrAu, Pt(100)PdIr and Pt(100)RhAu nanoalloys	174
Figure 78:	HRTEM images of Pt(100)PdIr nanoalloys (A), Pt(100)Rh nanoalloys (B), Pt(100)RhAu nanoalloys (C), Pt(100)Ir nanoalloys (D) and Pt(100)IrAu nanoalloys (E)	176
Figure 79:	EDX Spectrum of Pt(100)PdIr nanoalloys	177
Figure 80:	EDX Spectrum of Pt(100)RhAu nanoalloys	177
Figure 81:	EDX Spectrum of Pt(100)Rh nanoalloys	178
Figure 82:	EDX Spectrum of Pt(100)IrAu nanoalloys	178
Figure 83:	Cyclic voltammograms of (a) Pt(100)RhNPs, Pt(100)IrNPs, Pt(100)IrAuNPs and (b) Pt(100)PdIrNPs, Pt(100)RhAuNPs modified	

	Pt electrode in 0.5 M H <sub>2</sub> SO <sub>4</sub> at different scan rates	180
Figure 84:	Cyclic voltammograms of Pt Pt(100)IrNPs, Pt Pt(100)IrAuNPs, and Pt Pt(100)PdIrNPs (a) and Pt Pt(100)RhNPs and Pt Pt(100)RhAuNPs in 1 M KOH at a scan rate of 100 mV s <sup>-1</sup>	181
Figure 85:	Cyclic voltammograms of (a) Pt Pt(100)IrNPs, (b) Pt Pt(100)RhNPs, (c) Pt Pt(100)IrAuNPs, (d) Pt Pt(100)PdIrNPs and (e) Pt Pt(100)RhAuNPs in 1 M KOH and 0.1 M ammonia at a scan rate of 100 mV s <sup>-1</sup>	183
Figure 86:	Cyclic voltammograms of Pt(100)Ir, Pt(100)Rh, Pt(100)IrAu, Pt(100)PdIr and Pt(100)RhAu nanoalloys modified Pt electrode in 0.1 M ammonia and 1 M KOH at a scan rate of 100 mV s <sup>-1</sup>	184
Figure 87:	Cyclic voltammograms of 10 mM hydrazine at Pt(100)NPs/GCE (curve a) and bare GCE (curve b) in 0.1 M PBS (pH 7.4) at scan rate 50 mV s <sup>-1</sup> . The voltammograms c and d are the backgrounds.	188
Figure 88:	Cyclic voltammograms of Pt(100)NPs/GCE in 0.1 M PBS (pH 7.4) containing 10 mM hydrazine at various scan rates	190
Figure 89:	Randles-Sevcik plot of Pt(100)NPs/GCE in 0.1 M PBS (pH 7.4) containing 10 mM hydrazine.	191
Figure 90:	Relationship between the oxidation peak potential (E <sub>p</sub> ) and log of scan rate for Pt(100)NPs/GCE in 0.1 M PBS (pH 7.4) containing 10 mM hydrazine	191
Figure 91:	Cyclic voltammograms of 10 mM hydrazine at Pt(100)PdNPs/GCE (curve a) and bare GCE (curve b) in 0.1 M PBS (pH 7.4) at scan rate 50 mV s <sup>-1</sup> . The voltammograms c and d are the backgrounds.	192
Figure 92:	Cyclic voltammograms of Pt(100)PdNPs/GCE in 0.1 M PBS (pH 7.4)	



	containing 10 mM hydrazine at various scan rates.	193
Figure 93:	Randles-Sevcik plot of Pt(100)PdNPs/GCE in 0.1 M PBS (pH 7.4) containing 10 mM hydrazine	194
Figure 94:	Relationship between the oxidation peak potential ( $E_p$ ) and log of scan rate for Pt(100)PdNPs/GCE in 0.1 M PBS (pH 7.4) containing 10 mM hydrazine	196
Figure 95:	Cyclic voltammograms of 10 mM hydrazine at (a) Pt(100)AuNPs/GCE and (b) bare GCE in 0.1 M PBS (pH 7.4) at scan rate $50 \text{ mV s}^{-1}$ . The voltammograms c and d are the backgrounds.	198
Figure 96:	Cyclic voltammograms of Pt(100)AuNPs/GCE in 0.1 M PBS (pH 7.4) containing 10 mM hydrazine at various scan rates	199
Figure 97:	Randles-Sevcik plot of Pt(100)AuNPs/GCE in 0.1 M PBS (pH 7.4) containing 10 mM hydrazine	199
Figure 98:	Relationship between the oxidation peak potential ( $E_p$ ) and log of scan rate for Pt(100)AuNPs/GCE in 0.1 M PBS (pH 7.4) containing 10 mM hydrazine	200
Figure 99:	Cyclic voltammograms of 10 mM hydrazine at bare GCE (curve a), Pt(100)IrNPs/GCE (curve b), Pt(100)PdIrNPs/GCE (curve c), and Pt(100)IrAuNPs/GCE (curve d) in 0.1 M PBS (pH 7.4) at a scan rate of $50 \text{ mV s}^{-1}$ . The voltammograms e, f and g are the backgrounds.	201
Figure 100:	Cyclic voltammograms of Pt(100)IrNPs/GCE in 0.1 M PBS (pH 7.4) containing 10 mM hydrazine at various scan rates and a plot of peak current versus the square root of scan rate	202
Figure 101:	Cyclic voltammograms of Pt(100)IrAuNPs/GCE in 0.1 M PBS (pH 7.4) containing 10 mM hydrazine at various scan rates and a plot of	

peak current versus the square root of scan rate 203

Figure 102: Cyclic voltammograms of Pt(100)PdIrNPs/GCE in 0.1 M PBS (pH 7.4) containing 10 mM hydrazine at various scan rates and a plot of peak current versus the square root of scan rate 203

Figure 103: Cyclic voltammograms of 10 mM hydrazine at bare GCE (curve a), Pt(100)RhNPs/GCE (curve b) and Pt(100)RhAuNPs/GCE (curve c) in 0.1 M PBS (pH 7.4) at scan rate  $50 \text{ mV s}^{-1}$ . Curves e, f and g represent CVs at 0 mM hydrazine. 205

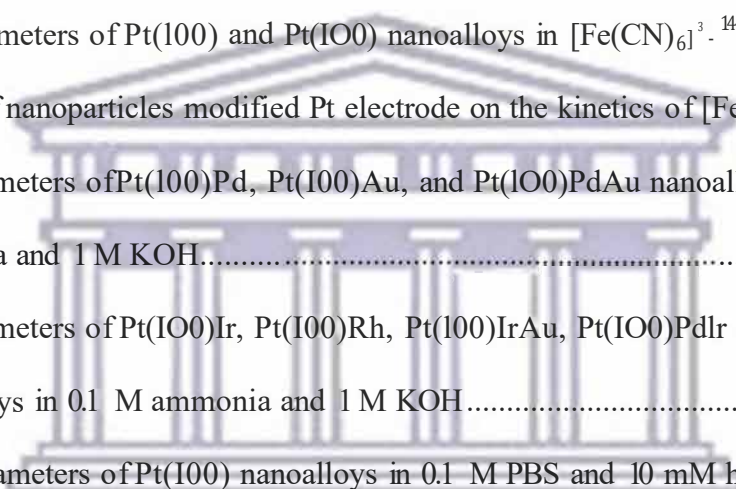
Figure 104: Cyclic voltammograms of Pt(100)RhNPs/GCE in 0.1 M PBS (pH 7.4) containing 10 mM hydrazine at various scan rates and a plot of peak current versus the square root of scan rate 206

Figure 105: Cyclic voltammograms of Pt(100)RhAuNPs/GCE in 0.1 M PBS (pH 7.4) containing 10 mM hydrazine at various scan rates and a plot of peak current versus the square root of scan rate 206



## LIST OF TABLES

<b>TABLE</b>	<b>TITLE</b>	<b>PAGE</b>
Table 1:	Comparison of different generation systems.....	15
Table 2:	CV parameters of Pd nanoalloy systems in 0.1 M ammonia and 1 M KOH .....	127
Table 3:	Active surface area values for the different nanoparticles.....	155
Table 4:	EIS parameters of Pt(100) and Pt(100) nanoalloys in 1 M KOH .....	158
Table 5:	CV peak parameters of Pt(100) and Pt(100) nanoalloys in $[\text{Fe}(\text{CN})_6]^{3-14}$ .....	160
Table 6:	EIS parameters of Pt(100) and Pt(100) nanoalloys in $[\text{Fe}(\text{CN})_6]^{3-14}$ .....	162
Table 7:	Effect of nanoparticles modified Pt electrode on the kinetics of $[\text{Fe}(\text{CN})_6]^{3-14}$ .....	163
Table 8:	CV parameters of Pt(100)Pd, Pt(100)Au, and Pt(100)PdAu nanoalloys in 0.1 M ammonia and 1 M KOH.....	167
Table 9:	CV parameters of Pt(100)Ir, Pt(100)Rh, Pt(100)IrAu, Pt(100)PdIr and Pt(100)RhAu nanoalloys in 0.1 M ammonia and 1 M KOH.....	184
Table 10:	CV parameters of Pt(100) nanoalloys in 0.1 M PBS and 10 mM hydrazine.....	207
Table 11:	CV peak parameters of Pt(100) nanoalloys in 0.1 M ammonia and 1 M KOH ....	212

  
 UNIVERSITY of the  
 WESTERN CAPE

## LIST OF SCHEMES

SCHEME	TITLE	PAGE
Scheme 1:	Research framework.....	10
Scheme 2:	Methodology used for the synthesis of PdAgAu nanoalloys.....	88
Scheme 3:	Methodology used for the synthesis of Pt(100)PdAu nanoalloys.....	90
Scheme 4:	Schematic representation of Pt electrode surface with Pd nanoparticles .....	112
Scheme 5:	Schematic representation of hydrazine oxidation.....	189

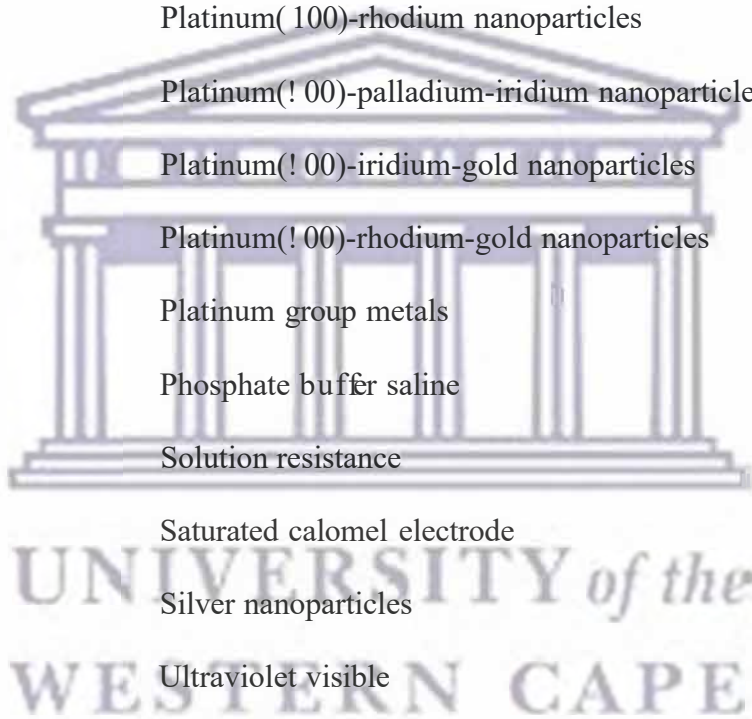


UNIVERSITY *of the*  
WESTERN CAPE

## LIST OF ABBREVIATIONS

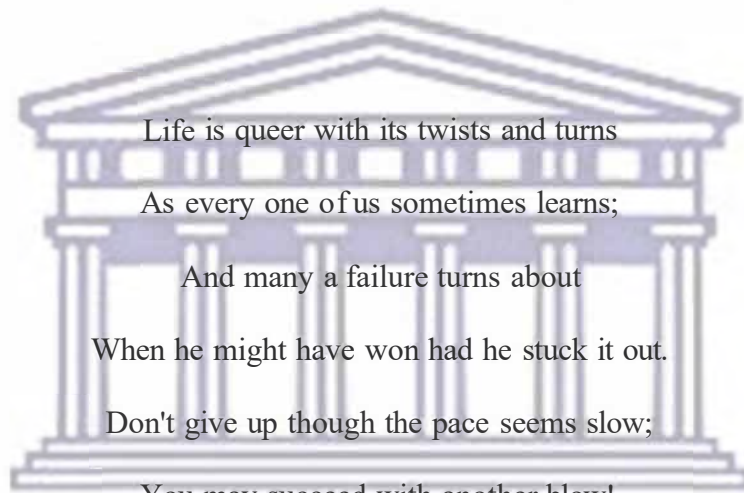
CV	Cyclic voltammetry
CPE	Constant phase element
$R_{ct}$	Charge transfer resistance
$I$	Current
DBFC	Direct borohydride fuel cell
DHFC	Direct hydrazine fuel cell
DMFC	Direct methanol fuel cell
$\Delta E_p$	Difference in potential peak potentials
EIS	Electrochemical impedance spectroscopy
EDX	Energy dispersive X-ray spectroscopy
$E^{\circ}$	Formal potential
$E^{\circ}$	Standard potential
AuNPs	Gold nanoparticles
GCE	Glassy carbon electrode
HFC	Hydrogen fuel cell
HRTEM	High resolution transmission electron microscopy
NPs	Nanoparticles
PGM	Platinum group metal
PVP	Polyvinylpyrrolidone
$E_{p,a}$	Peak anodic potential
$E_{p,c}$	Peak cathodic potential
$i_{p,a}$	Peak anodic current
$i_{p,c}$	Peak cathodic current
PdAuNPs	Palladium-gold nanoparticles

PdAgNPs	Palladium-silver nanoparticles
PdAuAgNPs	Palladium-gold-silver nanoparticles
Pt(100)NPs	Platinum(100) nanoparticles
Pt(100)AuNPs	Platinum(100)-gold nanoparticles
Pt(100)PdNPs	Platinum(100)-palladium nanoparticles
Pt(100)PdAuNPs	Platinum(100)-palladium-gold nanoparticles
Pt(100)IrNPs	Platinum(100)-iridium nanoparticles
Pt(100)RhNPs	Platinum(100)-rhodium nanoparticles
Pt(100)PdIrNPs	Platinum(100)-palladium-iridium nanoparticles
Pt(100)IrAuNPs	Platinum(100)-iridium-gold nanoparticles
Pt(100)RhAuNPs	Platinum(100)-rhodium-gold nanoparticles
PGMs	Platinum group metals
PBS	Phosphate buffer saline
$R_s$	Solution resistance
SCE	Saturated calomel electrode
AgNPs	Silver nanoparticles
UV-vis	Ultraviolet visible

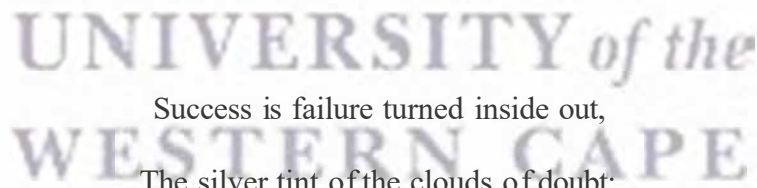


## DON'T QUIT

When things go wrong, as they sometimes will,  
When the road you're trudging seems all uphill,  
When the funds are low and the debts are high,  
And you want to smile but you have to sigh,  
When care is pressing you down a bit,  
Rest if you must, but don't you quit.



Life is queer with its twists and turns  
As every one of us sometimes learns;  
And many a failure turns about  
When he might have won had he stuck it out.  
Don't give up though the pace seems slow;  
You may succeed with another blow!



Success is failure turned inside out,  
The silver tint of the clouds of doubt;  
And you never can tell how close you are,  
It may be near when it seems so far.  
So stick to the fight when you're hardest hit;  
It's when things seem worst that you mustn't quit.

*Unknown author*

# CHAPTER ONE

## INTRODUCTION

### *Summary*

*This chapter gives a brief background on the aspects involved in this project namely, fuel cells and nanoalloys with particular emphasis on the use of nanoalloys as electrocatalysts for the oxidation of ammonia and hydrazine. The focus in this chapter is the relationship between the structure of the nanoalloys and their catalytic effects. The project's rationale and motivation, the aim and specific objectives and the thesis outline are also included in the chapter.*

The logo of the University of the Western Cape, featuring a stylized classical building with six columns and a pediment.

UNIVERSITY of the  
WESTERN CAPE



## 1.1 Background information

Fuel cells are increasing in popularity as alternative energy suppliers. They have the potential to revolutionise the way we power our nation, offering cleaner, more-efficient alternatives to the combustion of gasoline and other fossil fuels. They also have the potential to replace the internal combustion engine in vehicles and provide power in stationary and portable power applications because they are energy-efficient, clean, and fuel-flexible [1-2]. Electric energy generated by the fuel cell can either be stored in batteries or used directly to feed an electric motor to power an electric vehicle. The commonly used fuels in fuel cells are hydrogen, hydrazine, methanol and ethanol [3-4]. The combustion of hydrocarbons and alcohols such as methanol and ethanol generate various pollutant gases such as carbon monoxide, carbon dioxide and ozone which lead to environmental hazards or pollution. Hydrogen and hydrazine have been identified as suitable fuels for fuel cells. However, one problem with hydrogen is its safe handling, although it is the main fuel source for power generation in many of the fuel cells. Its storage and transportation is a major issue. The use of hydrogen as a fuel for wide-spread distribution in either gaseous or liquid form poses numerous safety, technical, and economic problems that make its use as a fuel prohibitively difficult [5]. In the absence of a hydrogen pipeline network, small-scale users purchase merchant hydrogen as compressed gas in steel cylinders, or as liquid hydrogen in cryogenic containers which is quite dangerous [6].

Moreover, interest in hydrogen fuel-cell vehicles (HFCVs) has been increasing in popularity over the past decade. This is primarily a result of the shrinking oil reserves which are expected to last only 42 years as of 1998 [7]. HFCVs have also found a niche in the environmental and political fields because the scientific community has begun to acknowledge the threat posed by harmful air pollutants such as nitrogen oxides ( $\text{NO}_x$ ),

volatile organic compounds (VOCs), carbon monoxide (CO), and sulphur dioxide (SO<sub>2</sub>) caused by hydrocarbon-dependent vehicles [8-9]. In addition to being environmentally friendly, HFCVs are efficient and convert 50-60% of the energy available in hydrogen to power the automobile rather than the mediocre 20-30% efficiency of today's internal combustion engines [10-11]. The demand for the use of hydrogen is not only driven by the transportation sector but by a movement for reducing oil imports in general and eliminating the dependence on petroleum for daily energy production. By 2020, the world population is expected to increase from 6 to 7.4 billion. Understandably, the energy demand is expected to increase from  $101 \times 10^{12}$  to  $160 \times 10^{12}$  kWh [7]. Thus, there is a need for a movement to refocus attention on in-situ hydrogen generating technologies for fuel cell utilisation. For a hydrogen economy to evolve in our lifetime, hydrogen will need to be produced, distributed, and stored on a mass scale in a manner that is cost effective, environmentally advantageous and efficient. One approach to resolve the drawbacks of hydrogen as a fuel includes considering less expensive and simpler materials that can act as hydrogen carrier. Several on-site methods of producing hydrogen have been considered; for example, water electrolysis, by reforming of alcohols, hydrocarbons and by dissociation of liquid ammonia. Liquid ammonia has been identified as a suitable hydrogen carrier. It offers a significant advantage over pure hydrogen in cost and it is a convenient way of storing hydrogen as an alternative fuel for clean energy supply [12]. It contains 1.7 times the amount of hydrogen that is contained in the same volume of liquid hydrogen, boasts a specific energy density 50% higher than liquid hydrogen for a given volume, is characterised by being produced in large quantities, non-flammable and is readily obtained and handled in liquid form without need for expensive and complicated refrigeration technology [13-14]. Moreover, it has a higher power density and lower cost per kW than methanol and can be electrolysed to release hydrogen and nitrogen with minimum effects to the environment [14]. Liquid ammonia is therefore an

excellent storage medium for hydrogen even though the endothermic ammonia cracking results in some efficiency penalty. Ammonia can be cracked into hydrogen and nitrogen in a suitable separation unit according to the reaction:  $2\text{NH}_{3(g)} \rightarrow \text{N}_{2(g)} + 3\text{H}_{2(g)}$ . The dissociation rate is dependent on temperature, pressure and catalysts [14]. Since the cracking of ammonia is a slow process, there is a need for use of a suitable catalyst to aid in faster dissociation of the ammonia to nitrogen and hydrogen.

Several studies have been devoted to the development of efficient catalysts for ammonia oxidation in alkaline and neutral solutions. Platinum is the most active catalyst for this process, however it is expensive and gets deactivated easily by adsorbed nitrogen  $\text{CN}_x(\text{s})$ . To lower the deactivation rate of Pt, various bimetallic catalysts have previously been investigated such as Pt-Ir, Pt-Ir-Rh, Pt-Ru, Pt-Ni and Pt-Pd [15-20]. Moreover, ammonia electro-oxidation has also been studied using metal oxide electrodes, e.g.  $\text{IrO}_2$ ,  $\text{PtO}_x$ - $\text{IrO}_x$  and  $\text{Ni/NiO}_x$  electrodes in alkaline and neutral solutions [21-25]. Most of these reactions were done using bulk metal or metal oxide electrodes with high precious metal loading. In order to develop efficient and economically viable electrodes, the amount of precious metals must be reduced. This can be achieved by using electrocatalysts in the form of nanoparticles which are considered as required materials for practical purposes [15] and which are known to improve the reaction rates of systems they catalyse due to their better physicochemical properties [26-27]. However, it has been found that majority of the electrocatalytic reactions such as  $\text{O}_2$  reduction,  $\text{N}_2\text{H}_4$  oxidation,  $\text{CO}_2$  reduction and ammonia oxidation are structure-sensitive or site demanding; thus controlling the crystallographic surface orientation of Pt and Pt based nanoparticles could result in much improved catalysts [28]. Ammonia oxidation on platinum surfaces being a very structure-sensitive reaction occurs predominantly on Pt(100) sites [29]. Therefore, in order to develop good electrocatalysts for the oxidation of ammonia,

a major goal would be the preparation of nanoparticles with the largest density of Pt(100) sites. Vidal-Iglesias *et al.* studied the oxidation of ammonia using Pt-based nanoparticles (Pt-Ir, Pt-Rh, Pt-Pd, Pt-Ru) and preferentially oriented Pt(100) nanoparticles [30]. The authors showed that Pt(100) nanoparticles had higher current density than polycrystalline Pt nanoparticles and Pt-based nanoparticles towards the oxidation of ammonia denoting that the reaction is highly surface-sensitive and takes place almost exclusively on Pt(100) domains. Extensive studies have also been done on the use of model electrodes (single crystal electrodes) towards the oxidation of ammonia with Pt(100) single crystal electrodes showing the highest electrocatalytic effect [29]. It is well known that bimetallic and multi-metallic nanoparticles show higher catalytic properties than monometallic nanoparticles [31-34]. Alloying Pt(100) with other metals is expected to show better catalytic properties due to the unique synergistic properties that is exhibited by nanoalloys [35]. The catalytic effect that exists in Pt(100) nanoparticles upon the inclusion of adatoms such as Au, Pd, Rh and Ir to form binary and ternary nanoalloys as electrocatalysts for the oxidation of ammonia is worth investigating.

On the other hand, hydrazine is also considered a potential fuel to power fuel cells for mobile applications [3]. Carbon-free fuel such as hydrazine ( $N_2H_4$ ) is of particular interest since its consumption yields  $N_2$  as the main product [36]. The utilisation of hydrazine for direct hydrazine fuel cells (DHFCs) in an alkaline electrolyte solution has been suggested since the 1960s [37]. However, a report on the toxicity of hydrazine published in 1977 hindered further research on DHFCs as it was reported that hydrazine is both highly toxic and mutagenic [37]. Daihatsu Motor Co. addressed the toxicity concerns of using hydrazine by developing a detoxification technique in which hydrazine is safely stored as hydrazone ( $>C=N-NH_2$ ) or

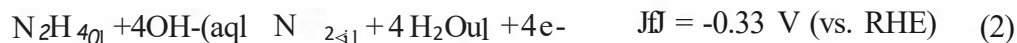
hydrazide (-CO-NH-NH<sub>2</sub>). Hydrazine is then released by the addition of a solvent when required [3 7].

Hydrazine (N<sub>2</sub>H<sub>4</sub>) is a compound with high hydrogen content (12.5 wt.%). Its hydrogen storage capability is higher than that of sodium borohydride (10.6 wt.%) and equivalent to that of methanol [3-4]. Direct hydrazine fuel cells (DHFCs) demonstrate a high electric motive force (EMF) of 1.61 V which is close to that of the direct borohydride fuel cell (DBFC) (1.64 V) and higher than that of direct methanol fuel cell (DMFC) (1.21 V). When hydrazine is used as a fuel to power the DHFCs, nitrogen and water are formed as shown in the following reaction [3]:



Nitrogen and water can be directly released to air without any harm to environment. This makes the fuel cell system design of the DHFC very simple. More so, nitrogen as the raw material for hydrazine synthesis can easily be obtained from air. The theoretical cell voltage for a direct hydrazine fuel cell is 1.56 V, higher than that of a hydrogen fuel cell. The electrochemical half-reactions are as follows:

Anode reaction:



Cathode reaction:



Overall cell reaction:



A number of different catalysts have been reported for the anodic oxidation of hydrazine. Among these catalysts are Pt, Pd, Ag, Au, Hg, and Co [37]. However, the oxidation of hydrazine on these electrodes has been shown to exhibit high overpotentials and less power density [28]. Hydrazine oxidation is a structure-sensitive reaction and the employment of binary and ternary metal catalytic systems with (100) domains is expected to provide stability, increased reactivity and functionality over single-metal catalytic systems [28].

This dissertation covers the improvements of ammonia and hydrazine oxidation in alkaline and neutral media using Pt(100) based nanoalloys. Novel preferentially oriented Pt(100) based binary and ternary ultrasensitive nanoalloys will be synthesised and interrogated as electrocatalysts towards the electrocatalytic oxidation of ammonia and hydrazine for fuel cell applications.

## 1.2 Problem statement

The problem that prevails currently with the production of hydrogen from the electro-oxidation of ammonia involves the slow kinetics of the reaction:  $2NH_3(aq) \rightarrow N_2(g) + 3H_2(g)$ . Though expensive, platinum is commonly used to improve the kinetics of ammonia electro-oxidation reaction [14]. Previous studies have centred on the research for cheaper alternative electrocatalysts for the reaction. Miura *et al.* [38-40] performed a series of experiments on ammonia electro-oxidation on noble metal Pt and Pt-Me (Me = Ni, Ir, Ru, Cu) binary alloys. Single crystal surfaces have also been investigated and found out to be good materials for the electro-oxidation of ammonia. Rosca and Koper [41] investigated the ammonia electro-oxidation on Pt(100) and Pt(111) surfaces and proposed the ammonia oxidation mechanism. Despite all these attempts, the rate of ammonia cracking has remained slow resulting in the

need to search for better electrocatalysts to accelerate it. Moreover, hydrazine has been identified as a suitable fuel for fuel cells. However, its oxidation on electrodes has been shown to occur with low current densities and high overpotentials demanding the search for suitable catalysts. In this study, preferentially oriented platinum (100) based nanoalloy electrocatalysts with high reaction time, low overpotential and high current density will be synthesised and used as electrocatalysts for the oxidation of ammonia and hydrazine.

### 1.3 Rationale and motivation

Ammonia is one of the highly used commodity chemicals in the world; its storage, transportation, and handling procedures are well known and documented [12]. The use of ammonia as a feedstock for hydrogen production via catalytic cracking has been researched as early as the 1960's due to the high hydrogen density of the molecule. It contains as much as 1.7 times the amount of hydrogen that is contained in the same volume of liquid hydrogen. However, the catalytic cracking process requires high temperatures, is a slow process, proves to have a low efficiency and requires purification of the production gases [42]. The electro-oxidation of ammonia, conversely, can be carried out at ambient temperature, has an efficiency of 100% on platinum catalysts and produces pure streams of nitrogen and hydrogen gases [43]. On the other hand, the oxidation of hydrazine on these electrodes has shown to exhibit larger overpotentials and less power density. Based on their better physicochemical properties, nanostructured materials are known to improve the reaction rates of systems they catalyse [26]. The incorporation of the nanomaterials and the platinum catalysts is expected to offer better catalytic properties compared to Pt catalysts alone. This research will therefore involve the development of novel electrocatalysts (nanoalloys), combining the high surface area of nanomaterials and the Pt(100) catalysts. The

electrocatalysts will involve ultrasensitive nanostructured binary and ternary nanoalloys of platinum group metals (PGMs) and some selected transition metals such as Au and Ag.

## 1.4 Research aim and objectives

### 1.4.1 Aim

The aim of this research is to examine the electro-oxidation of ammonia and hydrazine using novel electrocatalysts. The electrocatalysts will be based on the use of Pd and ultrasensitive nanostructured oriented Pt(100) nanoalloy systems.

### 1.4.2 Objectives

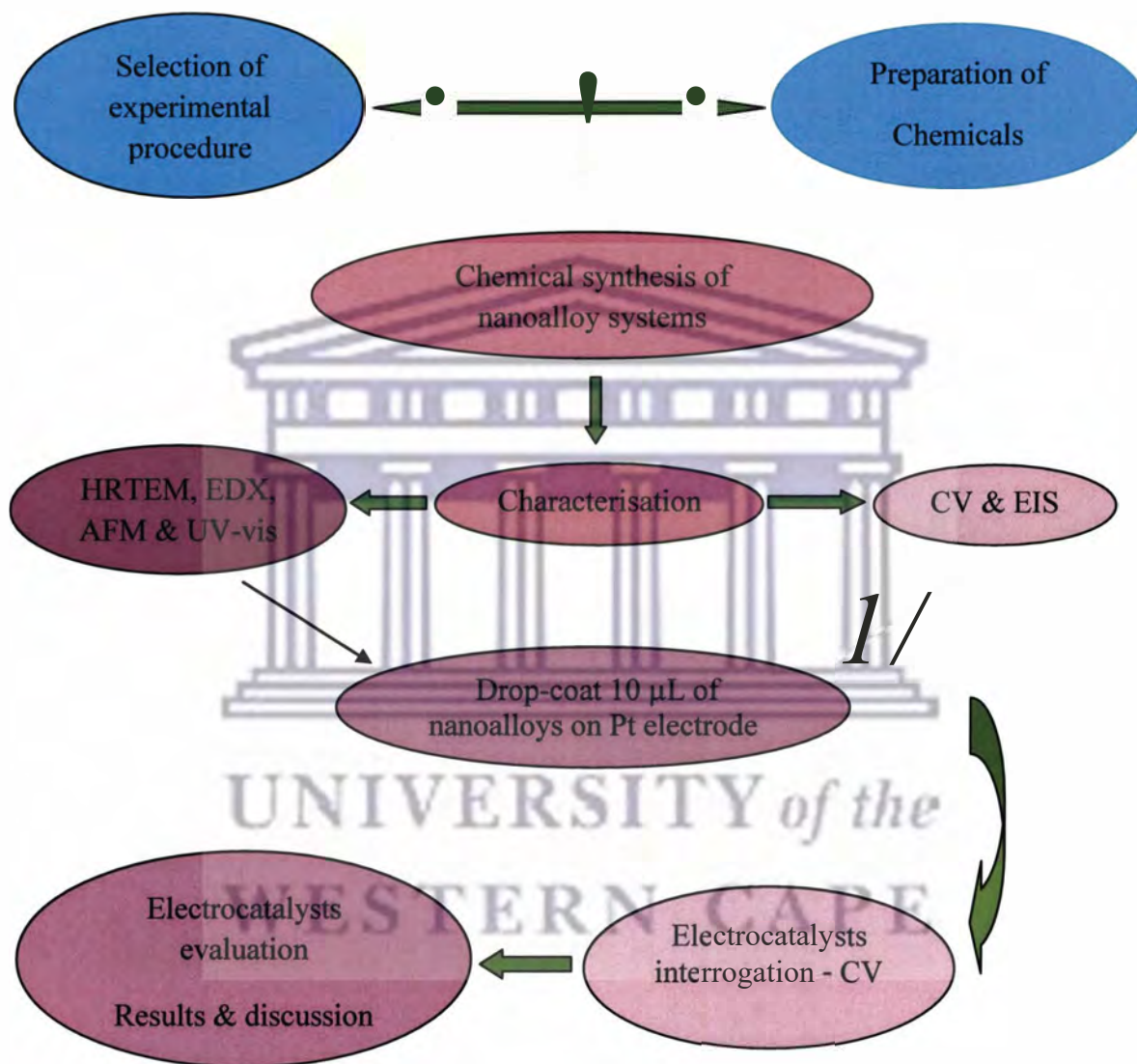
The objectives of this study include:

1. To chemically synthesise novel PdAu, PdAg, and PdAuAg nanoalloys
2. To chemically synthesise novel oriented Pt(100) based nanoalloys such as Pt(100)Pd, Pt(100)Au, Pt(100)Ir, Pt(100)Rh, Pt(100)PdAu, Pt(100)PdIr, Pt(100)IrAu and Pt(100)RhAu.
3. To interrogate the structural, spectroscopic and electrochemical characteristics of the nanoalloys using techniques such as high resolution transmission microscopy (HRTEM), energy dispersive x-ray spectroscopy (EDX), atomic force microscopy (AFM), electrochemical impedance spectroscopy (EIS), cyclic voltammetry (CV) and UV-visible spectroscopy.
4. To investigate the electrocatalytic effect of the Pd and oriented Pt(100) based nanoalloy systems towards the catalytic oxidation of ammonia and hydrazine.



## 1.5 Research framework

In line with the study objectives, the research framework is shown on the scheme below.



Scheme 1: Research framework.

## 1.6 Thesis statement

Preferentially oriented platinum (100) nanoalloy systems should have suitable electrochemical and electrocatalytic properties that make them applicable as electrocatalysts for the oxidation of ammonia and hydrazine.

## 1.7 Thesis outline

This thesis consists of eight chapters and will be presented as outlined below:

**Chapter 1** presents a brief background on the aspects involved in this project namely; fuel cells and nanoalloys with particular emphasis on the use of the nanoalloys as electrocatalysts for the oxidation of ammonia and hydrazine. Also included in the chapter are the project's rationale and motivation, the research aim and the thesis outline.

**Chapter 2** provides a detailed literature review comprising of definition of fuel cells, their principle of working, classification and their sources of fuel. The unique electrocatalytic properties of nanoalloys, their method of synthesis and their possible applications have also been focused in this chapter. The chapter will also cover a brief background of the characterisation techniques used in this study, mainly cyclic voltammetry (CV), square wave voltammetry (SWV), electrochemical impedance spectroscopy (EIS), UV-visible spectroscopy, atomic force microscopy (AFM), and high resolution transmission electron microscopy (HRTEM).

**Chapter 3** consists of the general experimental procedures used for the success of this work. Also included in this chapter are the list of materials and instruments used.

**Chapter 4** provides the morphological, spectroscopic and amperometric results obtained from the characterisation of PdAu, PdAg and PdAuAg nanoalloys and the subsequent application of the nanoalloys in the oxidation of ammonia.

**Chapter 5** illustrates the morphological, spectroscopic and amperometric results obtained from the characterisation of oriented Pt(100), Pt(100)Pd, Pt(100)Au and Pt(100)PdAu nanoparticles and their catalytic effects in ammonia oxidation.

**Chapter 6** consists of results on the morphological, spectroscopic and amperometric characterisation results of oriented Pt(100)Ir, Pt(100)Rh, Pt(100)IrAu, Pt(100)PdIr and Pt(100)RhAu nanoalloys and the subsequent application of the nanoalloys in the oxidation of ammonia.

**Chapter 7** presents the results on the catalytic properties of the oriented nanoalloys towards the oxidation of hydrazine.

**Chapter 8** outlines the general conclusion, recommendations and future work.

The following chapter provides the literature review.

## CHAPTER TWO

### LITERATURE REVIEW

#### *Summary*

*This chapter is an elaborated follow up of chapter one. Based on the ever increasing energy consumption, rising public awareness for environmental protection and existing nature of fossil fuels, there is a need to focus on alternative energy sources. Fuel cells play an important role in meeting the consumers' energy demands. This chapter focuses on the definition of fuel cells, their principle of working, classification and their sources of fuel. Hydrogen fuel cells are discussed with specific focus on ammonia as a hydrogen carrier. The chapter also focuses on hydrazine as a fuel for fuel cells. Since the decomposition of ammonia is a slow process and hydrazine oxidation on electrodes results in high overpotentials, nanomaterials in the form of nanoalloys are discussed as possible electrocatalysts. The unique electrocatalytic properties, the methods of synthesising the nanoalloys and their characterisation techniques are also discussed in this chapter.*

## 2.1 Fuel cells

### 2.1.1 Introduction

Ever increasing energy consumption, rising public awareness for environmental protection and existing nature of fossil fuels demands the need to focus on renewable energy sources. The small-scale generation systems such as wind turbine, photovoltaic, micro-turbines and fuel cells play an important role to meet consumers' demand using concepts of distributed generation which entails location of small-scale generation systems closer to the customers rather than central or remote locations [44]. These distributed generation systems have several major benefits which include; saving in losses over long transmission and distribution lines, installation cost, local voltage regulation and the ability to add a small unit instead of a larger one during peak load conditions [45]. Among the different distributed generations, more attention is being focussed on fuel cells because they have the potential capability of providing both heat and power.

Fuel cells are static energy conversion devices that convert chemical reaction of the fuels used, directly into electrical energy and produces water as its by-product [46-47]. Electricity is generated from a reaction between a fuel supply such as hydrogen and an oxidising agent (e.g. oxygen). The reactants flow into the cell, and the reaction products flow out of it, while the electrolyte remains within it. Fuel cells can operate continuously as long as the necessary reactant and oxidant flow is maintained. They are different from conventional electrochemical cell batteries in that they consume reactant from an external source, which must be continuously replenished [48]. They combine the best features of engines and batteries; can operate for as long as fuel is available without any intermediate mechanical energy conversion and their characteristics are similar to those of a battery under load conditions [49]. **Table 1** shows a comparison of different generation systems. It can be

observed that the efficiency of fuel cells is always higher as compared with conventional systems and other distributed generation systems. Moreover, fuel cells offer more advantages such as high energy conversion efficiency, zero emission, modularity, scalability, quick installation as well as gives good opportunities for cogeneration operations as compared to other distributed generation technologies [50].

**Table 1: Comparison of different generation systems.**

	Reciprocating engine: diesel	Turbine generator	Photo voltaics	Wind turbine	Fuel cells
Capacity Range	500 kW to 5 MW	500 kW to 25 MW	1 kW to 1 MW	10 kW to 1MW	200 kW to 2 MW
Efficiency	35%	29-42%	6-19%	25%	40-60%
Capital Cost (\$/kW)	200-350	450-870	6600	1000	1500-3000
O & M Cost (\$/kW)	0.005-0.015	0.005-0.0065	0.001-0.004	0.01	0.002-0.153

### 2.1.2 Fuel cells technology

The basic principle of the fuel cell was discovered in the year 1838 by Swiss scientist Christian Friedrich Schonbein [44]. In 1839 Sir William Grove developed the first fuel cell based on reversing the electrolysis of water by sheer accident [47]. In 1950 Francis Bacon at Cambridge University demonstrated the first 5 kW alkaline fuel cell [44]. After the successful development of alkaline fuel cell, National Aeronautics and Space Administration (NASA) needed a compact system to generate electricity for space shuttle applications. In 1970s, international fuel cells developed a 12 kW alkaline fuel cell for NASA's space shuttle orbiter which supplied reliable power without the use of any backup power like batteries. In the mid-1960s, the research work was focused on further development of various fuel cells for applications in stationary powers and transportations. In all these attempts, the high cost of

installation of fuel cells has been a major drawback to fuel cell technology. However, after the development of power conversion devices, much research has been directed towards reducing the high installation cost of the fuel cells [44].

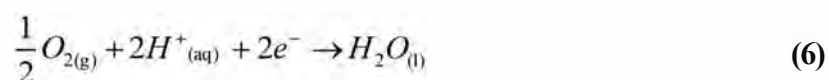
### 2.1.3 Operating principle of fuel cells

A fuel cell is an energy conversion device that converts the chemical energy of a reaction directly into electricity with by-products as water and heat [51]. The structure of a simplified fuel cell is shown in **Figure 1** [48]. The fuel cell is made up of three segments: the anode, the electrolyte, and the cathode. Two different chemical reactions occur at the interfaces of the three different segments. The net result of the two reactions is that the fuel is consumed, water or carbon dioxide is liberated, and an electric current is generated, which can be used to power electrical devices, normally referred to as the load. At the anode, a catalyst oxidises the fuel, usually hydrogen, turning the fuel into a positively charged ion and a negatively charged electron. The electrolyte is a medium specifically designed so that ions can pass through it, but the electrons cannot. The free electrons travel through a wire from the anode to the cathode creating electric current. The ions travel through the electrolyte to the cathode. On reaching the cathode, the ions are reunited with the electrons whereby they react with a third chemical, usually oxygen or an oxidizing agent, to form water. The chemical reactions involved in the anode and cathode and its overall reactions are given as follows:

Anode reaction:



Cathode reaction:



Overall reaction:

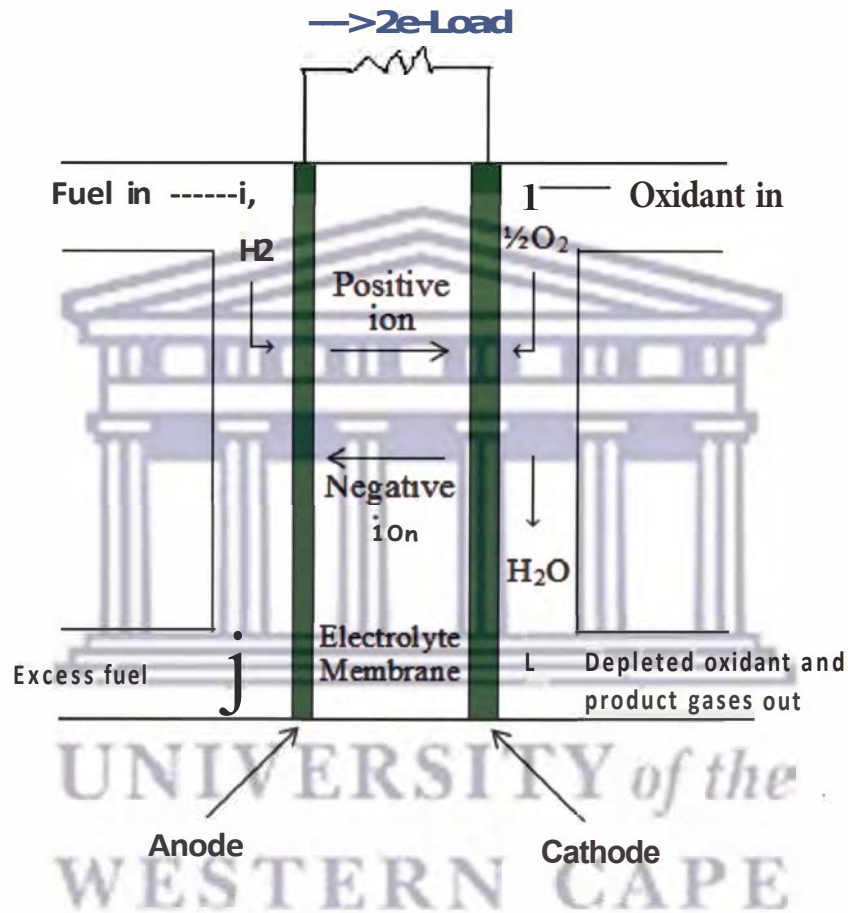
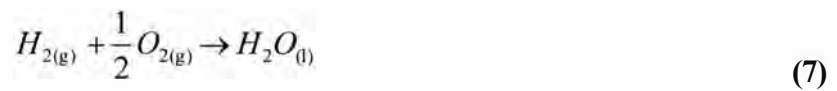


Figure 1: Fuel cell operation diagram [48].

#### 2.1.4 Classification of fuel cells

The fuel cells are classified according to the choice of electrolyte and fuel. There are six major different types of fuel cells, namely;

- (i) Proton exchange membrane fuel cell (PEMFC)
  - (a) Direct formic acid fuel cell (DFAFC)
  - (b) Direct Ethanol Fuel Cell (DEFC)



- (ii) Alkaline fuel cell (AFC)
  - (a) Proton ceramic fuel cell (PCFC)
  - (b) Direct borohydride fuel cell (DBFC)
- (iii) Phosphoric acid fuel cell (PAFC)
- (iv) Molten carbonate fuel cell (MCFC)
- (v) Solid oxide fuel cell (SOFC)
- (vi) Direct methanol fuel cell (DMFC)

They are further classified on the basis of operating temperatures. The low operating temperature is in the range of 50-250 °C for fuel cells such as PEMFC, AFC and PAFC, and high operating temperature is in the range of 650-1000 °C like MCFC and SOFC [44].

#### **2.1.4.1 Proton exchange membrane fuel cell (PEMFC)**

The PEMFC uses a solid polymer electrolyte (Teflon-like membrane) to exchange the ions between two porous electrodes, which is an excellent conductor of protons and an insulator for electrons [44]. Its major fuel is hydrogen. The operating temperature of the fuel cell is as low as around 100 °C. The chemical reactions involved at the anode and cathode and their overall reactions are given in **equations 5-7** (refer to **section 2.1.3**) [52]. The PEMFC has several advantages such as its higher power density and quick start up for automotive vehicles. The low operating temperature makes the technology viable in transportation and commercial applications like laptop computers, bicycle, and mobile phones. The major drawbacks of the PEM fuel cell are its low operating efficiency (40-45%) and use of high cost platinum as a catalyst at the anode. It is also intolerant to carbon monoxide [44].

#### **2.1.4.1.1 Direct formic acid fuel cell (DFAFC)**

Formic acid (HCOOH) consisting of small organic molecules is directly fed to the anode electrode as the fuel. Formic acid does not crossover the polymer (electrolyte) rendering it a higher efficiency (20-40%) as compared to when methanol is used [44]. The DFAFC produces an open circuit voltage of 0.55 V at an operating temperature of 60 °C which is very low compared to the theoretical value of 1.45 V [53]. It is considered as a safer fuel in case of leakage in the fuel tank. The major drawback of this kind of fuel cell is the high electrochemical over voltage during loading conditions by using platinum as a catalyst [44].

#### **2.1.4.1.2 Direct ethanol fuel cell (DEFC)**

The major fuel for DEFC is ethanol. The ethanol fuel can easily be extracted from biomass through fermentation process from renewable energy sources such as sugar cane, wheat, corn or even straw. At the anode, the liquid ethanol is oxidised to generate CO<sub>2</sub>, in addition to hydrogen ions and electrons. The reaction involved at cathode is the same as PEMFC and the generated voltage at its terminal is in the range of 0.5-0.9 V [44].

#### **2.1.4.2 Alkaline fuel cell (AFC)**

Alkaline fuel cell was invented by Bacon (British scientist) hence also called Bacon fuel cell [44]. It operates at a low temperature of around 100 °C like PEMFC and it has the capability to reach 60-70% of its efficiency. It uses an aqueous solution of potassium hydroxide (KOH) as an electrolyte and hydrogen as the fuel. Negatively charged ions are transported from anode to cathode and water is released as its by-product. The major advantage of this kind of fuel cell is that it gives a quick start [44]. However, it is very sensitive to CO<sub>2</sub> because it takes more time to react and consumes the alkaline in the electrolyte thereby reducing the concentration of hydroxide ions during chemical reactions [54-55]. AFC needs a separate

system to remove the  $\text{CO}_2$  from the air. The use of a corrosive electrolyte is also a disadvantage because it has shorter life span. These shortcomings render AFC commercially inapplicable.

#### **2.1.4.2.1 Proton ceramic fuel cell (PCFC)**

PCFC is a relatively new type of a fuel cell whose electrolyte is a ceramic material. It is operated at high temperature of  $750\text{ }^\circ\text{C}$  and can electrochemically oxidise gaseous molecules of the hydrocarbon fuel directly supplied to the anode without the need of additional reformer [44]. PCFC has a solid electrolyte, so the membrane cannot dry out as with PEMFCs or the liquid cannot leak out as with PAFCs [44]. The open circuit voltage produced by the PCFC is almost close to the theoretical value. The major drawback of PCFC is the low current density that can be increased by reducing the electrolyte thickness, improved conductivity and optimised electrodes [44].

#### **2.1.4.2.2. Direct borohydride fuel cell (DBFC)**

Sodium borohydride ( $\text{NaBH}_4$ ) is used as input fuel mixed with water to generate hydrogen by decomposing it into  $\text{NaBO}_2$  and  $\text{H}_2$  gas. The DBFC operates at low temperature of  $70\text{ }^\circ\text{C}$ . The major advantages of DBFC are high power density, no need of expensive platinum catalyst and high open circuit cell voltage (about  $1.64\text{ V}$ ). However, the efficiency of the DBFC is as low as 35% and the cost of the sodium borohydride is too expensive for portable power applications [44]. However, research is focused on the development of increased efficiency with the aim of minimising the borohydride hydrolysis by using different catalyst such as Au, Ni, and Pd [44].

#### **2.1.4.3 Phosphoric acid fuel cell (PAFC)**

The phosphoric acid fuel cell operates at a temperature range of 175-200 °C which is almost double that of PEMFC. It utilises a liquid phosphoric acid as an electrode. Unlike the PEMFC and AFC, it is very tolerant to impurities in the reformed hydrocarbon fuels. The chemical reaction involved in this fuel cell is the same as that of PEMF where pure hydrogen is used as its input fuel [54]. The drawbacks of PAFC are the same as those of PEMFC and its cost also increases due to use of platinum as a catalyst.

#### **2.1.4.4 Molten carbonate fuel cell (MCFC)**

The molten carbonate fuel cell operates at very high temperature, which is about 600-700 °C. It consists of two porous electrodes with good conductivity which is in contact with a molten carbonate cell. Due to its internal reforming capability, it separates the hydrogen from carbon monoxide fuel and decomposition of hydrogen is taken through the water shift reaction to produce hydrogen. The resultant reaction occurs as it does in PEMFC to produce electricity. The major advantages of MCFC include higher efficiency (50-60%), no need of metal catalyst as well as a separate reformer due to its high operating temperature [54]. This fuel cell is intolerant to sulphur and has a slow start up. It is mainly used for medium and large power applications.

#### **2.1.4.5 Solid oxide fuel cell (SOFC)**

The SOFC produces electricity at a high operating temperature of about 1000 °C. They use dense yttria stabilised zirconia, which is a solid ceramic material as its electrolyte. The main advantages of the SOFC is that they have a high efficiency of 50-60% and a separate reformer is not required to extract hydrogen from the fuel due to its internal reforming capability. Waste heat can be recycled to make additional electricity by cogeneration

operation [54]. The slow start up, high cost and intolerant to sulphur content of the fuel cell are some of its drawbacks. SOFC is mainly used for medium and large power applications.

#### **2.1.4.6 Direct methanol fuel cell (DMFC)**

The DMFC technology is relatively new as compared to the rest of the fuel cells. Like PEMFC, the DMFC uses polymer electrolyte but uses liquid methanol or alcohol as fuel instead of reformed hydrogen fuel. During chemical reactions, the anode draws hydrogen by dissolving liquid methanol in water eliminating the need for an external reformer. At the cathode, the recombination of the positive ions and negative ions takes place, which are supplied from anode through the external circuit and combines with oxidised air to produce water as a by-product. Normally a single DMFC can supply a power density of about 0.3-0.5 V under loaded conditions. It is mainly used in cameras, notebook computers and other portable electronic applications in the range of 1 W to 1 kW capacity. The main advantage of DMFC is that the anode catalyst itself draws the hydrogen from the methanol and reduces the overall cost due to the absence of reformer [44]. Its characteristics are similar to those of PEMFC. However, its performance is limited by two important factors; crossover of methanol from anode to cathode which lowers the system efficiency and the slow kinetics of the electrochemical oxidation of methanol at the anode [56].

#### **2.1.5 Sources of fuel for fuel cells**

The commonly used fuels in fuel cells are hydrogen gas, methanol, ethanol, sodium borohydride, formic acid, hydrazine and hydrocarbons. However, sodium borohydride is too expensive for portable power applications and the combustion of hydrocarbons and alcohols such as methanol and ethanol in air generates various pollutant gases, including carbon monoxide, carbon dioxide and ozone which lead to environmental pollution [44]. Hydrogen

and hydrazine are the major fuel for fuel cells based on their few ill effects to the environment. In our study and discussion, more attention has been paid to hydrogen gas and hydrazine as the main fuel for fuel cells.

### **2.1.5.1 Hydrogen gas**

Hydrogen is the main fuel source for power generation in fuel cells based on its few ill effects to the environment. The chemical reaction for the breakdown of hydrogen gas to release energy is described in **equations 5-7** (refer to **section 2.1.3**). However, its storage and transportation are still major issues. Its use as a fuel for wide-spread distribution in either gaseous or liquid form poses numerous safety, technical, and economic problems that make its use as a fuel prohibitively difficult. In the absence of a hydrogen pipeline network, small-scale users purchase merchant hydrogen as compressed gas in steel cylinders, or as liquid hydrogen in cryogenic containers. One approach to resolve the drawbacks of hydrogen as a fuel includes considering less expensive, simpler, and cheaper materials that can act as hydrogen carrier. This has been done through storing and transporting hydrogen via other chemical compounds, such as alcohols, hydrocarbons and ammonia. Ammonia is the best option so far as a major source of hydrogen gas based on its less ill effects on the environment. This study pays more attention to ammonia as a major source of hydrogen gas.

#### **2.1.5.1.1 Oxidation of ammonia for hydrogen production**

Liquid ammonia has been identified as a suitable hydrogen carrier. It offers a significant advantage in terms of cost and convenience over pure hydrogen and is a convenient way of storing supplies of hydrogen as an alternative fuel for clean energy supply [12]. It contains

1.7 times the amount of hydrogen that is contained in the same volume of liquid hydrogen, boasts a specific energy density 50% higher than liquid hydrogen for a given volume [14]. It is characterised by being produced in large quantities, is non-flammable and readily obtained and handled in liquid form without need for expensive and complicated refrigeration technology [13-14]. Moreover, it has a higher power density and lower cost per kW than methanol and can be electrolysed to release hydrogen and nitrogen with minimum effects to the environment according to **equation 8**



The use of hydrogen as a source of fuel for fuel cells as well as the emergence of legislation promoting hydrogen economy has made the production of hydrogen a very key aspect. At this time, hydrogen production costs for distributed power cannot compete with traditional power generation methods, and the storage and transportation of hydrogen are both inefficient and dangerous [17]. The nitrogen gas that is produced during the process is already found in large quantities in air, and could be purged from the decomposition process to the atmosphere with few ill effects on the environment [57]. The absence of oxygen in the reaction prevents the production of harmful oxides, and in contrast to other hydrogen media such as methane, ammonia contains no carbon which can produce carbon monoxide or greenhouse gases.

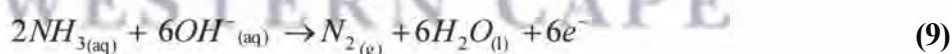
#### **2.1.5.1.2 Ammonia as a hydrogen carrier/hydrogen storage medium**

In many ways, ammonia is an excellent hydrogen carrier [58]; liquid ammonia represents a convenient way of storing supplies of hydrogen, boasting a specific energy density (kWh/l) 50% higher than liquid. Ammonia is also easily condensed (at ambient temperature and under a pressure of 8 bar) which makes it a good choice for transportation and storage. Even though

ammonia is flammable within defined limits (16% - 25% by volume in the air) and toxic (above 25 ppm) its presence can be detected by its characteristic odour (above 5 ppm). It is produced world-wide in large quantities (more than 100 million ton/year), which allows the effect of economy of scale on the cost of production. Its decomposition by electro-oxidation in alkaline media at low overpotential is  $\text{NO}_x$  and  $\text{CO}_x$  free with nitrogen and water as products of reaction [14, 59].

### 2.1.5.1.3 Electro-oxidation of ammonia: thermodynamics

Recently, Botte *et al.* proposed a new technology for the production of hydrogen on demand based on the electrolysis of ammonia [60]. The ammonia electro-oxidation reaction can thus be coupled with the hydrogen evolution reaction in an alkaline electrolytic cell for the production of high purity hydrogen. Hydrogen is oxidised at the anode (**equation 9**) at a potential of 0.77 V (vs. standard hydrogen electrode, SHE) [61]. Alkaline reduction of water occurs at the cathode (**equation 10**) and requires -0.83 V vs. SHE. Overall (**equation 11**), 0.06 V is required [12];



The thermodynamics favour the production of hydrogen coupled to the ammonia oxidation compared to hydrogen production by electrolysis of water, whose theoretical cell voltage is 1.223 V [14]. The high capacity for hydrogen storage has led to increased interest in using ammonia as an alternative energy carrier.



#### 2.1.5.1.4 Technological challenges faced during hydrogen production from ammonia

The decomposition of ammonia is a slow reaction demanding need for the use of suitable catalysts to increase its reaction rate. Pt catalysts are the major catalysts used in the electrolysis of ammonia for the production of hydrogen gas. However, the deactivation of the Pt-catalyst is observed at higher current densities [62]. Therefore, hydrogen production from ammonia electrolysis requires development of improved catalysts for ammonia electro-oxidation [12]. In the past, several metals and alloys have been considered as potential catalysts. A study on bulk platinum and bulk iridium electrodes [62] showed that these metals have the best activity among noble and coinage metals towards ammonia oxidation. However, the current densities observed on those catalysts were very low. Metal alloys, metal oxides, and bimetallic electrocatalysts have shown higher activity towards ammonia oxidation compared to monometallic catalysts. For example, Ag-Pb alloys [63] and Ru oxides [64] showed high catalytic activity but at very high overpotentials. Ammonia adsorption and decomposition have also been investigated experimentally on Pt(111), Pt(210), Pt(410), Pt(557) and polycrystalline Pt [65]. The decomposition shows only moderate structure sensitivity to the catalyst. Moreover, ammonia electro-oxidation has also been studied using metal oxide electrodes, e.g., IrO<sub>2</sub>, PtOx-IrOx and Ni/NiOx electrodes in alkaline and neutral solutions [21-25]. Most of these reactions were carried out using bulk metal or metal oxide electrodes with high precious metal loading. In order to develop efficient and economically viable electrodes, the amount of precious metals must be reduced. This can be achieved by using electrocatalysts in the form of nanoparticles which are considered as required materials for practical purposes [15]. This study aims at examining the production of hydrogen from electro-oxidation of ammonia while using nanotechnology to synthesise nanomaterials as novel electrocatalysts. The novel electrocatalysts that will be

used in this study will combine high surface area and catalytic properties of binary and ternary oriented (100) platinum based nanoalloys.

### **2.1.5.2 Hydrazine**

Hydrazine is an inorganic compound with the formula  $N_2H_4$ . It is a colourless flammable liquid with an ammonia-like odour. It is highly toxic and dangerously unstable unless handled in solution form [66].

#### **2.1.5.2.1 Effects of exposure of hydrazine on humans**

Hydrazine is neurotoxin in nature and has been classified as human carcinogen by Environmental Protection Agency (EPA) [67]. Symptoms of acute exposure to high levels of hydrazine include irritation of eyes, nose and throat, temporary blindness, dizziness, nausea, pulmonary oedema and coma in humans [68]. Hydrazine causes liver, kidney, lungs, respiratory tract infection and long-term effects on the central nervous system when people are exposed to air containing 10 ppb hydrazine [69]. It is also a hepatotoxic substance with adverse health effects on the brain and capable of causing DNA damage [70].

#### **2.1.5.2.2 Uses of hydrazine**

In spite of its hazardous effects on humans, hydrazine has many practical applications in various fields such as pharmaceutical intermediates, blowing agents, photographic chemicals, corrosion, and protection treatments for boilers, as a fuel in rocket propulsion systems, as orbit adjusting materials for satellite and missiles in aerospace and military field pesticides and fuel cells [71]. Hydrazine is also applied as intermediate in chemical industry to synthesise pesticides and herbicides as well as in the production of anti-tuberculosis and anti-

diabetes medicines [72-73]. It is a highly reactive base and reducing agent which has a wide range of applications in many industrial processes, such as in the manufacture of antioxidants and insecticides [74]. It is widely used as a polymerisation catalyst and in various rocket fuels [75]. Hydrazine and its derivatives are excellent reducing agents. These families of agents are widely used in different industries and agriculture as emulsifiers, catalysts, corrosion inhibitors, explosives, and rocket propellants [67]. Hydrazine is also an ideal fuel for direct fuel cell system given that the electro-oxidation of the fuel does not suffer any catalyst poisoning effects, has high energy density and reactive properties [76-77].

#### **2.1.5.2.3 Hydrazine as a fuel for fuel cells**

Hydrazine has been proposed as an alternative to hydrogen in fuel cells. The chief benefit of using hydrazine is that it can produce over  $200 \text{ mW/cm}^2$  of energy more than a similar hydrogen cell without the need to use expensive platinum catalysts. Since the fuel is liquid at room temperature, it can be handled and stored more easily than hydrogen. By storing the hydrazine in a tank full of a double-bonded carbon-oxygen carbonyl, the fuel reacts and forms a safe solid called hydrazone. Then by flushing the tank with warm water, liquid hydrazine is released. Hydrazine has a higher electromotive force of 1.56 V compared to 1.23 V for hydrogen. Hydrazine breaks down in the cell to form nitrogen and hydrogen which bonds with oxygen, releasing water.

Hydrazine as a fuel for alkaline fuel cells has been studied since the 1970s [78]. The reasons for considering hydrazine as a promising fuel are:

- ▶ Its electro-oxidation produces no  $\text{CO}_2$ , reducing the overall emission of greenhouse gases.

- ▶ The absence of carbon atoms in hydrazine leads to zero production of species that may poison the electrocatalysts (e.g., CO and products of incomplete C-molecules oxidation).
- ▶ The theoretical electromotive force is relatively high, with a value of 1.56 V which results in high power density [79].

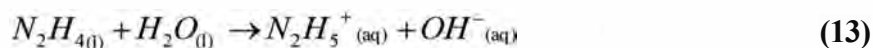
The high toxicity of hydrazine should be taken into account during the design of complete system to prevent any contact of customers with fuel (either from fuel tank or with unreacted one). A safe method of storing hydrazine in fuel tanks as a solid hydrazone form (>C = N-NH<sub>2</sub>) has been developed by Daihatsu Motor [78]. This form does not exhibit mutagenic properties as well as its solid nature is much safer as compared to liquid hydrazine in case of tank damage. The hydrazine can be released from its hydrazone form by adding water into the fuel tank [78].

#### 2.1.5.2.4 Oxidation of hydrazine

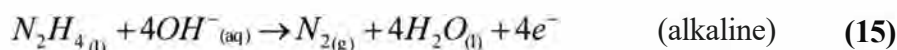
Hydrazine overall electro-oxidation reaction can be written as [78]:



Hydrazine-water solutions easily undergo hydrolysis, producing the hydrazonium cation:



N<sub>2</sub>H<sub>4</sub> can easily be oxidised both in acidic and alkaline media by the following reactions:



Operation of fuel cells requires catalysts based on stable, non-corrosive noble metals, usually platinum or platinum-group metals. Noble metals such as platinum, palladium, silver and gold are very active in the anodic oxidation of hydrazine [80]. However, these catalysts have

been found to portray high overpotentials and lower current densities. Carbon based electrodes (nanotubes) have been explored but hydrazine oxidation has been found to be poor at ordinary carbon electrodes [81]. However, hydrazine oxidation is a structure-sensitive reaction [28, 82]. It is hence necessary to explore the catalytic effect of oriented Pt(100) based nanoparticles and nanoalloys as electrocatalysts for the oxidation of hydrazine.

## **2.2 Nanotechnology**

### **2.2.1 Introduction**

Nanotechnology is the term given to those areas of science and engineering where phenomena that takes place at dimensions in the nanometre scale are utilised in the design, characterisation, production and application of materials, structures, devices and systems [83]. Although in the natural world there are many examples of structures that exist with nanometre dimensions, including essential molecules within the human body and components of foods, and that many technologies have incidentally involved nanoscale structures for many years, it has only been in the last quarter of a century that it has been possible to actively and intentionally modify molecules and structures within the nano range. It is this control at the nanometre scale that distinguishes nanotechnology from other areas of technology [83].

### **2.2.2 Definitions and scope in nanotechnology**

Several definitions of nanotechnology terms and of the products of nanotechnology have been formulated. According to the UK Royal Society and Royal Academy of Engineering, the range of the nanoscale is from the atomic level, at around 0.2 nm up to around 100 nm [84]. It is within this range that materials can have substantially different properties compared to the same substances at larger sizes, both because of the substantially increased ratio of

surface area to mass, and also because quantum effects begin to play a role at these dimensions, leading to significant changes in several types of physical properties. According to published Publicly Available Specification on the Vocabulary for Nanoparticles of the British Standards Institution [85], the major terms used in nanotechnology have been defined as follows:

**Nanoscale:** Having one or more dimensions of the order of 100 nm or less.

**Nanoscience:** The study of phenomena and manipulation of materials at atomic, molecular and macromolecular scales, where properties differ significantly from those at a larger scale.

**Nanomaterial:** Material with one or more external dimensions, or an internal structure, which could exhibit novel characteristics compared to the same material without nanoscale features.

**Nanocomposite:** Composite in which at least one of the phases has at least one dimension on the nanoscale.

**Nanostructured:** Having a structure at the nanoscale.

Nanotechnology has recently become one of the most exciting forefront fields in analytical chemistry with a wide variety of nanomaterials, especially nanoparticles of different properties that have found broad applications in many kinds of analytical methods [86].

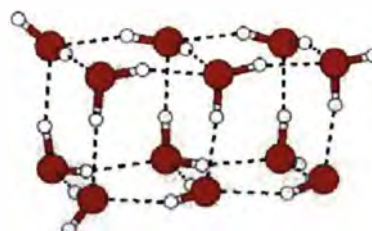
### 2.2.3 Nanoparticles

Nanoparticles can be defined as clusters of atoms, ions or molecules, typically with one or more dimensions at the nanoscale [83]. This is a particularly interesting size range, which bridges the gap between small molecules (with discrete energy states) and bulk materials (with continuous energy states). They constitute a new type of material, since they often have unique chemical, physical and electronic properties which are fundamentally different from

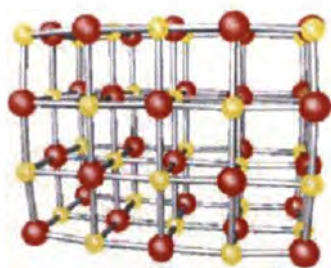
those of discrete molecules or bulk solids/materials [26]. Nanoparticles are formed by most of the elements in the periodic table and they can be classified according to the types of atoms of which they are composed and the nature of the bonding [87]. Examples of nanoparticles include; weakly bound rare gas and molecular nanoparticles (e.g. Ar and H<sub>2</sub>O), covalently bonded semiconductor nanoparticles (e.g. carbon fullerenes and CdS), electrostatically bound ionic nanoparticles (e.g. NaCl and MgO) and nanoparticles of metallic elements (**Figure 2**) [88]. Metallic elements form a wide variety of nanoparticles ranging from the s-block metals (such as the alkali and alkaline earth metals), p-block metals (such as aluminium; where the bonding involves both the s and the p orbitals) and the transition metals (where the bonding involves the valence d orbitals) [89]. Metal nanoparticles may be composed of a single metallic element (monometallic nanoparticles) or more than one metal usually referred to as nanoalloys [90-91]. Metal nanoparticle catalysts composed of two or more different metal elements are of greater interest from both technological and scientific point of view for improving the catalyst quality or properties and they have been reported to have higher catalytic properties compared to their corresponding monometallic nanoparticles due to their increased surface area and synergetic effects [92-95].



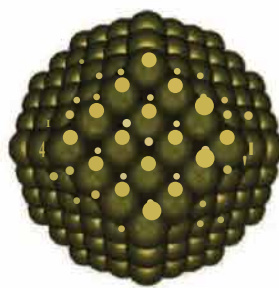
Fullerenes



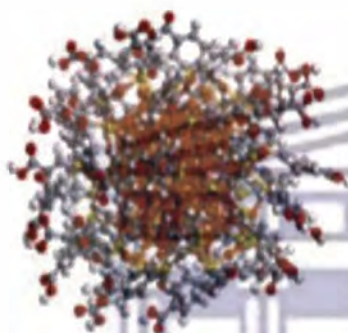
Molecular nanoparticles



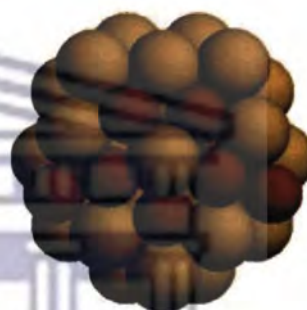
Ionic nanoparticles



Metal nanoparticles



Passivated metal nanoparticles



Nanoalloys

**Figure 2: Examples of types of nanoparticles [88].**

### 2.2.3.1 Prehistory of metal nanoparticles

Metal nanoparticles and nanoalloys have been used (albeit unknowingly) for many centuries, primarily for their optical properties [90]. For example, copper, silver and gold nanoparticles are responsible for many of the colours of stained glass windows dating from the middle ages. The Romans were known to use nanoparticles to colour glass; the most famous case being the fourth century AD Lycurgus cup which contains Ag-Au nanoalloys particles. It is also believed that colloidal gold nanoparticles were used in cosmetics by the ancient Egyptians. Silver and copper nanoparticles and Ag-Cu nanoalloys have also been used since the middle ages to give metallic lustre to ceramic glazes [88]. More recently (at least until the advent of digital cameras), silver nanoparticles were important in the photographic process. They have also found an increased use due to their antimicrobial properties [88].



### 2.2.3.2 Passivated (capped) metal nanoparticles

To enable the investigation of approximately uniformly sized metal nanoparticles, and to exploit their properties in various applications, it is necessary to protect them with a ligand surfactant shell, as this avoids coalescence at high cluster densities. Two types of stabilisation can be distinguished [96]:

- i) *Electrostatic stabilisation*; due to coulombic repulsion between metal nanoparticles, caused by ions adsorbed at the particle surface (e.g. sodium citrate gold sols).
- ii) *Steric stabilisation*; due to the coordination of polymers and other bulky organic molecules, especially those with P-, N- and S-donor groups (e.g. thiols and thioethers).

### 2.2.4 Nanoalloys

Nanoalloys (also known as alloy nanoparticles) are multicomponent metallic particles in the 1-100 nm diameter range [83]. Nanoalloys present very complex structures and properties, which crucially depend on their size, composition and chemical ordering, and which can therefore be tailored for specific and industrially relevant applications such as in data storage, optical devices and catalysis [97]. They are of greater interest from both technological and scientific point of view for improving the catalyst quality or properties. The desire to fabricate materials with well defined, controllable properties and structures on the nanometre scale coupled with the flexibility afforded by intermetallic materials has generated interest in bimetallic and multi-metallic nanomaterials [91]. A very wide range of combinations and compositions are possible for nanoalloys. For example, bimetallic nanoalloys ( $A_mB_n$ ) can be generated with more or less, controlled size ( $m + n$ ) and composition ( $min$ ). Nanoalloys can

be generated in a variety of media, such as cluster beams, colloidal solutions, immobilised on surfaces, or inside pores.

#### **2.2.4.1 Reasons for studying nanoalloys.**

1. They are of interest in catalysis (e.g. catalytic converters in automobiles), and for electronic, magnetic and biomedical applications [91].
2. They can be used in the fabrication of materials with well-defined and controllable properties. This results from the combination of the flexibility of intermetallic materials with structure on the nanoscale. Surface structures, compositions, and segregation properties portrayed by nanoalloys are of great interest as they are important in determining chemical reactivity as well as catalytic activity [91].
3. Their chemical and physical properties can be tuned by varying the nanoparticle/cluster size, composition and atomic ordering (segregation or mixing) [91].
4. They sometimes display structures and properties distinct from pure elemental nanoparticles. For example, the structures of binary nanoalloys may be quite different from those of pure metal nanoparticles of the same size and synergism is sometimes observed in catalysis by nanoalloys [91].
5. Finite size effects can also be important for nanoalloys giving rise to properties which are distinct from bulk alloys (e.g. Ag and Fe are miscible in clusters/nanoparticles but not in bulk alloys) [91].

#### **2.2.4.2 Isomerism in nanoalloys**

Isomers are compounds with the same molecular formula but different structural formula.

Nanoalloys exhibit geometrical (different skeletal structures) and permutational (unlike

atoms) isomerism. Based on permutational isomerism, Jellinek introduced the term 'homotops' [44].

#### 2.2.4.2.1 Homotops

Homotops are nanoalloy isomers with a fixed number of atoms, composition and the same geometrical arrangement of atoms, but differ in the way in which the various atom types are arranged in that particular geometry [88]. The number of homotops rises combinatorially with cluster size and is maximised for equal mixtures of the component elements. Ignoring point group symmetry, a single geometrical isomer of an N-atom nanoalloy gives rise to:

$$N_H = N P_{A,B} = \frac{N!}{N_A! N_B!} = \frac{N!}{N_A! (N - N_A!)} \quad (16)$$

Where  $N_A$  is the number of atoms of type A and  $N_B$  is the numbers of atoms of type B and N is the total number of atoms.

UNIVERSITY of the  
WESTERN CAPE

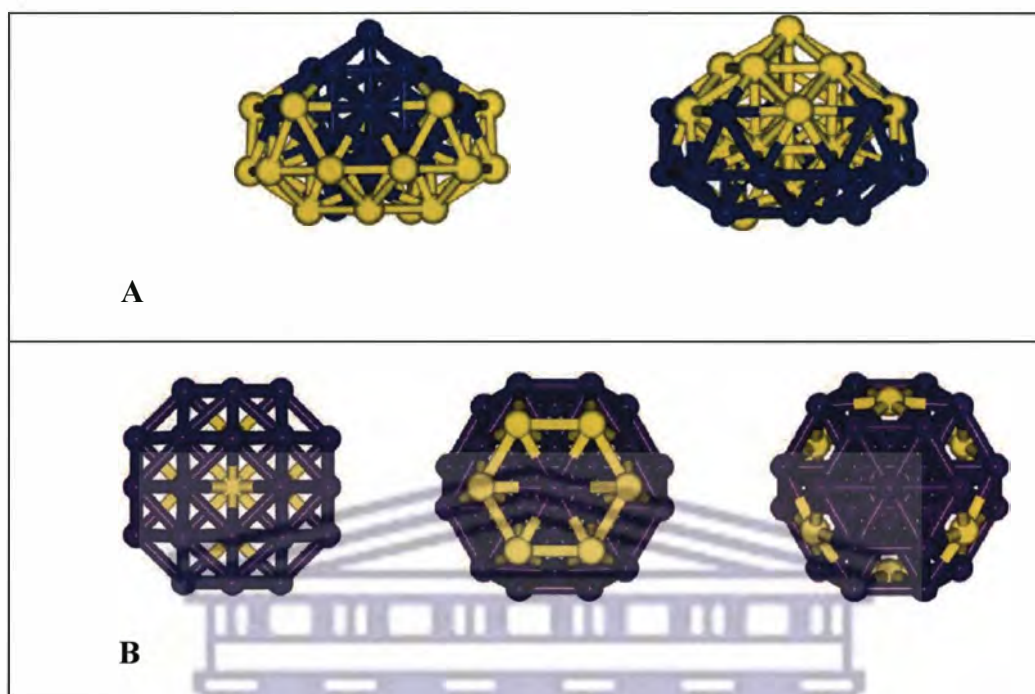


Figure 3: Examples of homotops in small nanoalloys: (A) complete inversion of configuration in a fivefold symmetric 38-atom  $A_{19}B_{19}$  nanoalloy; (B) high symmetry homotops for a 38-atom  $A_6B_{32}$  truncated octahedral nanoalloy [88].

#### 2.2.4.3 Types and structures of nanoalloys

Nanoalloys can be classified according to their mixing pattern (chemical ordering). Four main types of mixing patterns can be identified for nanoalloys [91].

- a) **Mixed A-B nanoalloys:** They are randomly mixed nanoalloys and are often termed as "alloyed" nanoparticles.
- b) **Core-shell segregated nanoalloys:** consist of a shell of one type of atom surrounding a core of another. There may be some mixing between the shells. They are usually denoted  $A_{core}B_{shell}$ .
- c) **Subcluster segregated nanoalloys:** consist of A and B subclusters, which may share a mixed interface or may only have a small number of A-B bonds.
- d) **Multishell nanoalloys:** may present layered or onion-like alternating -A-B-A- shells.

However, it is noteworthy that the mixed A-B nanoalloys usually referred to as "alloyed" nanoparticles based on the random and uniform mixture of the elements portray superior qualities and forms the basis of this study (see **Figure 4**).

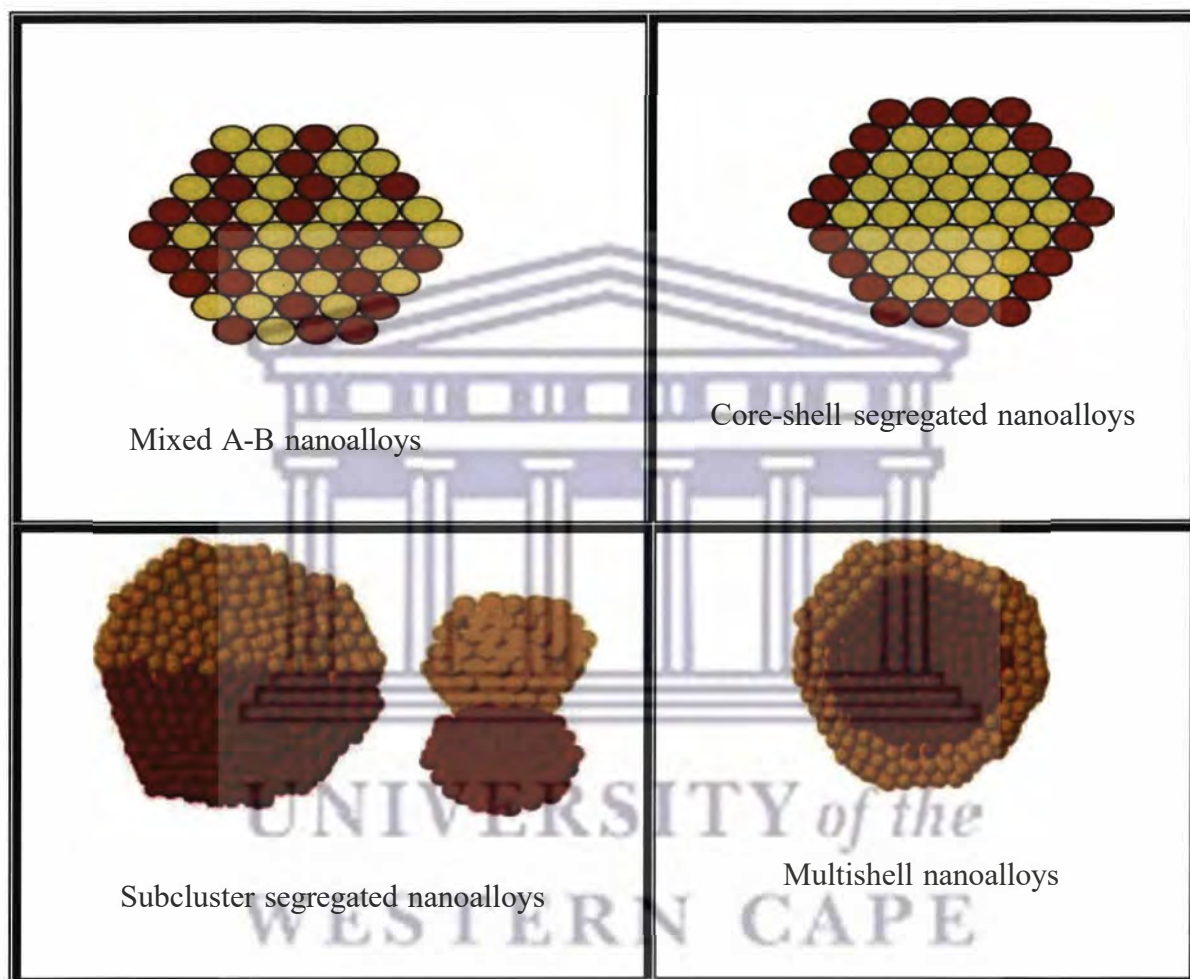


**Figure 4: Schematic representation of some nanoalloy mixing patterns (44).**

### 2.2.4.3.1 Factors influencing the chemical ordering of nanoalloys

The chemical ordering in A-B nanoalloys depends on the following factors [88].

- *Relative strengths of A-A, B-B and A-B bonds:* If A-B bonds are strongest, this favours A-B mixing, otherwise segregation is favoured, with the species forming strongest homonuclear bonds tending to be in the core of the nanoparticles.
- *Surface energies of bulk elements A and B:* The element with lowest surface energy tends to segregate to the surface.
- *Relative atomic sizes:* Smaller atoms tend to occupy the more sterically confined core, especially in icosahedral clusters, where the core undergoes compression; location of smaller atoms in the core can relieve elastic strain.
- *Charge transfer:* Electron transfer from less to more electronegative elements favours mixing by maximising attractive coulombic interactions. In smaller nanoalloys, more electronegative elements may preferentially occupy surface sites.
- *Strength of binding to substrates or surface ligands (surfactants):* For supported or passivated clusters, the element that binds most strongly to the support or the ligands may be pulled out towards the surface or interface.
- *Specific electronic/magnetic effects:* Certain sizes, compositions and/or segregation arrangements may be stabilised by electronic shell structure or electron spin interactions.

The chemical ordering observed for a particular nanoalloy depends critically on the balance of the factors explained above, the preparation method and experimental conditions, which may give rise to kinetic, rather than thermodynamic products [88].

#### **2.2.4.4 Application of nanoalloys**

Nanoalloys can be used in a number of technologically important areas such as:

##### **a) Catalysis**

Nanoalloys have higher catalytic properties compared to monometallic nanoparticles. They have been applied in many areas of catalysis such as fuel cells, sensors and biosensors based on their unique catalytic properties as explained below [97].

##### **i) Fuel cell catalysts**

Fuel cell technology attracts a great deal of interest because it allows the direct conversion of chemical energy into electricity. Catalysts in fuel cells are special materials that are used in order to facilitate the reaction of oxygen and hydrogen. The catalysts systems form an integral part of the electrochemical reactor utilised in fuel cells. They have been used as catalysts to oxidise methanol and ethanol in DMFCs [98].

##### **ii) Application in sensors and biosensors**

A sensor is a small device that as a result of a chemical interaction between the analyte and the sensor device transforms chemical or biochemical information of quantitative type into an analytically useful signal. The unique chemical and physical properties of nanoparticles make them extremely suitable for designing new and improved sensing devices. It has been shown that metal nanoparticles and nanoalloys provide three important functions for electroanalysis; improved mass transport, high effective surface area and catalytic properties. However, nanoalloys play four major roles in biosensors. These include [97]:

**Immobilisation of biomolecules:** Nanoparticles have large specific surface area and high surface free energy. This enables them to adsorb biomolecules strongly and play an important role in the immobilisation of biomolecules in biosensor construction. They enable the biomolecules which are adsorbed on the surface of the electrodes to retain their biocompatibility. This is because some of them carry charges and can electrostatically adsorb biomolecules with different charges. For example Ag-Au and Au-Pt nanoalloys have been applied in the immobilisation of enzymes [97]. Electrochemical immunosensors based on immobilisation of antigen or antibodies with nanoalloys have also been extensively applied or studied. They also increase the stability and maintain the activity of biomolecules [97].

**Catalysis of electrochemical reactions:** Nanoalloys have excellent catalytic properties. The introduction of nanoparticles with catalytic effects into electrochemical sensors and biosensors can decrease overpotentials of many analytically important electrochemical reactions and even realise the reversibility of some redox reactions, which are irreversible at common unmodified electrode. For example, bimetallic Ag-Au alloy nanoparticles have been used as electrocatalyst in the electrocatalytic oxidation of glucose [99].

**Enhancement of electron transfer:** Enzymes usually lack direct electrochemical communication with electrodes. The active centres are surrounded by thick insulating protein shells; blocking the electron transfer between electrodes and the active centres. Conductivity properties of nanoparticles, mostly metal nanoparticles at nanoscale dimensions makes them suitable for enhancing the electron transfer between the active centres of enzymes and the electrodes. They act as electron transfer "mediators" or "electrical wires". For example Ag-Au nanoalloys have good conductivity and have been used to enhance electron transfer between proteins and electrodes [100].



**Labelling biomolecules:** The labelling of biomolecules, such as antigen, antibody and DNA with nanoparticles has increasingly played an important role in developing sensitive electrochemical biosensors. Biomolecules labelled with nanoparticles can retain their bioactivity and interact with their counterparts and consequently the amount or concentration of analyte can be determined. Metal nanoparticle labels are used in immunosensors and DNA sensors. Gold nanoparticles are the most frequently used among all the metal nanoparticles labels available. However; nanoalloys based on Au can also be used as labels [97].

**Nanoparticles acting as reactant:** Nanoparticles are chemically more active than their counterpart bulk materials due to their high surface energy [97]. However, the application of the special reactivity of nanoparticles in biosensors and electrochemical sensors has not been extensively studied.

#### **b) Optoelectronics**

Some nanoalloys show strong absorption bands in the visible region caused by plasmons [91]. Based on their unique optical properties, they have found great applications in optoelectronics.

#### **c) Magnetic applications**

Recently there has been much interest in granular materials formed by embedding clusters/nanoparticles in a solid host [91]. When embedded in nonmagnetic metals, or even insulators, magnetic 3d metal nanoparticles (e.g. of Cr, Fe, Co, Ni or mixtures of these metals) are known to exhibit the phenomenon of giant magneto-resistance (GMR) with a change in resistance upon application of a magnetic field. Such GMR materials show considerable promise for applications as magnetic sensors and magnetic recording. This has

led to the study of bimetallic nanoalloys formed between magnetic 3d metals and nonmagnetic 4d (e.g. Rh, P, and Ag) or 5d metals (e.g. Pt, Au). The combination of 3d metals (e.g. Co and Ni) with large local magnetic moments and 4d metals (e.g. Rh) with strong spin-orbit coupling may be an effective way of obtaining a high magnetic moment and anisotropy which is required in high-density magnetic recording [91]. 3d-5d Fe-Pt and Co-Pt nanoalloys are also candidates for ultrahigh density magnetic recording media due to their high magnetic anisotropy with associated high magnetic susceptibility [90].

#### **d) Medical applications (Biodiagnostics)**

Nanoalloys have found great application in biodiagnostics such as for bioconjugation, as cellular labels, and in assays for gases, metal ions, and DNA/protein markers for diseases [101]. Nanoalloys offer possibility of enhanced robustness, sensitivity and selectivity. Based on their tunability, (of composition and ordering as well as size and shape) nanoalloys show considerable promise as biodiagnostic agents [91].

#### **2.2.4.5 Platinum group metal (PGM) nanoalloys**

The platinum group metals (PGMs) or a platinum group element (PGEs) is a term used collectively to refer to the six metallic elements clustered together in the periodic table. These elements are all transition metals lying in the d-block. The six platinum group metals include ruthenium (Ru), rhodium (Rh), palladium (Pd), osmium (Os), iridium (Ir) and platinum (Pt). They have similar physical and chemical properties and tend to occur together in the same mineral deposits. The position of the elements is shown in the periodic table below (**Figure 5**):

IA	IIA	IIIA	IVA	VA	VIA	VIIA	VIIIA	VIIIA	VIIIA	18	118	1118	IVB	VB	VIB	VII B	VIII B
1 H												♦metals	Non metals				2 He
PERIODIC TABLE OF THE ELEMENTS																	
3 Li	4 Be											5 B	6 C	7 N	8 ( )	9 F	10 Ne
11 Na	12 Mg											13 Al	14 Si	15 P	16 S	17 Cl	18 Ar
d Transition Elements																	
19 K	20 Ca	21 Sc	22 Ti	23 V	24 Cr	25 Mn	26 Fe	27 Co	28 Ni	29 Cu	30 Zn	31 Ga	32 Ge	33 As	34 Se	35 Br	36 Kr
37 Rb	38 Sr	39 Y	40 Zr	41 Nb	42 Mo	43 Tc	44 Ru	45 Rh	46 Pd	47 Ag	48 Cd	49 In	50 Sn	51 Sb	52 Te	53 I	54 Xe
55 Cs	56 Ba	57 La	72 Hf	73 Ta	74 W	75 Re	76 Os	77 Ir	78 Pt	79 Au	80 Hg	81 Tl	82 Pb	83 Bi	84 Po	85 At	86 Rn
87 Fr	88 Ra	89 Ac	104 Unq	105 Unp	106 Uns												
f Transition Elements																	
		•Lanthanides	58 Ce	59 Pr	60 Nd	61 Pm	62 Sm	63 Eu	64 Gd	65 Tb	66 Dy	67 Ho	68 Er	69 Tm	70 Yb	71 Lu	
		••Actinides	90 Th	91 Pa	92 U	93 Np	94 Pu	95 Am	96 Cm	97 Bk	98 Cf	99 Es	100 Fm	101 Md	102 No	103 Lr	

Figure 5: The periodic table showing platinum group metals (highlighted in green).

Nanoalloys formed based on these PGMs and other noble metals play important roles in many applications because of their extraordinary physical and chemical properties [102-104]. For example, Pt serves as a major catalyst in industrial synthesis of nitric acid, reduction of pollutant gases emitted from automobiles, oil cracking, and proton-membrane-exchange (PME) fuel cells [105]. When two or more PGM and noble metals form nanoalloys, improved properties such as reduced catalyst poisoning are observed and these colloidal metallic alloy nanocrystals have been explored for catalytic applications such as in fuel-cell technology, hydrogen production, and gas sensing [105]. Platinum is one of the most useful metals used in fuel cell technology, chemical synthesis, and environmental protection, with extraordinary catalytic activities. It has been well documented that alloying Pt with two or three metals often improve the catalytic activity of Pt as well as reduce the cost [106]. Consequently, these PGM-based nanoalloys have found great application in fuel cells, oxidation of methanol, hydrogen activation, biosensors and immunosensors [106-108].

#### 2.2.4.6 Single crystal Pt(111) and Pt(100) materials

A single crystal material (SCM) is a material that is composed of a single crystal or a few large crystals. It consists of a monocrystal or a single grain without any grain boundaries. The atoms maintain the same unit cell pattern and orientation throughout the material. SCMs exhibit desirable piezoelectric, optical or magnetic properties that cannot be obtained with a polycrystalline ceramic material. Since the pioneering work by Clavilier and co-workers at the beginning of the 80s [109-110], there has been an increasing interest in several aspects of the electrochemical behaviour of platinum single crystals. The reactivity of bimetallic surfaces formed by combining platinum single crystals and adatoms has been a long-standing subject of research based on their specific and beneficial properties [111-112]. The study of the chemical properties of bimetallic surfaces have drawn considerable attention, particularly since the development of bimetallic catalysts for hydrocarbon reforming in the 1970's [113-114]. In recent years, increasing numbers of surface studies have been published [115-117], driven by the desire to gain a more fundamental understanding of the structural, electronic and chemical properties of bimetallic single crystalline surfaces. The preparation, characterisation and reactivity of bimetallic surfaces have been recently reviewed by Rodriguez [117]. Motivated by these studies, Fruehberger *et al.* investigated the surface reactivity of Ni/Pt(111) bimetallic surfaces produced by thermal evaporation of Ni onto a Pt(111) substrate [114]. He showed that the generation of model bimetallic surfaces offered several advantages over bulk alloy systems as it frequently enabled one to prepare and study bimetallic surfaces that had no stable bulk analogue and allowed one to readily compare the reactivity with those of pure metal components, and to investigate surface chemistry as a function of different bimetallic atomic ratios. **Figure 6** shows the top view of Pt(100) and Pt(111) single crystal surfaces. Pt(111) has the most compact surface with a coordination

number of 9 for each surface atom; it's less reactive and more saturated than Pt(100) which has a coordination number of 8 and has more open surfaces.

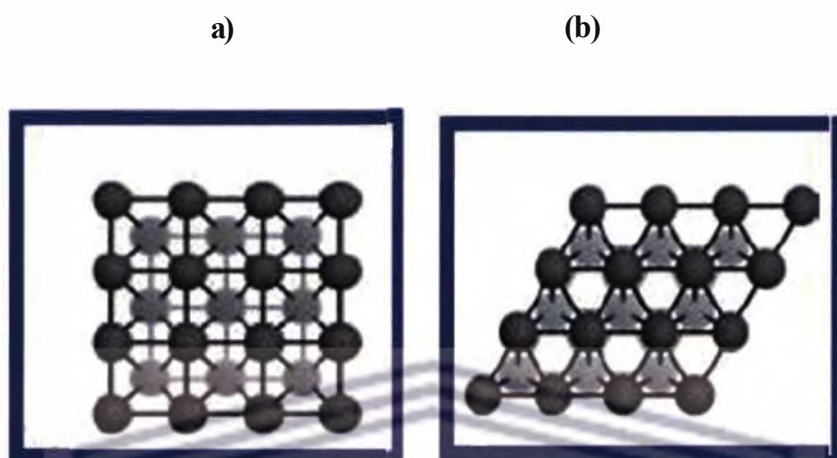


**Figure 6: Top view of (a) Pt(100) and (b) Pt(111) surfaces.**

SCMs have been found to have dense active sites for the adsorption of oxidation species such as ammonia. Vidal-Iglesias *et al.* investigated ammonia oxidation on Pt(111) and Pt(100) SCMs and found out that Pt(100) showed the highest active sites for the adsorption of ammonia [29]. However, polishing of SCM's has proved to be quite demanding. Fabrication of oriented nanomaterials is thus worthwhile. Well dispersed oriented nanoparticles have been found to portray similar active sites and are considered as required materials for practical purposes. Pt nanoparticles with (111) and (100) orientation have similar characteristics to the single crystal materials [29]. It is thus of great importance to investigate the effect of preferentially oriented platinum (100) ultrasensitive nanoparticles and nanoalloy systems on the oxidation of ammonia.

#### 2.2.4.6.1 Preferentially oriented Pt(100) and (111) nanoparticles

Catalytic reactivity of metal particles is undoubtedly linked to the nature of surfaces involved in the catalysis. Determining the particle shape and consequently the atomic arrangements in the crystal planes forming the surfaces is essential to our understanding of the whole phenomena of catalysis and the design of more "ideal" catalysts for different chemical transformations [118]. Preferentially oriented Pt(100) and (111) nanoparticles show similar properties to single crystal Pt(100) and Pt(111) materials which have been reported to have high active sites for ammonia oxidation (see section 2.2.4.6). Pt(100) nanoparticles investigated under high resolution transmission microscope (HRTEM) (ex situ characterisation) show cubic shaped nanomaterials while Pt(111) show tetrahedron/octahedron shaped nanoparticles [119]. Electrochemistry provides some surface sensitive reactions that can be used as a tool to characterise the surface structure. The so-called hydrogen adsorption/desorption process is very sensitive to the Pt surface structure [120] and this fact is used to characterise the type of orientation of the nanoparticles with voltammetric profiles similar to those portrayed by single crystal materials. **Figure 7** shows the voltammogram of oriented Pt(100) and (111) nanoparticles. It shows very clearly the presence of adsorption states associated to (110) and (100) sites at -131 mV and -33 mV, respectively (**Figure 7 A**). A peak at around 29 mV is observed associated to (100) site [29, 119]. A poorly defined peak around 445 mV is usually observed characteristic of small (111) ordered surface domains. The voltammetric profile is similar to that of a Pt(100) single crystal electrode. For the Pt(111) nanoparticles (**Figure 7 B**) the peaks around 0.5 V was well pronounced indicating the presence of (111) domains [121].

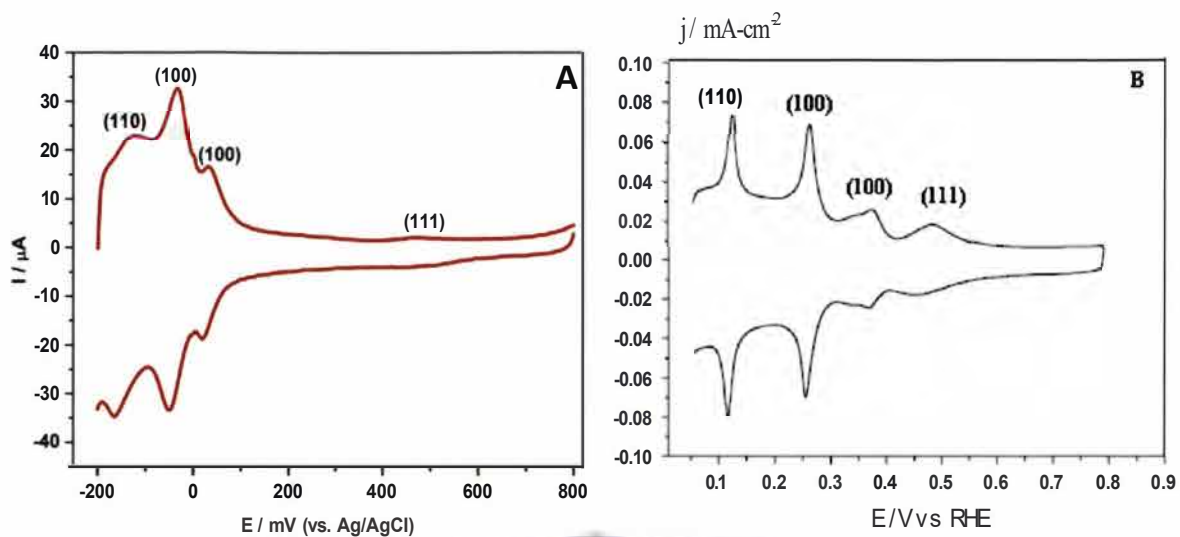


**Figure 7: Cyclic voltammograms of Pt(100) nanoparticles (A) and Pt(111) nanoparticles (B) modified Pt electrode in 0.5 M  $\text{H}_2\text{SO}_4$  at a scan rate of  $20 \text{ mV s}^{-1}$  [121].**

#### 2.2.4.7 Methods of synthesising nanoalloys

The synthesis of metal nanoparticles and nanoalloys has developed into a large field with diverse interests and applications. There are a number of methods used for the synthesis of metal nanoparticles. These methods include:

##### i) Electrochemical methods

This is a very versatile method of generating nanoalloys in solution. It involves the application of current at a certain potential in a solution containing the metal salts (precursors) in the presence of a supporting electrolyte. The nanoalloys are deposited on the cathode (for the two electrode system) and at the working electrode (for the three electrode system). It has some advantages over traditional methods in synthesis of metal nanoparticles such as simplicity, avoiding contamination with by-products resulting from chemical reducing agents in conventional methods, low cost and simple control of the metal content of bimetallic nanoparticles [122]. However, it is not easy to control the particle size and

relatively low product yield is obtained. Simple set ups for the electrochemical synthesis are shown in **Figure 8** below.

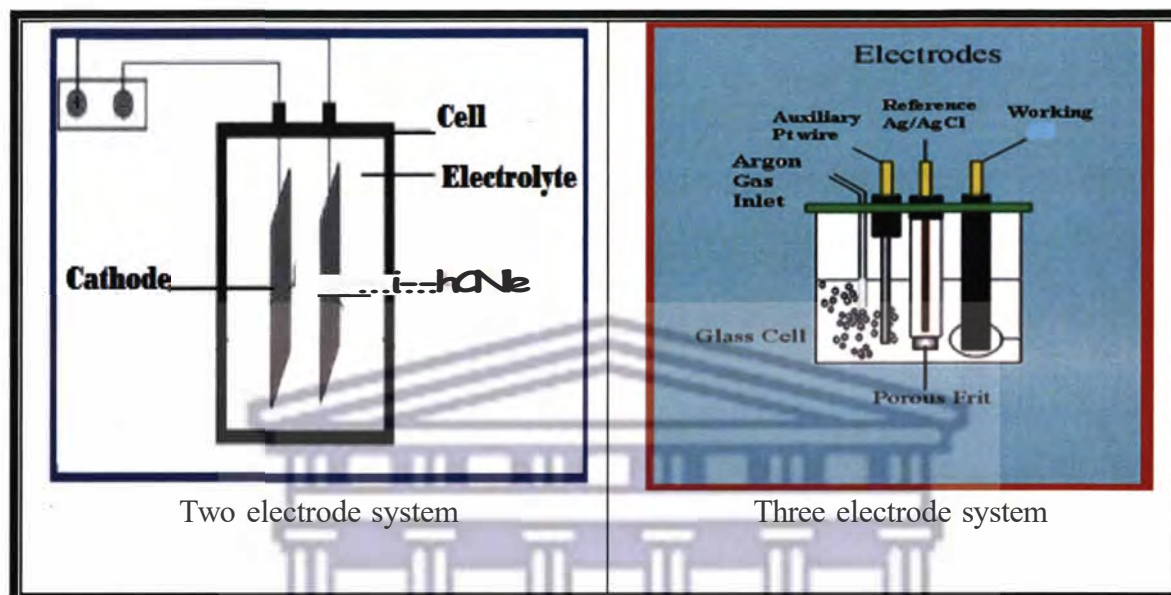


**Figure 8: Set-up for electrochemical synthesis of nanoalloys.**

## ii) Chemical reduction

Nanoalloys are produced chemically by simultaneous reduction of metal salts dissolved in appropriate solvent in the presence of surfactants such as citrate, alkylthiols or thioethers or polymeric ligands such as polyvinylpyrrolidone (PVP) which passivates the nanoalloys surface, stabilises them and prevent them from agglomeration [44]. The control of average particle size and size distribution can be achieved by tuning the preparation conditions (solvent, surfactant, reducing agent). The major advantage associated with chemical synthesis is that it is reproducible and allows colloidal nanoparticles with a narrow size distribution to be prepared on a multigram scale and is easy to scale up. However, the contamination from surfactants/capping agents and by-products is a major drawback of this method.



**Microemulsion method:** microemulsion is made up of water, oil and surfactant. Synthesis of mixed metal nanoparticles by the microemulsion method allows simultaneous control of size and composition. Microemulsion is a liquid droplet containing the noble metal precursor being engulfed by the surfactant molecules and uniformly dispersed in an immiscibly continuous organic phase which serves as a micro or nano-scaled reactor in which the chemical reaction takes place [123]. The size of the microemulsions is of the order of a few to hundred nanometres and is determined by the balance of the surface free energy mediated by the surfactant molecules and the difference in free energy caused by the immiscibility of the two liquid phases. Reduction of the metal can be carried out by adding the reducing agent directly into the microemulsion system, or by the introduction of another reducing agent containing microemulsion. The reducing agent must be stable in an aqueous environment and must not react with the other components of the system. Thus, all non-aqueous reducing agents are excluded. The most commonly employed reducing agents are borohydride and hydrazine. The surfactant molecules serve the role of a protective agent, thus preventing the agglomeration of nanoparticles. The main attractiveness of the microemulsion method is its ease in controlling the size distribution and composition of the metal particles within a narrow distribution by varying the synthetic conditions. The particle sizes depend on the precursor concentration and the amounts of surfactant. Metal nanoalloys can be synthesised if the salts of different metals are dissolved in the solution before the reduction is carried out, provided that the metal salts are miscible in the metallic state. The final composition of the mixed metal nanoparticles can easily be controlled by the ratio of the metal precursor solutions. However, the microemulsion method employs costly surfactant molecules and substantial number of separation and washing steps are needed before usage. Thus, this method may not be economical and suitable for large-scale production [123].

### **iii) Radiolysis**

This is an efficient method for reducing metal ions in order to generate nanoalloys. In the radiolytic method,  $\gamma$ -ray irradiation of water leads to solvated electrons which subsequently reduce the metal ions. This method can lead to formation of either core-shell or nanoalloys depending on the rate of radiolysis (which depends on the  $\gamma$ -ray dose), the relative concentrations of the metal salts, the rate of interion electron transfer, and the nature of the ligands which are coordinated to the metal ions. Higher doses favour core-shell formation while lower doses favour nanoalloy formation. Examples of nanoalloys synthesized using this method include: Cu-Pd, Ni-Pt, and Pd-Ag nanoalloys [124].

### **iv) Ion implantation**

The reduction of the metal salts is done using beams with energies of approximately 100 keV. The nanoalloys are synthesised on insulating matrices. The implantation of the metal salts is done on the matrix generating solid-solution nanoalloys. Examples of nanoalloys synthesised using this method include solid-solution Ag-Au, Cu-Pd, and Cu-Au nanoalloys implanted on silica [125].

### **v) Thermal decomposition of transition-metal complexes**

It involves the gentle thermolysis (e.g. heating to approximately 200 °C in vacuum for 2 h) of precursor organometallic metal salts (typically with carbonyl and phosphine ligands). Improved results are obtained if thermolysis is performed in the presence of stabilising ligands such as PVP. It has been used to synthesise nanoalloys particularly of the more noble metals such as Ru-Pd, Ru-Sn, Ru-Pt nanoalloys anchored within silica micropores with typical pore diameters of 3-30 nm [126].

## **vi) Biosynthesis**

This method involves the use of biomolecules as reducing agents. Certain microbes can reduce metal salts to their zero-valent metallic states. For example, bacterial hydrogenases have been used as reducing agents in the reduction of Pd(II) to Pd(0). Pd-Au hybrid nanoalloys have also been synthesised using the biosynthesis method. Biosynthesis of Ni-Ti nanoalloys has been done by reducing a solution of Ni and Ti ions mixed with a suspension of powdered milled alfalfa [127].

### **2.2.5 Characterisation techniques for the nanoalloys**

A variety of experimental techniques have been applied to characterise and study the properties of mono, bi- and multi-metallic nanoparticles. The following sub-section gives a brief overview of some of the most commonly applied techniques.

#### **2.2.5.1 Electrochemistry**

A variety of electrochemical techniques have been applied in the characterisation of nanoalloys such as cyclic voltammetry (CV) and electrochemical impedance spectroscopy (EIS). These measurements are particularly important for nanoparticles employed as electrode materials. Electrochemical techniques for surface measurement allow direct investigation of the surfaces of real catalysts under ambient conditions, thereby bridging the so-called "pressure" and "materials" gap between surface science and heterogeneous catalysis [128].

### 2.2.5.1.1 Cyclic voltammetry (CV)

Cyclic voltammetry (CV) is an electrochemical technique that is classified under sweep techniques. In cyclic voltammetry, the root word from voltammetry, "voltam-", refers to both potential ("volt-") and current ("am-"). During the voltammetric experiment, an applied potential at a working electrode is varied at a specific scan rate in both forward and reverse directions while the current is simultaneously monitored. The basic instrumentation for the cyclic voltammetry analysis requires controlled potential equipment (potentiostat) and an electrochemical cell consisting of three electrodes. The analysis is normally carried out using an electrochemical analyser connected to a three electrode cell, consisting of working electrode, reference electrode and counter electrode under an inert atmosphere. **Figure 9** shows an illustration of the three electrode system.

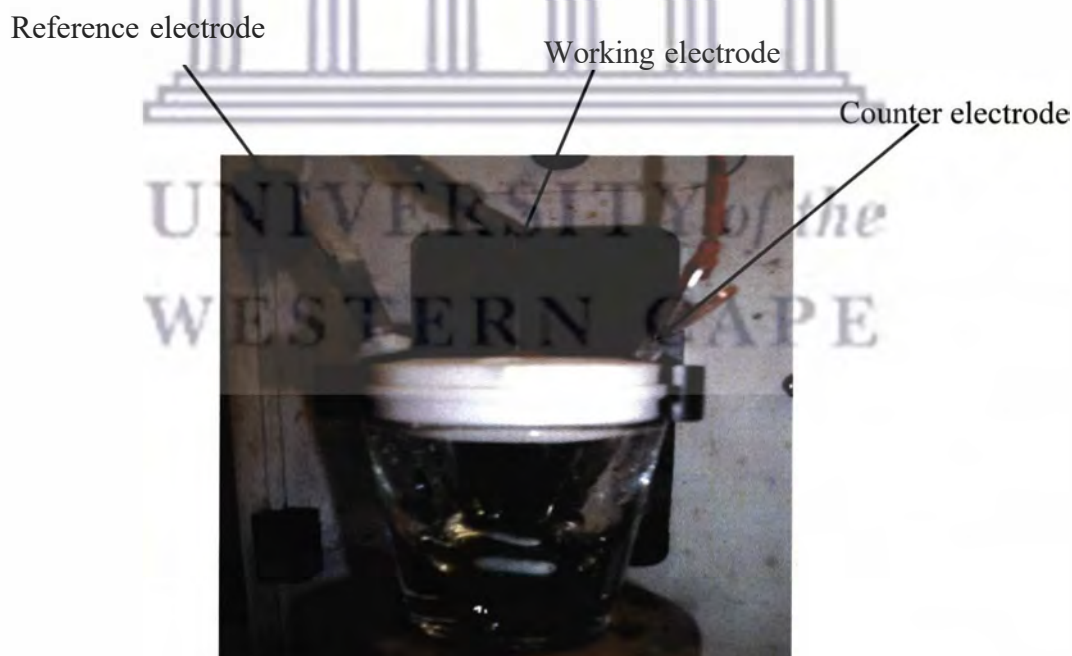


**Figure 9: Schematic representation of an electrochemical cell.**

The electrode where the reaction of interest takes place is called the working electrode. The common materials used for working electrode include platinum, gold and carbon (carbon can

be in the form of graphite, glassy carbon, or diamond). These electrodes are generally encased in an inert insulator with a disk exposed at one end and it should not be susceptible to oxidation or reduction. In addition, it is very important that materials used as a working electrode should be inert. The reference electrode provides a stable potential compared to the working electrode. Reference electrodes are used because their potentials are constant. There are different types of reference electrodes and the commonly used ones are the saturated calomel electrode (SCE), and the silver/silver chloride electrode, Ag/AgCl. The counter electrode, also known as the auxiliary or secondary electrode, can be made of any material which conducts current easily and will not react with the bulk solution. The auxiliary electrode is usually made up of a platinum wire or a mesh can also be used.

In cyclic voltammetry the potential is ramped from an initial potential ( $E_i$ ) and at the end of the linear sweep, the direction of the potential scan is reversed, usually stopping at the initial potential. The potential at which the change in direction occurs is also known as the switch potential ( $E_s$ ). The scan rate between  $E_i$  and  $E_s$  is the same as that between  $E_s$  and  $E_i$  and the values of the scan rate  $v_{\text{forward}}$  and  $v_{\text{reverse}}$  are always written with positive numbers. Oxidation usually takes place during the forward part of the CV, if scanned from a negative to a positive potential. The reverse part of the CV will then represent reduction, with the potential running from a positive to a negative potential. However, if the potential is scanned from a positive to a negative value, then reduction would occur during the forward part of the CV scan and oxidation during the reverse CV scan. Important parameters are usually obtained from cyclic voltammograms for analysis of reversible, quasi-reversible and irreversible reaction properties of an electroactive sample. These parameters include anodic and cathodic peak potentials, denoted as  $E_{p,a}$  and  $E_{p,c}$ , respectively as well as anodic and cathodic peak currents

denoted as  $i_{p,a}$  and  $i_{p,c}$ , respectively. A typical cyclic voltammogram illustrating these parameters is shown in **Figure 10**.

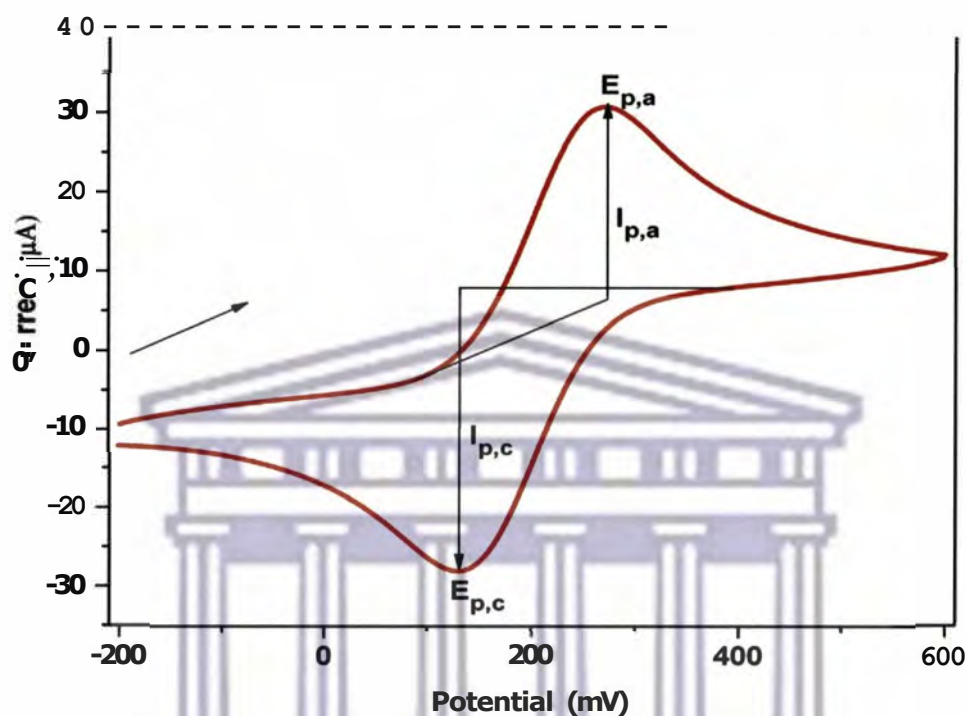


**Figure 10:** A typical cyclic voltammogram showing the basic peak parameters.

In voltammetry the magnitude of the current in a reversible system is proportional to the concentration of the analyte, so the equality between  $i_{p(\text{forward})}$  and  $i_{p(\text{reverse})}$  (where 'p' represents 'peak') implies a quantitative retrieval of electromodified material, which follows from Faraday's laws [129-131]. The position of both the cathodic and anodic peaks gives us thermodynamic information of the redox couple used. The anodic and cathodic peak potentials also helps in the calculation of the formal electrode potential,  $E^f$ , as follows:

$$E^f = \frac{E_{p,a} + E_{p,c}}{2} \quad (17)$$

The formal electrode potential (normally called the formal potential or the formal redox potential) is in concept similar to the standard electrode potential,  $E^\theta$  [130-131]. Cyclic

voltammetry is the most widely used technique for acquiring qualitative information about electrochemical reactions. The power of cyclic voltammetry results from its ability to rapidly provide considerable information on the thermodynamics of redox processes, on the kinetics of heterogeneous electron-transfer reactions, and on coupled chemical reactions or adsorption processes. It is often the first experiment performed in an electroanalytical study. In particular, it offers a rapid location of redox potentials of the electroactive species, and convenient evaluation of the effect of media upon the redox processes [132].

#### **2.2.5.1.1.1 Data interpretation**

The CV is characterised by several important parameters. Four of these observables; the two peak currents and two peak potentials, provide the basis for the diagnosis developed by Nicholson and Shain for analysing the cyclic voltammetric response [132]. Some important information about the sample under investigation can be obtained from the peak parameters. This includes whether the electrochemical process displayed by the sample is reversible, irreversible or quasi-reversible. It also gives insight into how fast the electron transfer process is, relative to other processes such as diffusion [133].

##### **a) Reversible systems**

The peak current for a reversible couple is related to the concentration of the electroactive species as depicted by the Randles-Sevcik equation.

##### **Randles-Sevcik equation**

The magnitude of the peak current of a reversible couple,  $I_p$ , in a CV is a function of the temperature ( $T$ ), bulk concentration ( $C_0$ ), electrode area ( $\text{cm}^2$ ) ( $A$ ), the number of electrons transferred ( $n$ ), the diffusion coefficient ( $D$ ), the Faraday constant ( $F$ ) ( $96\,486\text{ C mol}^{-1}$ ), the

gas constant ( $R$ ) ( $8.314 \text{ J mol}^{-1} \text{ K}^{-1}$ ) and the speed at which the potential is scanned ( $v$ ), according to Randles-Sevcik equation (129).

$$I_p = 0.4463nFA(nF/RT)^{1/2}D^{1/2}v^{1/2}C_0 \quad (18)$$

At  $25^\circ\text{C}$  the above equation reduces to (129, 132, 134):

$$I_p = 2.686 \times 10^5 n^{3/2} AD^{1/2} v^{1/2} C_0 \quad (19)$$

Accordingly, the current is directly proportional to the concentration and increases with the square root of the scan rate. The Randles-Sevcik equation is obeyed if a plot of peak current ( $I_p$ ) against analyte concentration ( $C_0$ ) yields a straight line. It also means that if the electrolyte composition is constant in terms of temperature, solvent, electrolyte, then the Randles-Sevcik equation can be used to determine the concentration of analyte by the construction of a suitable calibration curve (130, 134]. When the peak current is plotted against the square root of the scan rate, with  $I_p$  as the y-axis and  $v^{1/2}$  as the x-axis, often referred to as the Randles-Sevcik plot, a straight line is obtained that passes through the origin and the slope of the linear plot can be used to determine the concentration of the analyte ( $C_0$ ) if the diffusion coefficient  $D$  is known precisely (**Figure 11**) (130]. In addition, a Randles-Sevcik plot is also the best way to determine an experimental value of the diffusion coefficient,  $D$ , if it is not available in literature, in the case of a reversible reaction (129].



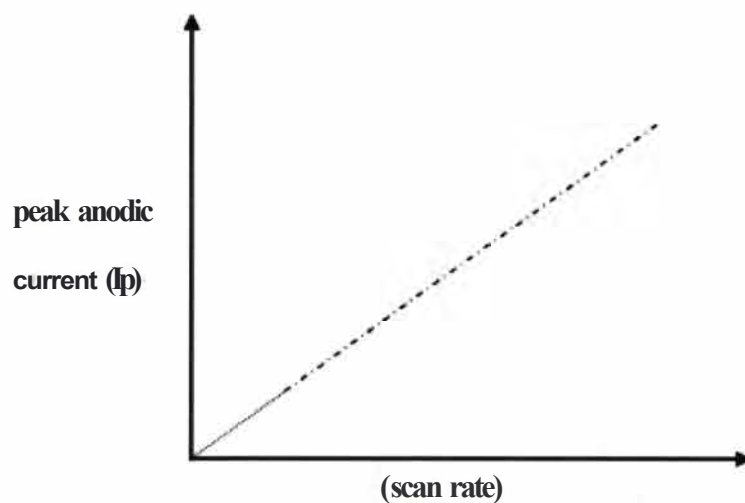


**Figure 11: The Randles-Sevcik plot ( $I_p$  against  $v^{1/2}$ ).**

From the Randles-Sevcik equation, it is also possible to calculate other variables listed in **equations 18** and **19**. That is, if the peak current ( $I_p$ ) at a certain scan rate ( $v$ ) is measured, and the area of the electrode ( $A$ ), the diffusion coefficient ( $D$ ) and the concentration ( $C_0$ ) of the species under study are known, one is able to calculate the number of electrons ( $n$ ) involved in the redox change. Similarly, if the number of electrons ( $n$ ) is known, one can calculate the diffusion coefficient ( $D$ ) of the species, and any of the other variables.

### **Diagnostic criteria to identify a reversible process**

To prove reversibility of the system when CV is performed, the following conditions should hold:

- ▶ the ratio of the currents: reduction ( $J_{p,c}$ ) and oxidation ( $I_{p,a}$ ) is near unity ( $J_{p,a} = I_{p,c}$  or  $I_{p,a} / I_{p,c} = 1$ )
- ▶ the peak potentials ( $E_{p,a}$  and  $E_{p,c}$ ) are independent of the scan rate,  $v$
- ▶ the formal potential ( $E^{\theta}$ ) is positioned midway between  $E_{p,a}$  and  $E_{p,c}$ , so that

$$E^{\theta} = (E_{p,a} + E_{p,c}) / 2$$

- ▶ the peak current ( $I_p$ ) is proportional to  $v^{1/2}$

- the separation between the peak potentials  $E_{p,a}$  and  $E_{p,c}$  is  $59 \text{ mV}/n$  for an  $n$ -electron couple at  $25 \text{ }^\circ\text{C}$  or  $|E_{p,a}-E_{p,c}|$  would be  $59 \text{ mV}$  for a 1 electron process and  $30 \text{ mV}$  for a 2 electron process. Thus, the separation can be used to determine the number of electrons transferred and as a criterion for Nernstian behaviour.

Moreover, if the electron transfer is fast relative to the diffusion of electroactive species from the bulk solution to the surface of the electrode, the reaction is said to be electrochemically reversible and the peak separation ( $\Delta E_p$ ) is given by **equation 20** below.

$$\Delta E_p = |E_{p,a} - E_{p,c}| = 2.30 \frac{RT}{nF} \quad (20)$$

where  $\Delta E_p$  is the peak separation (V),  $E_{p,a}$  is the anodic peak potential (V),  $E_{p,c}$  is the cathodic peak potential (V),  $n$ ,  $F$  and  $R$  are explained in **equation 18** [132]. According to **equation 20**, for reversible one-electron processes, the peak-to-peak separation assumes different values as a function of the temperature [131]. When the value of  $\Delta E_p$  is measured, a departure of 10 - 20 mV from the theoretical value, especially at high scan rates, does not compromise the criterion for reversibility. This is due to the fact that the eventual presence of solution resistance, if not adequately compensated by the electrochemical instrumentation, tends to shift the forward/reverse peaks system, thereby increasing the relative value of  $\Delta E_p$  [130-131].

### b) Quasi-reversible systems

A quasi-reversible process refers to one occurring in the transition zone between reversible and irreversible behaviour. A typical cyclic voltammogram for a quasi-reversible process is shown in **Figure 12** (Curve B). A quasi-reversible process is characterised by determining

either the thermodynamic parameter  $E^{\circ}$  (formal potential) or the kinetic parameters,  $\alpha$  (transfer coefficient) and  $k$  (rate constant) [130-131].

### Diagnostic criteria to identify a quasi-reversible system

For a quasi-reversible system, the following conditions should hold:

- $I_p$  increases with  $v^{1/2}$  but is not proportional to it
- $I_{p,a} = I_{p,c}$  OR  $I_{p,a} / I_{p,c} = 1$  provided  $\alpha_c = \alpha_a = 0.5$
- $E_p$  is greater than  $59/n$  mV and increases with increasing  $v$
- $E_{p,c}$  shifts negatively with increasing  $v$

The current for quasi-reversible process (with  $10^{-1} > k > 10^{-5}$  cm s<sup>-1</sup>) is controlled by both charge transfer and mass transport. In such a case, the shape of the CV is a function of

$\frac{k}{I_{r,c}}$  (where  $\alpha = \frac{nFv}{RT}$ ). When the values of  $\frac{k}{I_{r,c}}$  increase, the quasi-reversible process

approaches the reversible system and when its values decrease (i.e. at very fast scan rate) an irreversible process behaviour is observed. Compared to reversible system, cyclic voltammograms of a quasi-reversible system are more drawn-out and have a larger peak potential separation [132].

### c) Irreversible systems

The most important characteristic of a cyclic voltammogram of a totally irreversible system is the total absence of a reverse peak. For totally irreversible systems, the peak potential shifts with the scan rate. In addition, the individual peaks are reduced in size and widely separated as shown in **Figure 12** (curve A).

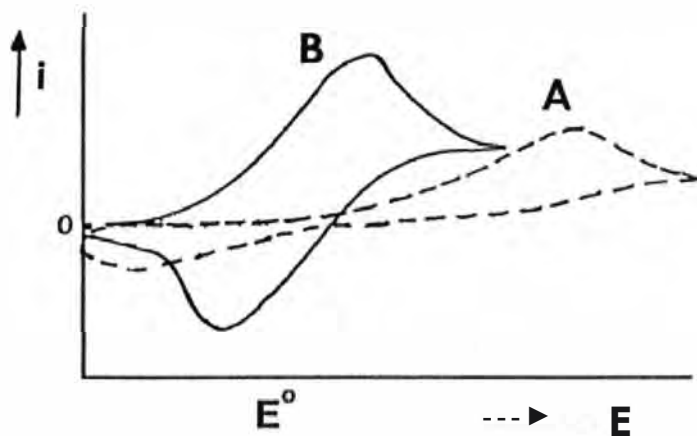


Figure 12: Typical cyclic voltammograms for an irreversible electrochemistry process (curve A) and for a quasi-reversible process (curve B) [132].

#### Diagnostic criteria to identify an irreversible process

The following conditions are required to identify whether an electrochemical process is irreversible:

- there is no reverse peak
- the  $I_{p,a}$  or  $I_{p,c}$  is proportional to  $\nu^{1/2}$
- the value of  $E_p$  shifts  $-30/a.n$  for each decade increase in  $\nu$
- $E_p - E_p^0 = -\frac{48}{an} V$

Totally irreversible systems are characterised by a shift of the peak potential with the scan rate [132].

$$E_p = E^0 - \frac{RT}{an_a F} \left[ 0.78 - \ln\left(\frac{k}{D\nu}\right) + \ln\left(\frac{an_a F \nu}{RT}\right) \right] \quad (21)$$

Where  $k$  is heterogeneous rate constant and  $a$  is the transfer coefficient and  $n$  is the number of electrons involved in the charge-transfer step. Thus,  $E_p$  occurs at higher potentials than  $E^0$ , with the over-potential related to  $k$  and  $a$ . In cases where  $E_p$  is independent of  $k$ , the

shift of the peak potential could be compensated by an appropriate change of the scan rate; the peak potential and the half-peak potential (at 25 °C) will differ by 48/an mV. Therefore, when an decreases, the voltammogram could become more drawn out. **Equation 21** also allows for the calculation of the heterogeneous rate constant,  $k$ , if the values of  $E^{\beta}$  and  $D$  are known. The peak current for an irreversible process is given by [135]:

$$I_p = (2.99 \times 10^5) n(\alpha n)^{1/2} A C_0 D^{1/2} \nu^{1/2} \quad (22)$$

For an irreversible process, the peak current ( $I_p$ ) is proportional to the bulk concentration ( $C_0$ ) but can be lower in value depending on the value of the transfer coefficient ( $\alpha$ ). Assuming that  $\alpha = 0.5$ , the ratio of reversible-to-irreversible peak current will be 1.27 (i.e. the peak currents for the irreversible process is about 80% of the peak for the reversible one). The chemical meaning of an irreversible electrochemical process implies that a large activation barrier to the electron transfer takes place causing breakage of the original molecular frame with the formation of new species [130-131].

#### d) Study of adsorption processes

Cyclic voltammetry can also be used for evaluating the interfacial behaviour of electroactive compounds. Both the reactant and the product can be involved in an adsorption - desorption process. Such interfacial behaviour can occur in studies of numerous organic compounds, as well as of metal complexes (if the ligands is specifically adsorbed) [132]. In some cases, the sample to be characterised may be immobilised onto the surface of a working electrode (chemically modified electrodes). In such a case, the surface concentration ( $\Gamma$ ) of the adsorbed species could be estimated from a plot of current ( $I_p$ ) versus scan rate ( $\nu$ ) in

accordance with the Brown Anson model (**equation 23**) where  $I'$  is the surface concentration (mol cm<sup>-2</sup>) [131-132].

$$I_p = \frac{n^2 F^2 r A v}{4RT} \quad (23)$$

During the reduction or adsorption of the adsorbed layer, the quantity of the charge (Q) consumed can also be used to calculate the surface coverage or surface concentration (I) [132].

$$Q = nFA\Gamma \quad (24)$$

Where Q is the charge in Coulomb (C) and  $\Gamma$  is a surface coverage in mol cm<sup>-2</sup>. Cyclic voltammetry is a good technique for studying the electrochemistry of nanomaterials since some nanomaterials exhibit reversible, quasi-reversible and irreversible behaviour.

#### 2.2.5.1.2 Electrochemical impedance spectroscopy (EIS)

For electrochemical studies of nanomaterials, the nanomaterials are usually immobilised on electrodes. Electrochemical Impedance spectroscopy (EIS) is an excellent, non-destructive, accurate and rapid in-situ technique for examining processes occurring at the electrode surface [136]. The measurement of EIS involves application of a sinusoidal voltage to an electrochemical cell, and measuring the current response. A frequency response analyser generates time-invariant amplitude (A), phase (0) and angular frequency ( $\omega$ ) voltage-current waves. The ratio of voltage (E) to current (I) gives the impedance and has units of resistance (ohms), in accordance with the Ohm's law; Voltage (E) = Current (I) x Resistance (R). The total impedance is therefore a function of frequency and is expressed in a complex form, with real and imaginary components as follows:

$$Z(j\omega) = \frac{E}{I}(\omega) = Z'(\omega) + jZ''(\omega) \quad (25)$$

where  $Z'(\omega)$  and  $jZ''(\omega)$  are the real and imaginary impedance respectively,  $j = -1$  and is an imaginary number while  $\omega$  is the radial frequency (rad. s<sup>-1</sup>) and equals  $2\pi f$ ,  $f$  being the exciting frequency (Hz). Impedimetric data is graphically represented in various forms. The most common is the Nyquist plot whereby the imaginary part of the impedance ( $Z_i$ ) is plotted against the real part ( $Z_r$ ) over a wide frequency range (normally 100 kHz to 0.1 Hz). The real part of the impedance represents the resistive component of the system while the imaginary part is due to insulating layers such as the double layer capacitance or any additional layers in the system. In the Nyquist plot, the low frequency data is represented on the right side while the high frequency data is represented on the left side of the diagram. The Nyquist plot of impedance spectra includes a semicircle portion and a linear portion, with the former at higher frequencies corresponding to the electron transfer process and the latter at lower frequencies corresponding to the diffusion process. The electron transfer resistance ( $R_{ct}$ ) at the electrode surface is equal to the semicircle diameter, which can be used to describe the interface properties of the electrode [137].

Another way of presenting impedance data is a Bode plot in which the logarithm of the absolute value of  $Z'$  and the phase ( $\theta$ ) are plotted against the logarithm of the frequency ( $f$ ) [138]. This can be plotted together or separately. Nyquist plots are more commonly displayed for historical reasons, the data is however often poorly resolved (particularly at high frequencies), and the explicit frequency dependence is not displayed in the plot. In contrast, the Bode plot directly displays the frequency dependence; in addition, the data is well resolved at all frequencies, since a logarithmic frequency scale is used. When the frequency

of the AC waveform is varied over a wide range of frequency (ca about  $10^4$  and  $> 10^6$  Hz), the impedance obtained for the system is a function of the operating frequency. Spectra of the resulting impedance at different frequencies reveal the different electrochemical kinetics involved in the system. While dipolar properties are manifested at high frequency regions, bulk and surface properties will be evident at intermediate and low frequencies respectively [138]. The total impedance of a system is determined by the impedances of the various components of the electrochemical cell; for example, electron transfer kinetics, diffusion and passivating layers. The relative contribution of the various components typically varies with frequency; for example, electron transfer kinetics may dominate at high frequencies, whereas diffusion may dominate at lower frequencies [138]. Measuring impedance over a wide frequency range allows processes with different time scales such as electron transfer, mass transport and chemical reaction to be detected within the same experiment. **Figure 13** shows the impedance diagram for the real impedance (x-axis) and imaginary impedance (y-axis) with low frequency data being on the right side of the plot and higher frequencies are on the left [138].

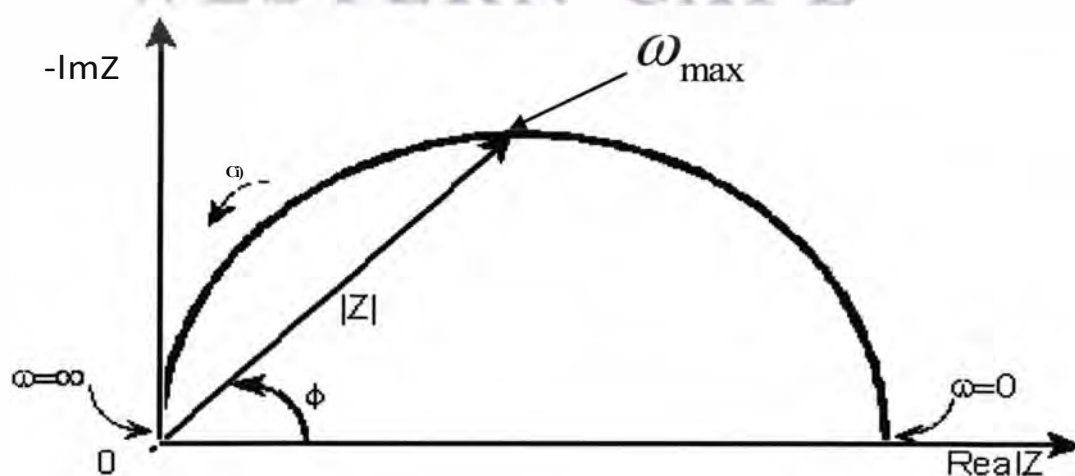


**Figure 13:** A typical impedance diagram.



A typical Nyquist plot for the impedance data is shown in **Figure 14**. The semi-circular shape is characteristic of a single "time constant".

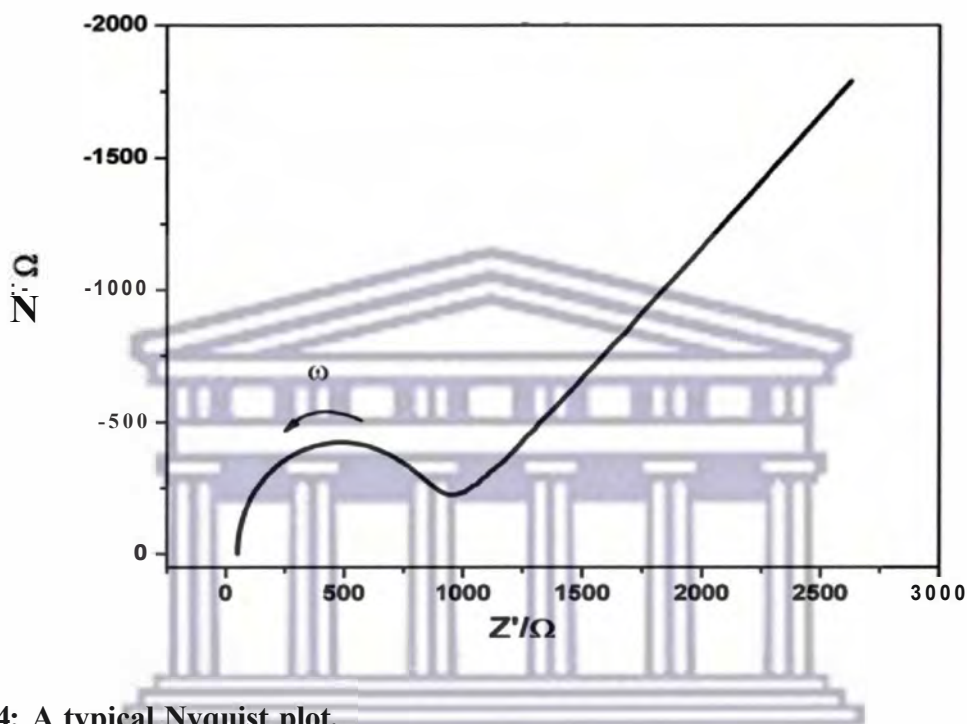


**Figure 14:** A typical Nyquist plot.

EIS is a useful tool in studying the kinetics of electrochemical reactions. Redox reactions usually involve charge transfer kinetics and mass transfer. The slower of these two determines the rate of the reaction. The mass transfer in EIS is limited to diffusion (concentration gradient) by the steady state conditions. **Figure 15** shows the Nyquist plot indicating the kinetically controlled (higher frequency) and the mass controlled (low frequency) parts of the plot.

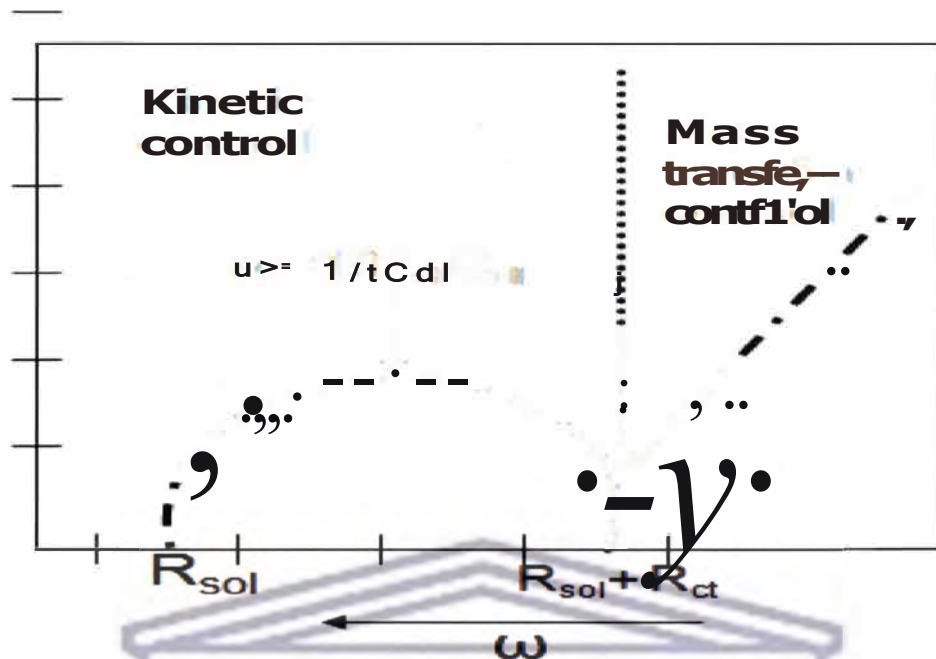


Figure 15: A typical Nyquist plot showing some kinetic parameters.

From  $\omega_{\max}$  (frequency at maximum imaginary impedance of the semicircle) useful kinetic parameters such as double layer capacitance ( $C_{dl}$ ), (obtained using **equation 26**), time constant (cycle life)  $\tau$ , (calculated using **equation 27**), exchange current  $I_0$ , (Calculated using **equation 28**) and heterogeneous rate constant  $k$  (calculated using **equation 29**) can be calculated:

$$\omega_{\max} = \frac{1}{R_{ct} C_{dl}} \quad (26)$$

$$\tau = R_{ct} C_{dl} \quad (27)$$

$$I_0 = \frac{RT}{nFR_{ct}} \quad (28)$$

$$k = \frac{I_0}{nFA C_0} \quad (29)$$

where  $C_{V_{max}} = 2 \gamma_t f R_s$  is the solution resistance,  $R_{c_1}$  is the charge transfer resistance,  $C_{dl}$  is the double layer capacitance,  $R$  is the gas constant ( $8.314 \text{ J K}^{-1} \text{ mol}^{-1}$ ),  $F$  is the Faradays constant ( $96486 \text{ C mol}^{-1}$ ),  $n$  is the number of electrons,  $\tau$  is the time constant or cycle life,  $i_0$  is the exchange current (relates rate constant to electron transfer at zero overpotential),  $C_0$  is the concentration ( $\text{mol cm}^{-3}$ ) and  $k$  is the heterogeneous rate constant. A representative plot of frequency as x-axis versus logarithm of real impedance as  $y_1$ -axis, and phase angle as  $y_2$ -axis called Bode plot is presented in **Figure 16** and **17**. Bode plot is a plot of log magnitude of impedance and phase angle versus log of frequency [139].

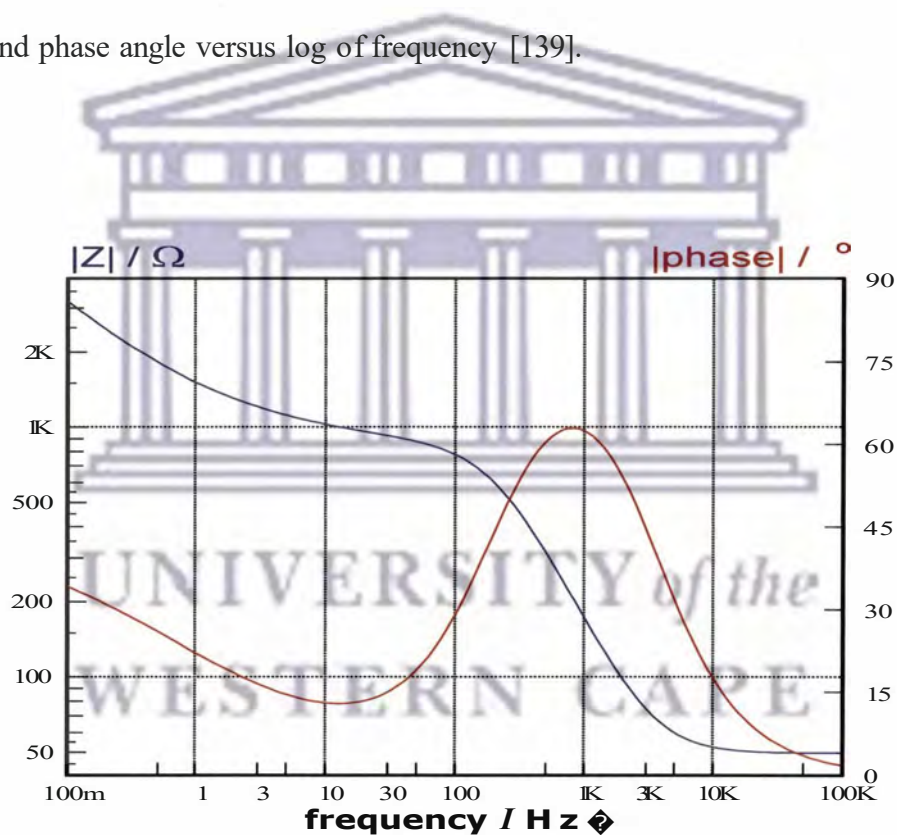


**Figure 16:** A typical Bode plot showing variation of impedance and phase angle with changes in frequency.

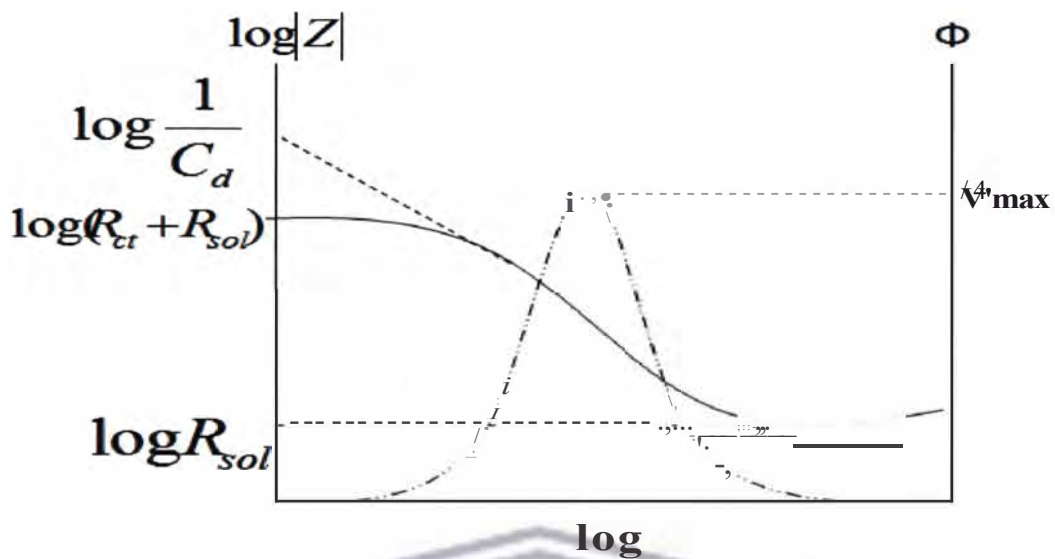


Figure 17: A Bode plot showing some kinetic parameters.

The Bode plot gives direct information on the frequency and phase angle. The frequency at maximum phase is a useful parameter in determining the double layer capacitance using equation 30:

$$\omega_{\Phi_{max}} = \frac{(1 + R_{ct} I_{o1})}{R_{ct} C_d} \quad (30)$$

Impedance data is commonly analysed by fitting it to an equivalent circuit model. The frequently used circuit, called the Randles equivalent circuit is composed of different elements such as resistors, capacitors, and inductors joined in series or in parallel (see Figure 18).

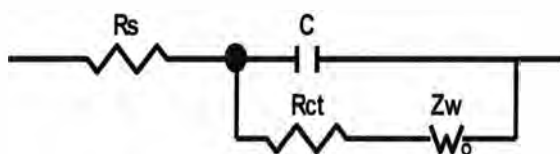


Figure 18: Randles equivalent circuit for a simple electrochemical cell.

$C$  is capacitance which is the ability of an electrochemical system to store or retain charge and  $Z_w$  is the Warburg impedance associated with the resistance as a result of the diffusion of ions across the electrode/electrolyte interface. Thus, EIS can give useful information on the basis of impedance changes at the electrode surface before and after its modification.

### **2.2.5.2 Microscopy**

For metal nanoparticles adsorbed onto a substrate or in colloid solutions, it is important to know the degree of aggregation, size, size distribution, and morphology of the particles. Microscopies of various types can be used to obtain this and other information.

#### **2.2.5.2.1 Electron microscopy**

Electron microscopy is particularly useful for studying nanoparticles as the electron beam can be focused down to very small dimensions [91].

##### **2.2.5.2.1.1 Transmission electron microscopy (TEM)**

Transmission electron microscopy (TEM) is a microscopic technique which involves the transmission of a beam of electrons through an ultra-thin specimen and interacts with the specimen as it passes through. An image is formed from the interaction of the electrons transmitted through the specimen; the image is magnified and focused onto an imaging device, such as a fluorescent screen on a layer of photographic film, or to be detected by a sensor such as a CCD camera. Transmission electron microscopes are capable of imaging at a significantly higher resolution than light microscopes, owing to the small de Broglie wavelength of electrons. This enables the instrument's user to examine fine detail-even as small as a single column of atoms, which is tens of thousands times smaller than the smallest resolvable image in a light microscope. The homogeneity of particle size or shape, aggregate

state and morphology on the atomic scale is quite important to reveal the physical properties of nano-sized materials. These can be obtained by the use of TEM which is an indispensable technique commonly used for metal nanoparticle studies. Through the use of TEM, one can view the finest structures [91].

The sample preparation for colloidal dispersions of metal nanoparticles for TEM observation is quite simple, involving evaporation of a small drop of dispersion onto a carbon coated micro-grid. However, the carbon coating must be thin enough to obtain a good contrast. Further, if the dispersion contains many additives, such as stabilisers or ligands, it may be diluted or filtered to obtain a clear view. TEM is particularly useful because of the high contrast between the metal atoms (especially heavy metals) and any passivating organic molecules or polymers. Recent improvement to a high-voltage electron beam technique has recently been done and the resolution of transmission electron microscopy is now sufficient to have a clear image of metal nanoparticles at the Angstrom level as described below.

#### **2.2.5.2.1.2 High resolution transmission electron microscopy (HRTEM)**

High-resolution TEM (HRTEM) offers resolution down to Angstrom level and enables information to be obtained on the structure (atomic packing) rather than just the morphology of the nanoparticles. It provides information not only on the particle size and shape but also on the crystallography of monometallic and bimetallic nanoparticles [140-141]. HRTEM can also estimate the area composition by fringe measurements. In this work HRTEM was used to determine the size, morphology and the crystallinity of the materials under study. The orientation of the instrument is depicted below, in **Figure 19**.

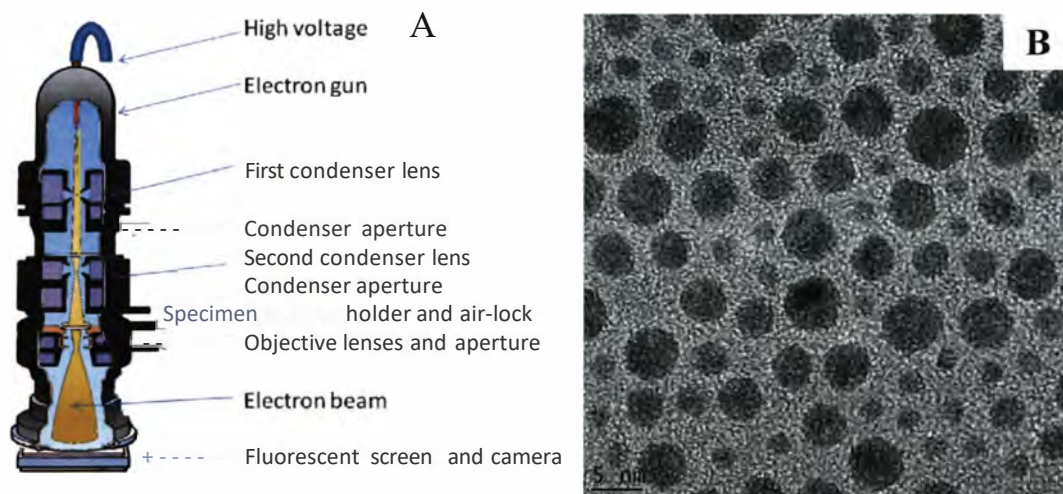


**Figure 19: Schematic presentation of HRTEM (A) and an example of a HRTEM image (B) [142].**

#### 2.2.5.2.1.3 Scanning transmission electron microscopy (STEM)

Scanning transmission electron microscopy (STEM) is a mode of operation of TEM in which an electron beam is scanned across the sample. This may be combined with "Z-contrast" imaging technique to reveal the internal structure of the nanoparticles, based on the different electron scattering powers of different elements, so that chemical information can be obtained in tandem with structural information [143]. This method is particularly useful for studying bimetallic nanoparticles where the constituent elements have similar lattice spacing e.g. Pd-Pt and Ag-Au.

#### 2.2.5.2.1.4 Scanning electron microscopy (SEM)

Scanning electron microscopy (SEM) is similar to STEM but the image is due to secondary electrons emitted by the sample surface following excitation by the primary electron beam. Although SEM images have lower resolution than TEM, SEM is better for imaging bulk samples and has a greater depth of view, giving rise to better 3D images of the sample. It is a facile imaging technique that is able to produce three-dimensional images of material

surfaces. It has high magnification, large depth of focus, great resolution and ease of sample observation. SEM basic operation entails the interaction of an accelerated highly mono-energetic electron beam, originating from cathode filament, with atoms at the sample surface. The electron beam is focused to a fine probe which is rastered over the sample. The rastered electrons are collected by a detector, modulated and amplified to produce an exact reconstruction of the sample surface and particle profile [144-145] A requirement for effective performance is that the surface of sample should be electrically conductive. Conductive materials such as metals and carbon are introduced directly to the SEM while non-metallic samples have to be coated with a gold metal layer to be observed. Energy dispersive spectrometer (EDX) detector system is usually coupled to SEM machines which are used to detect and display most of the spectra of elements making up the sample elemental composition.

#### **2.2.5.2.2 Scanning probe microscopy**

Scanning probe microscopes (SPM) define a broad group of instruments used to image and measure properties of material including, chemical, and biological surfaces. SPM images are obtained by scanning a sharp probe across a surface while monitoring and compiling the tip-sample interactions to provide an image. The measurement of the strength of the interaction is used to map out the topography, electronic/magnetic structure, or chemistry of the surface [146]. Prior to the invention and commercial availability of SPMs, researchers traditionally used (and still use) a variety of microscopes to image surfaces and measure surface morphology on a microscale. Optical microscopes are the most common instrument available to image any sample that is not completely optically transparent. Resolution is limited to about 1  $\mu\text{m}$  and only images and size measurements from features lying in the surface ( $x$ - $y$ ) plane are obtainable. Also, optical microscopy has a relatively small depth of field. SPMs



provide a number of advantages over these conventional microscopy techniques such as: it probes the sample and makes measurements in three dimensions;  $x$ ,  $y$ , and  $z$  (normal to the sample surface), thus enabling the presentation of three-dimensional images of a sample surface and can image materials at nanoscale. There are two primary forms of SPMs; scanning tunneling microscopy (STM) and atomic force microscopy (AFM).

#### **2.2.5.2.2.1 Scanning tunneling microscopy (STM)**

STM was first developed in 1982 at IBM in Zurich by Binnig, *et al.* [147]. The invention of the scanning tunneling microscope has had a great impact on technical community by providing a new and unique tool to advance fundamental science and technology [148]. A fine tip is brought extremely close to the surface, and a voltage is applied between the tip and the sample, which must be conducting, until a tunneling current flow, which is very sensitive to the distance between the tip and surface. We have two modes used in STM; constant current mode and constant height mode. In constant current mode, the STM tip is rastered across the surface and moved up or down to keep the current flow constant, thereby generating real-space, atomic resolution topographic images of the sample. In constant height mode, the tunneling current is measured with the tip maintained at constant height, which can provide information on electronic structure as well as topography. Scanning tunneling spectroscopy is an off shoot of STM, which measures the local electronic structure (which depends on the atomic species and its environment) of a surface atom.

Although the ability of the STM to image and measure material surface morphology with atomic resolution has been well documented, only good electrical conductors are candidates for this technique. This significantly limits the materials that can be studied using STM and thus led to the development, in 1986, of the atomic force microscope by Binnig Quate and

Gerber [149]. This enabled the detection of atomic scale features on a wide range of insulating surfaces that include ceramic materials, biological samples and polymers [149].

#### **2.2.5.2.2 Atomic force microscopy (AFM)**

Atomic force microscopy has become a standard technique for high-resolution imaging of the topography. It enables one to see nanoscopic surface features. This powerful probe microscopy operates by measuring the force between the probe and the sample. This force is attributed to repulsion generated by the overlap of the electron cloud at the probe tip with the electrode cloud at surface atoms [150]. It depends in part on the nature of the electrode, the distance between the electrode and the tip, any surface contamination and the tip geometry. The interaction of the force fields is sensed by a cantilever beam, to which the tip is attached. An image (revealing individual atoms) is created as the probe is rastered across the surface [150]. Such images can be formed by constant-force or constant-height mode (with known or measured deflections of the cantilever, respectively). Since AFM doesn't involve passage of current between the tip and the surface, it is useful for exploring both insulating and conducting regions [150]. A fine tip is brought into close (but not touching) contact with the sample and senses the small repulsive force between the probe tip and the surface. The tip is rastered over the sample to measure the surface topography. AFM provides a number of advantages over conventional microscopy techniques. It probes the sample and make measurements in three dimensions;  $x$ ,  $y$ , and  $z$  (normal to the sample surface), thus enabling the presentation of three-dimensional images of a sample surface. This provides a great advantage over any microscope available previously [150]. With good samples (clean, with no excessively large surface features), resolution in the  $x$ - $y$  plane ranges from 0.1 to 1.0 nm and in the  $z$  direction in 0.01 nm (atomic resolution) is possible. AFM requires neither a vacuum environment nor any special sample preparation, and they can be used in either an

ambient or liquid environment. With these advantages AFM has significantly impacted the fields of materials science, chemistry, biology, physics, and the specialised field of semiconductors [150]. **Figure 20A** illustrates an AFM probing a sample surface with a sharp tip while **(B)** is a topographical representation of the acquired image.

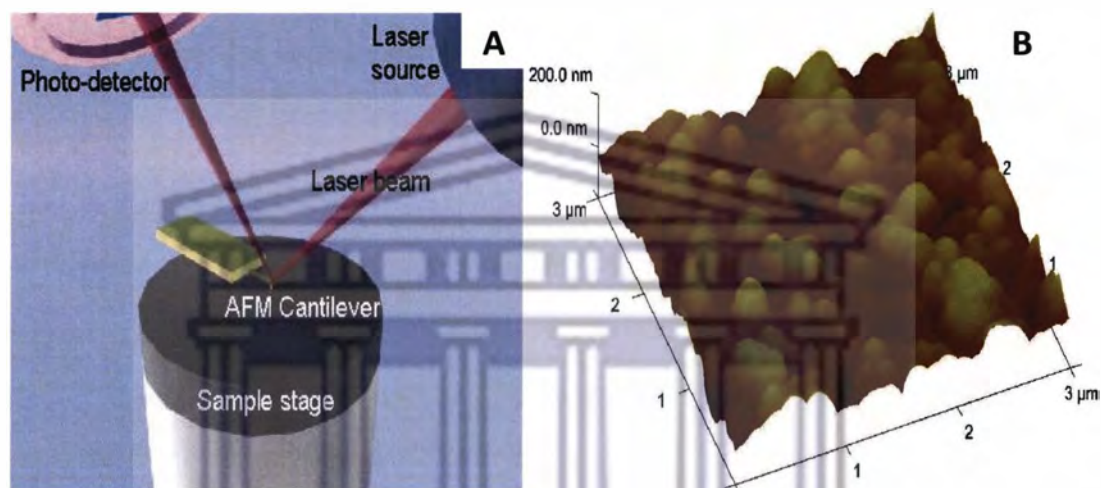


**Figure 20:** An illustration of AFM probing a sample surface with a sharp tip (A) and an example of an AFM image (B) [142].

UNIVERSITY of the  
WESTERN CAPE

### 2.2.5.3 Mass spectrometry

Mass spectrometry is used to study the mass abundance of clusters/nanoparticles in a cluster molecular beam by deflecting them (according to their mass) in an electric field after they have been ionised, generally by electron impact or laser ionisation. Mass abundances occasionally show peaks which are intense relative to their neighbours. These "magic numbers" can often be explained in terms of extra thermodynamic or kinetic stability at these particular sizes, which may be due to electronic or atomic packing effects [151].

## **2.2.5.4 Diffraction**

### **2.2.5.4.1 X-ray Diffraction (XRD)**

XRD is a technique that has widely been used to study nanoparticles, affording information on structure, crystallinity, lattice spacing (and hence some information on the degree of mixing or segregation, provided that the lattice spacing of the two metals are distinct), particle size, and qualitative chemical composition information. It can also be performed on single nanoparticles or arrays of nanoparticles [152].

### **2.2.5.4.2 Electron diffraction**

Electron diffraction is a diffraction technique that has been more widely used for molecular beams of clusters [91]. Although interpretation of the electron diffraction results is complex, information on the geometry, average size and temperature of the nanoparticles may be obtained [91].

### **2.2.5.5 X-ray spectroscopy**

High-energy X-ray radiation is particularly useful for studying metallic nanoparticles because the binding energies of the atomic core electrons are very sensitive to the atomic number of the element, generally allowing metals which are adjacent in the periodic table to be distinguished and the following techniques might be used [91].

#### **2.2.5.5.1 X-ray absorption spectroscopy (XAS)**

XAS is very useful technique for probing the internal structures of metal nanoparticles and species adsorbed on them [153]. Its use has increased due to the availability of synchrotron radiation facilities around the world [91]. Each element's X-ray absorption spectrum is unique and enables information to be obtained about the elements present in the nanoalloys

and the local atomic environment and geometry, electron density, oxidation state, electronic configuration, site symmetry, coordination number, and interatomic distances [91]. XAS comprises of a number of related techniques such as extended X-ray absorption fine structure, near-edge X-ray absorption fine structure, X-ray absorption near-edge structure, X-ray photoelectron spectroscopy and Auger electron spectroscopy.

**i) Extended X-ray absorption fine structure (EXAFS)**

A monochromatic X-ray beam is directed at the sample. The photon energy of the X-rays is gradually increased so that it traverses one of the absorption edges of the elements contained within the sample. Below the absorption edge the photons cannot excite the electrons of the relevant atomic level, and thus, absorption is low. However, when the photon energy is just sufficient to excite the electrons, a large increase in absorption occurs, which is known as the absorption edge. The resulting photoelectrons have low kinetic energies and can be backscattered by the atoms surrounding the emitting atom. The probability of X-ray absorption depends on the photon energy. The net result is a series of oscillations on the high photon energy side of the absorption edge. These oscillations can be used to determine the atomic number, distance, and coordination number of the atoms surrounding the element whose absorption edge is being examined.

**ii) Near-edge x-ray absorption fine structure (NEXAFS)**

It is generally applied to study chemisorbed molecules on surfaces. Information concerning the orientation of the molecule can be inferred from the polarisation dependence. NEXAFS is sensitive to bond angles, whereas EXAFS is sensitive to the interatomic distances.

### iii) X-ray absorption near-edge structure (XANES)

It uses radiation up to 40 eV from the X-ray absorption edge and can provide information about the vacant orbitals, electronic configuration, and site symmetry of the absorbing atom [91]. The absolute position of the edge contains information about the oxidation state of the absorbing atom. In the near edge region, multiple scattering events dominate. Theoretical multiple scattering calculations are compared with experimental XANES spectra in order to determine the geometrical arrangement of the atoms surrounding the absorbing atom.

#### 2.2.5.5.2 X-ray photoelectron spectroscopy (XPS)

XPS is a technique based on the photoelectric effect, whereby absorption of light by an atom, molecule, or solid/surface results in the ejection of electrons, provided that the photon energy is sufficient to overcome the binding energy of the electron. For XPS, Al K $\alpha$  (1486.6 eV) or Mg K $\alpha$  (1253.6 eV) photons are generally used [154]. Both valence and core electrons can be ejected by X-ray radiation. The core electron binding energies are characteristic of each element, and the peak areas can be used to determine the metal nanoparticles composition. As the peak shape and binding energy are sensitive to the oxidation and chemical state of the emitting atom, XPS can also provide chemical bonding information [155]. The XPS technique is highly surface specific due to the short range of the ejected photoelectrons.

#### 2.2.5.6 Energy disperse X-ray microanalysis (EDX)

Energy dispersive X-ray spectroscopy (EDX) coupled with a transmission electron microscope with high resolution is one of the most revealing analytical methods for analysing the composition of bimetallic, ternary and quaternary nanoparticles [92]. The electron beam can be focused on a single particle by TEM, to get information from individual particles. Each element in the chosen nanoparticle emits X-rays at their

characteristic energies by electron beam irradiation, and their intensity is proportional to the concentration of each element in the particle. For sufficiently large particles, the electron beam can be spotted on the surface area or on the centre of the particle, to investigate the regional composition, which often reveals non-uniformity in the composition. Such variations of each particle are important when the structure or the preparative process of these bimetallic nanoparticles is considered. When energy disperse X-ray analysis (EDX) is used in conjunction with TEM, localized elemental information of the nanoparticles and alloy nanoparticles can be obtained. EDX can also be used in conjunction with SEM. An electron beam (typically 10-20 keV) strikes the surface of a conducting sample, causing X-rays to be emitted, whose energies depend on the material under examination. The X-rays are generated in a region about of 2  $\mu\text{m}$  in depth. EDX is a high-resolution (with approximately 1.5 nm lateral resolution) variant of electron microprobe analysis or X-ray microanalysis whereby information can be obtained on the chemical composition of individual nanoparticles [91].



### **2.2.5.7 Other spectroscopic techniques**

#### **2.2.5.7.1 UV-visible spectroscopy**

It is a spectroscopic technique that involves the spectroscopy of photons in the UV-visible region. It uses light in the visible and adjacent (ultraviolet (UV) and near infrared (NIR) ranges). In UV-visible spectroscopy, one can monitor the colour of a material and current at the same time. The colour monitored is the wavelength at which the maximum of the absorption band(s) occurs,  $A_{\text{max}}$ , together with the absorbance at each of these wavelengths. The optical absorbance,  $Abs$ , is defined according to the equation:

$$Abs - \log_{10} \left( \frac{T \text{ with no sample}}{T \text{ with sample}} \right) \quad (31)$$

where  $T$  is the transmittance of light following its passage through the cell. Any changes in the absorbance relates to the amount of electro-active material as converted by the flow of current. It is a major technique that is used in the quantitative determination of solutions of transition metal ions and highly conjugated compounds. For example, if a material absorbs UV-visible light, then we can monitor its concentration using Beer-Lambert relationship;

$$Abs = E \epsilon c l \quad (32)$$

where the absorbance is determined at fixed wavelength  $\lambda$ ,  $E$  is the extinction coefficient (cited at the same value of  $\lambda$ ), and  $l$  is the optical path length. If the magnitude of the extinction coefficient at  $\lambda$  is known, then the amount of analyte ( $C_0$ ) can be quantified simply by determining the optical absorbance and inserting the values into **equation 32**. Most of the analytical techniques are not particularly useful for telling us what 'something' is, but are excellent at telling us how much of that 'something' is present, or has been formed or has been changed. Therefore, UV-visible spectroscopy is one of the best ways of identifying an analyte. This is because each specific analyte absorbs energy in the form of photons at different wavelengths [156].

The property most immediately observable for metal nanoparticles dispersions of certain metals is their colour. For example, Au, Ag and Cu nanoparticles and the alloys formed from them have characteristic colours related with their particle size [157]. Thus, for these metals, observation of UV-visible spectra can be a useful complement to other methods in characterising metal particles. Comparison of spectra of bimetallic, ternary and quaternary



nanoparticles with the spectra of physical mixtures of the respective monometallic particle dispersions can confirm the structures for the nanoparticles [158-160]. Furthermore, with the goal of revealing the formation processes of bimetallic ternary and quaternary nanoparticles, that is, the reduction of metal ions and the aggregation process, the observation of UV-visible spectral changes during reduction can provide quite important information [161]. The optical properties are sensitive to the chemical composition and degree of ordering of bimetallic nanoparticles, especially of the noble metals [162]. Changes in UV-visible spectra can also be used to study reduction of metal ions and their aggregation during cluster formation process [32]. **Figure 21** illustrates how a UV-vis spectrometer functions.

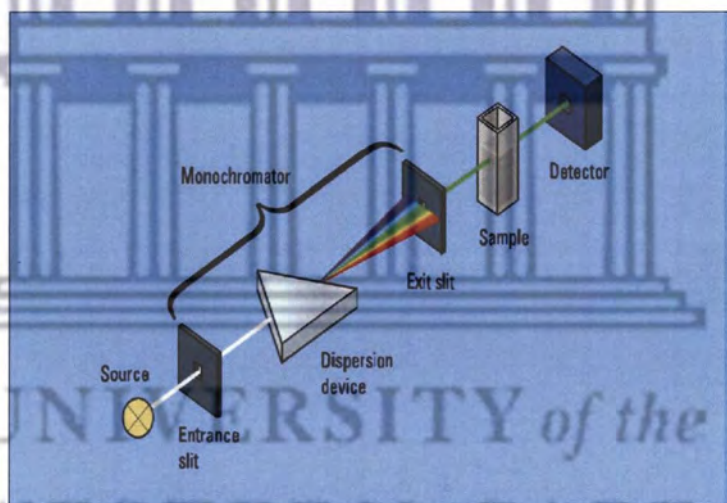


**Figure 21: Illustration of how a UV-visible spectrometer functions [142].**

#### 2.2.5.7.2 Infrared (IR) spectroscopy

IR (including Fourier transform IR (FT-IR)) spectroscopy is widely used to study the vibrational spectra of small molecules adsorbed on metallic clusters and nanoalloys. For example, by making comparisons with pure metal clusters or surfaces, IR spectroscopy of small molecules (e.g., CO) adsorbed on bimetallic nanoparticles can be used as a probe for the surface composition and structure of the sample [32, 162].

### **2.2.5.7.3 Photoelectron spectroscopy**

It is a technique that is used to investigate the electronic and dynamical properties of metal nanoparticles using lower energy radiation (from IR to UV).

### **2.2.5.7.4 Surface-enhanced Raman spectroscopy**

The Raman scattering intensity of molecules is greatly enhanced (by as much as 5 orders of magnitude) when they are adsorbed on certain metals [162]. The effect (which again probes vibrational structure) is used to study the binding of adsorbates on metallic nanoparticles and the cluster formation processes [162].

### **2.2.5.7.5 Nuclear Magnetic Resonance (NMR)**

NMR spectroscopy probes the local magnetic environment of a nucleus with non-zero magnetic moment in terms of its chemical shift (which depends on the amount of diamagnetic and paramagnetic shielding or deshielding) and line splitting due to magnetic coupling to the nuclear spins of neighbouring atoms. In the case of quadrupolar nuclei, the line shape and number of peaks can also give information on the symmetry of the atomic environment. Regarding mono- and bimetallic nanoparticles, NMR spectroscopy has been performed on metallic nuclei (e.g.,  $^{63}\text{Cu}$ ,  $^{103}\text{Rh}$ ,  $^{195}\text{Pt}$ , and  $^{197}\text{Au}$ ), where the chemical shift is dominated by the Knight shift, arising from the conduction electrons, thereby giving a measure of the metallic nature of the particles [162]. Nanoparticle paramagnetism and ferromagnetism can also be probed by NMR. It has also been used to investigate the structures of adsorbed organic molecules (including passivating molecules and polymers), for which the most useful nuclei are  $^1\text{H}$ ,  $^{13}\text{C}$  and  $^{31}\text{P}$  [162].

#### **2.2.5.7.6 Electrochemical NMR spectroscopy (EC-NMR)**

ECNMR was introduced in the late 1980s for the study of electrochemical surfaces, providing an electronic level description of electrochemical interfaces based on the local density of states at the Fermi level.  $^{13}\text{C}$  and  $^{195}\text{Pt}$  are particularly useful nuclei for investigating electrochemical interfaces and probing nanoparticles and nanoalloys [91].

#### **2.2.5.8 Ion Spectroscopy/Scattering (IS)**

Ion spectroscopic techniques involve accelerating ions onto a sample and detecting the energies and distribution of scattered ions. Ion energies are as follows: 1-10 keV for low-energy IS (LEIS), 20-200 keV for medium-energy IS, and 200-2000 keV for high-energy IS. The higher the incident ion energy, the smaller the target atoms appear, though the yields are smaller, so low energies are best for surface-specific information [154]. The energy and angle of the scattered ions are analysed simultaneously, allowing measurement of atomic mass (and hence composition), depth (down to 1 atomic layer is possible), and surface structure [91]. Depending on the incident ion energy, ion scattering may be accompanied by surface etching. Following the time evolution of the surface composition therefore allows depth profiling of the composition of bimetallic nanoparticles [163].

In this study, the electrochemical studies of the nanoalloys were carried out using CV and EIS. The size, shape and topography of the nanoalloys were obtained using microscopic techniques such as HRTEM and AFM. EDX was used to determine the elemental composition of the nanoalloys while the complete reduction of the metal salts to nanoalloys was investigated using UV-visible spectroscopy.

## CHAPTER THREE

### EXPERIMENTAL SECTION

#### *Summary*

*This chapter describes the general experimental procedures for the chemical synthesis of PdAg, PdAu and PdAuAg polycrystalline nanoalloys and preferentially oriented Pt(100) nanoalloy systems. The spectroscopic, microscopic and electrochemical characterisation of the synthesised nanoalloys is also outlined. Also described in this chapter are procedures for the fabrication of the nanoalloys towards the oxidation of ammonia and hydrazine.*



UNIVERSITY of the  
WESTERN CAPE

### 3.1 Reagents and materials

Analytical grade palladium chloride (PdCl<sub>2</sub>), hydrogen tetrachloroaurate (III) trihydrate (HAuCl<sub>4</sub>·3H<sub>2</sub>O), silver nitrate (AgNO<sub>3</sub>), potassium hexachloroplatinate (IV) (K<sub>2</sub>PtCl<sub>6</sub>), hydrogen hexachloroiridate (IV) hydrate (H<sub>2</sub>Cl<sub>6</sub>Ir·H<sub>2</sub>O), sodium hexachlororhodate (III) (Na<sub>3</sub>RhCl<sub>6</sub>), hydrazine (N<sub>2</sub>H<sub>4</sub>), sodium polyacrylate (PA), ammonium hydroxide (NH<sub>4</sub>OH), sulphuric acid (H<sub>2</sub>SO<sub>4</sub>, 98%), ascorbic acid, polyvinylpyrrolidone (PVP, MW = 55000), lithium perchlorate (LiClO<sub>4</sub>), sodium hydroxide (NaOH) (99%), potassium hydroxide (KOH), sodium borohydride (NaBH<sub>4</sub>), disodium hydrogen phosphate (Na<sub>2</sub>HPO<sub>4</sub>) (> 98%), sodium dihydrogen phosphate (NaH<sub>2</sub>PO<sub>4</sub>) (>99%), potassium hexacyanoferrate (III) [K<sub>3</sub>Fe(CN)<sub>6</sub>] (99%) and potassium hexacyanoferrate (II) [Fe(CN)<sub>6</sub>] (99%) were all purchased from Sigma-Aldrich (Cape Town, South Africa). All chemicals were of analytical reagent grade and were used without further purification. Deionized water (18.2 MQ cm) purified by a Milli-QTM system (Millipore) was used as reagent water for aqueous solution preparations. 5 mM [Fe(CN)<sub>6</sub>]<sup>3-</sup> was prepared from Fe(CN)<sub>6</sub> and K<sub>3</sub>Fe(CN)<sub>6</sub> in a 1:1 ratio. Analytical grade argon gas was purchased from Afrox Company, South Africa. Alumina polishing pads and powder (0.05, 0.3 and 1.0 μm) were obtained from Buehler, Illinois, USA and were used for polishing the Pt electrodes.

### 3.2. Measurements and instrumentations

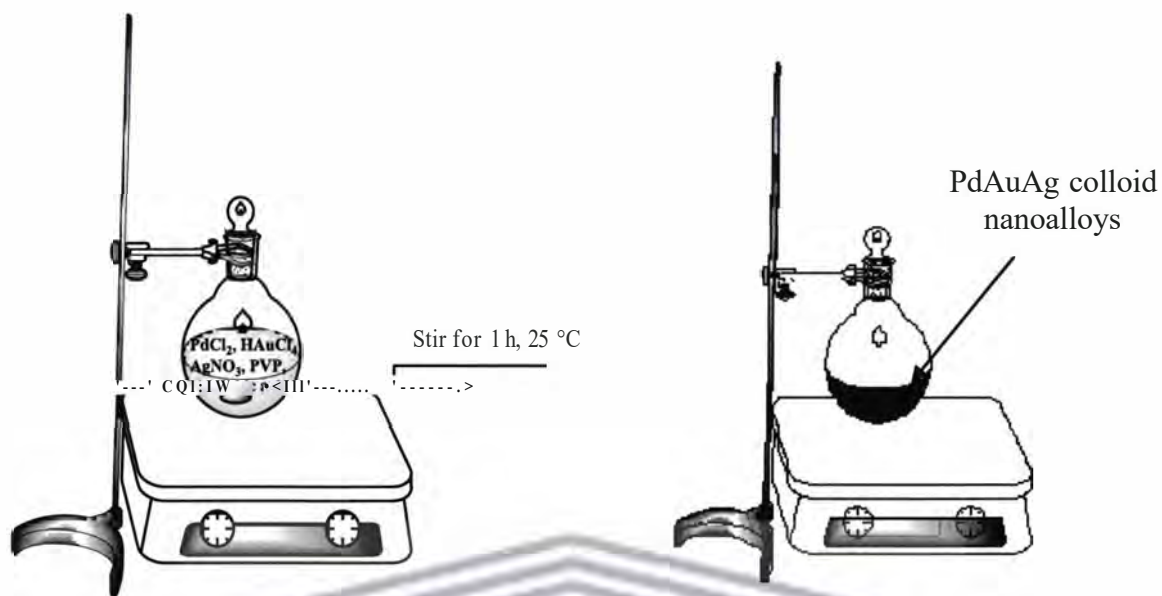
The synthesised nanoalloys were characterised using electrochemical, microscopic and spectroscopic techniques. The electrochemical techniques used for characterisation of the nanoalloys were mainly cyclic voltammetry (CV) and electrochemical impedance spectroscopy (EIS). The voltammetric measurements were performed on a BAS 100W electrochemical workstation from BioAnalytical Systems Incorporation (Lafayette, USA) using a three-electrode cell system consisting of nanoalloy modified Pt electrode (1.6 mm

diameter,  $0.0201 \text{ cm}^2$ ), Ag/AgCl (saturated NaCl) and platinum wire as working, reference and counter electrodes, respectively. The platinum auxiliary electrode was cleaned by burning in a flame for several minutes and the Ag/AgCl electrode was cleaned by rinsing with copious amounts of distilled water. All experimental solutions were purged with high purity argon gas and blanketed with the same during measurements. The experiments were carried out at controlled room temperature ( $25 \text{ }^\circ\text{C}$ ). The electrochemical impedance spectroscopy (EIS) measurements were done on a Voltalab PGZ 402 from Radiometer Analytical (Lyon, France) using a three electrode configuration set up described above. The microscopic and spectroscopic techniques used were high resolution transmission electron microscopy (HRTEM), atomic force microscopy (AFM) and Ultra-violet visible spectroscopy (UV-vis).

### 3.3 Preparation of the nanoalloys

#### 3.3.1. Synthesis of PdAu, PdAg and PdAuAg nanoalloys

In a typical synthesis of PdAuAg ternary nanoalloy, 1.5 mL of a 5 mM aqueous solution of PdCh/HAuCl<sub>4</sub>·3H<sub>2</sub>O/AgNO<sub>3</sub> mixtures was added to a 45.5 mL of highly purified water. To this solution, 1.5 mL of 0.1 M ascorbic acid (reducing agent) was added. After 15 s, an aqueous solution of PVP (5 mg/mL, 1.5 mL) was added (as a capping agent) drop wise with vigorous stirring and the solution was stirred further for 30 min. The resulting hydrosol was subjected to centrifugation to remove excess PVP (see **scheme 2**). Pd, PdAu and PdAg nanoparticles were prepared in the same way by substituting aqueous solutions of PdCh/HAuCl<sub>4</sub>·3H<sub>2</sub>O/AgNO<sub>3</sub> mixtures for the preparation of PdAuAg by PdCh, PdCh/HAuCl<sub>4</sub>·3H<sub>2</sub>O and PdCh/AgNO<sub>3</sub> solutions, respectively.



**Scheme 2: Methodology used for the synthesis of PdAgAu nanoalloys.**

### 3.3.2. Synthesis of polycrystalline Pt nanoparticles

Polycrystalline Pt nanoparticles were synthesised by adding drop wise 20 mL of a  $1 \times 10^{-2}$  M  $\text{NaBH}_4$  solution aged for 3 h to 20 mL of a  $6.5 \times 10^{-4}$  M  $\text{K}_2\text{PtCl}_6$  solution with vigorous stirring for 1 h at ice cold temperature. After complete reduction, 2-3 NaOH pellets were added to produce a precipitate of the nanoparticles and then washed 3-4 times with ultra-pure water.

### 3.3.3 Synthesis of preferentially oriented Pt(100) nanoparticles

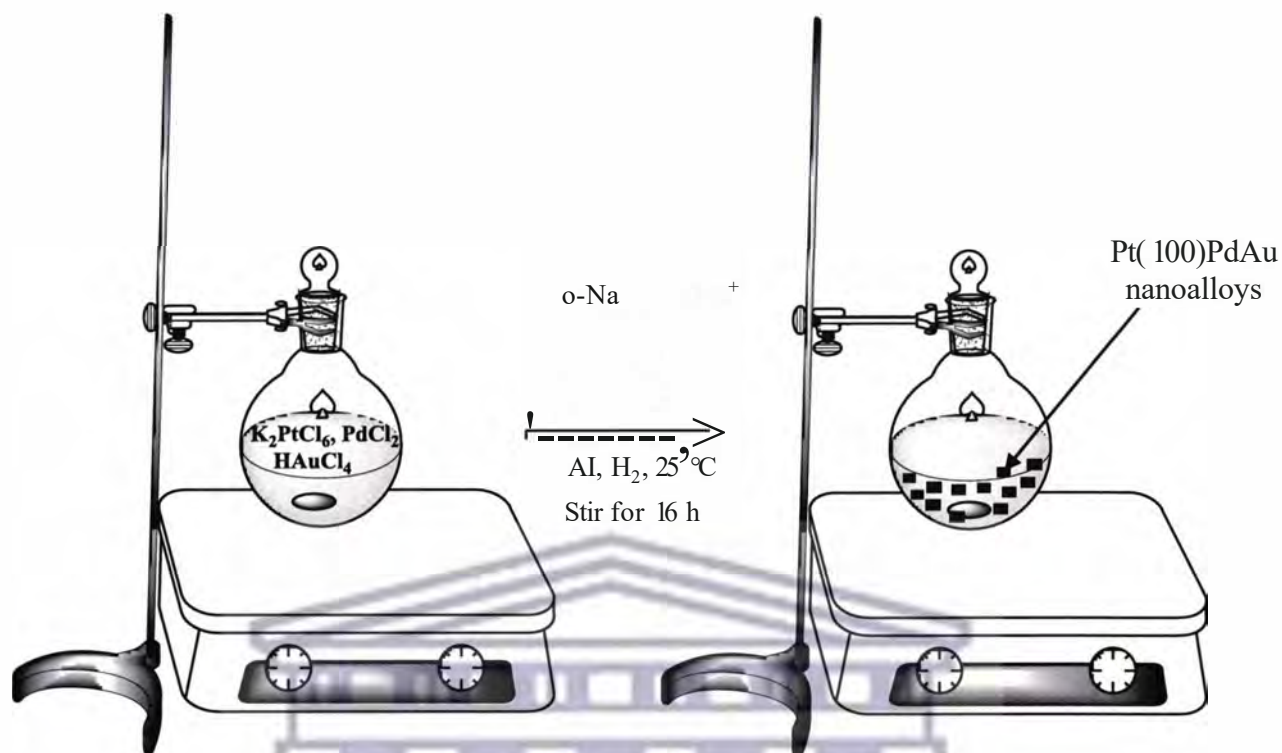
Preferentially oriented Pt(100) nanoparticles were prepared by using the so-called colloidal method [119]. 0.1 mL of a 0.1 M sodium polyacrylate/poly(acrylic acid sodium salt) (average MW 2100) was added to a 100 mL of an aged  $1 \times 10^{-4}$  M  $\text{K}_2\text{PtCl}_6$  solution. The pH of the solution was adjusted to 7 with 0.1 M HCl. Argon gas was bubbled for 20 min followed by the reduction of the Pt ions using  $\text{H}_2$  gas for 5 min. The reaction vessel was then sealed and the solution was left overnight. After complete reduction (16 h) two NaOH pellets were

added to the solution to produce a precipitation of the nanoparticles. After complete precipitation, the nanoparticles were washed 3-4 times with ultra-pure water.

### 3.3.4 Synthesis of Pt(100)M (M: Au, Pd, Ir, Rh, PdAu, IrAu, Pdlr, RhAu) nanoalloys

Pt(100)PdAu nanoalloy was synthesised following the procedure that was used in the synthesis of Pt(100) nanoparticles. Briefly stating, 0.1 mL of a 0.1 M sodium polyacrylate (average MW 2100) was added to a 100 mL of an aged solution containing  $1 \times 10^{-4}$  M  $K_2P Cl_6$ ,  $1 \times 10^{-4}$  M PdCh and  $1 \times 10^{-4}$  M  $HAuCl_4$ . The pH of the solution was adjusted to 7 with 0.1 M HCl. Argon gas was bubbled for 20 min followed by the reduction of the metal ions using  $H_2$  gas for 5 min. The reaction vessel was then sealed and the solution left over night. After complete reduction (16 h) two NaOH pellets were added to the solution to produce a precipitation of the nanoparticles. After complete precipitation, the nanoalloys were washed 3-4 times with ultra-pure water (see **scheme 3**). All the other Pt(100)M nanoalloys were synthesised following the same procedure by using the respective salts of the metals.





**Scheme 3: Methodology used for the synthesis of Pt(100)PdAu nanoalloys.**

### 3.4. Fabrication of Pt electrode with nanoalloys

Prior to modification, the bare Pt electrode was polished to a mirror finish with 1.0, 0.3, and 0.05  $\mu\text{m}$  alumina slurries, respectively, and rinsed thoroughly with distilled water in between polishing with different sized alumina slurries followed by sonication in ethanol and water in the end. 10  $\mu\text{L}$  solutions of already synthesised nanoalloys were drop-coated onto the Pt electrode and allowed to dry at room temperature. The modified electrodes were taken out and rinsed with water and were ready for electrochemical characterisation and application.

## 3.5 Characterisation of the nanoalloys

### 3.5.1 Electrochemical characterisation

#### 3.5.1.1 Cyclic voltammetry (CV)

For the electrochemical characterisation of the nanoparticles, the nanoalloy modified Pt electrodes (**described in section 3.4 above**) were gently rinsed with de-ionized water to remove any excess or weakly adsorbed nanoalloys and were further used for electrochemical characterisation. Electrochemical measurements were performed in 0.1 M LiClO<sub>4</sub>, 0.5 M H<sub>2</sub>SO<sub>4</sub>, 1 M KOH solutions over a potential range of -600 mV to 1000 mV, -200 mV to 800 mV and -1000 mV to 600 mV respectively at different scan rates. 0.5 M H<sub>2</sub>SO<sub>4</sub> solution was used as the test solution for the oriented nanoalloys. Fresh electrolyte solutions were prepared every time an experiment was carried out.

To study the electrochemistry of the PdAuAg colloid nanoalloy, 2 mL of the freshly prepared PdAuAg nanoalloys solution and 3 mL of 0.1 M LiClO<sub>4</sub> supporting electrolyte solutions were put in a 10 mL electrochemical cell and de-aerated with argon gas for 10 min. Electrochemical measurements were performed over a potential range of -500 mV to 1000 mV. The voltammograms were recorded under argon atmosphere.

#### 3.5.1.2 Electrochemical impedance spectroscopy (EIS)

Electrochemical impedance spectroscopy (EIS) of the nanoalloy modified electrodes were measured using Voltalab PGL 402 from Radiometer Analytical (Lyon, France) in 1 M KOH and 5 mM Fe(CN)<sub>6</sub><sup>4-</sup> solutions and plotted in the form of complex plane diagrams (Nyquist plots) at a perturbation amplitude of 10 mV within a frequency range of 100 kHz to 100 mHz.

### **3.5.2 Morphological characterisation**

#### **3.5.2.1 High resolution transmission electron microscopy (HRTEM)**

Before analysis, liquid samples of nanoalloy from the mother solutions were pre-concentrated by centrifuging at 14000 rpm for 30 min. A small drop of a dilute solution of the nanoalloys was placed on a carbon coated copper grid and dried under electric bulb for 30 min. HRTEM analysis of the mounted nanoalloys was done using Tecnai G2 F20X-Twin MAT 200 kV Field Emission Transmission Electron Microscope from FEI (Eindhoven, Netherlands).

#### **3.5.2.2 Atomic force microscopy (AFM)**

Surface morphology of the nanoalloys was studied by atomic force spectroscopy (AFM) using a Veeco NanoMan V model (Cambridge, USA). The preparation of samples for AFM analysis was as follows: 10  $\mu\text{L}$  of liquid nanoalloys sample was dropped on a silicon substrate and left to dry at room temperature. The samples were scanned with a silicon tip at a spring constant of 1-5 *N/m* and resonance frequency of 60-100 kHz.

#### **3.5.3 UV-visible spectroscopy**

Freshly prepared samples were used for UV-vis analysis. UV-visible absorption measurements of samples were obtained in quartz cuvettes using a Nicolet Evolution I00 UV-visible spectrometer (Thermo Electron Corporation, UK) at a wavelength of 200 nm to 800 nm.

### 3.6 Electrochemical oxidation of ammonia

A Pt electrode was thoroughly cleaned by polishing it on a soft polishing pad using 1.00, 0.30 and 0.05  $\mu\text{m}$  slurries of alumina respectively, rinsing with de-ionized water after each polish. This was followed by ultrasonication in de-ionized water for 5 min. The well-polished Pt electrode was modified with nanoalloys as described in **section 3.4**. A freshly prepared electrode was used in all electrochemical measurements. The electrochemical measurements were performed at 25 °C in 0.1 M ammonia and 1 M KOH aqueous solutions saturated with argon gas. Cyclic voltammetric measurements were performed in the presence and absence of ammonia at sweep rates of 10 to 500  $\text{mV s}^{-1}$  between -1000 mV and 100 mV. The parameter effects on the working electrodes were investigated by altering the individual variables (both the concentrations of KOH and ammonia).

### 3.7 Electrochemical oxidation of hydrazine

For the electrochemical oxidation of hydrazine, a glassy carbon electrode (GCE) was used instead of Pt electrode based on its better response to hydrazine oxidation. The GCE was thoroughly cleaned following the procedure that was used in polishing the Pt electrode described in **section 3.4**. 10  $\mu\text{L}$  of the nanoalloy colloid solution was drop-coated on the thoroughly polished GCE and left to dry at room temperature. The modified electrode was then gently rinsed with de-ionized water to remove weakly adsorbed nanoalloys. A freshly prepared electrode was used in all electrochemical measurements. The electrochemical measurements were performed at 25 °C in 10 mM hydrazine in 0.1 M saline phosphate buffer solution (PBS), pH 7.4 aqueous solution saturated with argon gas. Cyclic voltammetric measurements were performed in the presence and absence of hydrazine at the sweep rates of 5 to 500  $\text{mV s}^{-1}$  within a potential range of -500 mV to 600 mV.

## CHAPTER FOUR

### RESULTS AND DISCUSSION: Part 1

#### NOVEL HIGH-PERFORMANCE ELECTROCATALYTIC PdAuAg NANOALLOYS FOR AMMONIA OXIDATION



##### *Summary*

*This is the first of four chapters outlining and discussing the results obtained from this study. This chapter deals specifically with the characterisation of PdAu, PdAg and PdAuAg nanoalloys and their subsequent application in the oxidation of ammonia. The chapter clearly illustrates how the polyvinylpyrrolidone (PVP)-capped nanoalloys were successfully synthesised by a simple chemical reduction method using ascorbic acid as a reducing agent. Spectroscopic, morphological, and electrochemical properties of these nanoalloys were interrogated using techniques such as UV-vis, HRTEM, AFM and CV. The potential application of the nanoalloys as electrocatalysts for ammonia electro-oxidation was further investigated.*

## 4.1 Introduction

Extracting hydrogen from ammonia can be accomplished through the use of electrochemical approaches. The development of electrocatalytic techniques for ammonia oxidation has attracted much attention as an alternative energy supply with platinum being the most commonly used electrocatalytic material. Gerischer and Mauerer [164] proposed the mechanism of ammonia oxidation on platinum and Pt-group metals [165-166]:



Where  $x = 1$  or  $2$ ,  $y = 1$  or  $2$ .

According to this mechanism, the partially dehydrogenated species  $\text{NH}_{\text{ads}}$  and  $\text{NH}_{2,\text{ads}}$  are the active intermediates to form the final product of  $\text{N}_2$  (**equation 37**), whereas  $\text{N}_{\text{ads}}$  formed (**equation 38**) tends to block the electrode surface and becomes a poison for it [167]. Vooyoys *et al.* [168] discussed the correlation between the electrocatalytic activity of ammonia oxidation and the adsorption energy of  $\text{N}_{\text{ads}}$  on various metals such as Ru, Rh, Pd, Ir, Pt, Au, Ag and Cu. Their  $\text{N}_{\text{ads}}$  adsorption energies were found to follow the trend (decreasing  $\text{N}_{\text{ads}}$  activity);  $\text{Ru} > \text{Rh} > \text{Pd} > \text{Ir} > \text{Pt} \gg \text{Au}$ , Ag and Cu. Pt is the best electrocatalyst because metals having smaller  $\text{N}_{\text{ads}}$  adsorption energy than Pt (e.g. Cu, Ag and Au) are inactive in

**equation 33** or **34** [168] and it is almost insensitive to poisoning. However, alloying platinum group metals (PGMs) with other noble metals is believed to increase the electrocatalytic activity for ammonia oxidation in alkaline solutions. Endo *et al.* [167] pointed out that alloying Pt and Ir leads to enhanced electrocatalytic activity for ammonia oxidation in alkaline solutions. Pd which has the same d-valence electrons as Pt, less expensive than Pt and one of the platinum group metals is also a promising electrocatalyst based on its high electroactivity towards ammonia. However, it has a high  $\text{N}_2$  adsorption ability making its application as an electrocatalyst a major challenge. Alloying it with noble metals having smaller  $\text{N}_2$  adsorption energy such as Ru, Cu, Au and Ag will lower its high  $\text{N}_2$  adsorption and increase its catalytic properties towards ammonia oxidation [169]. To the best of our knowledge, there is no literature report on the synthesis of PdAuAg ternary nanoalloy and its subsequent application in ammonia oxidation. In this chapter, PdAu, PdAg and PdAuAg nanoalloy systems have been chemically synthesised by the use of ascorbic acid as the reducing agent and polyvinylpyrrolidone (PVP) as the capping agent and utilised further in the oxidation of ammonia.

## 4.2 Spectroscopic and microscopic characteristics of the nanoalloys

### 4.2.1 UV-visible spectroscopy

The formation of the nanoparticles by reduction of  $\text{Pd}^{2+}$ ,  $\text{HAuCl}_4$  and  $\text{Ag}^+$  ions was confirmed by the use of UV-visible spectroscopy. **Figure 22** shows the UV-visible spectra of  $\text{PdCl}_2$ ,  $\text{AgNO}_3$  and  $\text{HAuCl}_4 \cdot 3\text{H}_2\text{O}$  solutions while **Figure 23** shows the UV-visible spectra of Pd, PdAu, PdAg, and PdAuAg nanoparticles. The absorption peaks observed at 260 nm for  $\text{Ag}^+$ , 285 nm for  $\text{Au}^{3+}$  and 420 nm for  $\text{Pd}^{2+}$  ions [170] disappeared after the reduction indicating that the metal ions were completely reduced. The synthesised nanoparticles

showed no absorption peaks indicating a complete reduction of the metal ions to zero-valent nanoparticles. The colour of the solution turned from pale yellow to black.

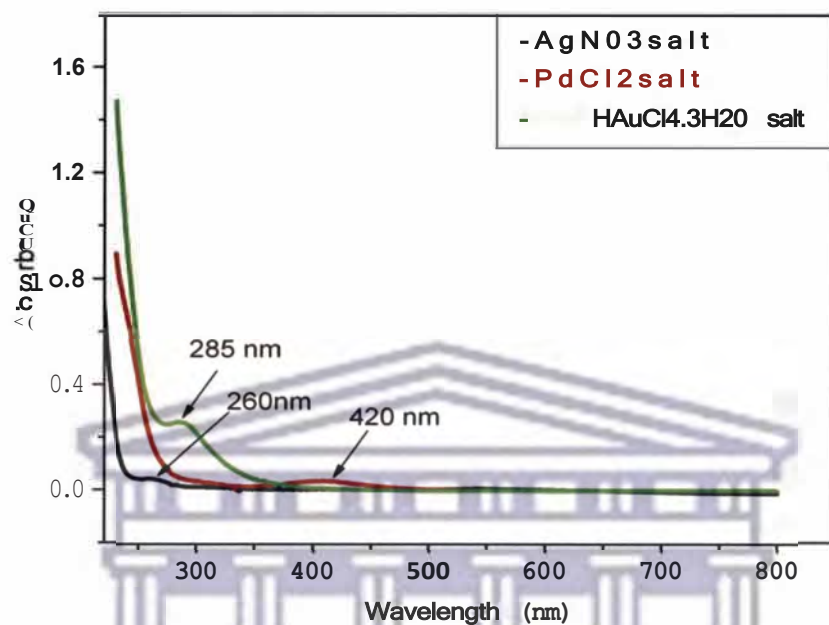


Figure 22: UV-vis spectra of palladium chloride, silver nitrate and hydrogen tetrachloroaurate (III) trihydrate solutions.

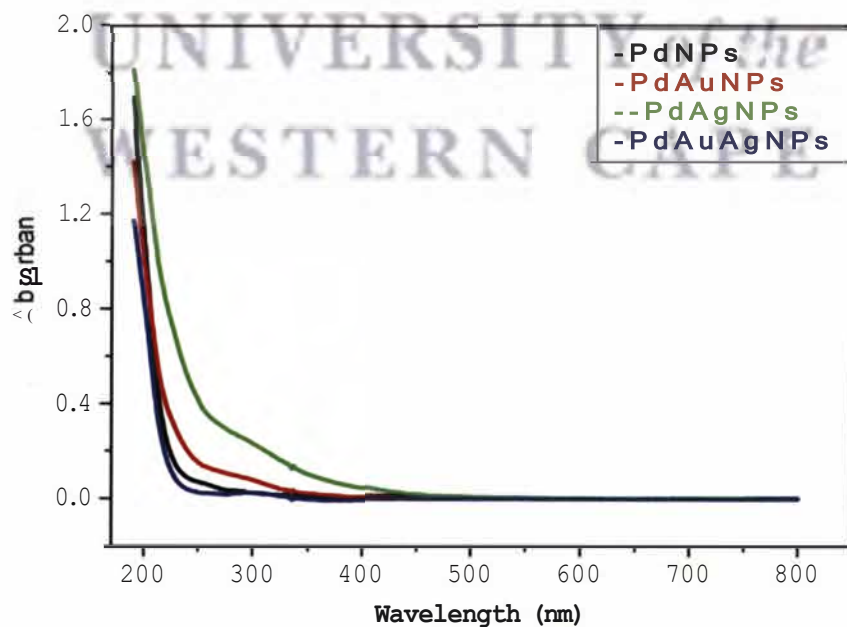


Figure 23: UV-vis spectra of Pd nanoparticles, PdAg, PdAu and PdAuAg nanoalloys.



#### 4.2.2 High resolution transmission electron microscopy

The size, shape and the crystalline properties of the nanoparticles were investigated using high resolution transmission microscopy (HRTEM). **Figure 24A** shows typical HRTEM images of the prepared Pd nanoparticles. The nanoparticles produced were found to be well dispersed, with an average diameter of 40-50 nm. HRTEM image of a single particle (not shown) revealed atomic lattice fringes demonstrating the crystalline nature of the nanoparticles. PdAg polycrystalline 5-12 nm sized bimetallic nanoparticles were obtained whose crystalline nature was evidenced by the presence of the lattice fringes (**Figure 24B**). Non-aggregated 20-30 nm sized PdAu bimetallic nanoalloys in form of clusters synthesised using the same procedure were observed as shown in **Figure 24C**. The non-aggregation of the nanoclusters is believed to have resulted from the electrostatic partial negatively charged oxygen atom present in the amide group of the PVP. The observed images are similar to those reported in literature for PdAu bimetallic nanoparticles [171]. For the PdAuAg ternary nanoalloys, crystalline non-aggregated 25-35 nm sized nanoalloys in form of clusters were observed (**Figure 24D**). Although the formation mechanism of PdAuAg alloy nanoclusters is not clear, it can be assumed that unstable small nanoparticles aggregate into the three-dimensional nanoclusters (flower-shaped nanoparticles). Close inspection of the HRTEM images shows that the nanoclusters are built up by sixes of elongated primary nanoparticles with average dimensions of approximately 10 nm, and boundaries and voids between the components are present (see inset of **Figure 24D**). The formation of nanoclusters with flower-shaped porous structures or multi-branched structures has also been reported in literature. Lee *et al.* [172] reported the synthesis of flower-shaped Au-Pd alloy nanoparticles. Teng *et al.* [173] proposed a 'self-organization' mechanism for the fabrication of porous Pt nanoparticles. Flower-shaped Rh nanoparticles were also reported by Hoefelmeyer and co-workers [174]. It was found that ascorbic acid might promote the formation of multipodal or

porous particles [175-176]. However, we infer that the ascorbic acid reduction mechanism cannot explain the formation of the synthesised flower-shaped porous PdAuAg ternary nanoclusters entirely, because we could not obtain flower-shaped monometallic Pd and bimetallic PdAg nanoalloys under the same experimental conditions.

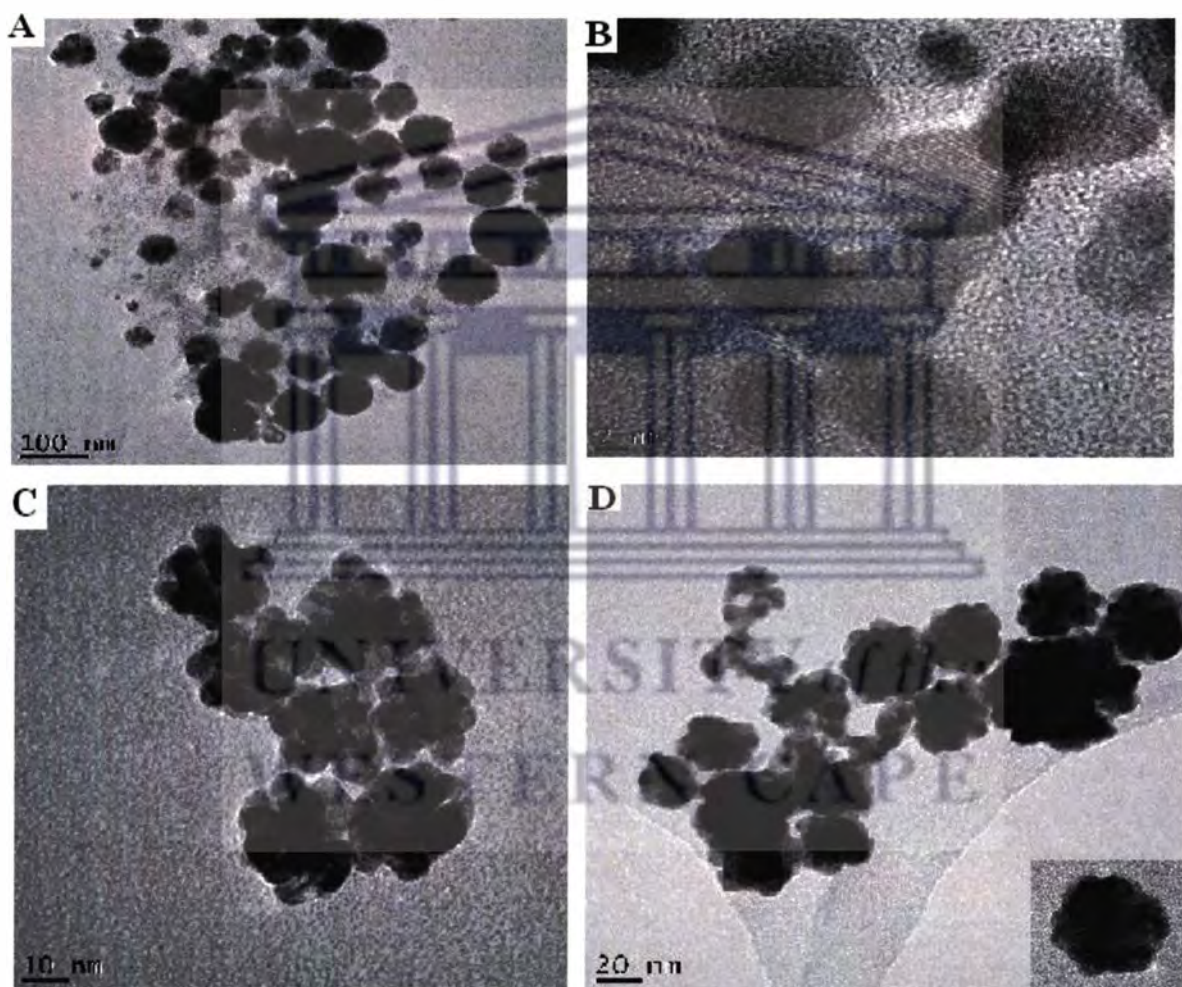


**Figure 24: HRTEM images of Pd nanoparticles (A), PdAg nanoalloys (B), PdAu nanoalloys (C) and PdAuAg nanoalloys (D).**

### 4.2.3 Energy dispersive X-ray spectroscopy (EDX) analysis

To investigate the elemental composition of the prepared nanoalloys, the PdAu, PdAg and PdAuAg nanoalloys were characterised using EDX. The EDX analysis (Figure 25 (a), (b), (c) and (d)) of the synthesised Pd, PdAu, PdAg and PdAuAg nanoparticles revealed the elemental composition of the nanoparticles and showed that all the three elements; Pd, Au and Ag were present in the nanoalloy systems. However, other elemental signals were also recorded namely; silicon, oxygen and copper. The presence of silicon may have originated from contamination during sample preparation, the oxygen was due to the presence of PVP in the nanoparticles while copper is as a result of the copper grid onto which the nanoparticles were immobilised for the HRTEM analysis.

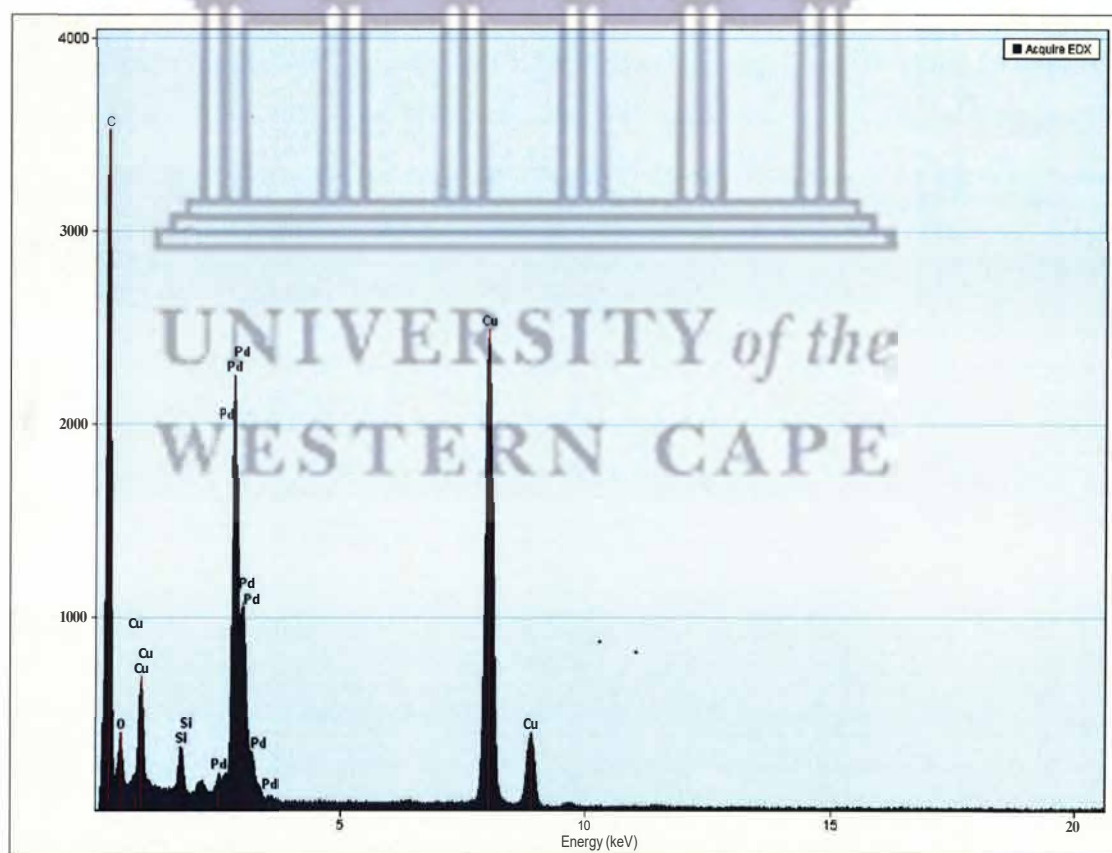


Figure 25a: Energy dispersive X-ray spectrum of Pd nanoparticles.

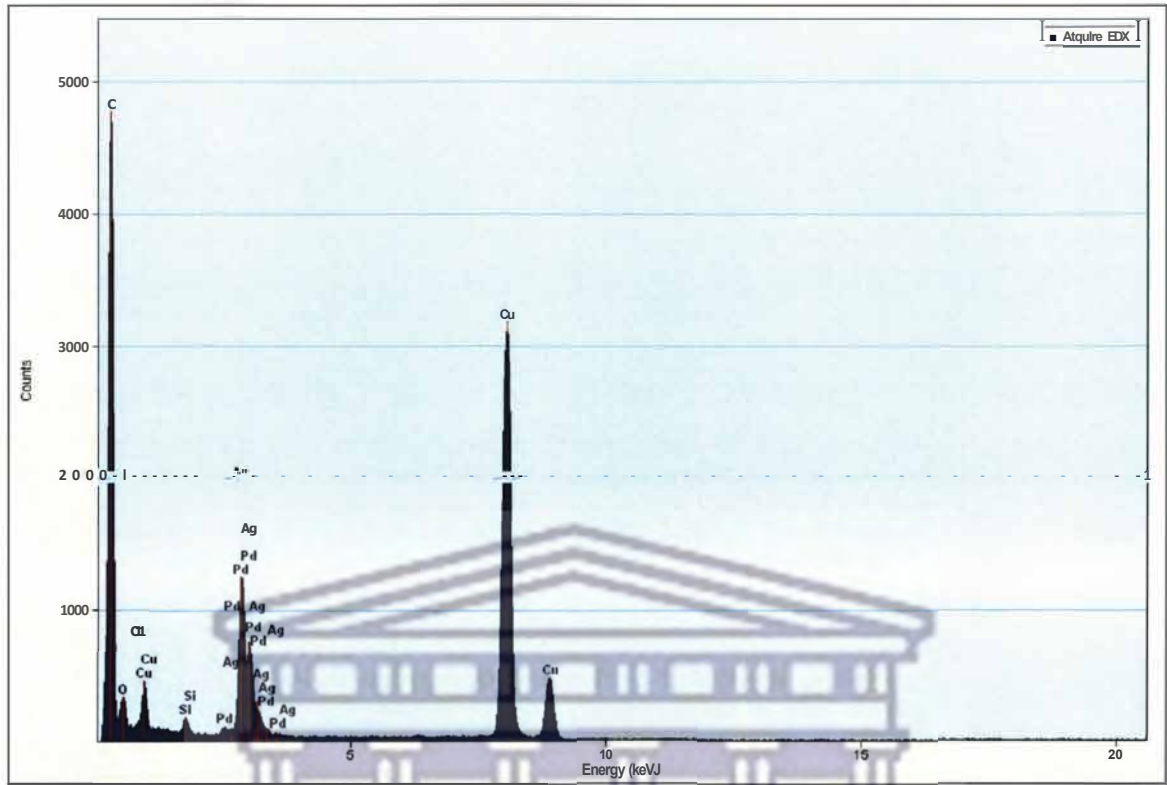


Figure 25b: Energy dispersive X-ray spectrum of PdAg nanoalloys.

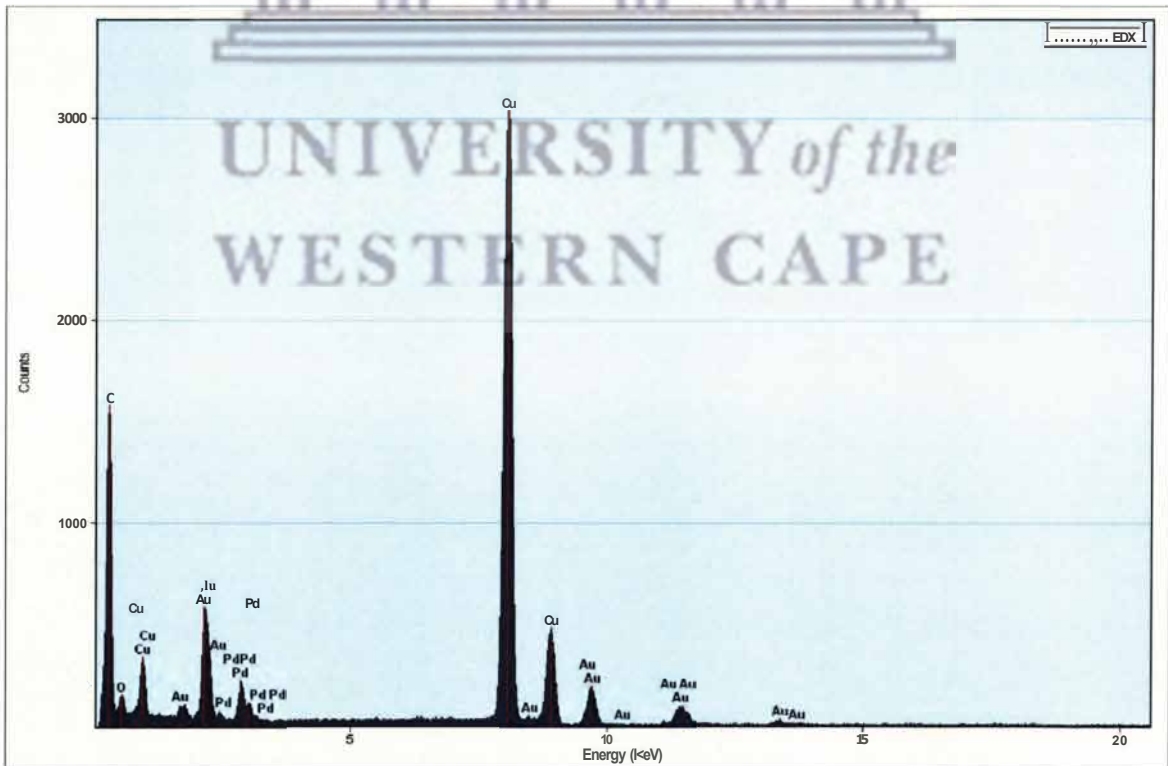
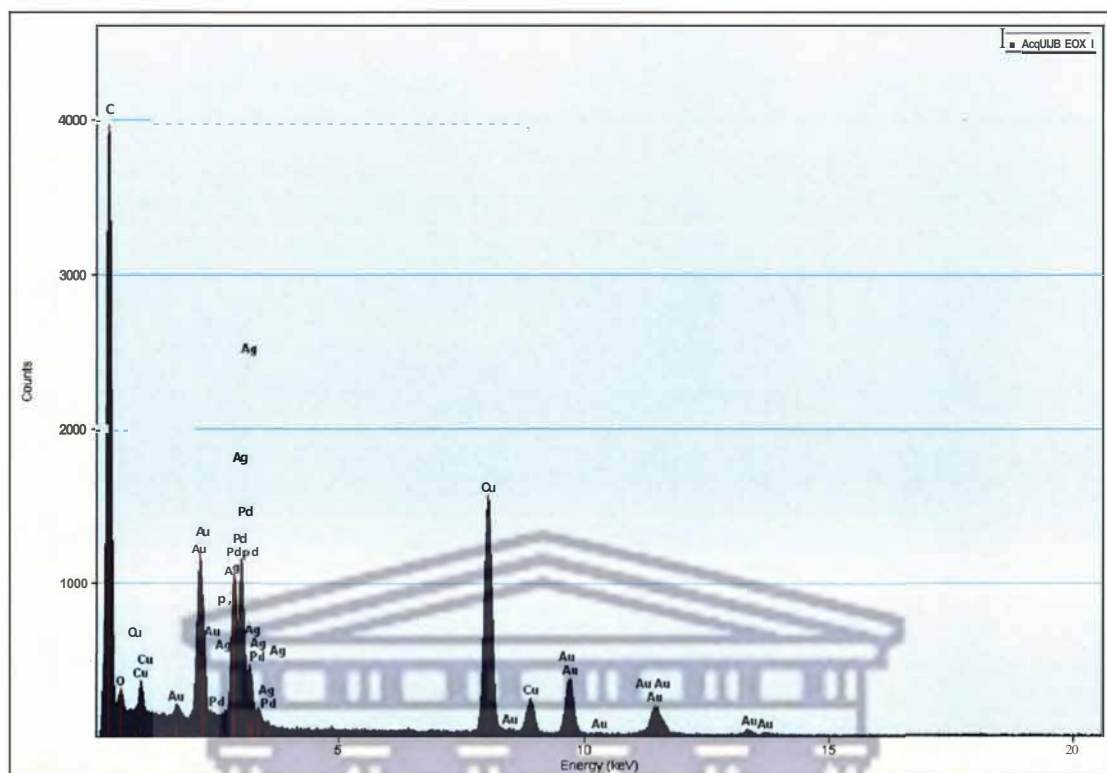


Figure 25c: Energy dispersive X-ray spectrum of PdAu nanoalloys.



**Figure 25d:** Energy dispersive X-ray spectrum of PdAuAg nanoalloys.

#### 4.2.4 Atomic force microscopy (AFM) analysis

Atomic force microscopy (AFM) has become a standard technique for high resolution imaging of the morphology and topography of surfaces. It operates by measuring the force between the probe and the sample. The interaction of the force fields is sensed by a cantilever beam, to which the tip is attached. An image (revealing individual atoms) is created as the probe is translated across the surface. Such images can be formed by constant-force or constant-height modes (with known or measured deflections of the cantilever, respectively). Since AFM does not involve passage of current between the tip and the surface, it is useful for exploring both insulating and conducting regions [177]. AFM analyses were carried out for Pd, PdAg, PdAu and PdAuAg nanoparticles in order to investigate the differences in their surface morphology and topography. **Figure 26** shows the AFM images of the silicon substrate used and the substrate modified with different nanoparticles. As can be seen from

**Figure 26B**, a random distribution of palladium nanoparticles over the silicon substrate was observed. The sizes of the formed palladium nanoparticles were found to be below 100 nm, which correlated well with the HRTEM results. PdAg nanoalloys (**Figure 26C**) showed well distributed nanoparticles on the substrate indicating the polycrystalline nature of the nanoparticles correlating well with the HRTEM images. PdAu nanoalloys (**Figure 26D**) showed well distributed nanoparticles on the substrate. The most interesting thing is the fact that round beaded patchy shaped surfaces of the PdAuAg nanoalloy (**Figure 26E**) were observed which corroborated the HRTEM images (nanoclusters).

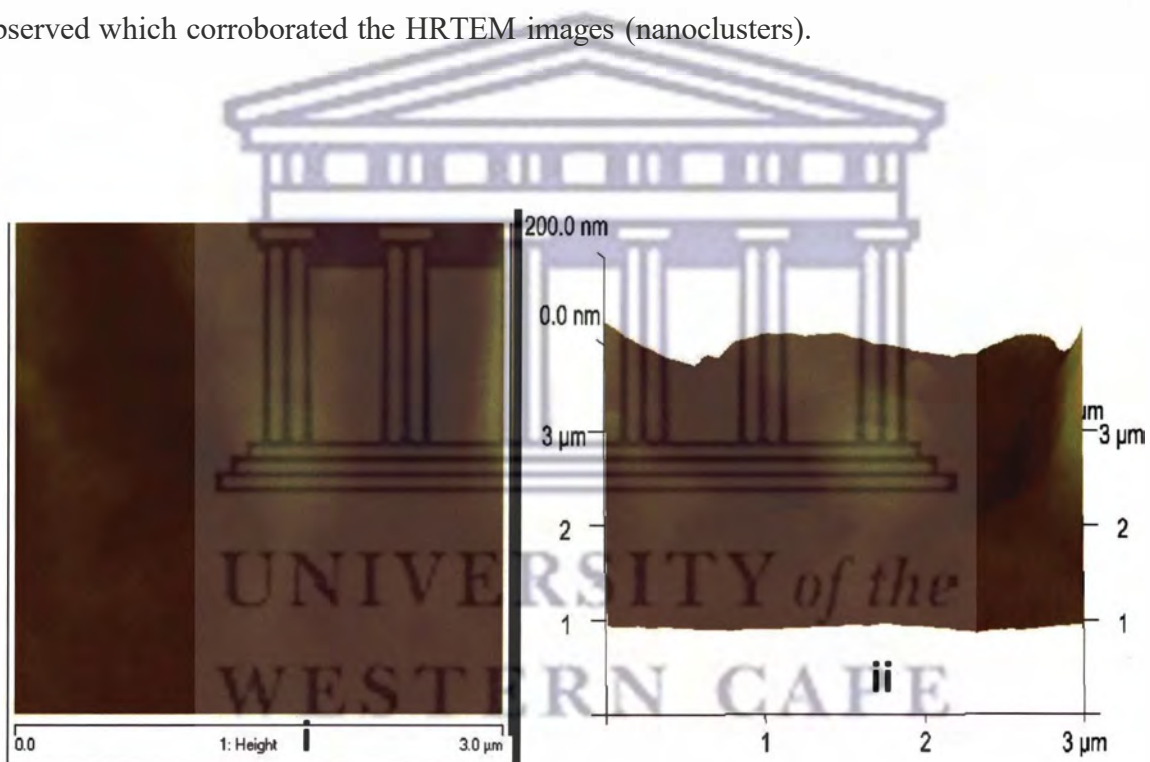


**Figure 26A: (i) 2D and (ii) 3D AFM images of silicon substrates.**

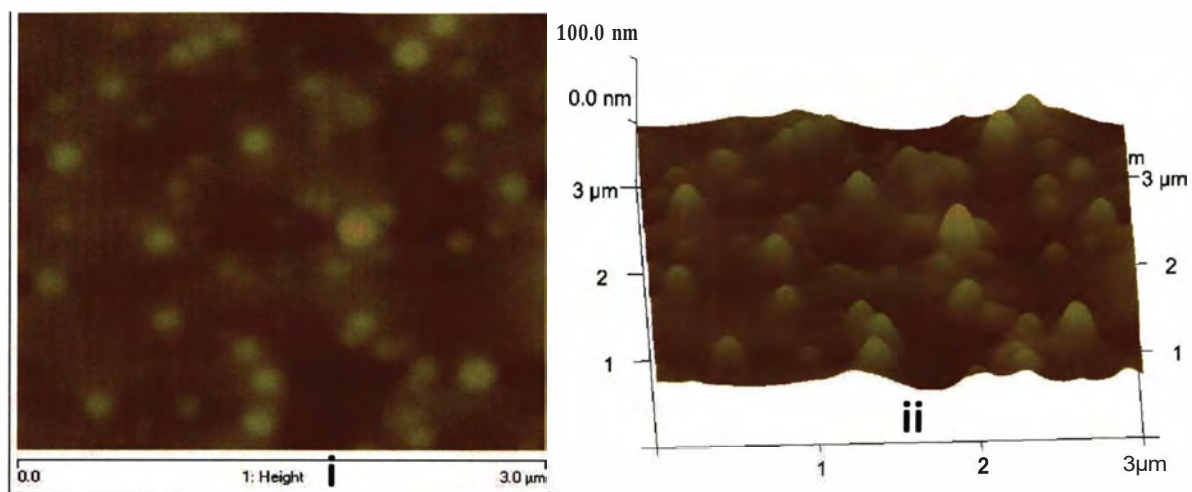


Figure 26B: (i) 2D and (ii) 3D AFM images of Pd nanoparticles.

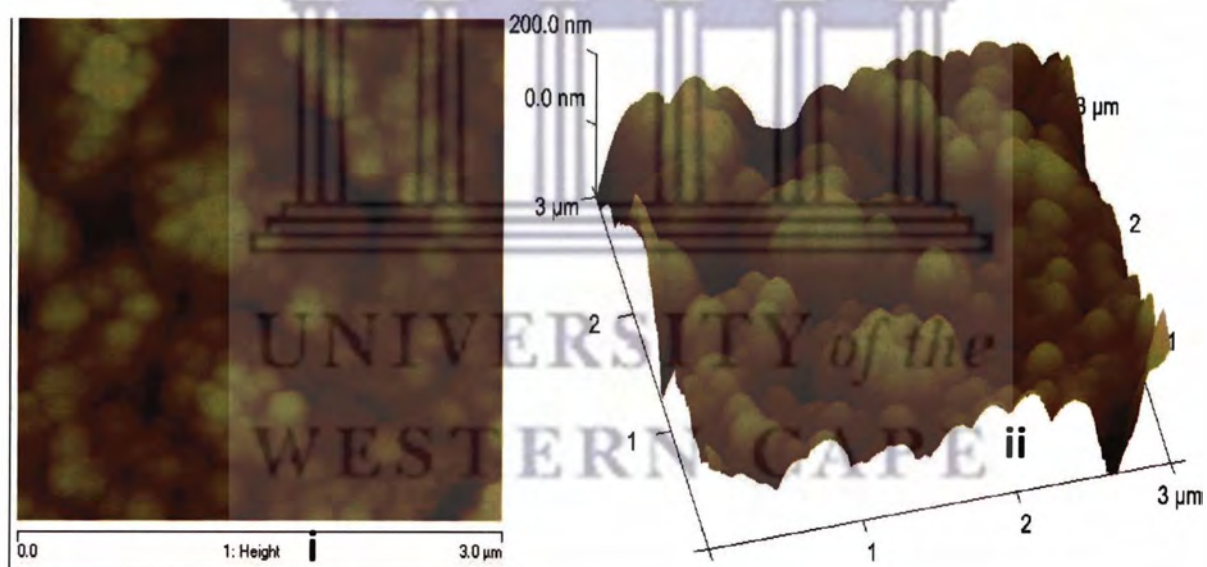


Figure 26C: (i) 2D and (ii) 3D AFM images of PdAg nanoalloys.

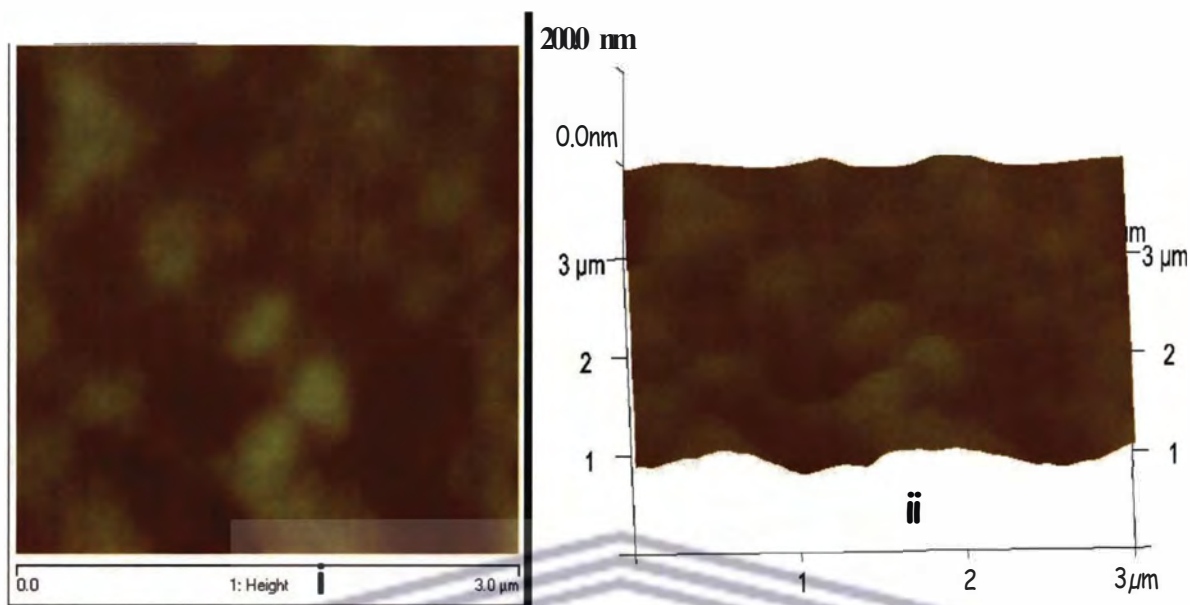


Figure 26D: (i) 2D and (ii) 3D AFM images of PdAu nanoalloys.

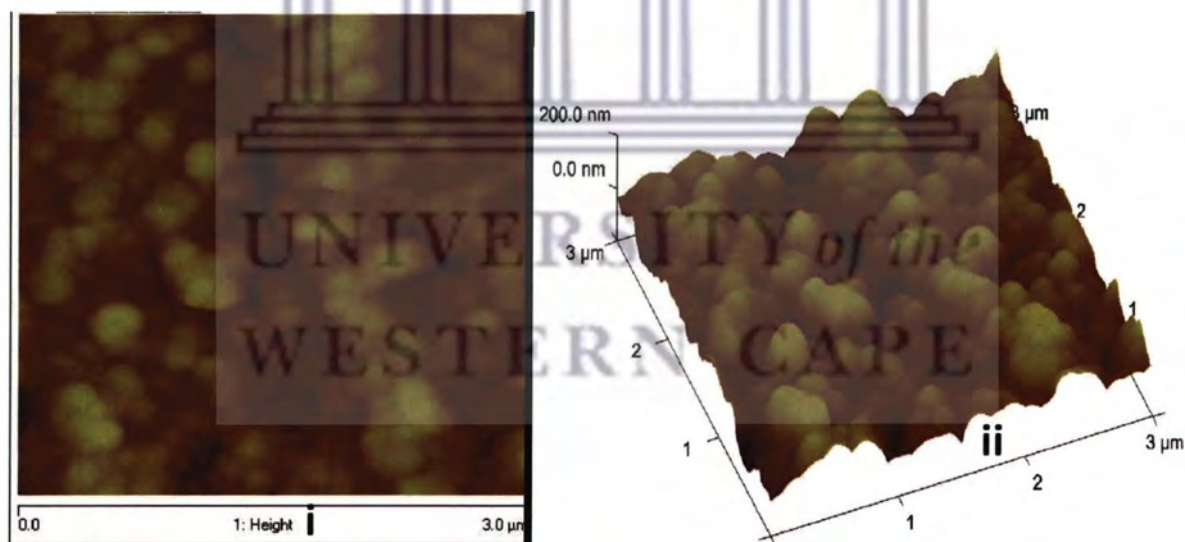


Figure 26E: (i) 2D and (ii) 3D AFM images of PdAuAg nanoalloys.



### 4.3 Electrochemistry of PdCh, AgNO<sub>3</sub> and HAuCl<sub>4</sub>.3H<sub>2</sub>O

To fully understand the electrochemistry of the chemically synthesised nanoparticles, the metal precursors were electrochemically interrogated in a 0.1 M LiClO<sub>4</sub> solution.

#### 4.3.1. Redox behaviour of palladium chloride (PdCh) in solution

The redox reactions of palladium on Pt electrode were investigated by CV in 5 mM PdCh in 0.1 M LiClO<sub>4</sub> Ar-saturated solution. The CVs were recorded over a potential range of -500 mV and 1000 mV at a scan rate of 100 mV s<sup>-1</sup>. Three oxidation peaks were observed; peak a, E<sub>p,a</sub> = -300 mV followed at more positive potentials by peaks b, E<sub>p,a</sub> = -158 mV and c, E<sub>p,a</sub> = 717 mV. On the cathodic scan, two reduction peaks were also observed c', E<sub>p,c</sub> = 284 mV, and b', E<sub>p,c</sub> = -253 mV (**Figure 27**). However, to ascertain whether there was a cathodic peak that was related to peak a, a wider potential range of -700 mV to 1000 mV was used and a third cathodic peak, a', E<sub>p,c</sub> = -467 mV (**Figure 28**) was observed. These CV measurements using Pt electrode immersed in a solution of PdCh clearly showed that various palladium redox processes can occur at the surface of the bare Pt electrode. These observed peaks can be related to the different possible palladium oxidation states such as Pd(0), Pd(II), and Pd(IV) that may undergo several redox reactions such as Pd(0) oxidation to Pd(II) and Pd(IV) [178]. Redox peaks a/a' and b/b' are due to the oxidation and reduction of adsorbed and absorbed hydrogen respectively. At positive potentials, Pd<sup>0</sup> nanoparticles deposited on the Pt surface during the cathodic scanning are oxidised to Pd<sup>2+</sup> (Pd<sup>0</sup> - Pd<sup>2+</sup> + 2e<sup>-</sup>) (peak c) and form a palladium oxide layer. The Pd oxide is reduced on the negative-going scans to Pd metal (Pd<sup>2+</sup> + 2e<sup>-</sup> - Pd<sup>0</sup>) (peak c'). It is noteworthy that Pd oxide layer reduction may occur in a reversible or irreversible manner depending on the upper switching potential. Based on the results obtained, the reduction of the palladium oxide layer behaved in an irreversible

manner ( $i_p/a_{p,c} \approx 1$  and  $\Delta E_p > 59$  mV) which can be explained by the formation of both PdO and Pd<sub>2</sub>Cl<sub>8</sub> [178].

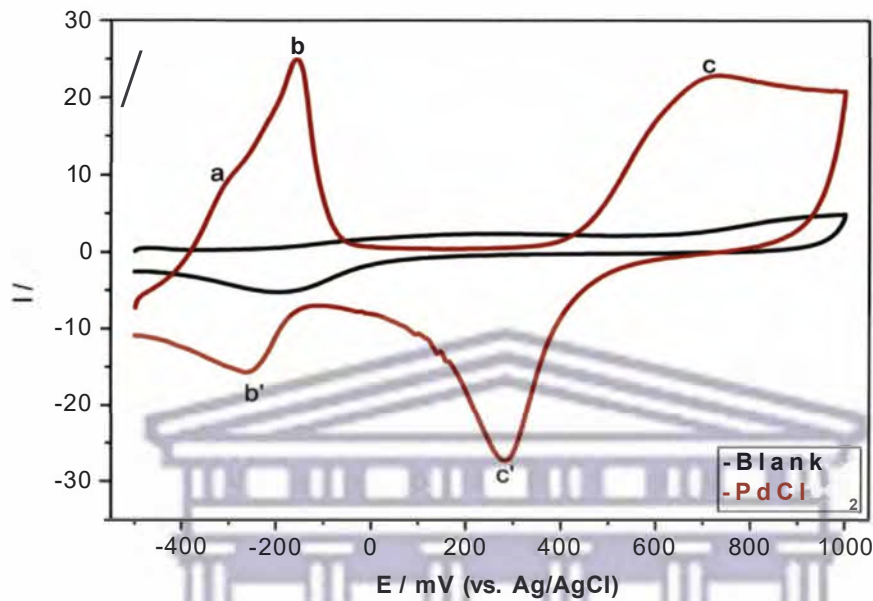


Figure 27: Cyclic voltammograms of bare Pt electrode in 0.1 M LiClO<sub>4</sub> (black curve) and 5 mM PdCl<sub>2</sub> in 0.1 M LiClO<sub>4</sub> (red curve), (-500 to 1000 mV s<sup>-1</sup>): Scan rate, 100 mV s<sup>-1</sup>.

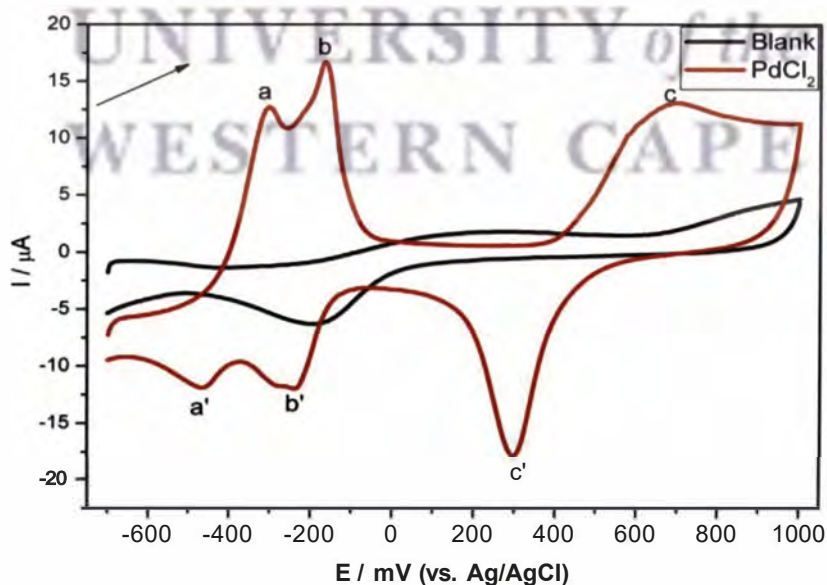


Figure 28: Cyclic voltammograms of bare Pt electrode in 0.1 M LiClO<sub>4</sub> (black curve) and 5 mM PdCl<sub>2</sub> in 0.1 M LiClO<sub>4</sub> (red curve), (-700 to 1000 mV s<sup>-1</sup>): Scan rate, 100 mV s<sup>-1</sup>.

### 4.3.2 Redox behaviour of silver nitrate ( $\text{AgNO}_3$ ) in solution

A pair of redox peaks was observed with an anodic peak potential ( $E_{p,a}$ ) at 211 mV (peak a) and cathodic peak potential ( $E_{p,c}$ ) at 11 mV (peak a') for  $\text{Ag}^+/\text{Ag}^0$  process by using 5 mM  $\text{AgNO}_3$  in 0.1 M  $\text{LiClO}_4$  at a scan rate of  $100 \text{ mV s}^{-1}$  [179] (Figure 29).

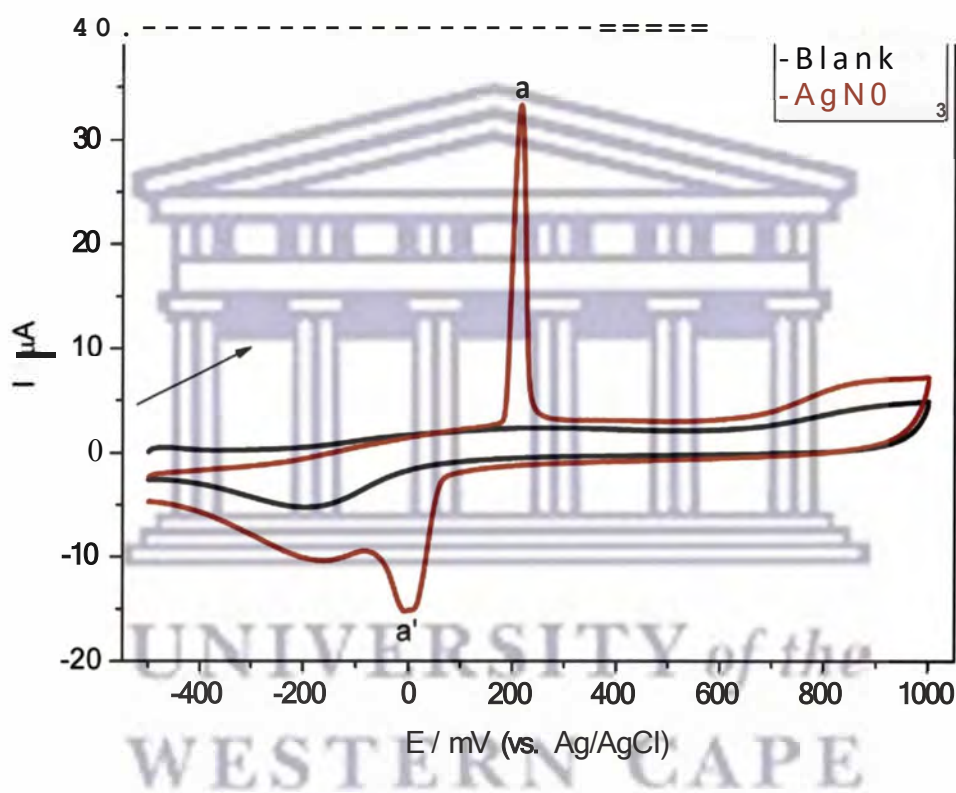


Figure 29: Cyclic voltammograms of bare Pt electrode in 0.1 M  $\text{LiClO}_4$  (black curve) and 5 mM  $\text{AgNO}_3$  in 0.1 M  $\text{LiClO}_4$  (red curve): Scan rate,  $100 \text{ mV s}^{-1}$ .

### 4.3.3 Behaviour of hydrogen tetrachloroaurate (III) trihydrate ( $\text{HAuCl}_4 \cdot 3\text{H}_2\text{O}$ ) in solution

One reduction peak at 704 mV was observed, which corresponds to the reduction of solution bound  $\text{Au(III)}$  to  $\text{Au(0)}$  [180]. A reduction shoulder peak appears at 930 mV which can be attributed to the reduction of adsorbed  $\text{AuCl}_4^-$ . No anodic peak for  $\text{Au(0)}$  was observed on the reverse scan indicating the irreversibility of the reduction of  $\text{Au(III)}$  (Figure 30) [180].

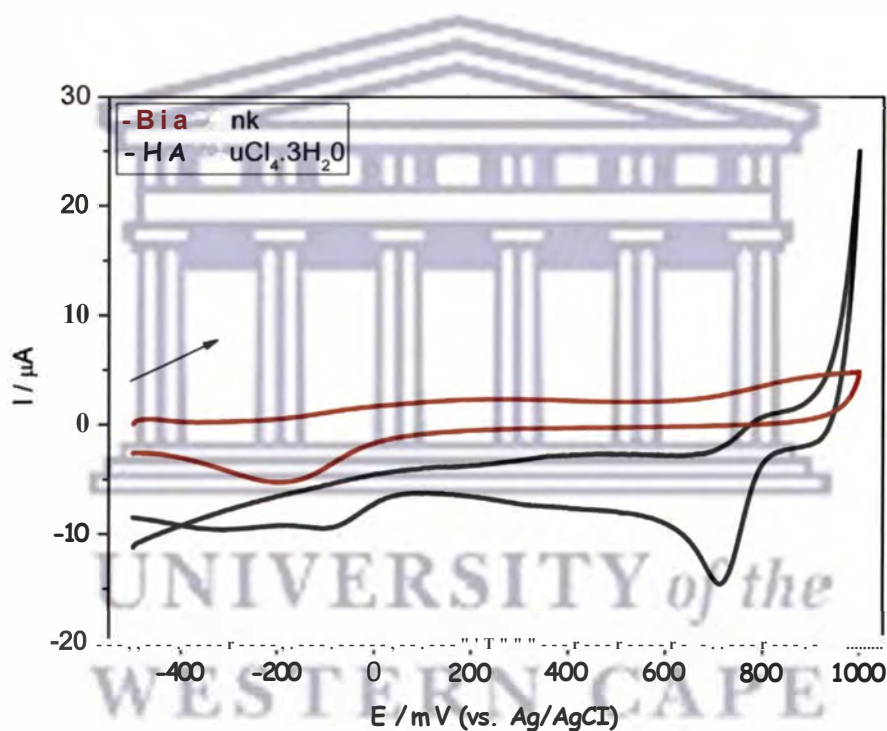


Figure 30: Cyclic voltammograms of bare Pt electrode in 0.1 M  $\text{LiClO}_4$  (red curve) and 5 mM  $\text{HAuCl}_4 \cdot 3\text{H}_2\text{O}$  in 0.1 M  $\text{LiClO}_4$  (black curve): Scan rate,  $100 \text{ mV s}^{-1}$ .

#### 4.3.4 Behaviour of a mixture of PdCl<sub>2</sub>, AgNO<sub>3</sub> and HAuCl<sub>4</sub>·3H<sub>2</sub>O solutions

Figure 31 shows the CV of a mixture of PdCl<sub>2</sub>, AgNO<sub>3</sub> and HAuCl<sub>4</sub>·3H<sub>2</sub>O solutions in 0.1 M LiClO<sub>4</sub> as a supporting electrolyte at different scan rates. Three oxidation peaks were observed; peak a,  $E_{p,a} = -244$  mV (for the oxidation of adsorbed hydrogen atoms), peak b,  $E_{p,b} = 222$  mV (oxidation of Ag to Ag<sup>+</sup>) and peak c,  $E_{p,c} = 857$  mV (oxidation of Pd to Pd<sup>2+</sup>). On the cathodic scan, four cathodic peaks were observed; peak d,  $E_{p,d} = 847$  mV (reduction of Au(III) to Au(0)), peak c',  $E_{p,c'} = 456$  mV (reduction of Pd<sup>2+</sup> to Pd), peak b',  $E_{p,b'} = 60$  mV (reduction of Ag<sup>+</sup> to Ag<sup>0</sup>) and peak a',  $E_{p,a'} = -371$  mV (reduction of hydrogen atoms to hydrogen adsorbed species). The obtained results correlated well with the CV measurements obtained from the individual metal solutions. All the peak currents increased with increase in scan rates.

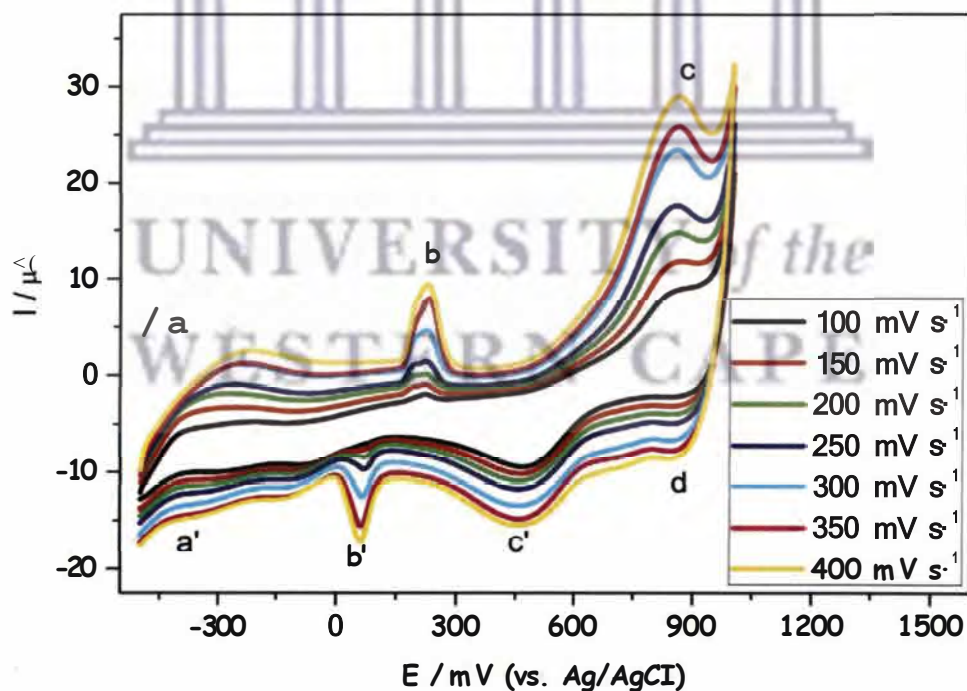
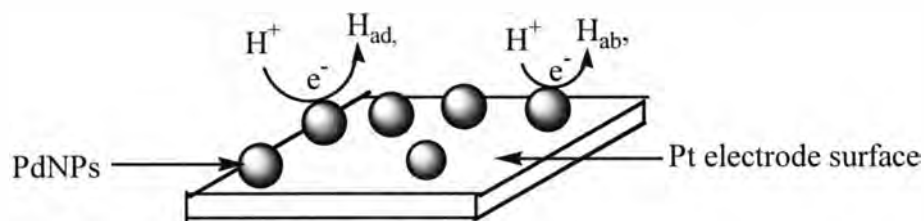


Figure 31: Cyclic voltammograms of bare Pt electrode in a mixture of 5 mM solutions of PdCl<sub>2</sub>, AgNO<sub>3</sub> and HAuCl<sub>4</sub>·3H<sub>2</sub>O in 0.1 M LiClO<sub>4</sub> Ar-saturated solution at different scan rates.

## 4.4 Electrochemical characteristics of PdAu, PdAg and PdAuAg nanoalloys

### 4.4.1 Electrochemistry of the nanoalloys in 0.1 M LiClO<sub>4</sub>

The characterisation of the surface of nanoparticles is a very important issue in the applications of nanoparticles as catalysts and sensors. For instance, catalytic effects are influenced strongly by the structure and composition of the surface of nanoparticles. PdAu, PdAg and PdAuAg nanoalloys were characterised by cyclic voltammetry which is a useful technique for interrogating the electrochemical behaviour of nanomaterials. **Figure 32** shows a series of cyclic voltammograms of the bare Pt electrode and those of the Pt electrode modified with the synthesised nanoparticles. The measurements were carried out in 0.1 M LiClO<sub>4</sub> at a scan rate of 100 mV s<sup>-1</sup> in a potential range of -500 mV to 1000 mV. The bare Pt electrode showed typical potential ranges for the hydrogen adsorption/desorption (-500 mV to 100 mV), double layer potential range (100 mV to 550 mV vs. Ag/AgCl) and the formation/reduction of the surface Pt oxide, Pt-OH<sub>ads</sub> (550 to 1000 mV)(Ag/AgCl) as described by Zhong *et al.* [181]. For the Pd modified Pt electrode (denoted as PtPdNPs), the appearance of an anodic peak (**Figure 32A**, peak a,  $E_{p,a} = -200$  mV) and a cathodic peak (**Figure 32A**, peak a',  $E_{p,c} = -110$  mV) is attributed to the desorption and adsorption of hydrogen atoms onto the Pd<sup>0</sup> nanoparticles, respectively as shown in **scheme 4** [182]. The Pd<sup>0</sup> nanoparticles on the Pt electrode surface were oxidised to Pd<sup>2+</sup> and formed a palladium oxide layer (**Figure 32A**, peak b,  $E_{p,a} = 650$  mV). On the cathodic CV scan, a reduction peak (**Figure 32A**, peak b',  $E_{p,c} = 310$  mV) occurred corresponding to the reduction of the Pd oxide layer. Lee *et al.* [183] observed similar peaks on Pd nanoparticles modified ITO electrodes.



**Scheme 4: Schematic representation of the surface of Pt electrode with Pd nanoparticles: the proton reduction takes place on the surface of the Pd nanoparticles.**

PdAu nanoalloys modified Pt electrode (denoted as PtJPdAuNPs)(Figure 32B) showed current peaks of hydrogen desorption/adsorption at low potentials (peak a,  $E_{p,a} = -245$  mV and peak a',  $E_{p,c} = -290$  mV) and surface oxidation/reduction at high potentials (peak b,  $E_{p,a} = +454$  mV and peak b',  $E_{p,c} = 363$  mV) which revealed a typical CV characteristics of a 'palladium-like' modified electrode. However, the reduction peak of surface oxide showed an anodic shift on the PdAu nanoalloys compared to that of Pd nanoparticles (310 mV to 363 mV) indicating an easier removal of adsorbed oxygen species from PdAu nanoalloys compared to that from Pd monometallic nanoparticles [184]. The CV of PdAg nanoalloys modified electrode (denoted as PtJPdAgNPs) (Figure 32C) showed hydrogen desorption/adsorption at low potentials (peak a,  $E_{p,a} = -180$  mV and peak a',  $E_{p,c} = -215$  mV, respectively) and surface oxidation/reduction at high potentials (peak c,  $E_{p,a} = 788$  mV and peak c',  $E_{p,c} = 291$  mV). A redox peak was observed, *bib'* (peak b,  $E_{p,a} = 250$  mV and peak b',  $E_{p,c} = 35$  mV) and was attributed to the  $Ag/Ag^+$  redox system (refer to Figure 29). For the PdAuAg nanoalloys modified electrode (PtJPdAuAgNPs) (Figure 32D), hydrogen desorption/adsorption peaks (peak a,  $E_{p,a} = -220$  mV and peak a',  $E_{p,c} = -270$  mV) and surface oxidation/reduction peaks (peak c,  $E_{p,a} = 810$  mV and peak c',  $E_{p,c} = 350$  mV) were observed. A redox peak was observed (peak b,  $E_{p,a} = 240$  mV and peak b',  $E_{p,c} = 55$  mV) which can be attributed to the  $Ag/Ag^+$  redox system. It is noteworthy that the reduction peak of surface

oxide showed an anodic shift and the hydrogen desorption/adsorption peak currents for the PtPdAuAgNPs decreased compared to that observed for PtPdAgNPs which can be attributed to the total incorporation of the Au in the nanoalloys system. Considering the reduction potentials of  $\text{Au}^{3+}$  ( $\text{AuCl}_4^-/\text{Au}$ , +1.002 V vs. SHE),  $\text{Pd}^{2+}$  ( $\text{Pd}^{2+}/\text{Pd}$ , +0.591 V vs. SHE) and  $\text{Ag}^+$  ( $\text{Ag}^+/\text{Ag}$ , +0.80 V vs. SHE), it can be assumed that the formation of the nanoalloys was initiated by nucleation of Au atoms followed by co-deposition/incorporation of residual Au, Ag and Pd atoms on the surface of the seeds which have higher Au content [183]. These results correlated well with the electrochemical behaviour of the metal precursor solutions studied in Figures 27-30.

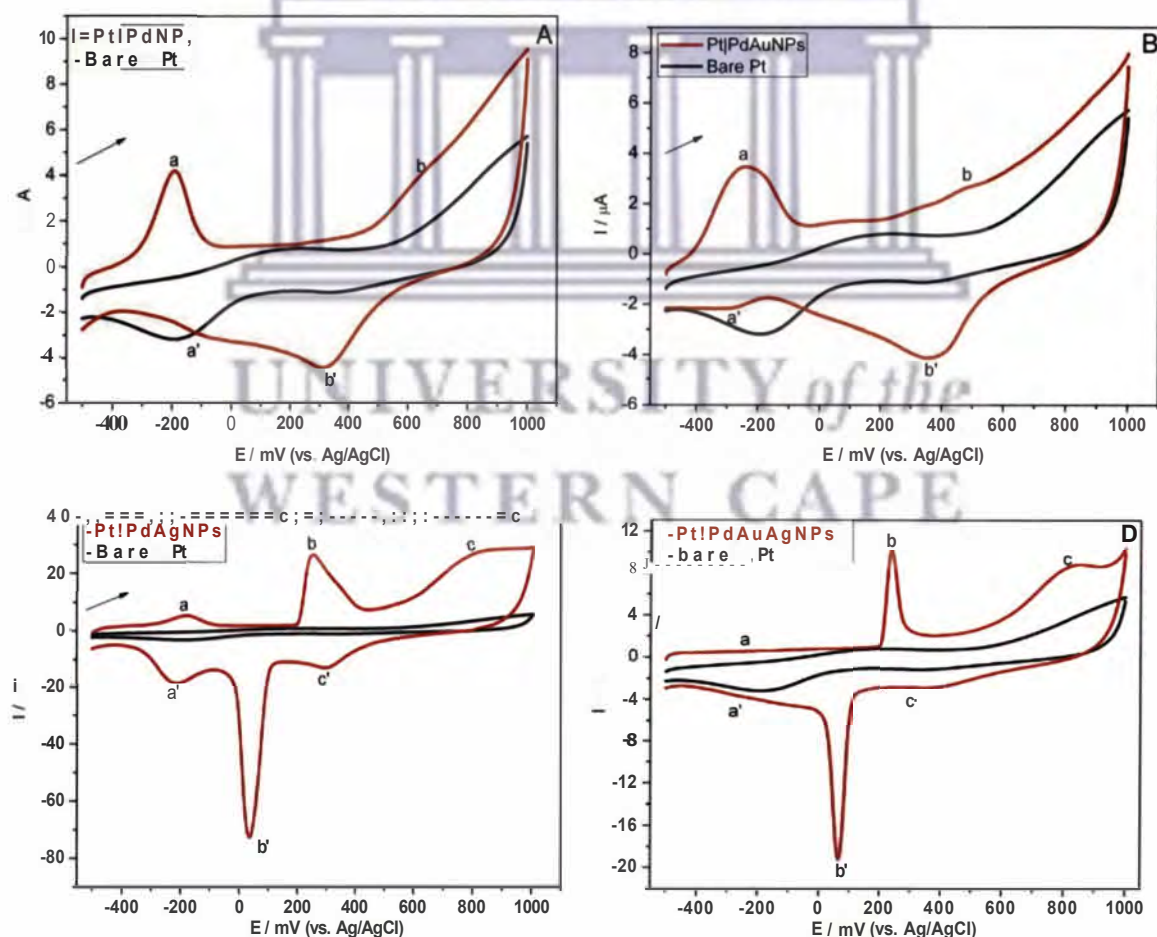


**Figure 32:** Cyclic voltammograms of (A) PtPdNPs, (B) PtPdAuNPs, (C) PtPdAgNPs and (D) PtPdAuAgNPs electrodes in 0.1 M  $\text{LiClO}_4$ : Scan rate,  $100 \text{ mV s}^{-1}$ .



#### 4.4.1.1 Effect of potential scan rates.

The results of cyclic voltammetry of the Pd, PdAu, PdAg and PdAuAg nanoparticles on Pt electrode in the potential window -500 to 1000 mV at different scan rates are shown in **Figure 33**. The peak currents increased with increase in scan rate.

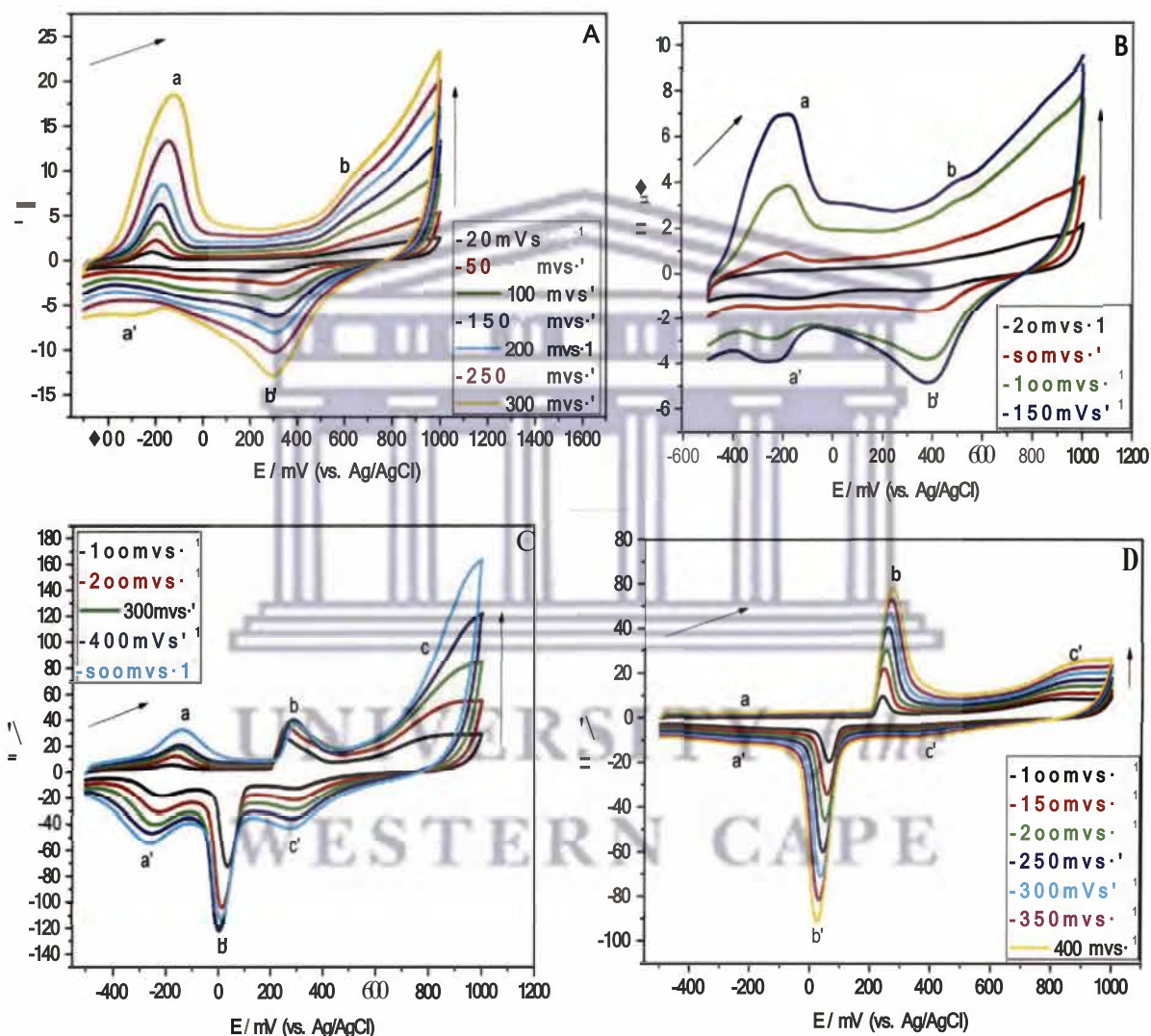


**Figure 33:** Cyclic voltammograms of (A) PtPdNPs, (B) PtPdAuNPs, (C) PtPdAgNPs and (D) PtPdAuAgNPs in 0.1 M LiClO<sub>4</sub> at different scan rates.

For further interrogation of the electrochemical behaviour of the nanoparticles, PdAuAg nanoalloys were used with specific focus on peak bib'. It can be seen from **Figure 34** that the peak currents ( $i_p$ ) for PdAuAg nanoalloy film on Pt electrode increased linearly with scan

rates ( $\nu$ ) up to 400  $\text{mV s}^{-1}$ . The results showed that the PdAuAg nanoalloys film was stable and electrochemically active in 0.1 M  $\text{LiClO}_4$  solution. **Figure 34** shows a plot of anodic and cathodic peak currents vs. scan rate for redox peaks b/b' that showed a close linear dependence with the scan rates, a characteristic feature of surface confined species. Additionally, the voltammetric data was subjected to analysis by plotting  $\log(i_p)$  versus  $\log(\nu)$ . The value of the slope of the linear plot of  $\log i_p$  versus  $\log \nu$  can be used to elucidate the nature of the processes influencing the electrochemistry of the surface confined species. Slopes with values of 1.0 and 0.5 refer to adsorption-controlled and diffusion-controlled electrochemical processes, respectively. Intermediate values for the slope indicate mixed diffusion/adsorption-controlled electrochemical processes [185]. In this work, the plots of  $\log i_p$  versus  $\log \nu$  (not shown) gave slopes of 0.7 for both the anodic and cathodic peaks which showed the occurrence of mixed diffusion/adsorption-controlled electrochemistry of the PdAuAg nanoalloys system and that the PdAuAg nanoalloys film was a non-monolayer film.

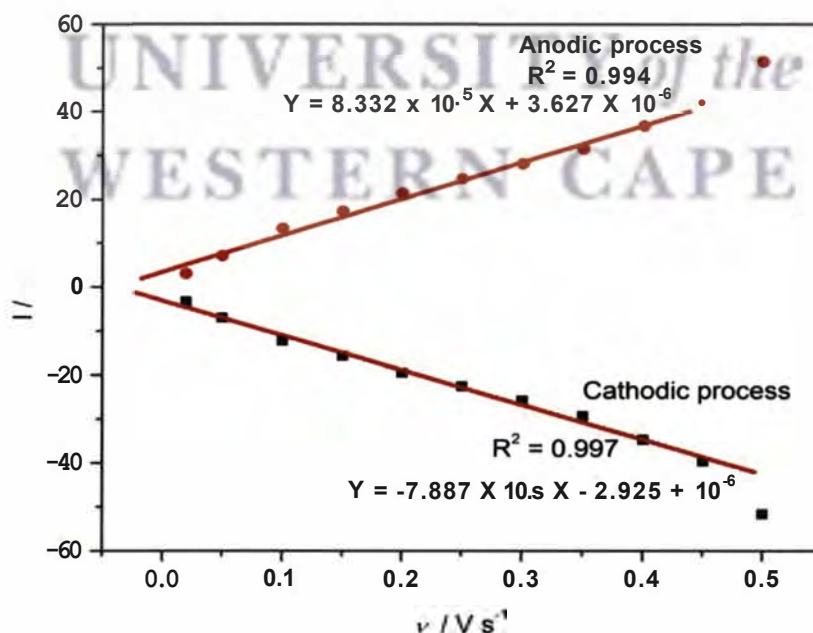
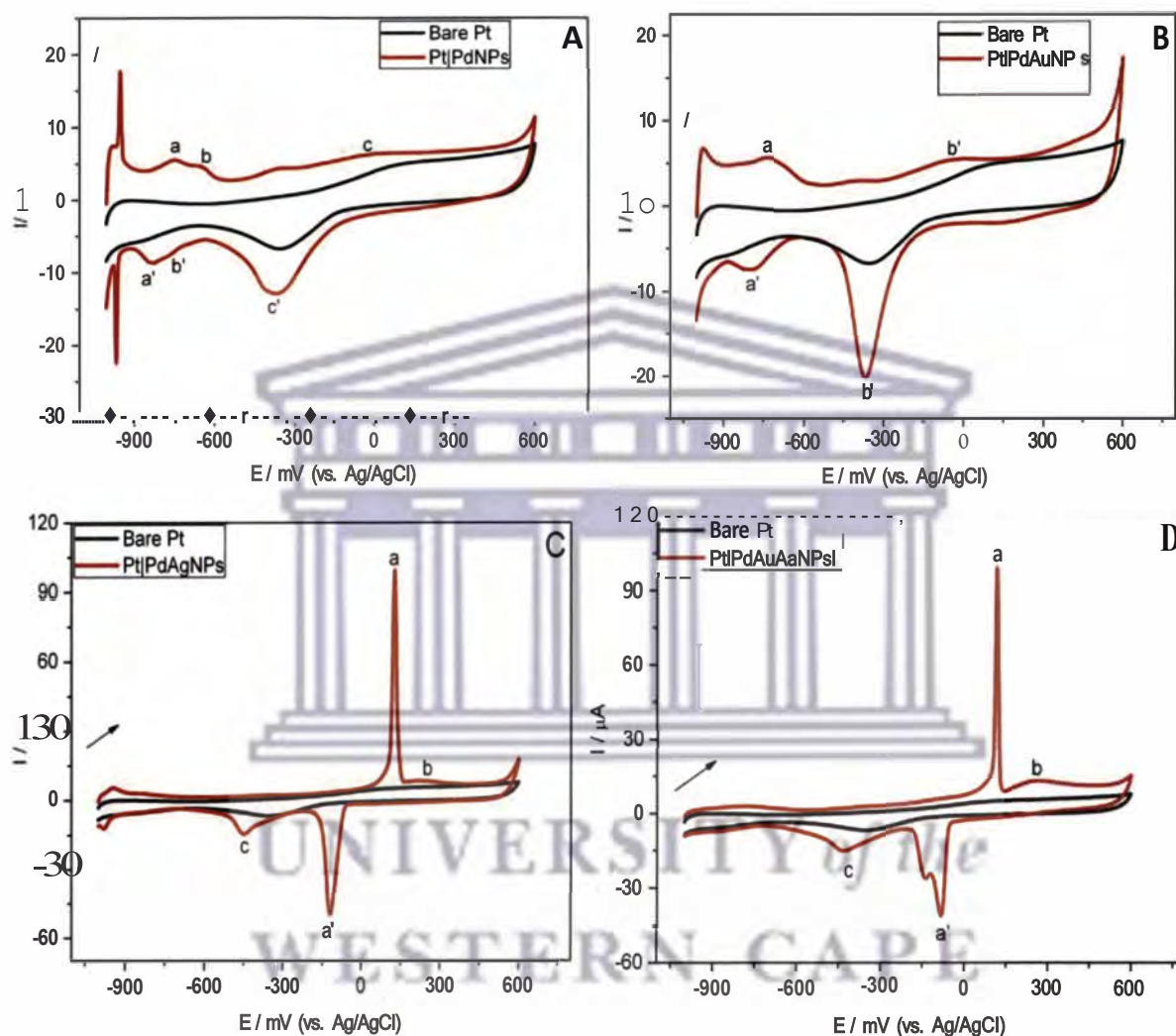


Figure 34: Relationship between the peak currents and scan rates for PtIPdAuAgNPs (peak b/b').

#### 4.4.2 Electrochemistry of the nanoalloys in 1 M KOH

The electrochemical behaviour of PdAg, PdAu and PdAuAg nanoalloys immobilised on platinum electrodes were investigated in basic medium using cyclic voltammetry. **Figure 35** shows the cyclic voltammograms of the bare Pt electrode and PtPdNPs, PtPdAuNPs, PtPdAgNPs, PtPdAuAgNPs electrodes in 1 M KOH. These were measured at a scan rate of  $100 \text{ mV s}^{-1}$  in a potential range of -1000 mV to 600 mV. For the Pd nanoparticles modified Pt electrode, the  $\text{Pd}^0$  nanoparticles on the Pt electrode surface were oxidised to  $\text{Pd}^{2+}$  and formed a palladium oxide layer (**Figure 35A**, peak c,  $E_{p,a} = -27 \text{ mV}$ ). On the reverse CV scan (cathodic scanning), a reduction peak (**Figure 35A**, peak c',  $E_{p,c} = -372 \text{ mV}$ ) occurred corresponding to the reduction of the Pd oxide layer. The anodic peaks a and b (**Figure 35A**, peak a,  $E_{p,a} = -744 \text{ mV}$ , peak b,  $E_{p,a} = -640$ ) and cathodic peaks a' and b' (**Figure 35A**, peak a',  $E_{p,c} = -826 \text{ mV}$ , peak b',  $E_{p,c} = -761 \text{ mV}$ ) are attributed to the desorption and adsorption of weakly and strongly adsorbed hydrogen atoms onto the  $\text{Pd}^0$  nanoparticles [182]. PdAu nanoalloys modified Pt electrode (PtPdAuNPs) (**Figure 35B**) showed current peaks of hydrogen desorption/adsorption at low potentials (peak a,  $E_{p,a} = -730 \text{ mV}$  and peak a',  $E_{p,c} = -803 \text{ mV}$ ) and surface oxidation/reduction at high potentials (peak b,  $E_{p,a} = 45 \text{ mV}$  and peak b',  $E_{p,c} = -364 \text{ mV}$ ). The CV of PdAg nanoalloys modified electrode (PtPdAgNPs) (**Figure 35C**) showed a redox peak a/a' (peak a,  $E_{p,a} = 128 \text{ mV}$  and peak a',  $E_{p,c} = -120 \text{ mV}$ ) which was attributed to the  $\text{Ag}/\text{Ag}^+$  redox system (refer to **Figure 29**). Surface oxidation/reduction occurred at high potentials (peak b,  $E_{p,a} = 231 \text{ mV}$  and peak c,  $E_{p,c} = -14 \text{ mV}$ ). For the PdAuAg nanoalloys modified electrode (PtPdAuAgNPs) (**Figure 35D**), a redox peak was observed (peak a,  $E_{p,a} = 120 \text{ mV}$  and peak a',  $E_{p,c} = -87 \text{ mV}$ ) which can be attributed to the  $\text{Ag}/\text{Ag}^+$  redox system. Surface oxidation/reduction peaks (peak b,  $E_{p,a} = 247 \text{ mV}$  and peak c,  $E_{p,c} = -440 \text{ mV}$ ) were observed. A shoulder was observed at -145 mV which may have

resulted from some contaminants in the nanoparticles. These results correlated well with the electrochemical behaviour of the metal precursor solutions observed in **Figures 27-30**.



**Figure 35:** Cyclic voltammograms of (A) PtPdNPs, (B) PtPdAuNPs, (C) PtPdAgNPs and (D) PtPdAuAgNPs electrodes in 1 M KOH: Scan rate,  $100 \text{ mV s}^{-1}$ .

#### 4.4.3 Electrochemistry of PdAuAg nanoalloys in solution

It is quite interesting to interrogate the behaviour of the nanoalloys in solution rather than being adsorbed on the surface of the electrode. The cyclic voltammetry of PdAuAg nanoalloys solution was studied in a potential range of -500 mV to 1000 mV. The results are shown in **Figure 36**. A redox peak a/a' whose potential shifted slightly with increase in scan rate was attributed to the oxidation and reduction of the PdAuAg nanoalloys while peak b originated from the electrode system. A plot of log peak current versus log scan rate for the redox peaks (results not shown) showed a linear relationship with a slope of 0.9 ( $r^2 = 0.99$ ) for the anodic, and 0.7 ( $r^2 = 0.99$ ) for the cathodic peak indicating adsorption-diffusion controlled reaction (peak). In order to estimate the number of electrons transferred, **equation 39** (Laviron's equation) and **equation 40** [186-187] were re-expressed to give **equation 41**;

$$I_p = \frac{n^2 F^2 A r v}{4RT} \quad (39)$$

$$Q = nFAr \quad (40)$$

$$I_p = \frac{nFQv}{4RT} \quad (41)$$

Where  $\Gamma$  is the surface concentration of the electrode materials ( $\text{mol cm}^{-2}$ ),  $A$  is the electrode area ( $\text{cm}^2$ ) and  $Q$  is the quantity of charge (C) calculated from the reduction and oxidation peak areas of the voltammograms; and  $n$ ,  $I_p$ ,  $F$ ,  $R$  and  $T$  have their usual meanings. From the slopes of  $i_p$  versus  $v$  plots (**Figure 37**),  $n$  was calculated to be 0.51 and 0.531 for the anodic and cathodic processes respectively, indicating that PdAuAg nanoalloys in solution undergo a one-electron redox reaction at the Pt electrode in a 0.1 M  $\text{LiClO}_4$  solution. The average value for the ratio of cyclic voltammetric anodic to cathodic peak currents of PdAuAg nanoalloys in 0.1 M  $\text{LiClO}_4$  was 1.0587, which indicates a one-electron quasi-reversible electrochemistry

[188]. The formal potential,  $\{E^0 = \frac{\xi_{pa} + \xi_{pc}}{2}\}$ , was unaffected by the scan rate (SD = 0.7039 for 8 scan rates). This is an indication that the electron transfer coefficients,  $u_a$  and  $u_c$  for anodic and cathodic processes respectively, are similar ( $u_a = u_c = 0.5$ ). Since  $n|E_p| < 200$  mV, the direct electron transfer rate constant ( $k$ ) of the PdAuAg nanoalloys can be obtained by **equation 42** [187].

$$\log k = a \log(1-a) + (1-a) \log a - \log \frac{RT}{nFv} - a(1-a) \frac{nFM_p}{2.3RT} \quad (42)$$

Where  $u$  is the charge-transfer coefficient,  $|E_p|$  is the peak potential separation,  $v$  is the scan rate,  $n$  is the number of electron transferred, and  $F$  is the Faradays constant. Taking the charge-transfer coefficient  $u$  of 0.5 ( $0.3 < u < 0.7$  in general) at a scan rate of  $350 \text{ mV s}^{-1}$ , the  $k$  of the PdAuAg nanoalloys was estimated to be  $1.5 \text{ cm s}^{-1}$ . The large  $k$  value ( $> 0.02 \text{ cm s}^{-1}$ ) indicated a reversible electron transfer system.

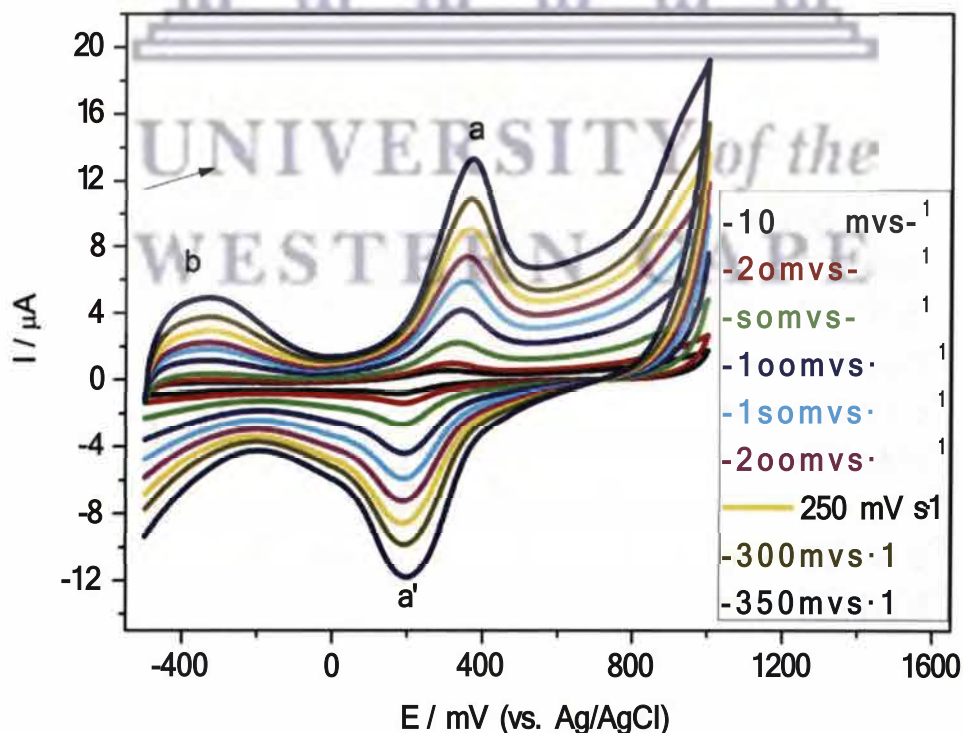


**Figure 36:** Cyclic voltammograms of PdAuAg nanoalloys in solution (the colloidal nanoalloys were added in 2 mL of 0.1 M LiClO<sub>4</sub> solution).

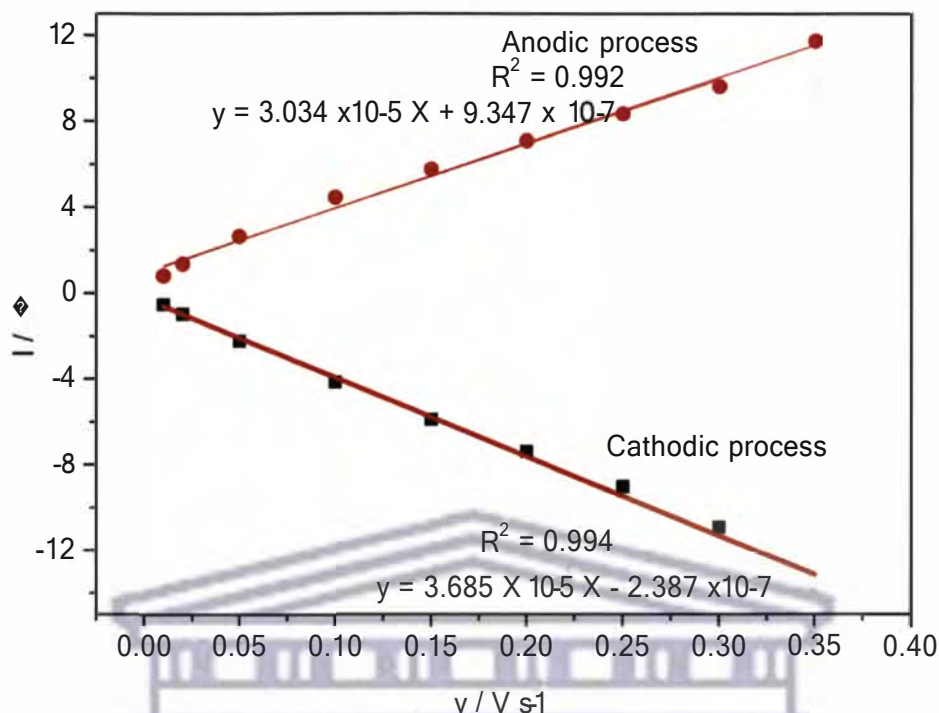


**Figure 37: Relationship between the peak currents and scan rates for PdAuAg nanoalloys.**

#### 4.5 The catalytic performance of PdAg, PdAu and PdAuAg nanoalloys

##### 4.5.1 Catalytic oxidation of ammonia

##### 4.5.1.1 Choice of potential window

**Figure 38** shows the typical cyclic voltammograms of a platinum electrode in 1 M KOH aqueous solutions in the presence and absence of ammonia (**Figure 38**, curves a and b, respectively). The anodic current peak at -292 mV (Ag/AgCl) can be assigned to the oxidation of ammonia to  $N_2$  [189]. Other oxidation products such as nitrite and nitrogen oxide form at above -200 mV according to Endo *et al.* and Wasmus *et al.* [59, 167]. The peak as a result of the oxidation of these products was not observed when the upper potential limit was lowered to 100 mV as shown in **Figure 39**. During the cathodic scan down to -336 mV, no reduction peak of a possible surface oxide (like as seen on PtOx on curve b at -336 mV)

can be observed and two reduction peaks appear at -500 mV and -839 mV. These cathodic peaks are dependent on the upper sweep limit of the preceding anodic scan as shown in **Figure 39**. The cathodic peak at -500 mV was observed when the preceding anodic scan was reversed at higher than -200 mV, suggesting that the cathodic current was related either to the reduction or desorption of oxidized species of ammonia such as  $\text{NH}_4\text{ads}$  and  $\text{NH}_2\text{ads}$  (**Figure 39**). On the other hand, the cathodic peak at -839 mV corresponding to the reduction of other oxidized species such as nitrite anions [167] appears clearly when upper sweep limit was set above -200 mV. The optimum potential window for the oxidation of ammonia was chosen to be -1000 mV to -100 mV based on the well resolved ammonia oxidation peak at -292 (**Figure 40**).

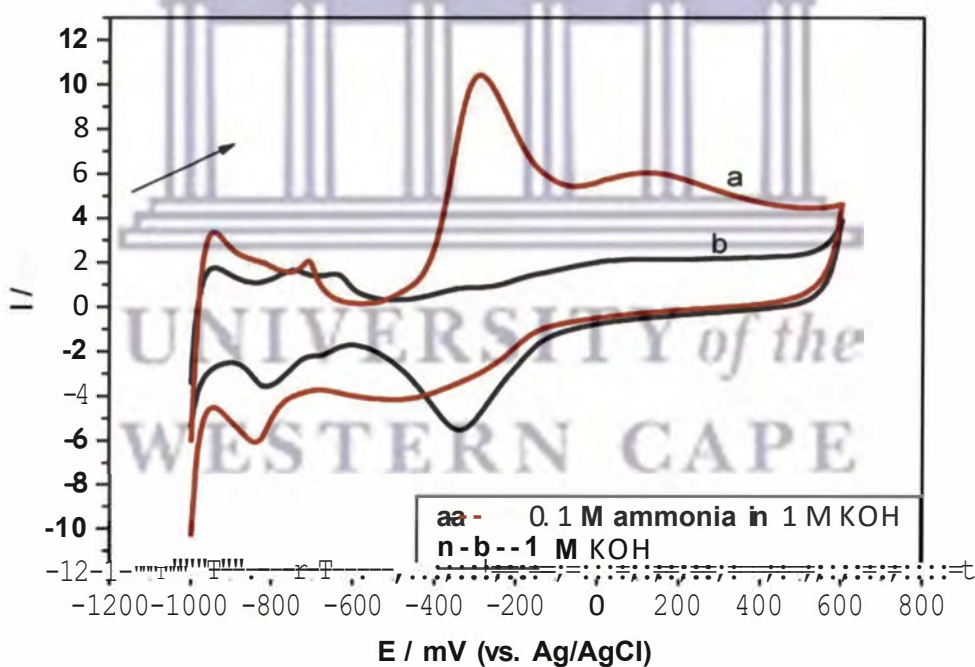


Figure 38: Cyclic voltammograms of bare Pt electrode (a) with and (b) without 0.1 M ammonia in 1 M **KOH**: Scan rate, 50 mV s<sup>-1</sup>.



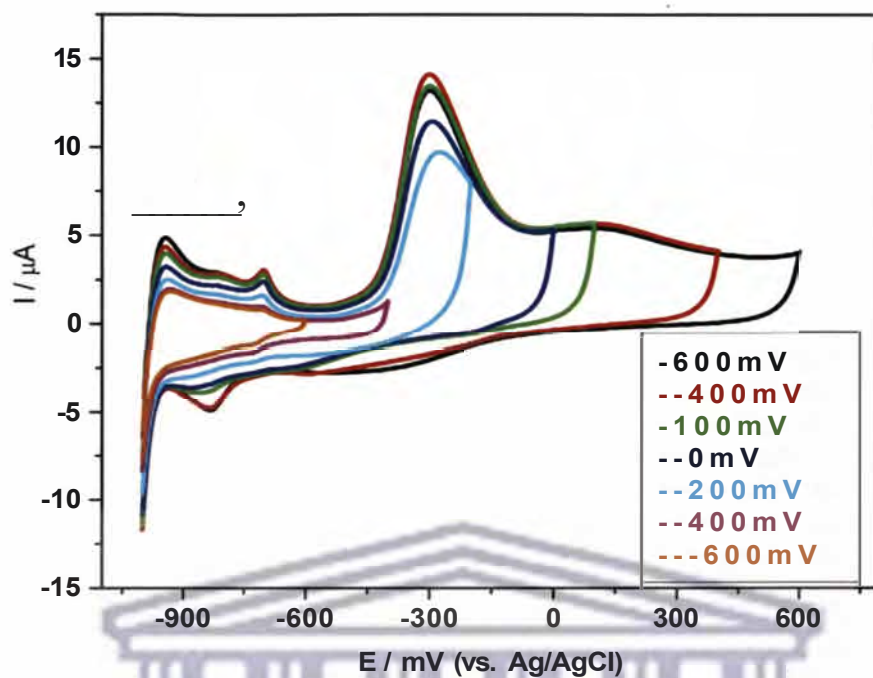


Figure 39: Cyclic voltammograms of bare Pt electrode in 0.1 M ammonia and 1 M KOH aqueous solution with various upper sweep limits; (600, 400, 100, 0, -200, -400, -600 mV): Scan rate,  $50 \text{ mV s}^{-1}$ .

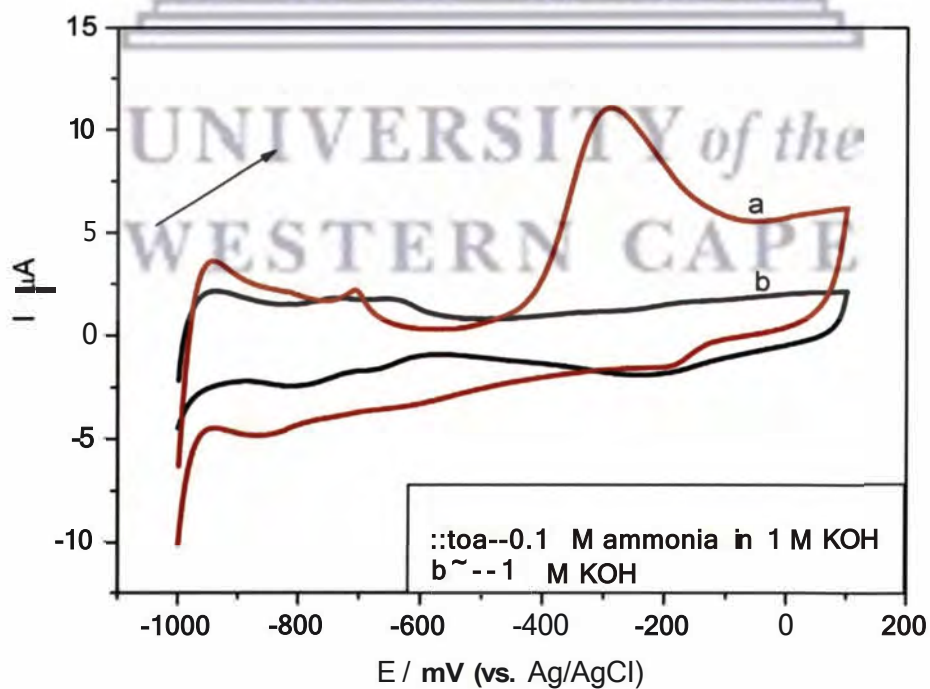


Figure 40: Cyclic voltammograms of bare Pt electrode (a) with and (b) without 0.1 M ammonia in 0.1 M KOH (vs. Ag/AgCl) (-1000 mV to 100 mV).

#### 4.5.1.2 Choice of supporting electrolyte

0.1 M LiClO<sub>4</sub> and 1 M KOH solutions were interrogated to ascertain the best electrolyte for the oxidation of ammonia (see **Figures 41 and 42**). In absence of ammonia, there was no ammonia oxidation peak observed when the voltammograms was carried out in 0.1 M LiClO<sub>4</sub>. The voltammogram obtained in 0.1 M ammonia without any supporting electrolyte showed an oxidation peak at -41 mV. However, in presence of 0.1 M ammonia and 0.1 M LiClO<sub>4</sub>, a slight reduction of overpotential (from -40 mV to 90 mV) was observed (**Figure 41**). This can be attributed to increased ion transfer introduced by the supporting electrolyte. **Figure 42** shows the oxidation of ammonia in the absence and presence of 1 M KOH. In absence of 1 M KOH, ammonia oxidation peak was observed at -41 mV while in the presence of 1 M KOH, reduced overpotential and an increased peak current was observed. This can be attributed to the critical role of KOH in ammonia electro-oxidation which is to generate an alkaline environment for ammonia oxidation. Alkaline environment favours ammonia oxidation based on the Nemst equation for the reaction (**equation 43**) under the constant ammonia concentration:

$$\varphi_{\text{NH}_3/\text{N}_2} = \varphi_{\text{NH}_3/\text{N}_2}^0 - \frac{2.303RT}{nF} \log \frac{[\text{NH}_3]^2[\text{OH}^-]^6}{[\text{N}_2]} \quad (43)$$

Thus, 1 M KOH was chosen as the suitable supporting electrolyte for ammonia oxidation because it favours the oxidation of ammonia.

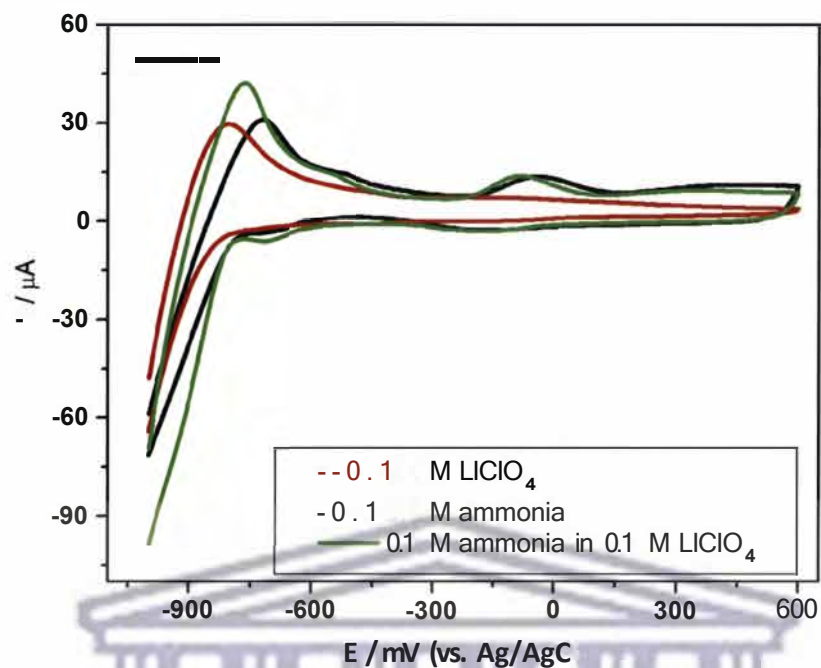


Figure 41: Cyclic voltammograms measured on bare Pt electrode with and without 0.1 M  $\text{LiClO}_4$ .

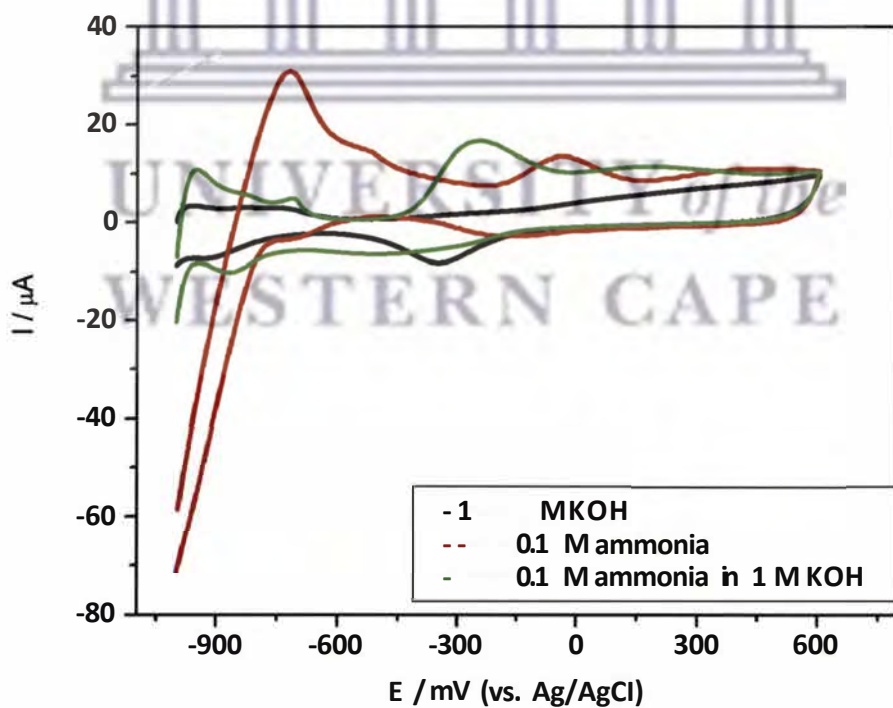
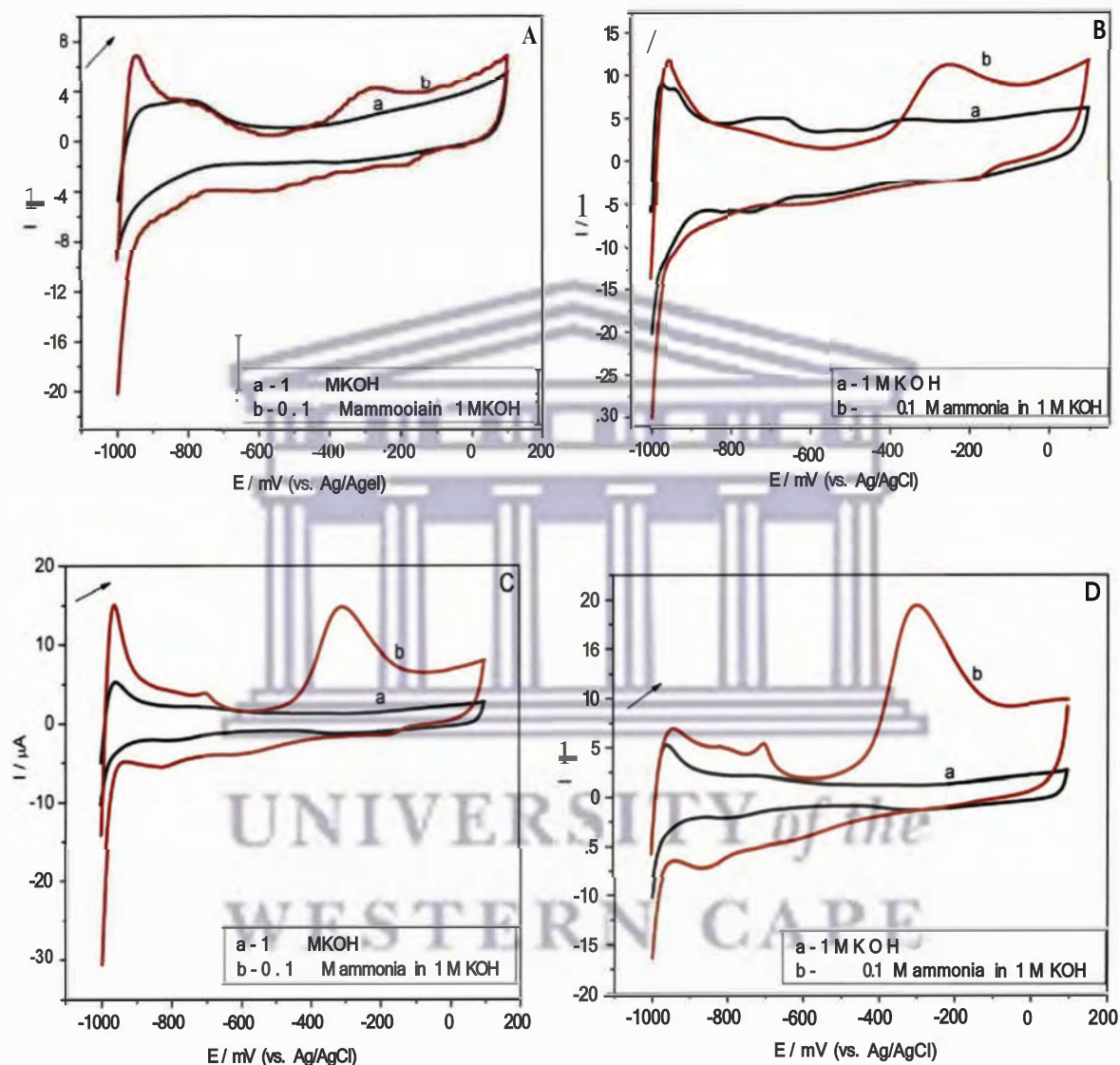


Figure 42: Cyclic voltammograms measured on bare Pt electrode with and without 1 M  $\text{KOH}$ .

**Figure 43** shows the cyclic voltammograms of Pd, PdAg, PdAu and PdAuAg nanoparticles modified Pt electrodes in 1 M KOH aqueous solution with and without 0.1 M ammonia. It is without doubt that ammonia oxidation (between -400 mV and -250 mV) proceeds on all of these electrodes; however both the potential and the peak currents of the oxidation peaks are dependent on the electrode material. When the Pt electrode was coated with Pd nanoparticles, there was a current increase and lower overpotential compared to the bare electrode while PdAg and PdAu nanoalloys modified Pt electrode showed a decreased peak current and higher overpotential. Since the ammonia concentration was kept constant in all the experiments, the decreased peak currents on PdAg and PdAu nanoalloys modified Pt electrodes may suggest that the active sites are less dense than on bare Pt electrode. Vooyoys *et al.* [168] highlighted that Cu, Ag and Au are inactive towards ammonia oxidation. Although the PdAg and PdAu nanoalloys were expected to have a higher catalytic effect than the monometallic Pd nanoparticles, the inactiveness of Ag and Au in the nanoalloys may have lowered the catalytic ammonia oxidation activity of the nanoalloys systems. Pd nanoparticles increased the surface area of the Pt electrode thus increasing the peak current and lowering the overpotential compared to that of the bare Pt electrode. The surface orientation of the electrodes used in ammonia oxidation determines their catalytic properties. A recent report [190] revealed that the catalytic activity of ammonia on Pt single crystals is highest on (100) plane. Since the orientation on the surface of the electrode used in this study was the same, the density of the active site could be assumed to be dependent on the constituents of the electrode material. Though the surface active sites of the Pt electrode are expected to become less available when coated with nanoparticles, PdAuAg nanoalloys were found to give slightly higher peak currents and lower overpotential than bare Pt (see **table 4**), which can be explained by cooperative effects between Pd and the noble metals, Au and Ag. This showed that PdAuAg nanoalloys were suitable electrocatalysts for the oxidation of ammonia based on

their reduced overpotential and increased current properties. An overlay of the different modified electrode is shown in **Figure 44**.



**Figure 43:** Cyclic voltammograms of PtjPdAgNPs (A), PtjPdAuNPs (B), PtjPdNPs (C) and PtjPdAuAgNPs (D) electrodes in 0.1 M ammonia and 1 M KOH aqueous solution: Scan rate, 50 mV s<sup>-1</sup>.

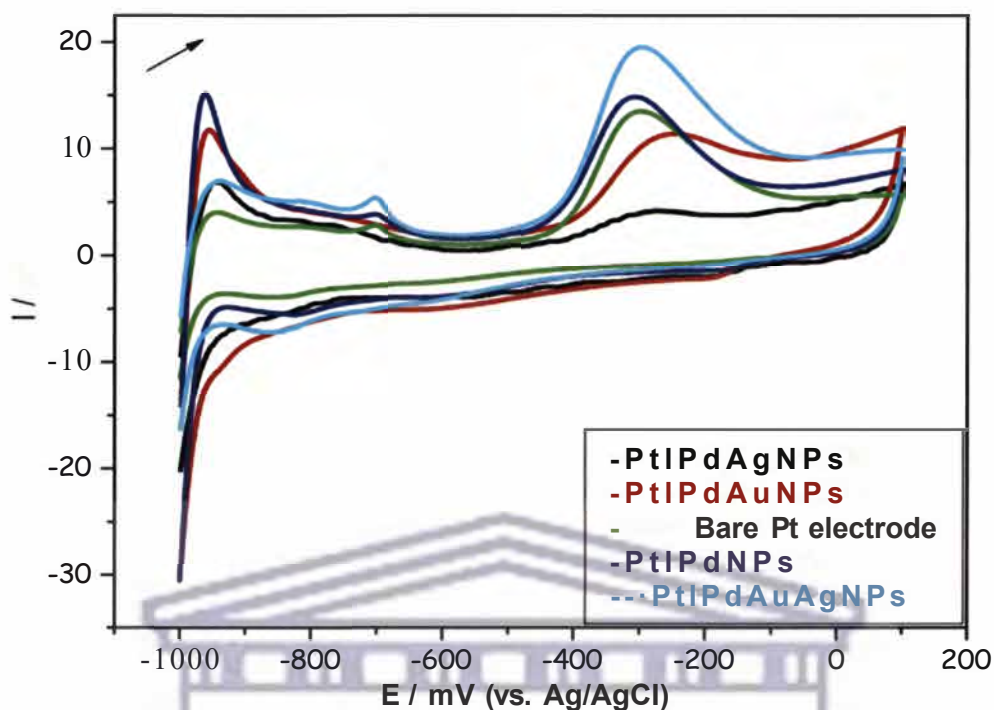


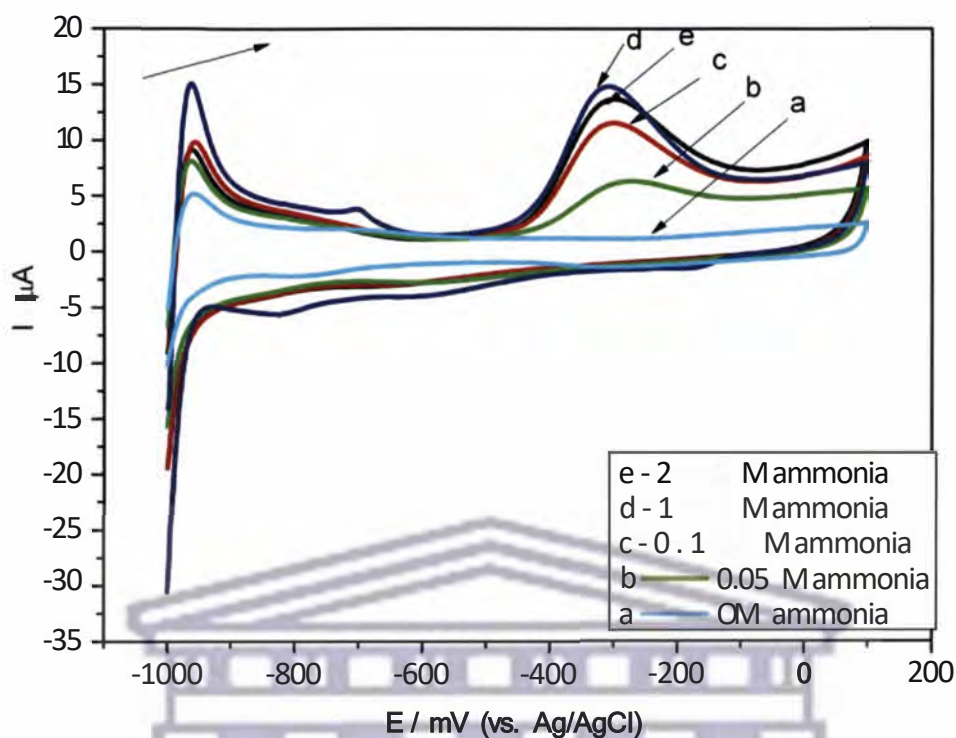
Figure 44: Overlay CVs of Pt, PtPdNPs, PtPdAgNPs, PtPdAuNPs and PtPdAuAgNPs electrodes in 0.1 M ammonia and 1 M KOH aqueous solution: Scan rate, 50 mV s<sup>-1</sup>.

Table 2: CV parameters of Pd nanoalloy systems in 0.1 M ammonia and 1 M KOH (experimental conditions as in Figure 44)

Electrode	$E_{p,a}$ (mV)	$i_{p,a}$ (A)
Pt electrode	-300	$1.371 \times 10^{-5}$
PtPdNPs	-311	$1.521 \times 10^{-5}$
PtPdAuNPs	-255	$1.145 \times 10^{-5}$
PtPdAgNPs	-282	$4.380 \times 10^{-6}$
PtPdAuAgNPs	-304	$1.992 \times 10^{-5}$

#### 4.5.2 Effects of ammonia concentration

To investigate the effect of ammonia concentration, PdAuAg nanoalloy systems which showed the highest ammonia oxidation current density and lower overpotential was used. **Figure 45** shows cyclic voltammograms measured on PtPdAuAgNPs in 1 M KOH solution with various ammonia concentrations. It can be seen that two anodic current peaks were observed at approximately -940 mV and -292 mV (Ag/AgCl) in all the curves, respectively. With an increase in ammonia concentration, the peak current at -292 mV increased continuously. This can be attributed to the adsorption of more ammonia on the electrode surface resulting in increased oxidation of the ammonia. Thus, the anodic current increases continuously with the ammonia concentration. In particular, there was a significant increase in peak current when the ammonia concentration increased from 0.05 M to 1 M. With respect to the influence of the ammonia concentration on peak current at -940 mV, there was an insignificant change in peak current. When the ammonia concentration reached a certain level, i.e. 1 M in this work, the adsorption of ammonia on PtPdAuAgNPs electrode achieved a relatively saturation status. The intermediates generated during ammonia oxidation, such as  $\text{NH}_{2,ads}$  and  $\text{NH}_{ads}$ , could remain on the electrode surface and block the ammonia adsorption. It is reasonable to assume that the blocking effect was significant when the solution contains a high concentration of ammonia. Therefore, an increase of the ammonia concentration beyond 1 M resulted in slight decrease in anodic peak current due to ammonia saturation on the electrode surface. The present results showed that ammonia can be oxidised effectively on PtPdAuAgNPs electrode from -1000 mV to 100 mV at a concentration range of 0.05 - 1 M.



**Figure 45:** Cyclic voltammograms of PtPdAuAgNPs in 1 M KOH solutions with various concentrations of ammonia (0.05-2 M ammonia): Scan rate, 50 mV s<sup>-1</sup>.

#### 4.5.3 Effects of KOH concentration

**Figure 46** shows cyclic voltammograms measured on PtPdAuAgNPs electrode in 0.1 M ammonia with various KOH concentrations. The critical role of KOH in ammonia electro-oxidation is to generate an alkaline environment for ammonia oxidation. The current work shows that, with increasing KOH concentration (increasing pH value), the increasing alkalinity decreased the ammonia oxidation overpotential, shifting the ammonia electro-oxidation potential negatively. Such an essential role of the alkalinity can be explained by Nernst equation for the reaction (see **equation 43** above) under the constant ammonia concentration. It is apparent that ammonia oxidation potential decreases with the increasing hydroxide ion concentration, i.e. the alkalinity of the solution. However, Zhou *et al.* [14] reported that increasing the solution alkalinity



reduces the amount of hydrogen ions and hence hydrogen evolution, causing the decrease in cathodic current density. Thus, an optimal KOH concentration is essential to the ammonia oxidation for hydrogen generation. In this study, 1 M KOH was used as the optimum concentration of the supporting electrolyte.

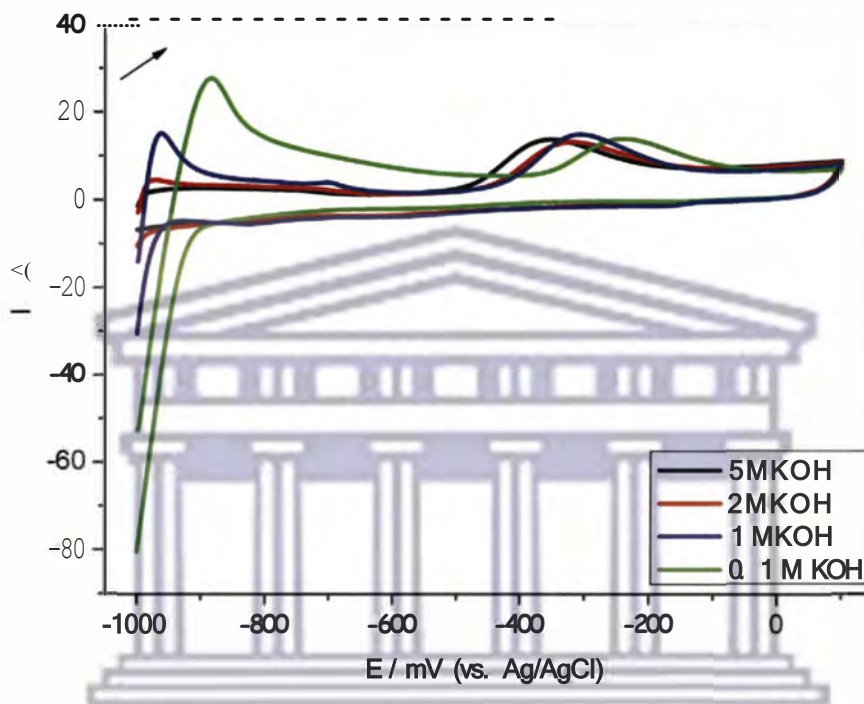


**Figure 46:** Cyclic voltammograms of PtPdAuAgNPs in 0.1 M ammonia solutions with various KOH concentrations: Scan rate, 50 mV s<sup>-1</sup>.

#### 4.5.4 Effects of scan rate

In order to study the nature of the oxidation of ammonia, we performed the CVs at different scan rates (**Figure 47**) measured on PtPdAuAgNPs electrode in 0.1 M ammonia and 1 M KOH solution. The anodic peak currents at about -292 mV increased significantly with the increasing potential scan rate. The peak currents followed a linear  $v^{1/2}$  ( $v$ : potential scan rate) dependence as shown in **Figure 48**, indicating a diffusion controlled rather than a surface controlled electron transfer kinetics. Additionally, the peak potential shifted positively with increasing scan rates demonstrating that the oxidation of ammonia was an irreversible process [191].

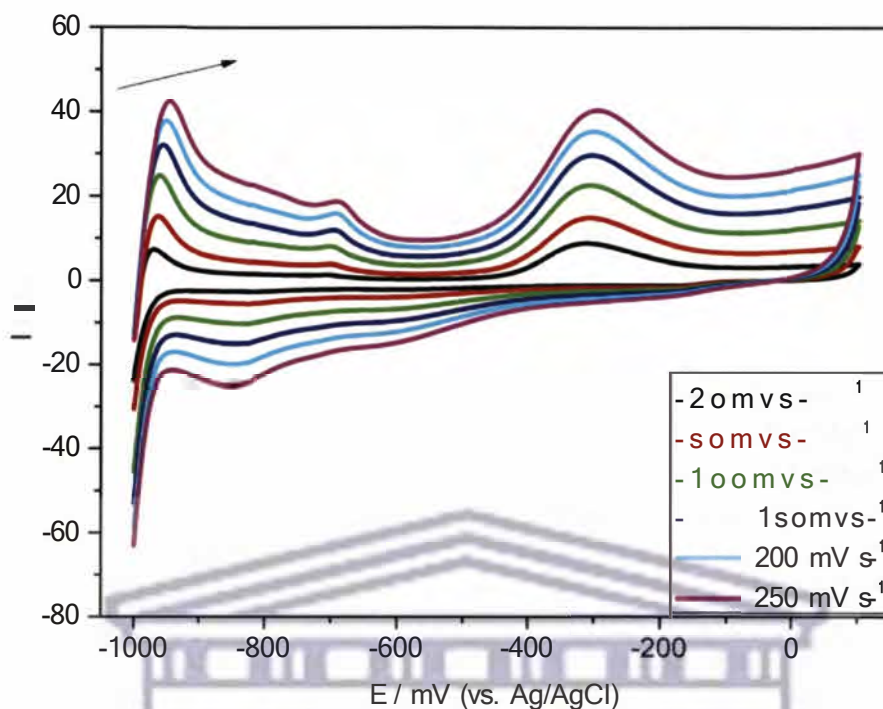


Figure 47: Cyclic voltammogram of PtPdAuAgNPs electrode in the presence of 0.1 M ammonia and 1 M KOH aqueous solution at different scan rates.

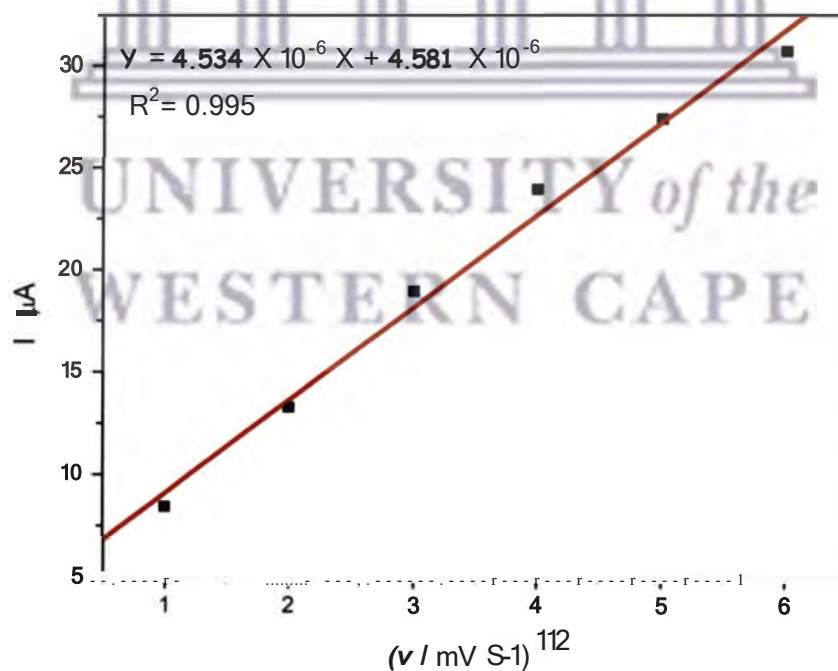


Figure 48: Randles-Sevcik plot of PtPdAuAgNPs electrode in the presence of 0.1 M ammonia and 1 M KOH aqueous solution.

For an irreversible diffusion-controlled process, the peak potential ( $E_p$ ) is proportional to the logarithm of potential sweep rate ( $\nu$ ) within the following equation: [192-193]

$$E_p = \frac{b}{2} \log \nu + \text{constant} \quad (44)$$

On the basis of this equation, the linear plot of  $E_p$  versus  $\log \nu$  is  $b/2$ , where  $b$  indicates the Tafel slope whose value was calculated to be about 31 mV per decade (**Figure 49**). This value is reasonably close to the theoretical value of 40 mV per decade, typical for an electrochemical reaction involving at least two electron-transfer steps, the second electron transfer being the rate determining step [41]. Transfer of more than two electrons allows us to exclude the  $\text{NH}_2$  adsorbate as the product of the process featured by the peak at -292 mV.

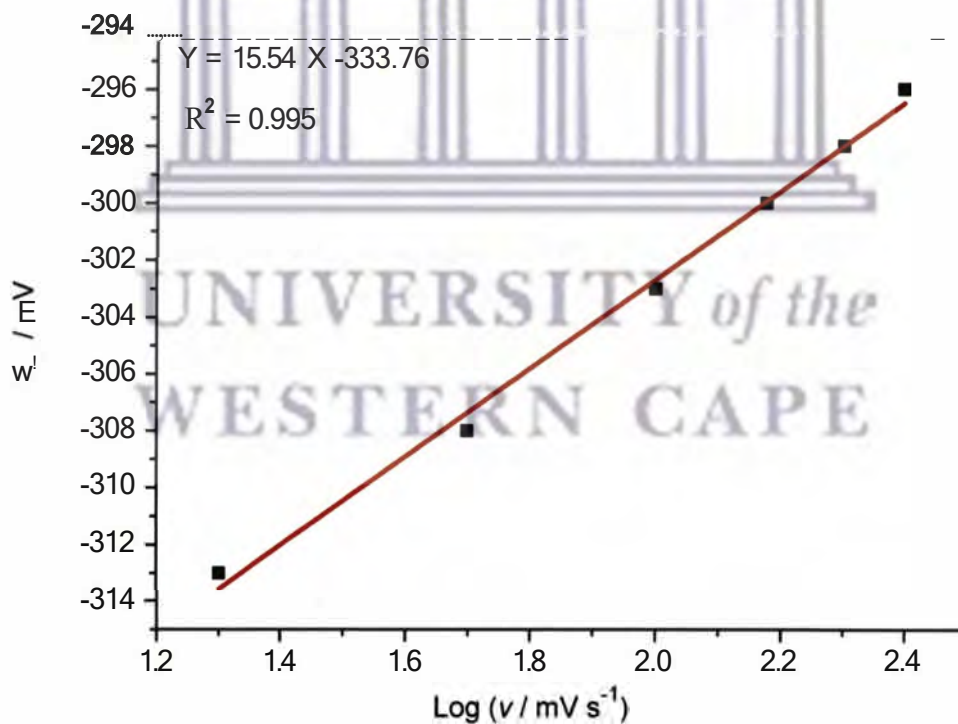
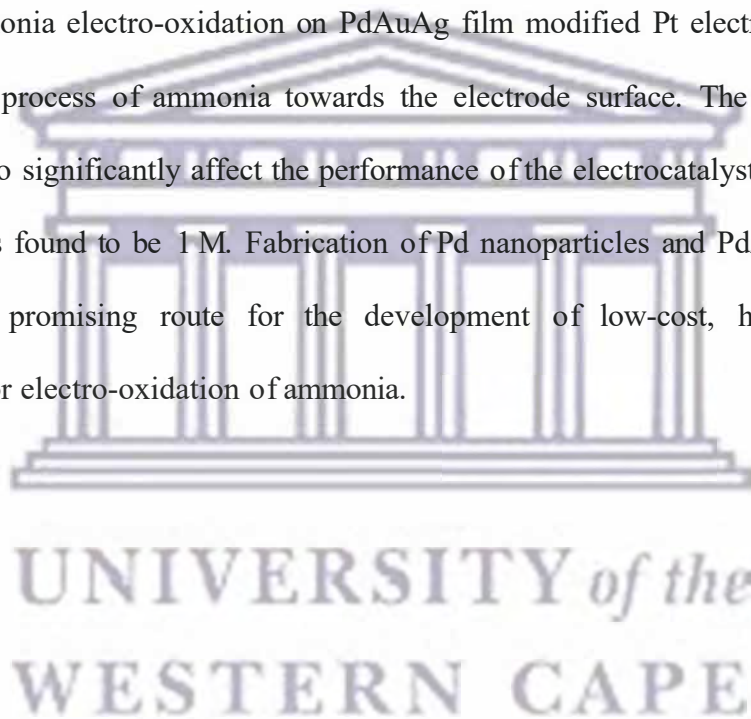


Figure 49: Relationship between the oxidation peak potential ( $E_p$ ) and log of scan rate.

#### 4.6 Sub conclusion

A simple and room-temperature method for the synthesis of PdAg, PdAu and PdAuAg nanoalloys has been demonstrated. The well-dispersed non-agglomerated PdAuAg nanoalloys exhibited a reduced overpotential and a 33%, 400%, 82% and 54% increase in current density for ammonia electro-oxidation compared to Pd, PdAg, PdAu nanoparticles and bare Pt electrode, respectively. The much improved current density of the well-dispersed PdAuAg nanoalloys is attributed to the increased electrochemically active surface area of the nanoalloys. Ammonia electro-oxidation on PdAuAg film modified Pt electrode is controlled by mass-transfer process of ammonia towards the electrode surface. The concentration of KOH was found to significantly affect the performance of the electrocatalysts and the optimal concentration was found to be 1 M. Fabrication of Pd nanoparticles and PdAuAg nanoalloys film provides a promising route for the development of low-cost, high performance electrocatalysts for electro-oxidation of ammonia.



## CHAPTER FIVE

### RESULTS AND DISCUSSION: Part 2

#### REACTIVITIES OF NOVEL ULTRASENSITIVE SYMMETRICAL Pt(100) NANOALLOY SYSTEMS IN AMMONIA OXIDATION



##### *Summary*

*The knowledge of electrochemical properties of nanoparticles has been the purpose of numerous studies in surface electrochemistry and electrocatalysts. However, little attention has been paid to the relationship between the surface structure of nanoparticles and their electrocatalytic activities. The oxidation of ammonia has been reported to be a structure sensitive reaction that takes place almost exclusively on Pt(100) sites. It is worth investigating the effect of oriented Pt(100) nanoparticles and Pt(100) based nanoalloys in the oxidation of ammonia. In this section, the characterisation of oriented Pt(100) nanoparticles, Pt(100)Pd, Pt(100)Au and Pt(100)PdAu nanoalloys and their electrocatalytic effects in ammonia oxidation is discussed.*

## 5.1 Introduction

The knowledge of the electrochemical properties of nanoparticles and their subsequent application has been the purpose of numerous studies in surface electrochemistry and electrocatalysis. These studies have been carried out both from a practical point of view, preparation and design of new materials for fuel cells as well as for the understanding of fundamental aspects of surface electrochemical reactivity [29]. It is worthy investigating the relationship between the surface structure of the nanoparticles and their electrocatalytic activity which has been extensively studied and is very well-known with model electrodes (single crystals) and which is expected to play a role in the case of nanoparticles [194]. Ammonia oxidation is a structure sensitive or site demanding reaction and controlling the crystallographic surface orientation of Pt nanoparticles could result in much improved catalysts [28]. It has been found that the oxidation of ammonia on platinum surfaces is a very structure sensitive reaction occurring predominantly on Pt(100) sites [29, 195]. Therefore, in order to develop good electrocatalysts for the ammonia oxidation, a major goal would be the preparation of nanoparticles with the largest density of Pt(100) sites. Vidal-Iglesias *et al.* [196] studied the oxidation of ammonia using Pt-based nanoparticles (Pt-Ir, Pt-Rh, Pt-Pd, Pt-Ru) and preferentially oriented Pt(100) nanoparticles. The authors showed that Pt(100) had higher current density than polycrystalline Pt nanoparticles and Pt-based nanoparticles towards ammonia oxidation denoting that ammonia electro-oxidation is highly surface sensitive and takes place almost exclusively at Pt(100) domains. Bimetallic and multi-metallic nanoparticles show higher catalytic properties than monometallic nanoparticles. In this chapter, we demonstrate the catalytic effects that exist on Pt(100) nanoparticles upon the inclusion of adatoms such as Au, Pd and PdAu to form nanoalloys for the ammonia oxidation reaction.

## 5.2 Spectroscopic and morphological characterisation of preferentially oriented Pt(100) nanoparticles, Pt(100)Pd, Pt(100)Au and Pt(100)PdAu nanoalloy systems.

### 5.2.1 UV-visible spectroscopy

The formation of the nanoparticles by reduction of  $\text{PtCl}_4^{2-}$ ,  $\text{HAuCl}_4^-$  and  $\text{Pd}^{2+}$  ions was confirmed by the use of UV-visible spectroscopy. **Figure 50** shows the UV-visible spectra of the starting materials ( $\text{PdCl}_2$ ,  $\text{HAuCl}_4 \cdot 3\text{H}_2\text{O}$  and  $\text{K}_2\text{PtCl}_6 \cdot \text{H}_2\text{O}$  salts) while **Figure 51** shows the UV-visible spectra of Pt(100), Pt(100)Pd, Pt(100)Au, Pt(100)PdAu nanoparticles. The absorption peaks observed at 262 nm for  $\text{Pt}^{4+}$ , 285 nm for  $\text{Au}^{3+}$  and 420 nm for  $\text{Pd}^{2+}$  ions [170] disappeared after 16 h of reduction indicating that the metal ions were completely reduced [197]. The synthesised oriented nanoparticles showed no absorption peaks indicating a complete reduction of the metal salts. The colour of the solution turned from pale yellow to black.

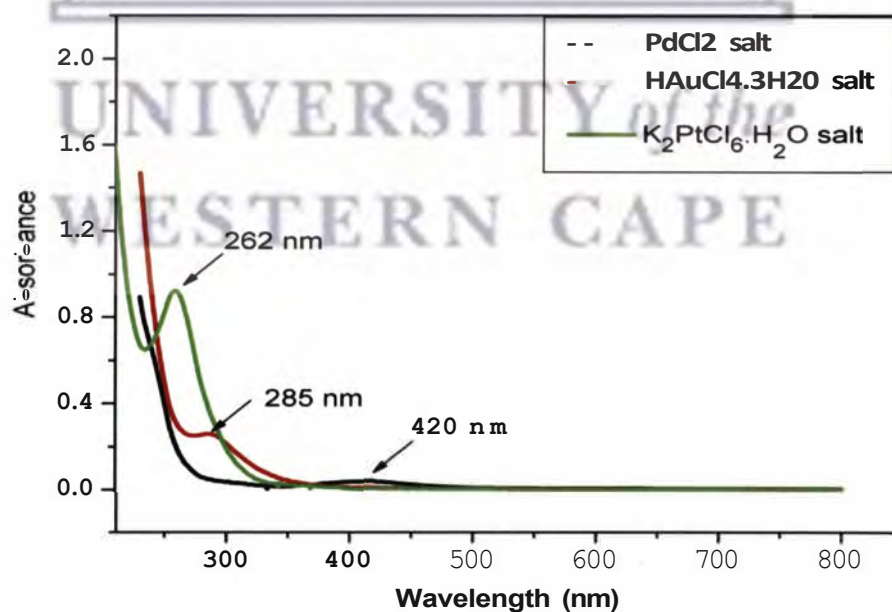
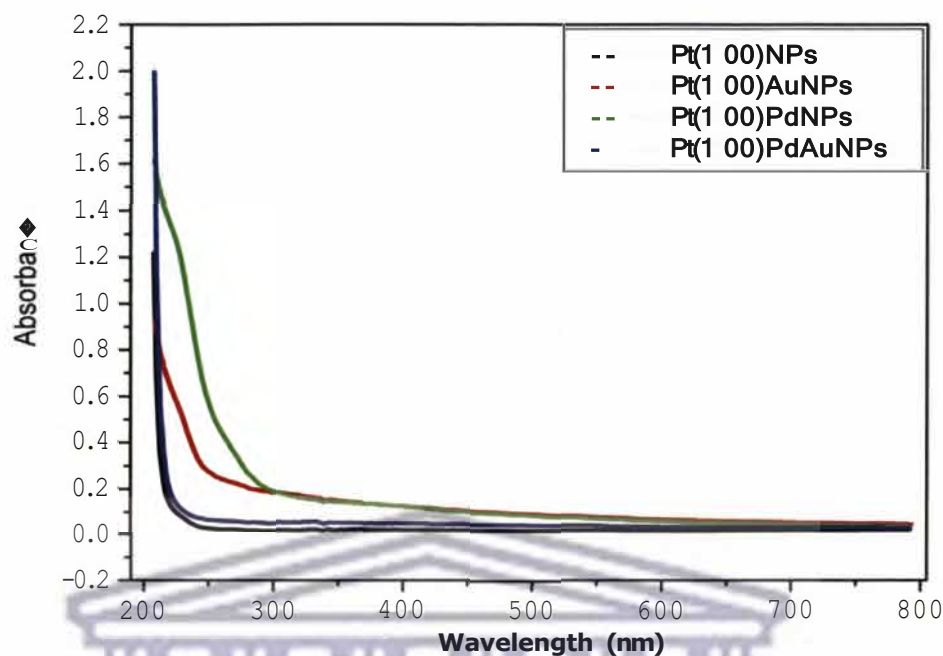


Figure 50: UV-visible spectra of  $\text{K}_2\text{PtCl}_6$ ,  $\text{HAuCl}_4 \cdot 3\text{H}_2\text{O}$  and  $\text{PdCl}_2$  salts.



**Figure 51: UV-visible spectra of Pt(100), Pt(100)Pd, Pt(100)Au and Pt(100)PdAu nanoparticles.**

### 5.2.2 High resolution transmission electron microscopy (HRTEM)

A very good characterisation of the structure, shape and size of a single nanoparticle can be obtained by ex situ HRTEM. Oriented Pt(100) nanoparticles are known to show cubic structures, Pt(111) nanoparticles portray tetrahedral and hexagonal shapes while poly-oriented nanoparticles show quasi-spherical shapes [119]. **Figure 52** shows the HRTEM images of polycrystalline platinum nanoparticles prepared through the reduction of the metal precursors using sodium borohydride. Quasi-spherical shaped nanoparticles with an average particle size of 5-10 nm were observed. The observed images can be considered as a representative of polyoriented, non-specifically structured polycrystalline nanomaterials.



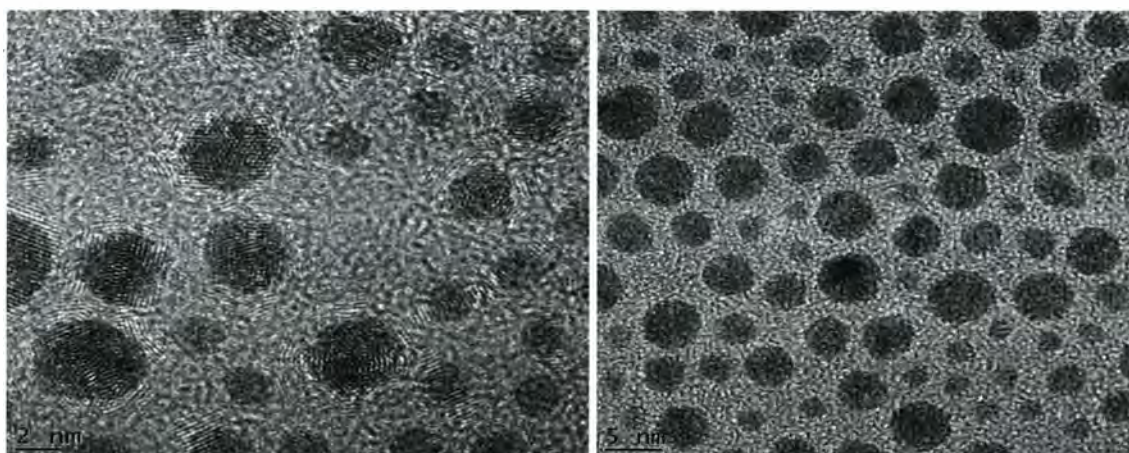


**Fig r. 52: HRTEM images of Pt nanoparticles.**

On the other hand, images of polyacrylate capped nanoparticles prepared through the  $H_2$  reduction method are shown in **Figure 53 A, B, C and D**. Well distributed 5-20 nm nanoparticles throughout the samples were evident with no agglomeration observed and all the nanoparticles showed lattice fringes on their surface indicating that the particles were crystalline. For the Pt(100) nanoparticles, a high amount of cubic shaped nanoparticles which is a characteristic feature of (100) oriented nanoparticles was observed (**Figure 53A**). Pt(100)Pd nanoalloys (**Figure 53B**) showed particles with triangular and cubic shapes while Pt(100)Au nanoalloys (**Figure 53C**) and Pt(100)PdAu nanoalloys (**Figure 53D**) showed well dispersed particles with some cubic shaped particles. The existence of the preferentially cubic shaped nanoparticles in the samples indicated that the nanoalloys had some (100) sites orientation/a significant amount of (100) sites at their surfaces [198]. It can be pointed out that image observation may be misleading and so alternative characterisation techniques are required [29].

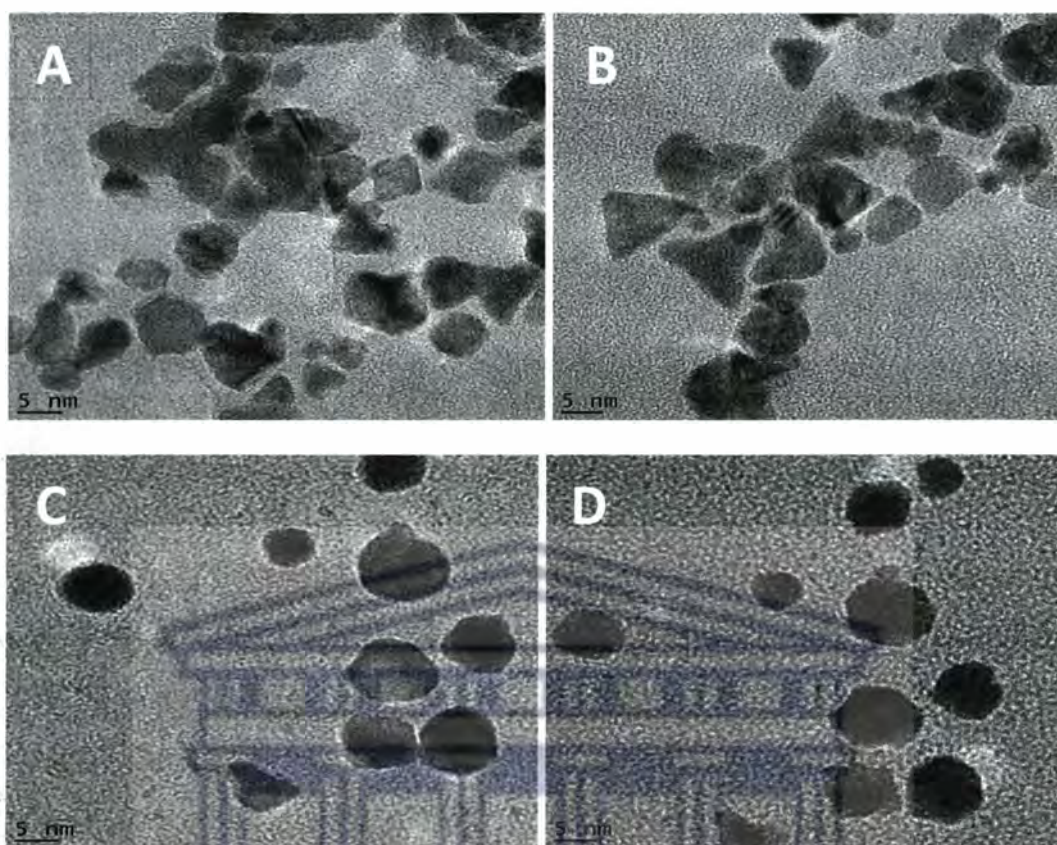


**Figure 53: HRTEM images of Pt(100) nanoparticles (A), Pt(100)Pd nanoalloys (B), Pt(100)Au nanoalloys (C) and Pt(100)PdAu nanoalloys (D).**

The nanoparticles of Pt(100) and Pt(100) based nanoalloys were formed in the presence of sodium polyacrylate (polymer) which acts as a capping material. The presence of the polymer in the colloidal solution of nanoparticles is believed to have mainly two functions. First, it stops the growth of the particles at a small size distribution. Second, it prevents individual colloidal particles from coalescing with each other, thus giving the colloids a higher degree of monodispersity [118]. This can be attributed to the electrostatic repulsion of negatively charged carboxyl groups present in the sodium polyacrylate as shown in **Figures 54 (a) and (b)**.

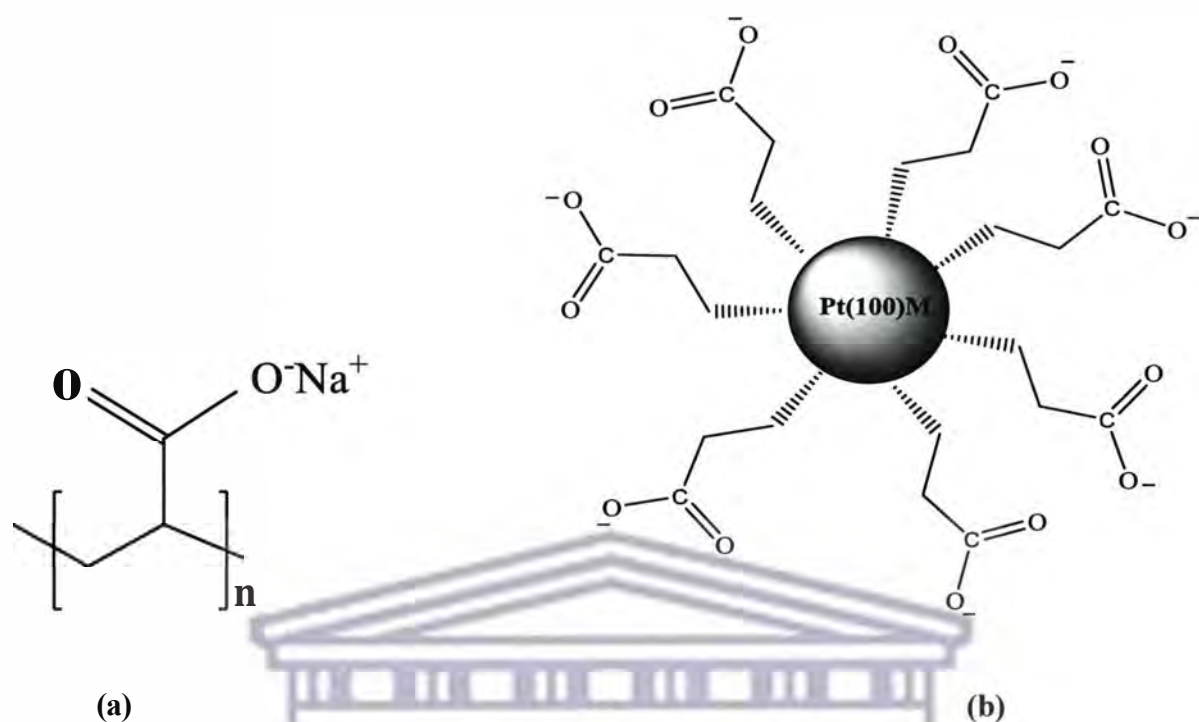


**Figure 54:** Schematic illustration of (a) sodium polyacrylate and (b) sodium polyacrylate-capped nanoparticle/nanoalloy.

### 5.2.3 Energy dispersive X-ray spectroscopy (EDX) analysis

The EDX analysis (**Figure 55 a-d**) revealed the elemental composition of the synthesised nanoparticles. Pt, PtPd, PtAu and PtPdAu elements were present in Pt(100), Pt(100)Pd, Pt(100)Au and Pt(100)PdAu samples respectively. Other elemental signals were also recorded namely; silicon, oxygen and copper. The presence of silicon may have originated from some contamination during sample preparation, the oxygen was due to the presence of polyacrylate in the nanoparticles while copper is as a result of the copper grid onto which the nanoparticles were immobilised for the HRTEM analysis.

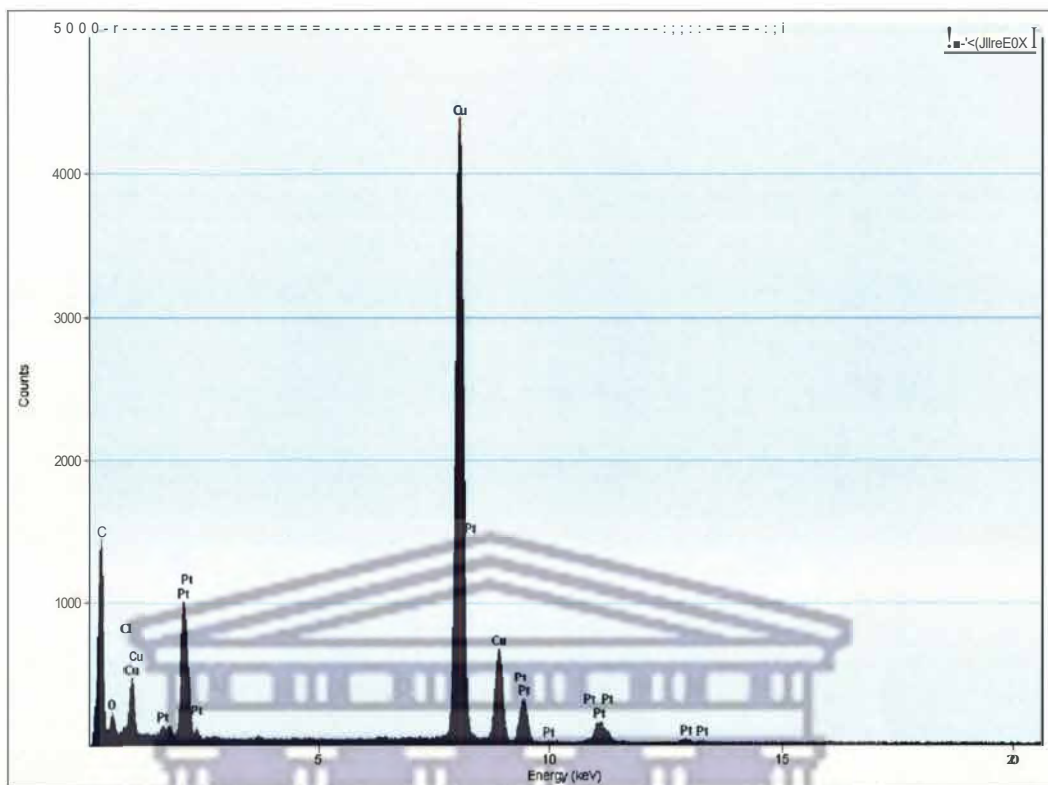


Figure 55a: Energy dispersive X-ray spectrum of Pt(100) nanoparticles.

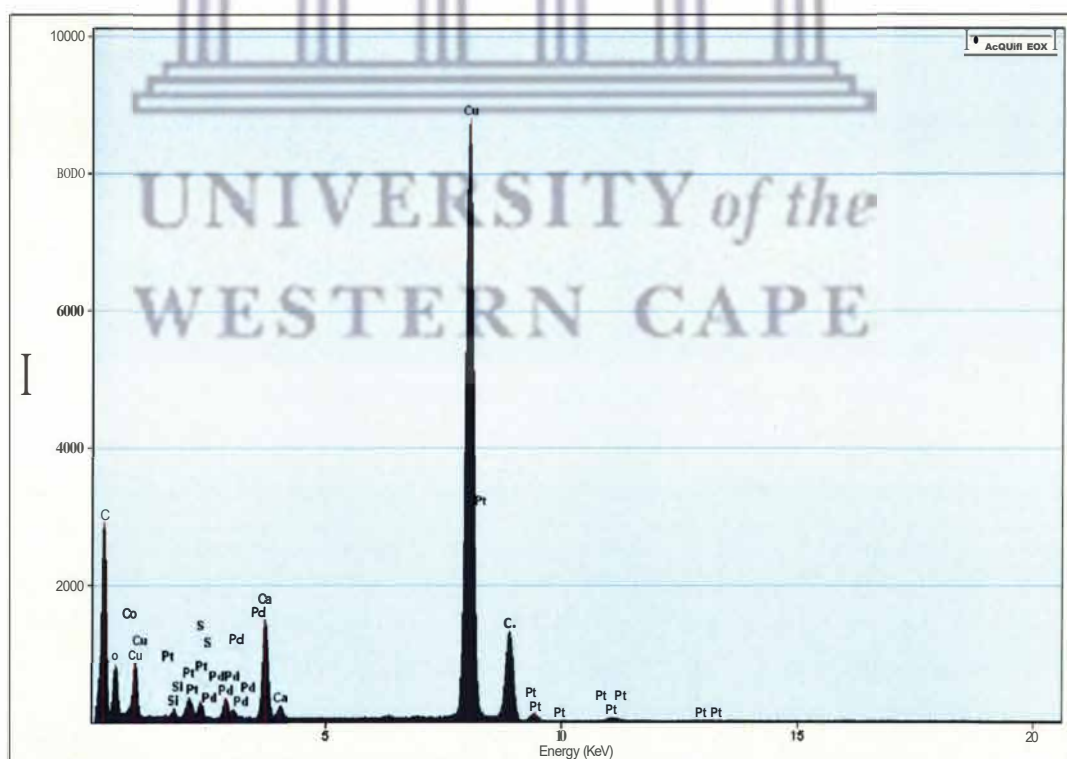


Figure 55b: Energy dispersive X-ray spectrum of Pt(100)Pd nanoalloys.

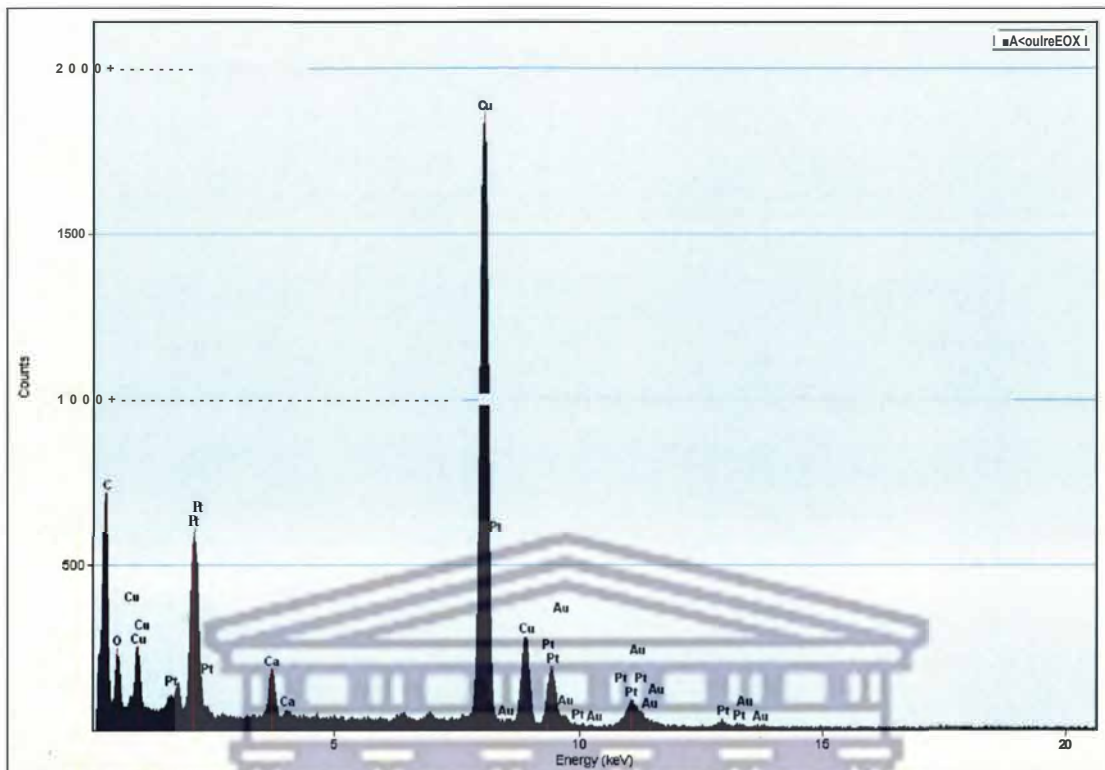


Figure 55c: Energy dispersive X-ray spectrum of Pt(100)Au nanoalloys.

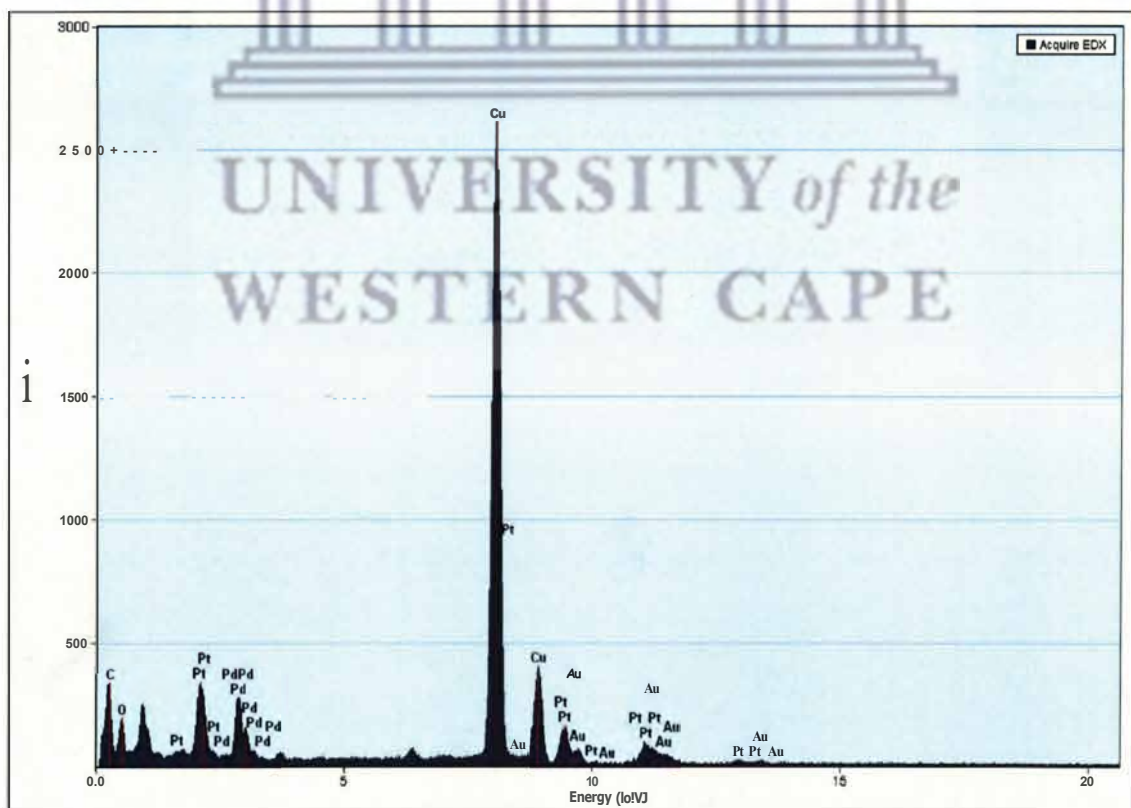


Figure 55d: Energy dispersive X-ray spectrum of Pt(100)PdAu nanoalloys.

### 5.2.4 Atomic force microscopy (AFM)

The AFM images of Pt(100) nanoparticles, Pt(100)Pd nanoalloys, Pt(100)Au nanoalloys and Pt(100)PdAu nanoalloys are shown in **Figures 56** (a), (b), (c) and (d). While it is not easy to determine the exact size of the nanoparticles based on AFM, the average size of the nanoparticles appear to be on the order of a few nanometers. It is however observable that significant size differences occur in the different nanoparticles. This correlates well with the HRTEM results.

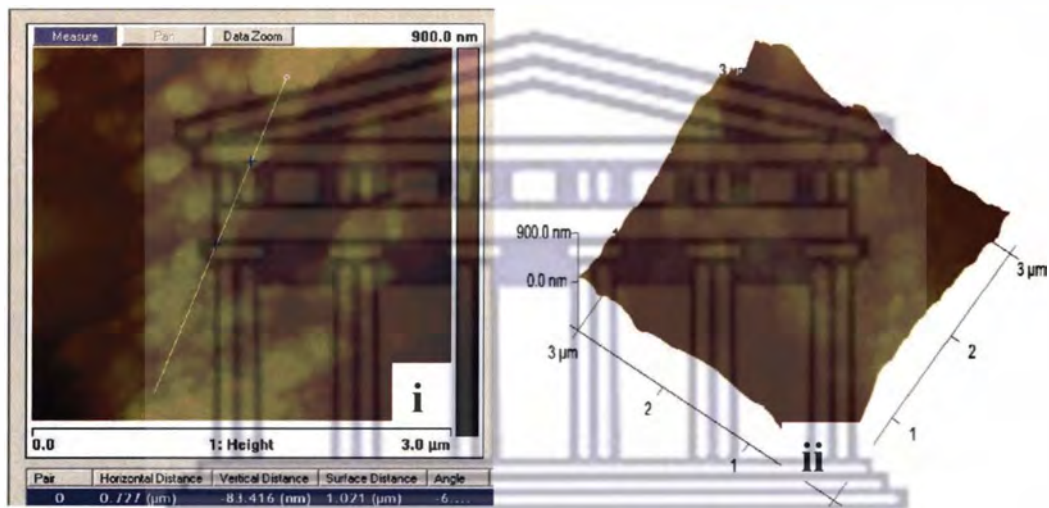


Figure 56a: (i) 2D and (ii) 3D AFM images of Pt(100) nanoparticles.

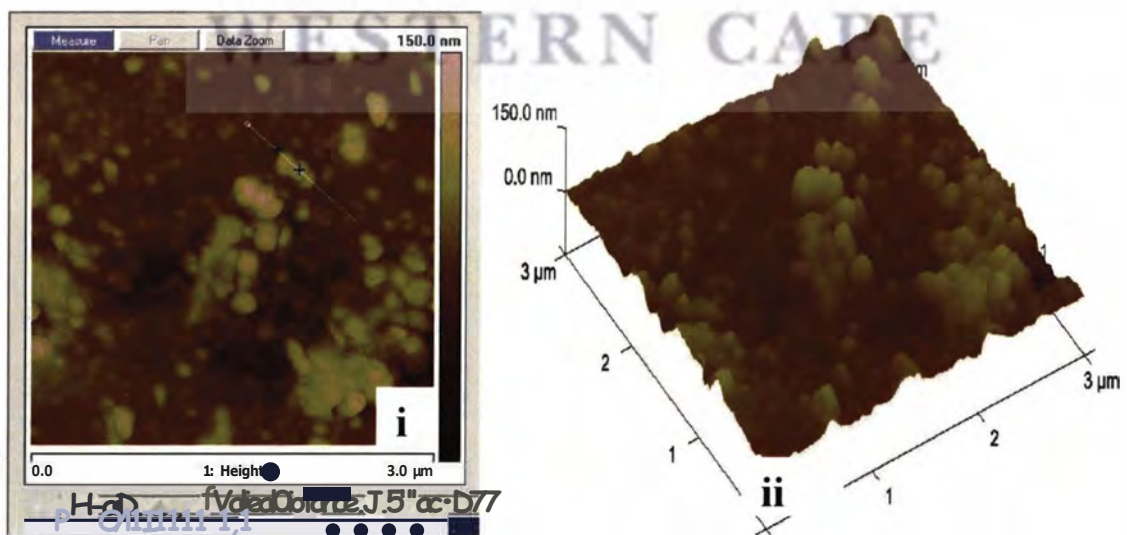


Figure 56b: (i) 2D and (ii) 3D AFM images of Pt(100)Pd nanoalloys.

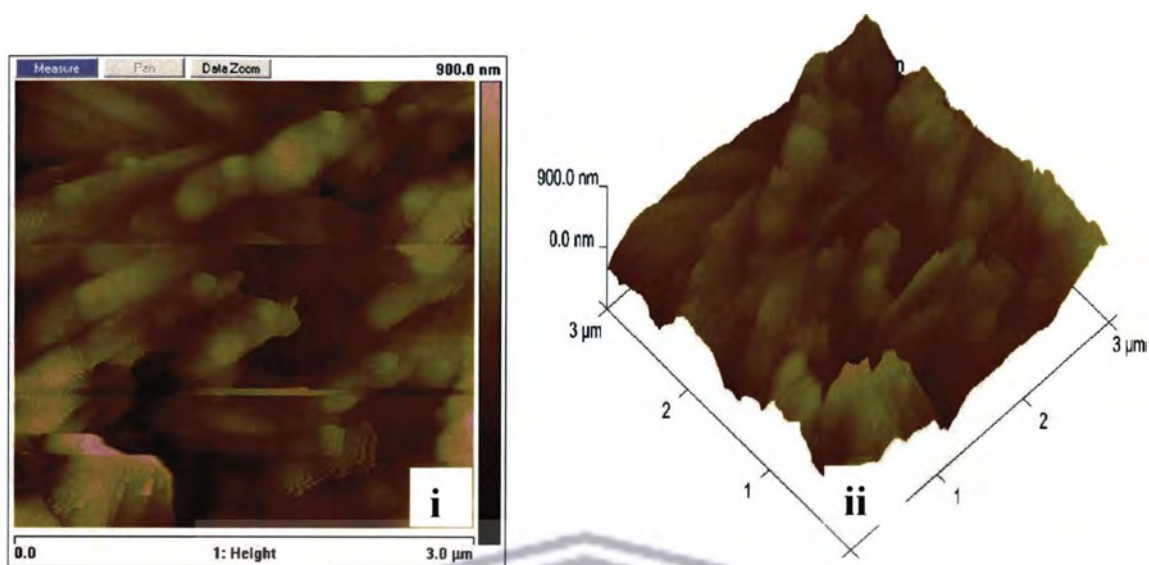


Figure 56c: (i) 2D and (ii) 3D AFM images of Pt(100)Au nanoalloys.

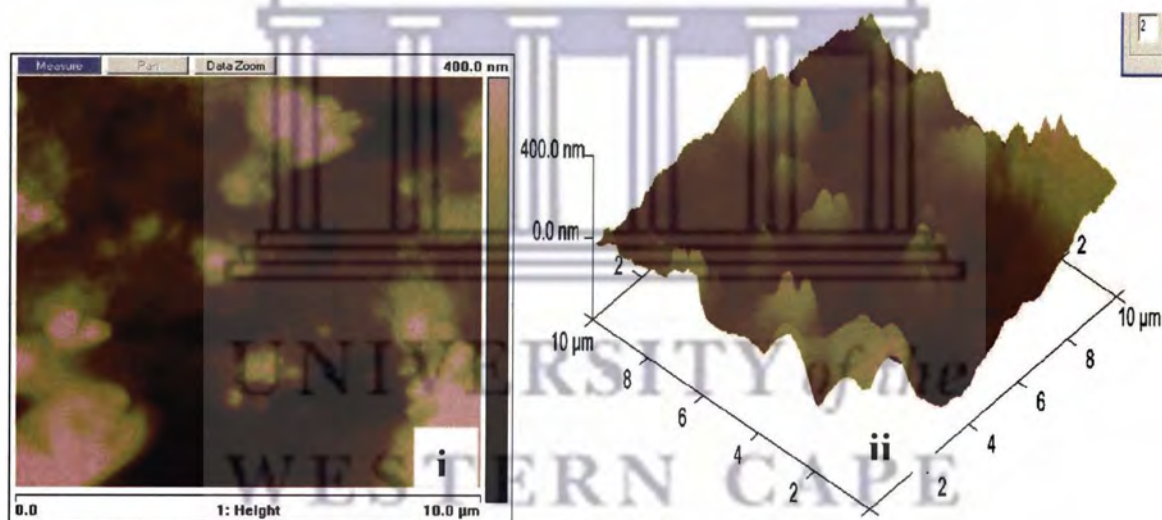


Figure 56d: (i) 2D and (ii) 3D AFM images of Pt(100)PdAu nanoalloys.

### 5.3 Electrochemistry of the starting materials

#### 5.3.1 Electrochemistry of $K_2PtCl_6$ in solution

Figure 57 shows the CV of 5 mM  $K_2PtCl_6$  in 0.1 M  $LiClO_4$  Ar-saturated solution. The CVs were recorded over a potential range of -600 mV to 1000 mV at a scan rate of  $100 \text{ mV s}^{-1}$ . Three redox peaks were observed; peak a,  $E_{p,a} = -334 \text{ mV}$  followed at more positive potentials by peaks b,  $E_{p,a} = -122 \text{ mV}$  and c,  $E_{p,a} = 900 \text{ mV}$ . On the cathodic scan, three reduction peaks were also observed c',  $E_{p,c} = +380 \text{ mV}$ , b',  $E_{p,c} = -315 \text{ mV}$  and a',  $E_{p,c} = -480 \text{ mV}$ . Peaks a and b were attributed to the oxidation of adsorbed and absorbed hydrogen atoms on the surface of platinum, respectively.



At positive potentials,  $Pt^0$  nanoparticles deposited on the Pt surface during the cathodic scanning were oxidised to  $Pt^{4+}$  and formed a platinum oxide layer.



On the cathodic scan, peaks a' and b' are due to the reduction of adsorbed and absorbed hydrogen atoms on the platinum surface. The Pt oxides are reduced on the negative-going scans to Pt metal (peak c').





The peak current increased with increase in scan rate as shown in **Figure 58**. The electrochemistry of PdCh and H<sub>2</sub>AuCl<sub>4</sub> salts were interrogated in **section 4.2**.

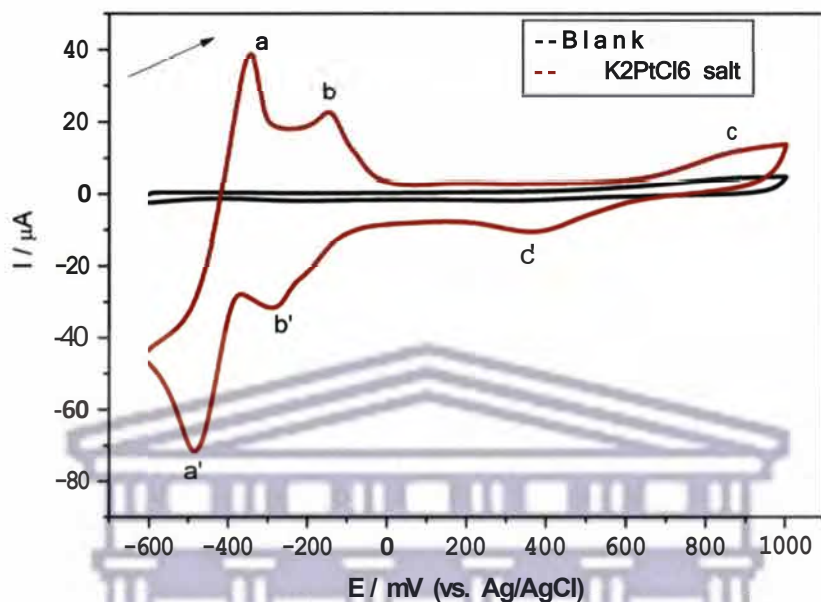


**Figure 57:** Cyclic voltammogram of Pt electrode in 5 mM K<sub>2</sub>PtCl<sub>6</sub> and 0.1 M LiClO<sub>4</sub> solution: Scan rate, 50 mV s<sup>-1</sup>.

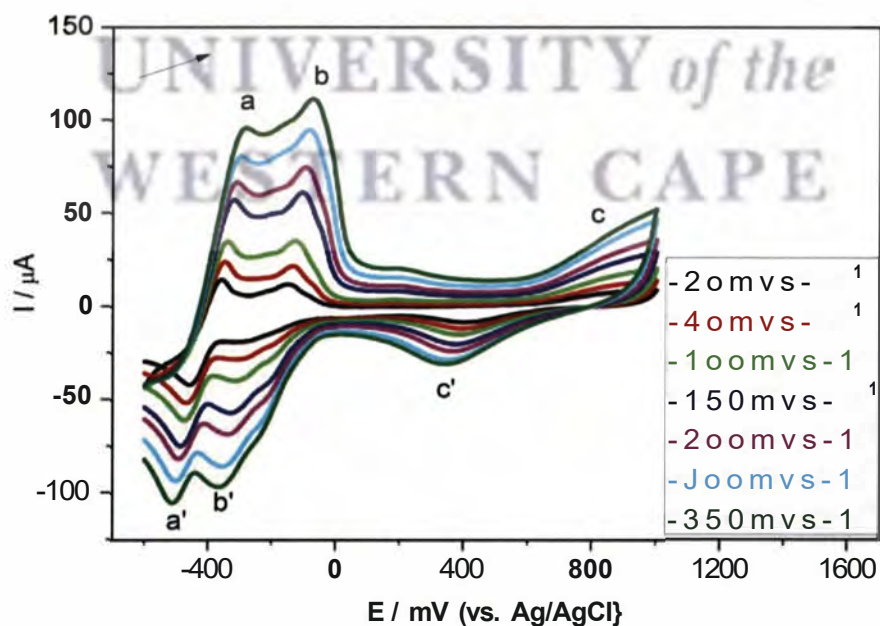


**Figure 58:** Cyclic voltammograms of Pt electrode in 5 mM K<sub>2</sub>PtCl<sub>6</sub> and 0.1 M LiClO<sub>4</sub> solution at different scan rates.

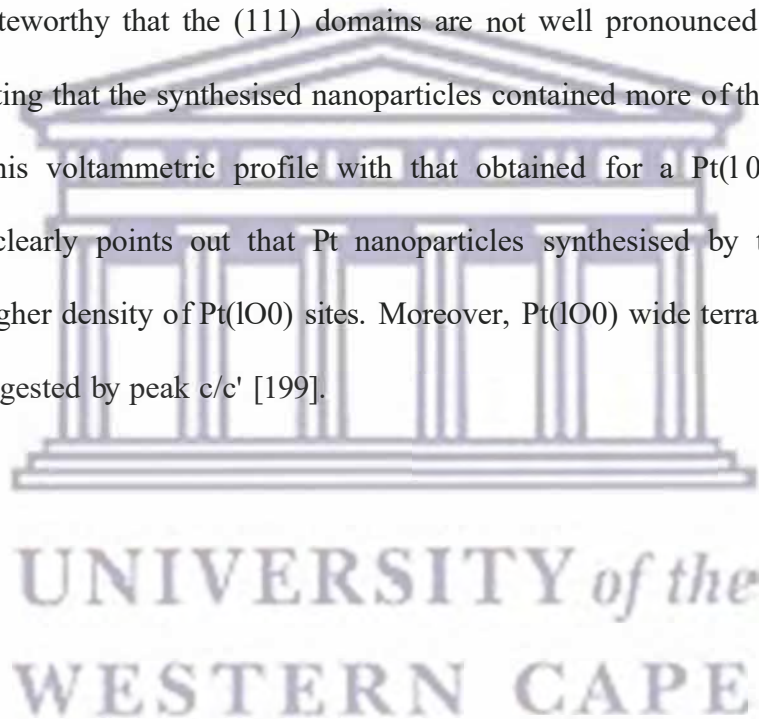
## 5.4 Electrochemistry of Pt(100)Au, Pt(100)Pd and Pt(100)PdAu nanoalloys

### 5.4.1 Cyclic voltammetric behaviour of the oriented nanoalloys

#### 5.4.1.1 Electrochemistry of the nanoalloys in 0.5 M H<sub>2</sub>SO<sub>4</sub> solution

Although HRTEM technique is able to show the size and ex situ shape of nanoparticles, the analysis of a statistically significant number of nanoparticles seems unrealistic and only partial information can be obtained for a given sample of nanoparticles and the real global distribution of surface sites in the nanoparticles cannot coincide with the partial distribution found using HRTEM [119]. In order to characterise in situ the structure of the Pt nanoparticles and nanoalloys, a surface sensitive technique or process has to be used [119]. Electrochemistry provides some surface sensitive reactions that can be used as a tool to characterise the surface structure. In the case of platinum, it is known that the so-called hydrogen adsorption/desorption process is very sensitive to the Pt surface structure [120] and this fact is put in evidence as shown in the voltammetric profiles in **Figure 59**. These profiles correspond to the so-called hydrogen adsorption/desorption. The voltammetric profiles work as a fingerprint for any Pt surface. However in a general way, the direct estimation of different sites present at the surface is not feasible, since it would require too complex deconvolution of the voltammograms. Nevertheless with the help of Pt model surfaces, it is possible to qualitatively characterise each feature of (100) oriented Pt nanoparticles and Pt (100) based nanoalloys in 0.5 M sulphuric acid. **Figure 59(a)** shows a voltammogram characteristic of quasi-spherical Pt nanoparticles prepared in presence of sodium borohydride. The voltammograms look similar to that reported for polycrystalline platinum electrodes [120]. It shows the presence of adsorption states associated with (110) sites (peak a/a') and (100) sites (peak bib') at -107 mV and -34 mV, respectively [29]. Moreover, a poorly resolved shoulder around 50 mV (peak c/c') is apparent, being characteristic of (100) terraces. Similar results were observed by Serrano-Ruiz *et al.* [119].

On the other hand, the voltammograms of oriented Pt(100) nanoparticles (**Figure 59b**) shows very clearly the presence of adsorption states associated with (110) sites (peak a/a') and (100) sites (peak b/b') at -131 mV and -34 mV, respectively. Redox peak b/b' is much sharper and well pronounced for Pt(100) nanoparticles than that observed for the polyoriented Pt nanoparticles characteristic of Pt(100) domains. A well resolved redox peak at around 29 mV (peak c/c') was also observed associated with (100) sites [29, 119]. A poorly defined redox peak around 445 mV (peak d/d') was observed characteristic of small (111) ordered surface domains. It is noteworthy that the (111) domains are not well pronounced compared to the (100) sites indicating that the synthesised nanoparticles contained more of the (100) sites. The comparison of this voltammetric profile with that obtained for a Pt(100) single crystal electrode [121] clearly points out that Pt nanoparticles synthesised by the H<sub>2</sub> reduction method have a higher density of Pt(100) sites. Moreover, Pt(100) wide terraces are present at the surface as suggested by peak c/c' [199].



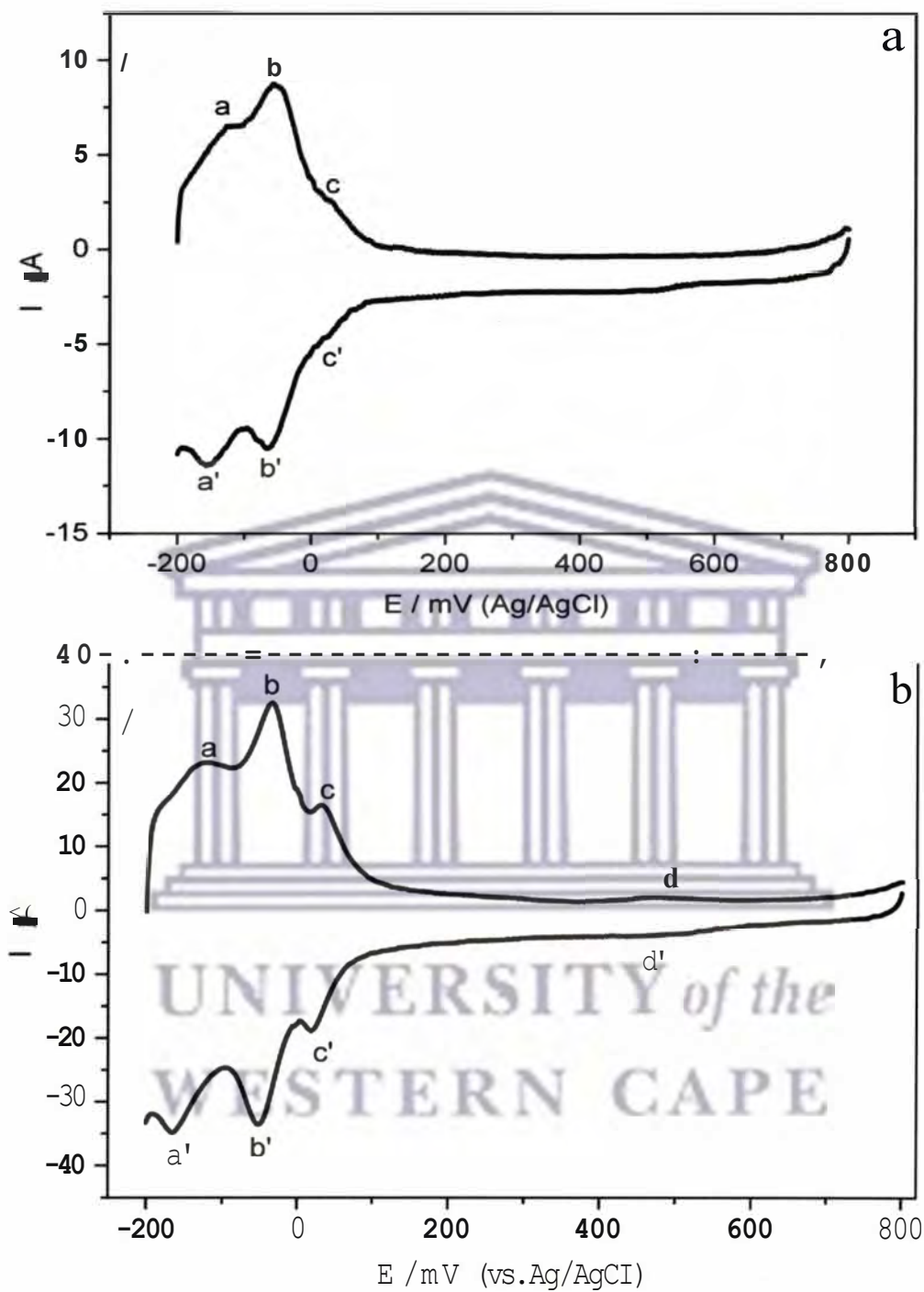


**Figure 59: Cyclic voltammograms of (a) polycrystalline Pt nanoparticles and (b) Pt(100) nanoparticles modified Pt electrode; Test solution, 0.5 M H<sub>2</sub>SO<sub>4</sub>; Scan rate, 20 mV s<sup>-1</sup>.**

The electrochemical behaviour of the Pt(100) nanoparticles in 0.5 M H<sub>2</sub>SO<sub>4</sub> was further interrogated at different scan rates as shown in **Figure 60**. It can be seen that the redox peak currents increased linearly with increase in scan rates (**Figure 61**) indicating that the pair of redox waves originated from the surface confined molecules. The cathodic and anodic peak currents (peak b/b') were linear functions of the scan rate in the range 10 mV s<sup>-1</sup> to 100 mV s<sup>-1</sup> and their linear regressions were  $I_{p,a} = 1.467 \times 10^{-6} \nu + 3.892 \times 10^{-6}$  ( $R^2 = 0.995$ ) and  $I_{p,c} = -1.521 \times 10^{-6} \nu - 3.422 \times 10^{-6}$  ( $R^2 = 0.999$ ). These results indicate that the electron transfer reaction in the sulphuric acid was adsorption controlled. To further verify surface electrochemistry occurring on the Pt(100) nanoparticles, the logarithmic linear relationship between the peak currents and scan rates of peaks b/b' was investigated. The value of the slope of the linear plot of log I<sub>p</sub> versus log  $\nu$  was used to elucidate the nature of the processes influencing the electrochemistry of the surface confined material. The plots of log I<sub>p</sub> versus log  $\nu$  (not shown) gave slopes of 0.97 and 0.96 for the anodic and cathodic peaks, respectively confirming the occurrence of adsorption-controlled electrochemistry.

As discussed in **section 5.2.2**, sodium polyacrylate salt was used as the surface-stabilising agent. This stabilising agent must be completely removed from the surface of the nanoparticles because chemical or electrochemical reactions can only be understood on "clean" surfaces. Obtaining reproducible measurements requires comparison between data on clean surfaces, because "contaminated" surfaces have unknown composition. The level of cleanliness of the Pt surfaces can be readily evaluated by simply visualising the so-called hydrogen adsorption desorption region [200]. Thus, the peak position, sharpness, and the reversibility of the adsorption states in the so-called hydrogen adsorption region can be employed as probes to estimate the surface cleanliness of the Pt(100) nanoparticles, an imperative prerequisite for a correct surface characterisation and further electrocatalytic

evaluation. As shown in **Figure 60**, the adsorption peaks were found to be reversible and sharp, denoting that the nanoparticles were well cleaned and ready for electrocatalytic applications.

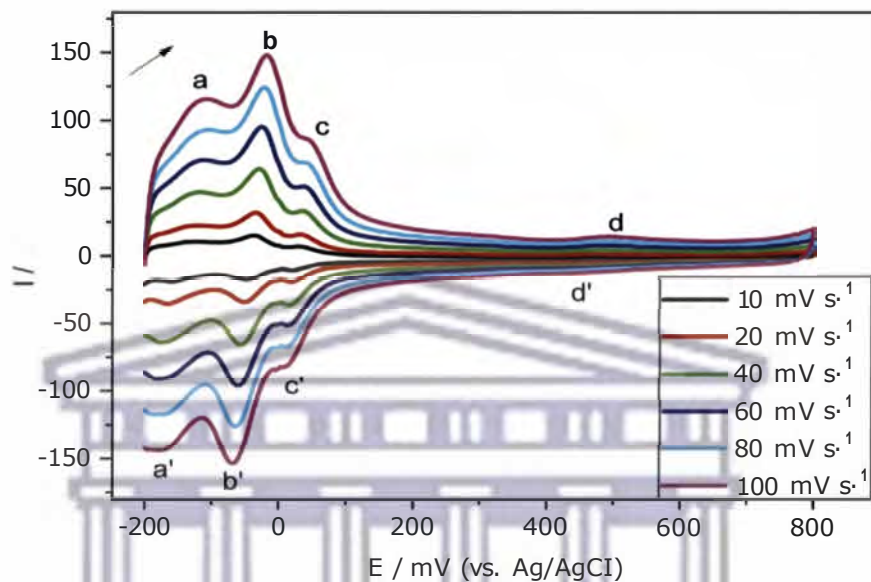


Figure 60: Cyclic voltammograms of Pt(100) nanoparticles modified Pt electrode at different scan rates; Test solution: 0.5 M H<sub>2</sub>SO<sub>4</sub>.

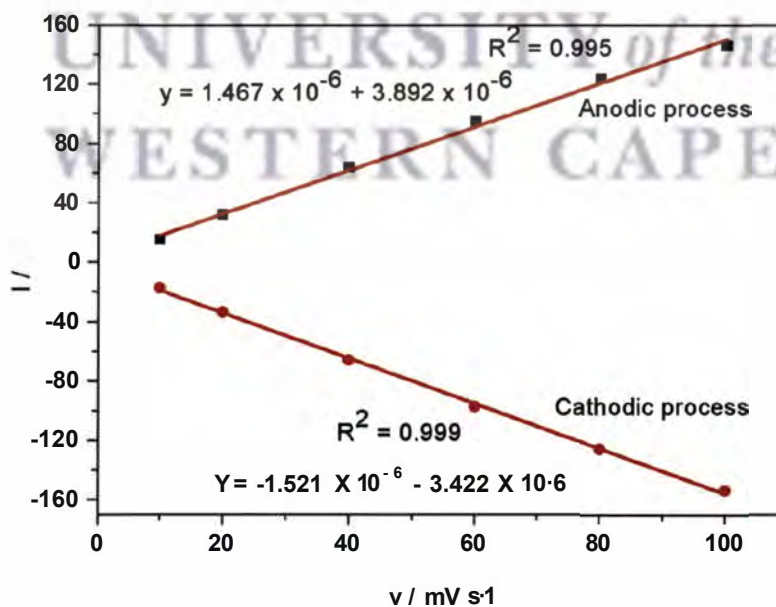
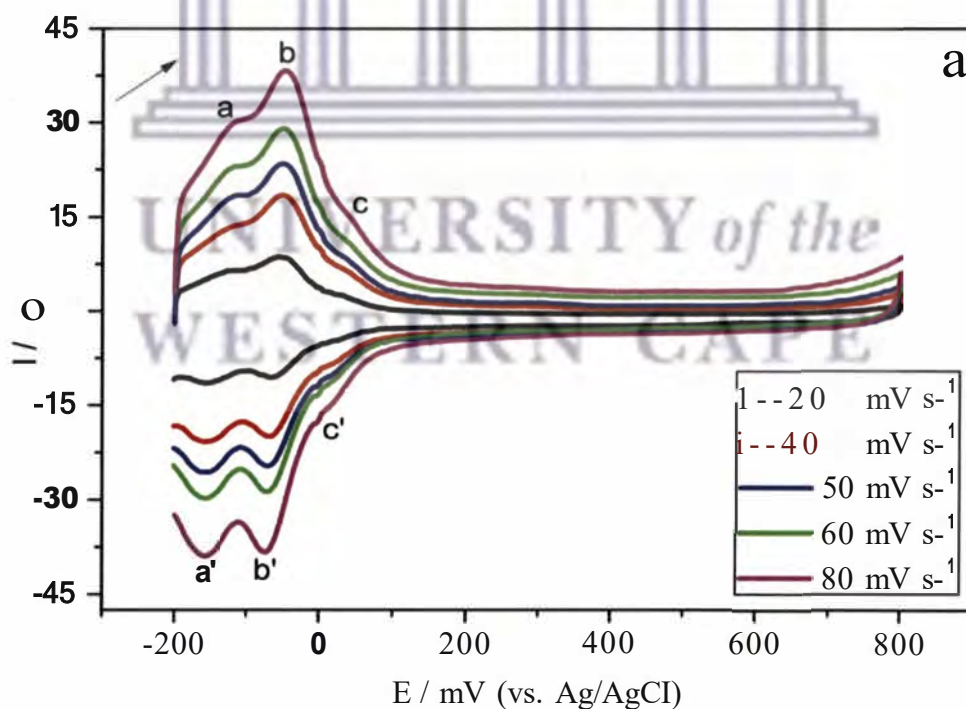
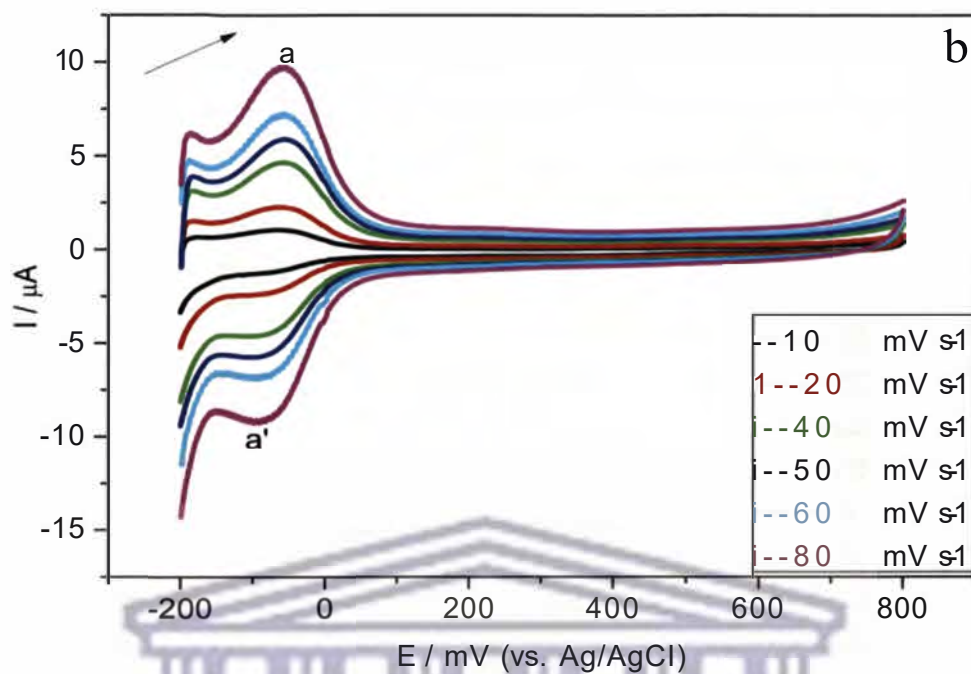


Figure 61: Relationship between the peak currents and scan rates for Pt(100) nanoparticles modified Pt electrode (peak b/b').

Pt(100)Pd nanoalloys (**Figure 62b**) showed a shoulder at 190 mV and a well-defined redox peak at -67 mV (peak a/a') for the (110) and (100) sites, respectively. However, it can be observed that the Pd in the alloy blocked some of the (100) terraces as indicated by the absence of the peak that was observed at 29 mV (see **Figure 59b** above). Similar results were obtained by Serrano-Ruiz [119] where the (100) terraces were blocked by Bi and Ge adatoms. However, Au was found to be moderately insensitive to the presence of Pt(100) surface sites as shown in **Figure 62a**. It is noteworthy that PdAu alloyed with Pt(100) was found to be sensitive to the Pt(100) sites and blocked some of the (100) terraces (**Figure 63**). A reduction peak (peak b) was observed denoting the reduction of the oxides formed in the anodic scan. In this experiment, 0.5 M H<sub>2</sub>SO<sub>4</sub> solution was used as the test solution.





**Figure 62:** Cyclic voltammograms of (a) Pt(100)Au nanoalloys and (b) Pt(100)Pd nanoalloys modified Pt electrode at different scan rates; Test solution: 0.5 M H<sub>2</sub>SO<sub>4</sub>.

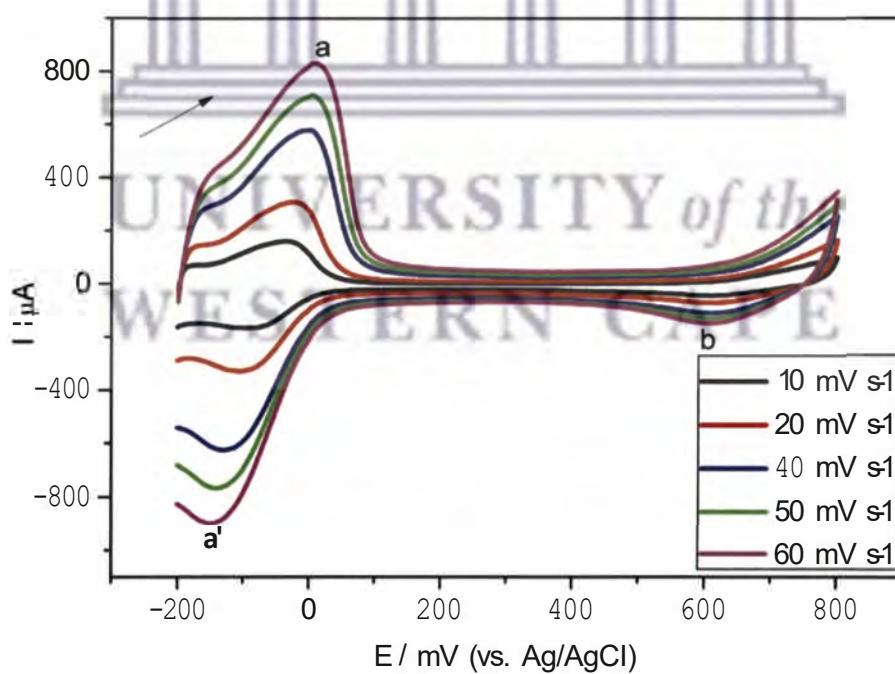


**Figure 63:** Cyclic voltammograms of Pt(100)PdAu nanoalloys modified Pt electrode at different scan rates; Test solution: 0.5 M H<sub>2</sub>SO<sub>4</sub>.



#### 5.4.1.1.1 Determination of the electrochemical active surface area (ESA)

The determination of the active area of electrocatalysts is essential, first of all, to compare the performance of the different electrocatalysts and, second, to prove any enhancement in their performance. Traditionally, the determination of the active area of platinum has been assessed using the charge measured under the adsorption states at low potentials (the so-called hydrogen adsorption region) for an electrode of known active area [200]. A reference value for the charge density for this region is obtained, and this value can be used to determine the active area of any electrode whose area cannot be measured directly by physical methods. The active surface areas (ESA) of Pt(100)nanoparticles and Pt(100) based nanoalloys were determined by the charge involved in the so-called hydrogen UPD region assuming  $0.21 \text{ mC cm}^{-2}$  (in sulphuric acid solutions) for the total charge after the subtraction of the double layer charging contribution [201]. ESA was estimated from the CVs according to the following equation [202-203].

$$ESA = \frac{Q_H}{Q} \quad (51)$$

Where  $Q_H$  is the charge for the hydrogen adsorption (mC) and  $Q$  is the specific charge for a monolayer of hydrogen on Pt ( $0.21 \text{ mC cm}^{-2}$ ) [202]. **Table 3** shows the calculated ESA values of the Pt(100) nanoparticles and Pt(100) based nanoalloys. The results show that the Pt(100) nanoparticles have higher ESA than the nanoalloys. This plays part in increasing the electrocatalytic activity of the nanoparticles.

**Table 3: Active surface area values for the different nanoparticles.**

Catalyst	ESA (cm <sup>2</sup> )
Pt(100) nanoparticles	12.6926
Pt(100)Au nanoalloys	8.8550
Pt(100)Pd nanoalloys	8.2239
Pt(100)PdAu nanoalloys	7.4217
Pt nanoparticles	0.0099

#### 5.4.1.2 Electrochemistry of the nanoalloys in 1 M KOH solution

As discussed in chapter 4, ammonia oxidation takes place effectively in alkaline medium. It is thus of interest to interrogate the behaviour of the nanoparticles in alkaline medium. Figure 64 shows a series of cyclic voltammograms of the bare Pt electrode and those of the Pt electrode modified with the synthesised nanoparticles and nanoalloys. These were measured in 1 M KOH at a scan rate of 100 mV s<sup>-1</sup> in the potential range of -1000 mV to 600 mV. The bare Pt electrode showed typical potential ranges for the hydrogen adsorption/desorption (-1000 mV to -600 mV), double layer potential range (-600 mV to 0 mV Ag/AgCl) and the formation/reduction of the surface Pt oxide, Pt-OH<sub>ads</sub> (0 to 600 mV)(Ag/AgCl). For the Pt(100) nanoparticles modified Pt electrode (denoted as Pt|Pt(100)NPs), the Pt<sup>0</sup> nanoparticles on the Pt electrode surface were oxidised and formed a platinum oxide layer (Figure 64A, peak c, E<sub>p,a</sub> = -300 mV). On the cathodic CV scan, a reduction peak (Figure 64A, peak c', E<sub>p,c</sub> = -450 mV) occurred corresponding to the reduction of the Pt oxide layer. The appearance of an anodic peaks (Figure 64A, peak a, E<sub>p,a</sub> = -800 mV and peak b, E<sub>p,a</sub> = -750 mV) and a cathodic peak (Figure 64A, peak b', E<sub>p,c</sub> = -800 mV) is attributed to the desorption and adsorption of hydrogen atoms adsorbed and absorbed

onto the Pt<sup>0</sup> nanoparticles, respectively. The nanoalloys modified Pt electrodes showed a similar behaviour (Figures 64B, C and D).

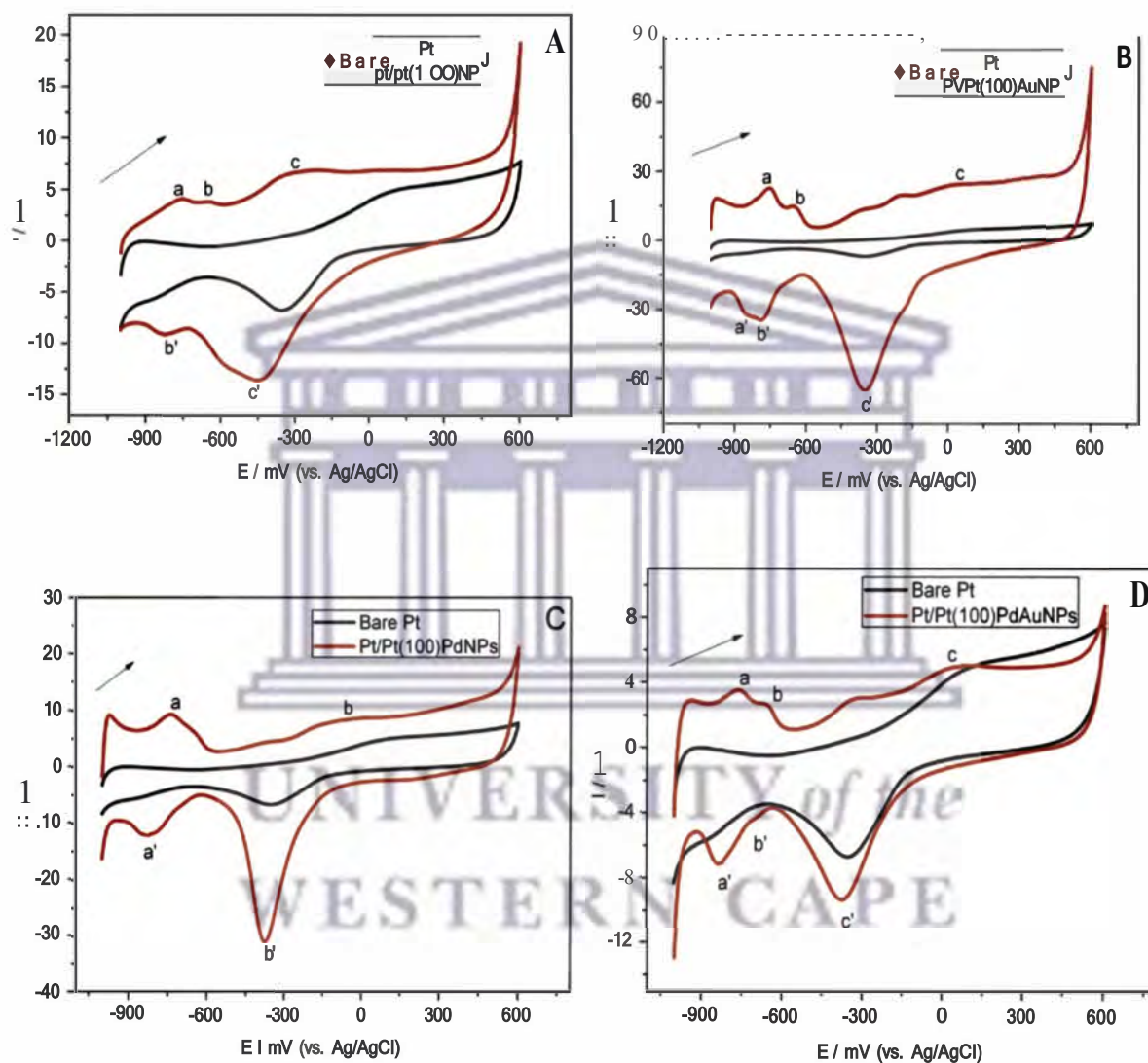


**Figure 64:** Cyclic voltammograms of Pt/Pt(100)NPs (A), Pt/Pt(100)AuNPs (B), Pt/Pt(100)PdNPs (C), Pt/Pt(100)PdAuNPs (D) in 1 M KOH: Scan rate, 100 mV s<sup>-1</sup>.

### 5.4.2 Impedimetric characteristics of the oriented nanoalloys in 1 M KOH solution

The resistance to charge transfer of the oriented Pt(100) nanoparticles and the Pt(100) based nanoalloys was monitored by electrochemical impedance spectroscopy (EIS), which is an effective method for probing the features of the surface of modified electrodes. The Nyquist plot of impedance spectra includes a semicircle portion and a linear portion, with the former at higher frequencies corresponding to the electron transfer process and the latter at lower frequencies corresponding to the diffusion process. The charge transfer resistance ( $R_{ct}$ ) at the electrode surface is equal to the semicircle diameter, which can be used to describe the interface properties of the electrode [204].

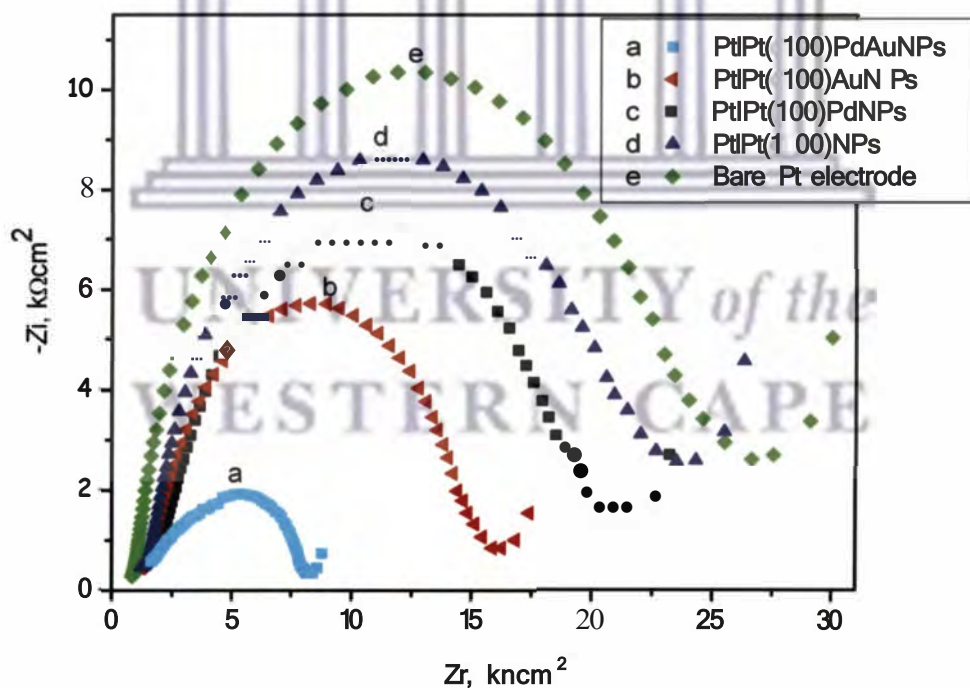
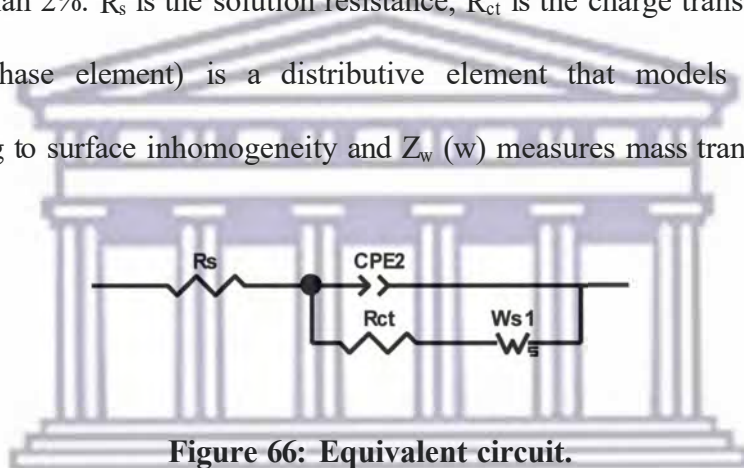


Figure 65: Nyquist plots of bare Pt electrode, Pt/Pt(100)NPs, Pt/Pt(100)PdNPs, Pt/Pt(100)AuNPs and Pt/Pt(100)PdAuNPs in 1 M KOH.

From **Figure 65** the charge transfer resistance ( $R_{ct}$ ) of Pt/Pt(100)PdAuNPs was the lowest ( $R_{ct} = 2.3954 \times 10^5 \text{ } \Omega$ ) compared to that of Pt/Pt(100)AuNPs ( $5.4205 \times 10^5 \text{ } \Omega$ ), Pt/Pt(100)PdNPs ( $5.7348 \times 10^5 \text{ } \Omega$ ), Pt/Pt(100)NPs ( $1.8905 \times 10^6 \text{ } \Omega$ ) and the bare Pt electrode ( $1.0982 \times 10^7 \text{ } \Omega$ ) indicating that the Pt(100)PdAu nanoalloy have good conductivity and played an important role in accelerating the transfer of electrons. This can be attributed to the increased catalytic and improved conductivity properties portrayed by nanoalloys. The impedance parameters (**table 4**) were obtained by fitting using an equivalent circuit (**Figure 66**) and the fitting errors were less than 2%.  $R_s$  is the solution resistance,  $R_{ct}$  is the charge transfer resistance, and CPE (constant phase element) is a distributive element that models the double layer capacitance owing to surface inhomogeneity and  $Z_w$  ( $\omega$ ) measures mass transport.



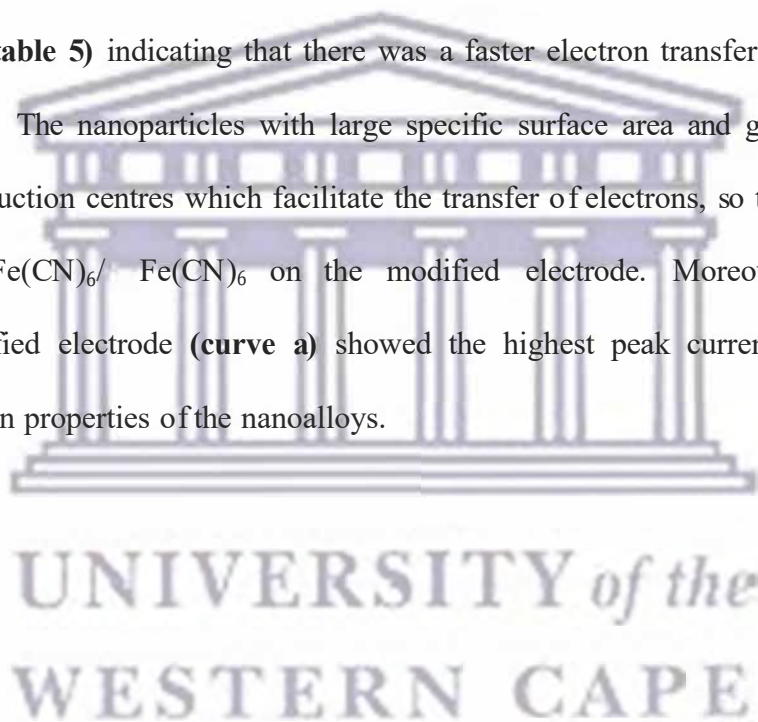
**Figure 66: Equivalent circuit.**

**Table 4: EIS parameters of Pt(100) and Pt(100) nanoalloys in 1 M KOH (data obtained from the circuit fitting of Figure 65).**

Circuit element	$R_s$ (Q)	$R_{ct}$ (O)	CPE (nF)	$Z_w$ (k Q s <sup>1/2</sup> )
Bare Pt electrode	7.6820	<b>1.0982</b> x 10 <sup>7</sup>	0.7212	0.5349
Pt/Pt(100)NPs	83.3600	<b>1.8905</b> x 10 <sup>6</sup>	0.9019	0.8999
Pt/Pt(100)PdNPs	100.2000	<b>5.7348</b> x 10 <sup>5</sup>	0.9105	0.4091
Pt/Pt(100)AuNPs	97.2800	5.4205 x 10 <sup>5</sup>	0.9547	1.2150
Pt/Pt(100)PdAuNPs	117.4000	2.3954 x 10 <sup>5</sup>	0.9533	0.8510

### 5.4.3 Electrochemistry of the oriented nanoalloys in $[\text{Fe}(\text{CN})_6]^{3-}$ .

Cyclic voltammetry of the ferricyanide system is a convenient and valuable tool to monitor the electrochemical characteristics of the surface of modified electrodes. CVs at the bare and the different nanoparticles modified electrodes in 5 mM  $\text{K}_3\text{Fe}(\text{CN})_6 / \text{Fe}(\text{CN})_6$  containing aq. KCl (0.1 M) were shown in **Figure 67**. Nanoalloys are known to portray higher catalytic and conduction properties compared to monometallic nanoparticles. From **Figure 67**, the nanoparticles modified electrode showed higher peak currents and lower peak to peak separations (see **table 5**) indicating that there was a faster electron transfer compared to the bare Pt electrode. The nanoparticles with large specific surface area and good conductivity could act as conduction centres which facilitate the transfer of electrons, so they accumulated much more  $\text{K}_3\text{Fe}(\text{CN})_6 / \text{Fe}(\text{CN})_6$  on the modified electrode. Moreover, the ternary nanoalloys modified electrode (**curve a**) showed the highest peak current portraying the highest conduction properties of the nanoalloys.



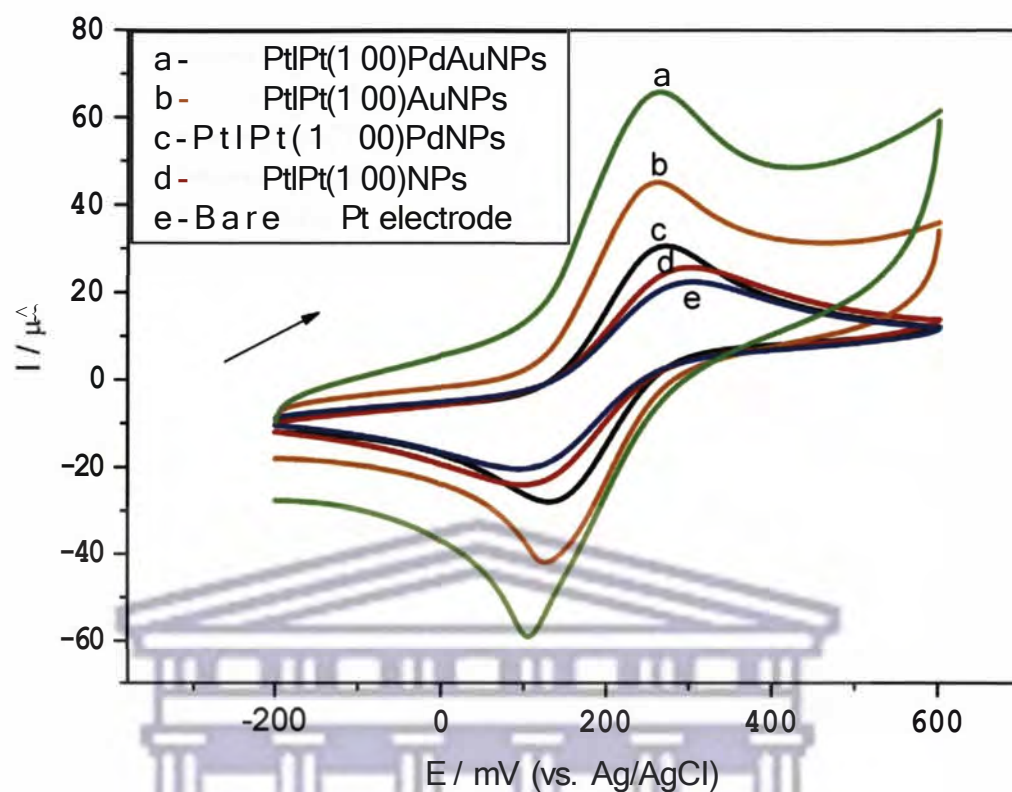
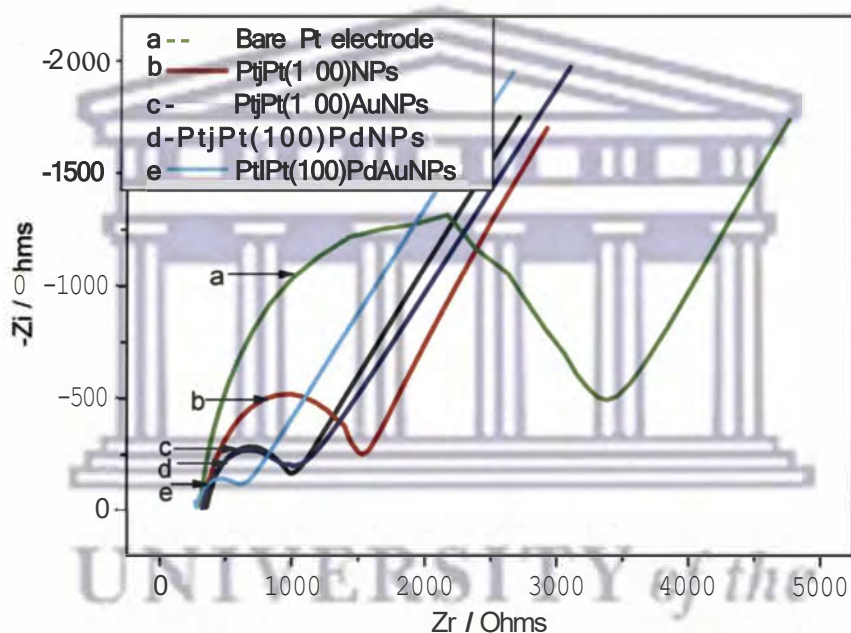


Figure 67: Cyclic voltammograms of Pt|Pt(100)PdAuNPs (curve a), Pt|Pt(100)AuNPs (curve b), Pt|Pt(100)PdNPs (curve c), Pt|Pt(100)NPs (curve d) and bare Pt electrode (curve e) in 5 mM  $K_3Fe(CN)_6$  1K $_4Fe(CN)_6$  solution: Scan rate, 100 mV s<sup>-1</sup>.

Table 5: CV peak parameters of Pt(100) and Pt(100) nanoalloy systems in  $[Fe(CN)_6]^{3-}$  (data obtained from Figure 67).

Electrode	$E_{p,a}$ (mV)	$E_{p,c}$ (mV)	$I_{p,a}$ (A)	$I_{p,c}$ (A)	$M_p$ (mV)
Bare Pt	294	106	$2.224 \times 10^{-5}$	$-1.997 \times 10^{-5}$	188
Pt(100)NPs	286	112	$2.602 \times 10^{-5}$	$-2.357 \times 10^{-5}$	174
Pt(100)PdNPs	264	131	$3.072 \times 10^{-5}$	$-2.813 \times 10^{-5}$	133
Pt(100)AuNPs	257	124	$4.559 \times 10^{-5}$	$-4.226 \times 10^{-5}$	133
Pt(100)PdAuNPs	262	104	$6.664 \times 10^{-5}$	$-5.942 \times 10^{-5}$	158

Electrochemical impedance spectra (EIS) measurements were performed in KCl (0.1 M) solutions containing  $[\text{Fe}(\text{CN})_6]^{3-}$  and plotted in the form of complex plane diagrams (Nyquist plots) with a frequency range of 100 kHz to 0.1 Hz. The amplitude of the applied sine wave potential was 10 mV, whereas the ambient applied potentials were set at the formal potentials which were obtained from the CV experiments of the  $[\text{Fe}(\text{CN})_6]^{3-}$  redox probe.



**Figure 68:** EIS Nyquist plots of bare Pt electrode (curve a), Pt/Pt(100)NPs (curve b), Pt/Pt(100)AuNPs (curve c), Pt/Pt(100)PdNPs (curve d), and Pt/Pt(100)PdAuNPs (curve e) in the presence of  $[\text{Fe}(\text{CN})_6]^{3-}$  redox system.

From **Figure 68**, significant difference of the charge transfer resistances ( $R_{ct}$ s) was observed upon the formation of the modified electrodes. The  $R_{ct}$  value for the bare Pt electrode (curve a) was  $2.899 \times 10^3 \Omega$ . After the Pt(100)NPs were deposited on the electrode, the  $R_{ct}$  value was found to be  $1.105 \times 10^3 \Omega$  (curve b). As compared to bare Pt electrode (curve a), the  $R_{ct}$  of Pt/Pt(100)NPs (curve b) decreased. This can be attributed to the presence of the



nanoparticles with high surface area and conduction properties thus lowering the resistance to charge transfer. After the bare Pt electrode was modified with Pt|Pt(100)PdNPs, the  $R_{ct}$  value ( $6.588 \times 10^2 \text{ Q}$ ) decreased obviously (curve d) implying that the Pt(100)PdNPs played an important role in accelerating the transfer of electrons. Similar results were observed when Pt(100)AuNPs were used. For the Pt|Pt(100)PdAuNPs, the  $R_{ct}$  value ( $3.66 \times 10^2 \text{ Q}$ ) decreased further (curve e) an indicator that the ternary nanoalloys was more facile to the electron transfer. This agrees well with the results presented in **Figures 65 and 67**. **Table 6** shows the EIS data.

**Table 6: EIS parameters of Pt(100) and Pt(100) nanoalloy systems in  $[\text{Fe}(\text{CN})_6]^{3-}$ . (data obtained from Figure 68).**

Electrode	$R_s$ (Ohms)	$R_{ct}$ (KOhms)	CPE (nF)	$Z_w$ (KDW)	f(Hz)
Bare Pt	303.5	2.899	523.7	1.961	84.98
Pt Pt(100)NPs	332.5	1.105	565.9	1.954	211.62
Pt Pt(100)PdNPs	330.9	0.658	673.6	2.244	333.94
Pt Pt(100)AuNPs	359.0	0.590	632.7	2.015	419.49
Pt Pt(100)PdAuNPs	271.6	0.366	582.0	2.243	831.53

From  $\omega_{max}$  (frequency at maximum imaginary impedance of the semicircle), useful kinetic parameters of  $\text{Fe}(\text{CN})_6^{3-} / \text{Fe}(\text{CN})_6^{4-} + e^-$  electron transfer such as time constant (cycle life)  $\tau$ , exchange current  $i_0$ , and heterogeneous rate constant  $k$  were calculated from **equations (52, 53, 54 and 55)** and shown in **table 7**.

$$\omega_{\max} = \frac{1}{R_{\text{ct}} C_{\text{dl}}} \quad (52)$$

$$\tau = R_{\text{ct}} C_{\text{dl}} \quad (53)$$

$$I_0 = \frac{RT}{nFR_{\text{ct}}} \quad (54)$$

$$k = \frac{I_0}{nFAC_0} \quad (55)$$

Where  $\omega_{\max} = 2\pi f$ ,  $C_{\text{dl}}$  is the double layer capacitance,  $R = 8.314 \text{ J K}^{-1} \text{ mol}^{-1}$ ,  $F = 96486 \text{ C mol}^{-1}$ ,  $n = 1$ ,  $C_0$  is the concentration of  $[\text{Fe}(\text{CN})_6]^{3-14-} = 5 \times 10^{-6} \text{ mol cm}^{-3}$ . The maximum frequency values ( $f$ ) were taken from **Figure 68**.

**Table 7: Effect of nanoparticles modified Pt electrode on the kinetics of  $[\text{Fe}(\text{CN})_6]^{3-14-}$ .**

Electrode	Bare	Pt(100)	Pt(100)Pd	Pt(100)Au	Pt(100)PdAu
$\omega_{\max} \text{ (rad s}^{-1}\text{)}$	534.05	1329.82	2098.48	2636.08	5225.33
$\tau \text{ (s rad}^{-1}\text{)}$	$1.872 \times 10^{-3}$	$7.500 \times 10^{-4}$	$4.765 \times 10^{-4}$	$3.794 \times 10^{-4}$	$1.914 \times 10^{-4}$
$I_0 \text{ (A)}$	$8.857 \times 10^{-6}$	$2.324 \times 10^{-5}$	$3.898 \times 10^{-5}$	$4.351 \times 10^{-5}$	$7.019 \times 10^{-5}$
$k \text{ (cm s}^{-1}\text{)}$	$9.134 \times 10^{-4}$	$2.396 \times 10^{-3}$	$4.02 \times 10^{-3}$	$4.486 \times 10^{-3}$	$7.235 \times 10^{-3}$

From **table 7**,  $I_0$  values for the electron transfer reaction of  $[\text{Fe}(\text{CN})_6]^{3-14-}$  on bare Pt and nanoparticles increases with Pt(100)PdAuNPs having the highest exchange current. A higher exchange current indicated an increase in the rate of electron transfer which was observed on

the nanoalloys modified electrodes. This increase in electron transfer (increase in reaction rate) can be attributed to the catalytic effect of the nanoparticles.

## 5.5 Catalytic performance of Pt(100)Au, Pt(100)Pd and Pt(100)PdAu nanoalloys

### 5.5.1 Electrocatalytic oxidation of ammonia

As can be seen from the voltammetric profiles of the nanoparticles, Pt(100)PdAu nanoalloys showed the lowest amount of Pt(100) sites as well as the lowest electroactive surface area (ESA) thus gave the lowest ammonia oxidation current while Pt(100)Pd and Pt(100)Au nanoalloys showed a higher current due to the increased Pt(100) sites and ESA. A significant enhancement on the ammonia oxidation current (at around -292 mV) was obtained when the preferential colloidal Pt(100) nanoparticles were employed. These voltammograms clearly points out that ammonia oxidation reaction is strongly influenced by the density of (100) sites on the nanoparticles (**Figures 69-70**). The Pt(100) nanoparticles showed a higher current density compared to the polycrystalline Pt nanoparticles (**Figure 71**). This can be attributed to the (100) sites which favoured ammonia oxidation. **Figure 72** shows an overlay of the bare Pt electrode and the nanoparticles modified Pt electrode towards the ammonia oxidation. Oxidation of ammonia starts at a lower potential on the Pt(100)NPs and has the highest peak currents (see **table 8**) denoting the effect of (100) sites on ammonia oxidation. This can also be explained by the increased ESA as explained in section 5.4.1.1.1. It is noteworthy that the introduction of Pd and Au adatoms into the Pt(100) systems to form nanoalloys showed better catalytic properties compared to the bare Pt electrode. This is attributed to the high catalytic properties attached to nanoparticles and nanoalloys. The Pd and Au adatoms may have lowered the density of the (100) sites in the nanoalloys thus lowering their catalytic properties towards ammonia oxidation.

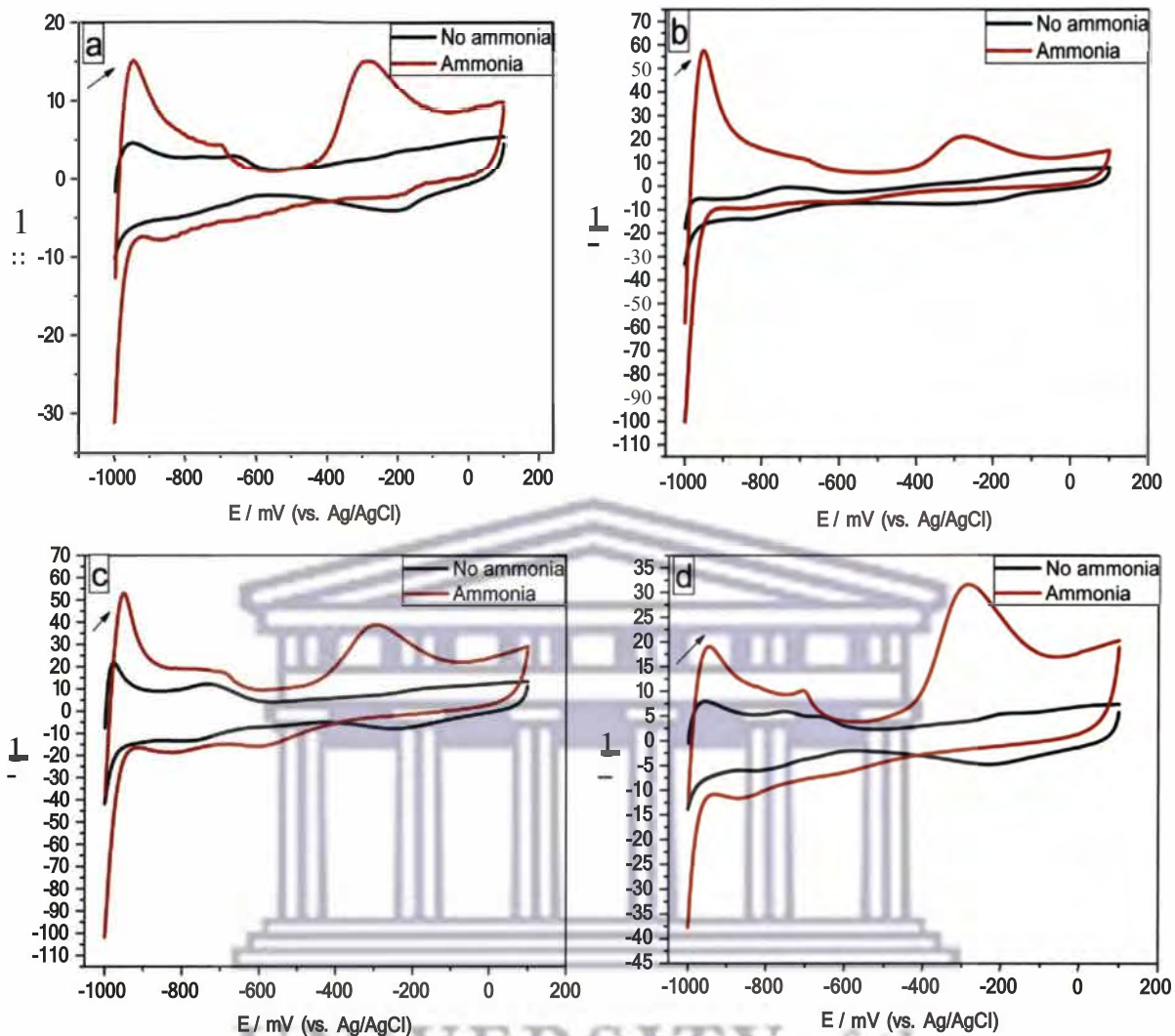


Figure 69: Cyclic voltammograms of (a) bare Pt electrode, (b) PtjPt(100)PdAuNPs, (c) PtjPt(100)AuNPs and (d) PtjPt(100)PdNPs electrodes in 1 M KOH and 0.1 M ammonia: Scan rate,  $100 \text{ mV s}^{-1}$ .

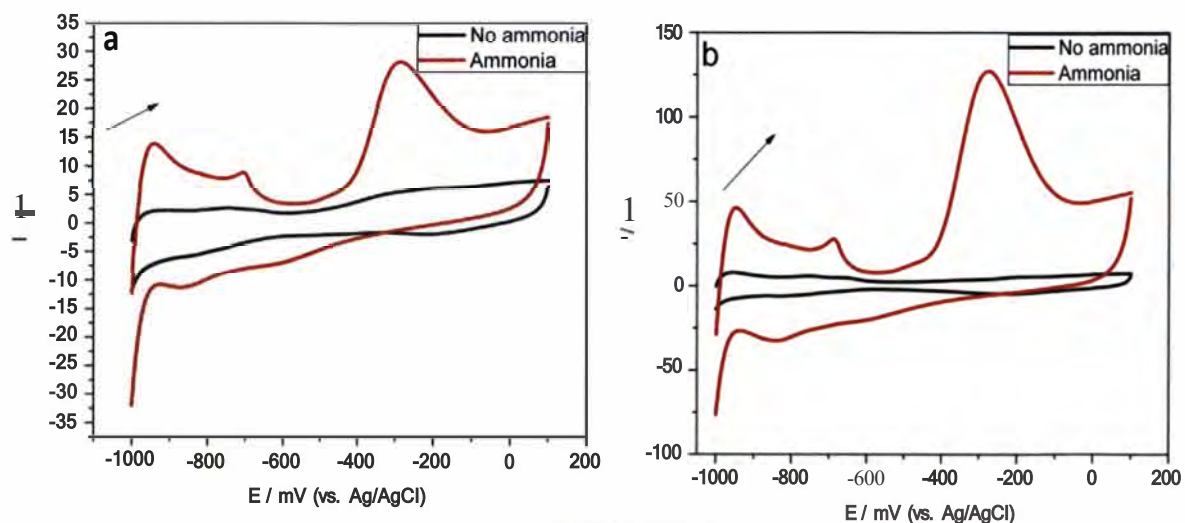


Figure 70: Cyclic voltammograms of a) PtIPtNPs electrode and b) PtIPt(100)NPs electrode in 1 M KOH and 0.1 M ammonia: Scan rate,  $100 \text{ mV s}^{-1}$ .

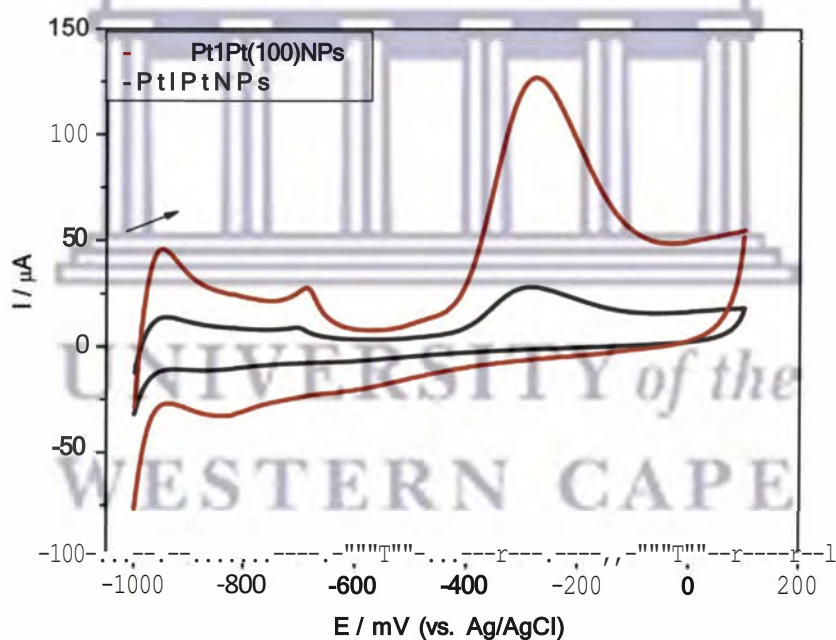


Figure 71: Overlay CVs of PtIPtNPs electrode and PtIPt(100)NPs electrode in 1 M KOH and 0.1 M ammonia: Scan rate,  $100 \text{ mV s}^{-1}$ .

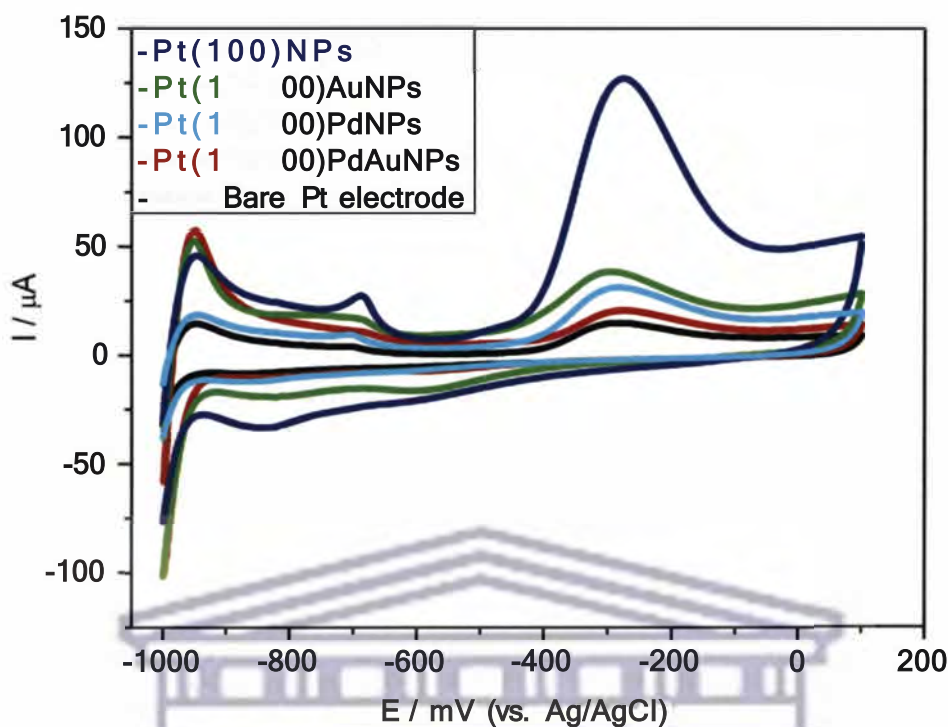


Figure 72: Cyclic voltammograms of bare Pt electrode, PtPt(100)PdAuNPs, PtPt(100)PdNPs, PtPt(100)AuNPs and PtPt(100)NPs electrodes in 1 M KOH and 0.1 M ammonia: Scan rate,  $100 \text{ mV s}^{-1}$ .

Table 8: CV parameters of Pt(100)PdAu, Pt(100)Pd and Pt(100)Au nanoalloys in 0.1 M ammonia and 1 M KOH (data extracted from Figure 72).

Electrode	$E_{p,a}$ (mV)	$i_{p,a}$ (A)
Bare Pt	-281	$1.525 \times 10^{-5}$
PtPt(100)PdAuNPs	-276	$2.028 \times 10^{-5}$
PtPt(100)PdNPs	-285	$3.185 \times 10^{-5}$
PtPt(100)AuNPs	-295	$3.972 \times 10^{-5}$
PtPt(100)NPs	-276	$1.274 \times 10^{-4}$

### 5.5.2 Effect of potential scan rates

In order to study the nature of the oxidation of ammonia, we performed the CVs at different scan rates (**Figure 73**) measured on Pt|Pt(100)NPs electrode in 0.1 M ammonia and 1 M KOH solution. The anodic peak currents increased significantly with the increasing potential scan rate. The peak currents followed a linear  $v^{1/2}$  ( $v$ : potential scan rate) dependence, as shown in **Figure 74**, indicating a diffusion controlled rather than surface controlled electron transfer kinetics. Additionally, the peak potential shifted positively with increasing the scan rates, demonstrating the oxidation of ammonia was an irreversible process [191].

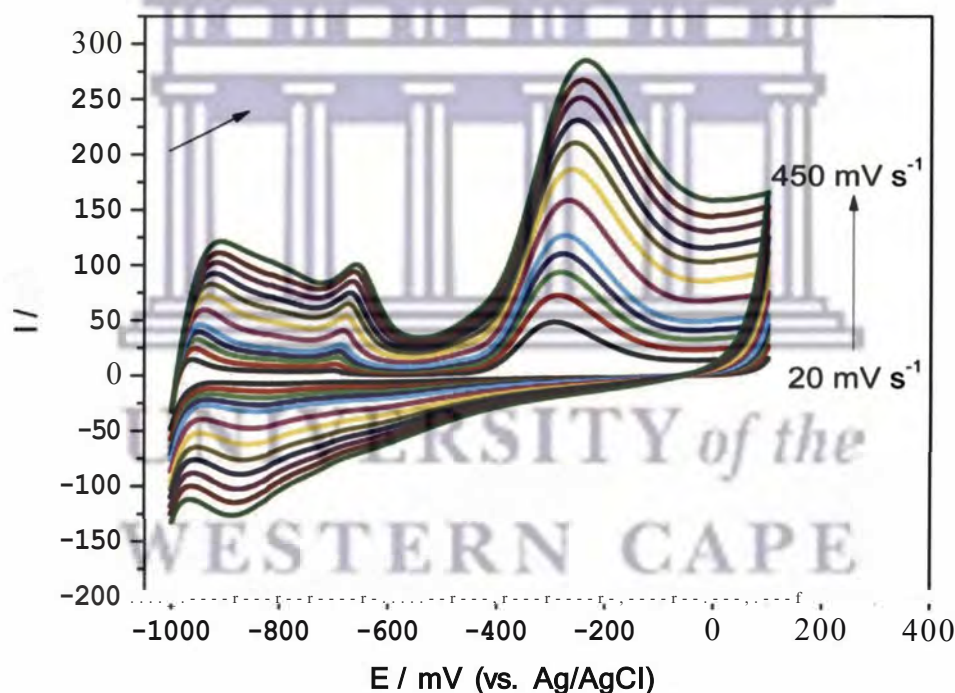


Figure 73: Cyclic voltammograms of Pt|Pt(100)NPs electrode in the presence of 0.1 M ammonia in 1 M KOH aqueous solution at different scan rates.

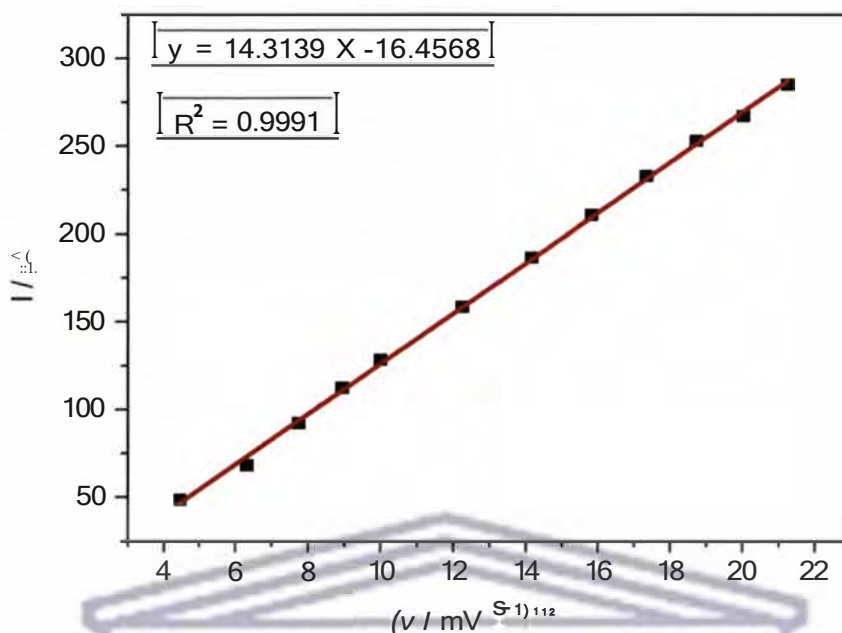


Figure 74: Randles-Sevcik plot of Pt|Pt(100)NPs electrode in the presence of 0.1 M ammonia and 1 M KOH aqueous solution.

### 5.5.3 Effect of ammonia concentration

Figure 75 shows the cyclic voltammograms measured on Pt|Pt(100)NPs in 1 M KOH solution with the various ammonia concentrations. It can be seen that three anodic current peaks were observed at approximately -940 mV, -700 mV and -292 V (Ag/AgCl). With the increase in ammonia concentration, the peak current at -292 mV (ammonia oxidation peak) increased continuously. This can be attributed to the adsorption of more  $\text{NH}_3(\text{aq})$  on the electrode surface to be oxidised, thus the anodic current increases continuously with the ammonia concentration. There was a significant increase in peak current when the ammonia concentration increased from 0.025 M to 0.1 M. With respect to the influence of the ammonia concentration on peak current at -940 mV and -700 mV, there was an insignificant change in peak current. When the ammonia concentration reached a certain level, i.e., 0.1 M, the



adsorption of ammonia on Pt/Pt(100)NPs electrode achieved a relatively saturation status. The further increase of the ammonia concentration in the solution apparently enhanced the amount of ammonia to be oxidised. However, the intermediates generated during ammonia oxidation, such as  $\text{NH}_2\text{ads}$  and  $\text{NH}_\text{a}\text{ads}$ , could remain on the electrode surface and block the ammonia adsorption. This observation may be due to the fact that the rate of  $\text{N}_\text{a}\text{ads}$  formation increases with concentration therefore, blocking active sites and preventing ammonia electro-oxidation. The electrode surface may also be saturated with different adsorbed species in agreement with the reaction mechanism described by equations 31-36 hence affecting the capability of the catalyst to oxidize at higher concentrations of ammonia. It is reasonable to assume that the blocking effect will be significant when the solution contains a high concentration of ammonia. Therefore, an increase in ammonia concentration beyond 0.1 M results in slight decrease in anodic peak current due to ammonia saturation on the electrode surface. The present results show that ammonia can be oxidized effectively on Pt/Pt(100)NPs electrode.

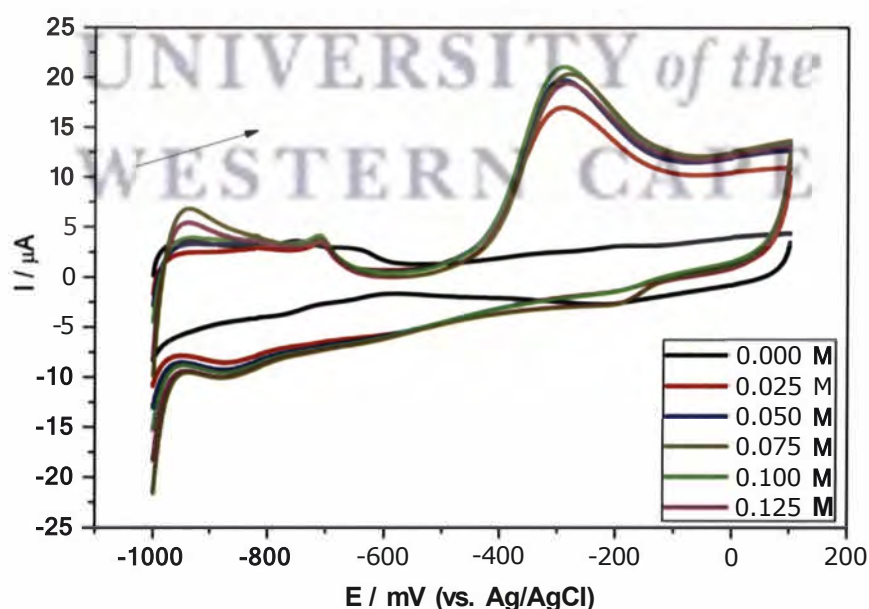
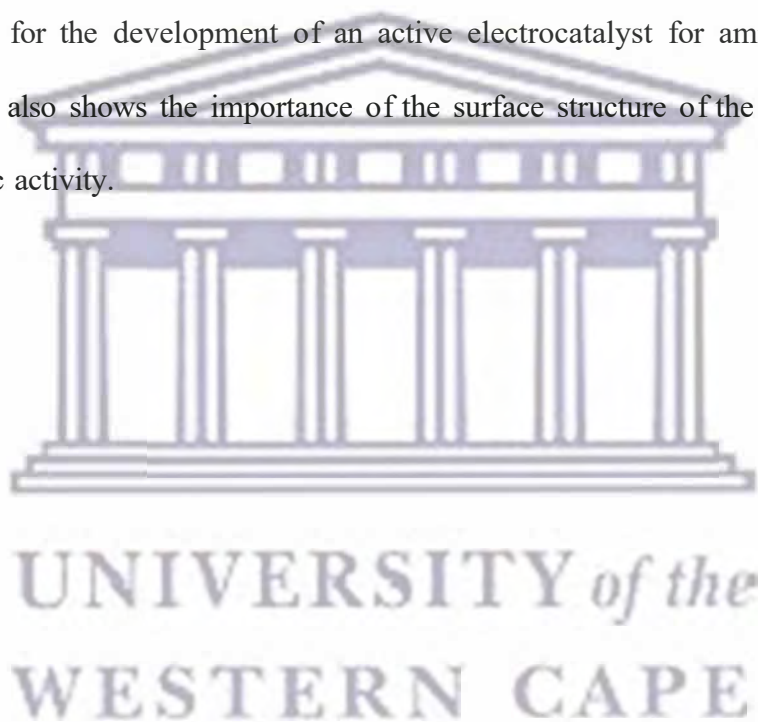


Figure 75: Cyclic voltammograms of Pt/Pt(100)NPs in 1 M KOH solution with various concentrations of ammonia (0-0.125 M): Scan rate,  $100 \text{ mV s}^{-1}$ .

## 5.6 Sub conclusion

Pt nanoparticles and Pt based nanoalloys with (100) preferentially oriented surface structures were successfully synthesised and their activities for ammonia oxidation in basic medium were studied. The results show that ammonia oxidation is very sensitive to the existence of Pt(100) sites. Oxidation currents for the Pt(100) nanoparticles towards ammonia oxidation eight times higher to that found for bare platinum electrode and six times higher to that found for Pt(100)PdAu were obtained showing the importance of controlling the surface structure of the nanoparticles for the development of an active electrocatalyst for ammonia oxidation. This contribution also shows the importance of the surface structure of the nanoparticles on its electrocatalytic activity.



## CHAPTER SIX

### RESULTS AND DISCUSSION: Part 3

#### AMMONIA OXIDATION ON Pt(100)Ir, Pt(100)Rh, Pt(100)IrAu, Pt(100)Pdlr and Pt(100)RhAu NANOALLOY SYSTEMS



*Summary*

*In this chapter, the characterisation of oriented Pt(100)Ir, Pt(100)Rh, Pt(100)IrAu, Pt(100)Pdlr and Pt(100)RhAu nanoalloys is discussed. Particle sizes, structures and surface compositions of the nanoalloys are investigated using HRTEM and EDX. The catalytic effects of the nanoalloys towards ammonia oxidation are also discussed.*

UNIVERSITY of the  
WESTERN CAPE

## 6.1 Introduction

As discussed in **Chapter 5**, ammonia oxidation on platinum is an extremely structure sensitive reaction which takes place almost exclusively on surface sites with (100) symmetry. Nanoalloys are known to exhibit better catalytic properties than their monometallic nanoparticles hence the synthesis of oriented Pt(100) based nanoalloys and their subsequent application in ammonia oxidation is worth investigating. In this chapter, ammonia electro-oxidation reaction will further be studied in alkaline solution using bimetallic and ternary Pt(100)Ir, Pt(100)Rh, Pt(100)IrAu, Pt(100)PdIr and Pt(100)RhAu nanoalloys. In these nanoalloys, Pt is employed as base metal not only because of its electrocatalytic properties but also due to the fact that  $N_2$  is formed at very high potentials on its surface in comparison with other metals.

## 6.2 Spectroscopic and morphological characterisation of the oriented nanoalloys

### 6.2.1 UV-visible spectroscopy

The formation of the nanoalloys by reduction of  $PtCl_4^{2-}$ ,  $Ir^{4+}$ ,  $HAuCl_4^-$ ,  $Rh^{3+}$  and  $Pd^{2+}$  ions was confirmed by the use of UV-visible spectroscopy. **Figure 76** shows the UV-visible spectra of the starting materials (salts) while the spectra of Pt(100)Ir, Pt(100)Rh, Pt(100)IrAu, Pt(100)PdIr and Pt(100)RhAu nanoalloys are shown in **Figure 77**. The absorption peaks observed at (bands at  $\lambda_{max}$ ) 234 nm, 304 nm, 432 nm and 488 nm for  $H_2IrCl_6 \cdot H_2O$  salt which are characteristic of iridium(III) and iridium(IV) chloride complexes disappeared after 16 h reduction indicating that the iridium ions were completely reduced [205]. The absorption peaks observed at 262 nm for  $Pt^{4+}$ , 285 nm for  $Au^{3+}$ , and 420 nm for  $Pd^{2+}$  ions (see **chapter 5, Figure 50**) disappeared indicating that the metal ions were completely reduced. The absence of the absorption peaks in the oriented nanoalloys indicated that there was complete reduction of the metal salts to zero-valent nanoparticles/nanoalloys.

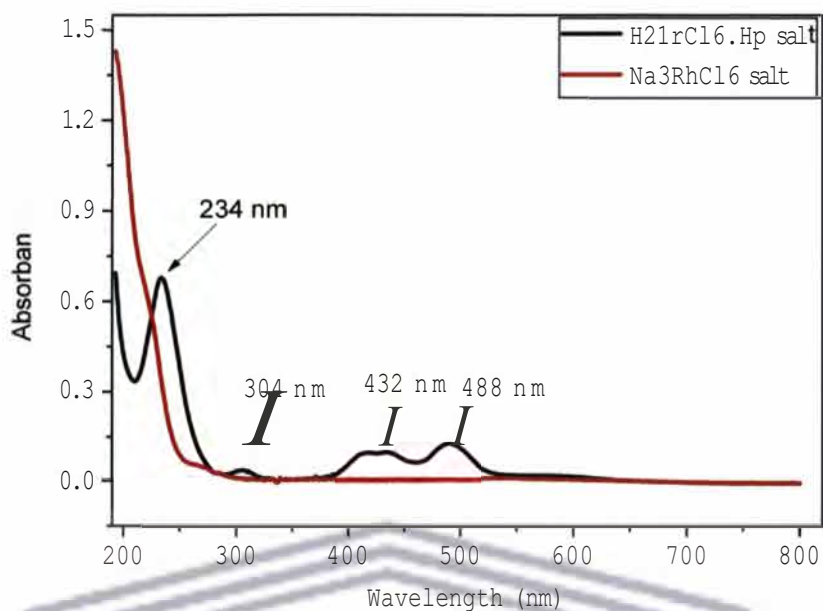


Figure 76: UV-visible spectra of H<sub>2</sub>IrCl<sub>6</sub>.H<sub>2</sub>O and Na<sub>3</sub>RhCl<sub>6</sub> salts.

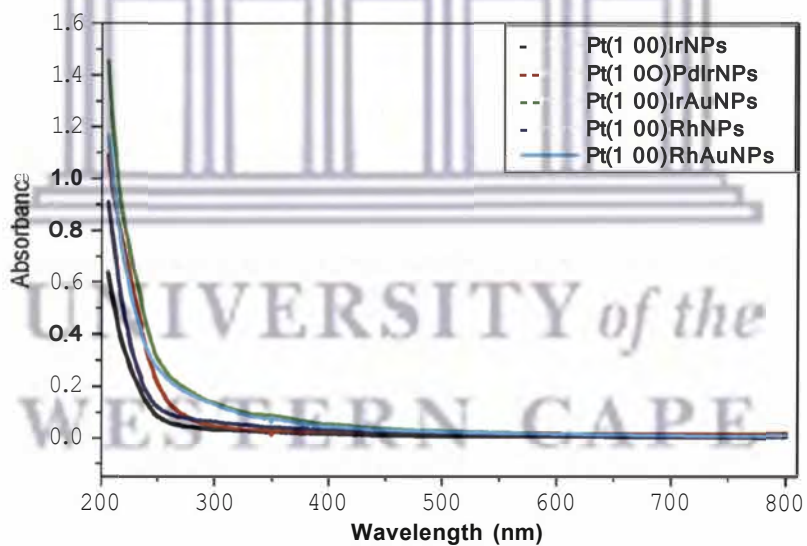
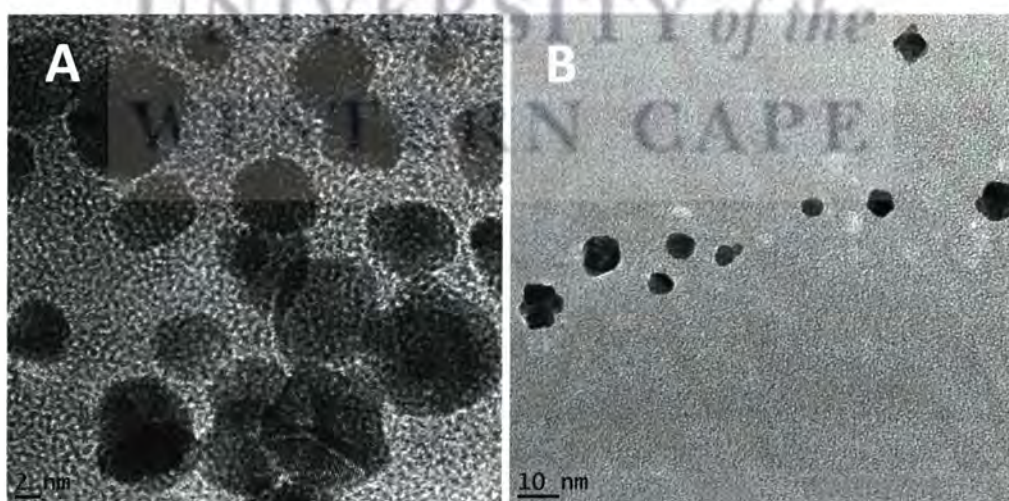
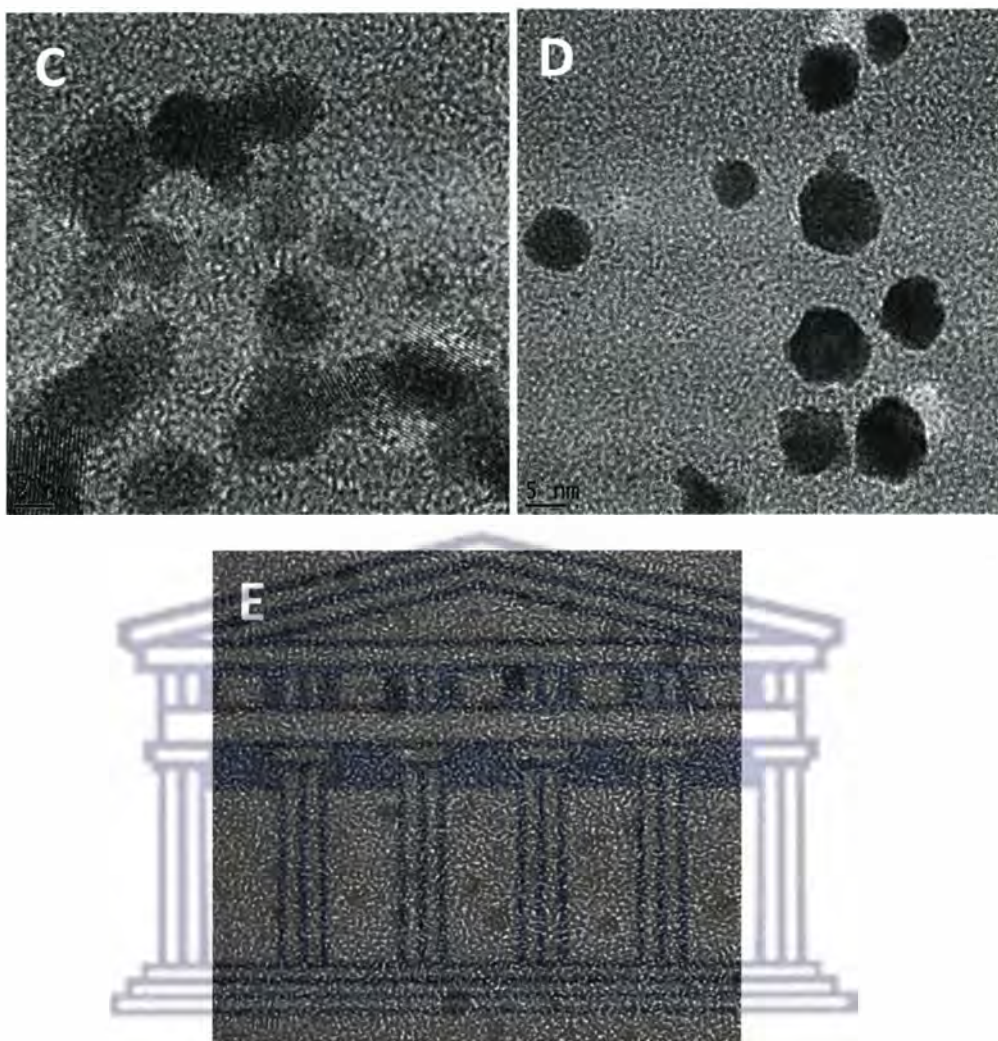


Figure 77: UV-visible spectra of Pt(100)Ir, Pt(100)Rh, Pt(100)IrAu, Pt(100)PdIr and Pt(100)RhAu nanoalloys.

## 6.2.2 High resolution transmission electron microscopy (HRTEM)

Figure 78 shows some representative HRTEM images of polyacrylate acid capped nanoalloys prepared using H<sub>2</sub> reduction colloidal method. From HRTEM results, it was possible to estimate the particle sizes that were very similar in all cases and ranged from 3-10 nm. Some cubic shaped particles were observed in the Pt(100)Rh system a characteristic of Pt(100) sites present in the nanoalloys. Well dispersed and non-agglomerated Pt(100)PdIr, Pt(100)RhAu, Pt(100)Ir and Pt(100)IrAu nanoalloy images were observed. This can be attributed to the use of sodium polyacrylate that was used as a capping/stabilising material. This surface-stabilising agent weakly interacts with the nanoalloy surfaces and therefore is easy to remove, which is crucial when the surface properties of the nanoparticles are under investigation. As explained in chapter 5, image observation may be misleading and so alternative characterisation techniques are required to obtain the orientation of the nanoalloys.





**Figure 78:** HRTEM images of Pt(100)PdIr nanoalloys (A), Pt(100)Rh nanoalloys (B), Pt(100)RhAu nanoalloys (C), Pt(100)Ir nanoalloys (D) and Pt(100)IrAu nanoalloys (E).

### 6.2.3 Energy dispersive X-ray spectroscopy (EDX analysis)

EDX used in conjunction with HRTEM was used to obtain the localized elemental information of the nanoalloys. EDX revealed the presence of all the elements present in the bimetallic and ternary alloy nanoparticles (**Figures 79-82**). However, for Pt(100)Ir, Pt(100)IrAu, and Pt(100)PdIr nanoparticles, EDX was not employed to determine the atomic composition of the sample due to the overlapping of the Pt and Ir signals [30].

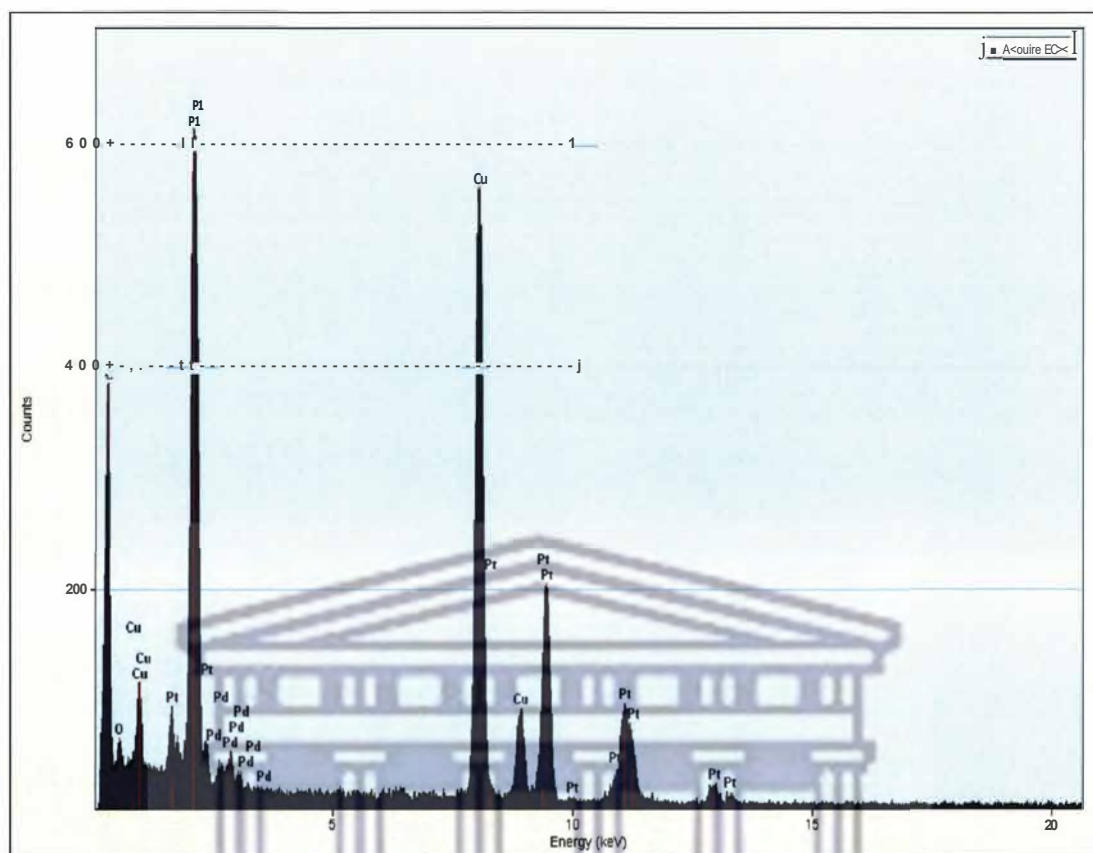


Figure 79: EDX spectrum of Pt(100)PdIr nanoalloys.

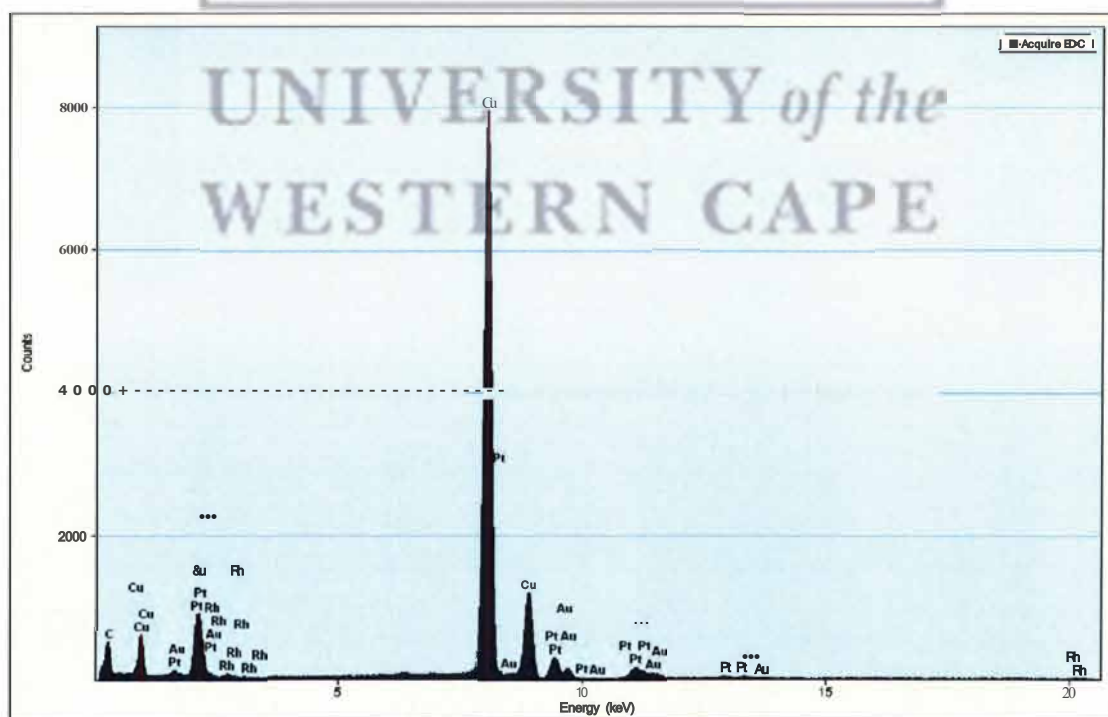


Figure 80: EDX spectrum of Pt(100)RhAu nanoalloys.



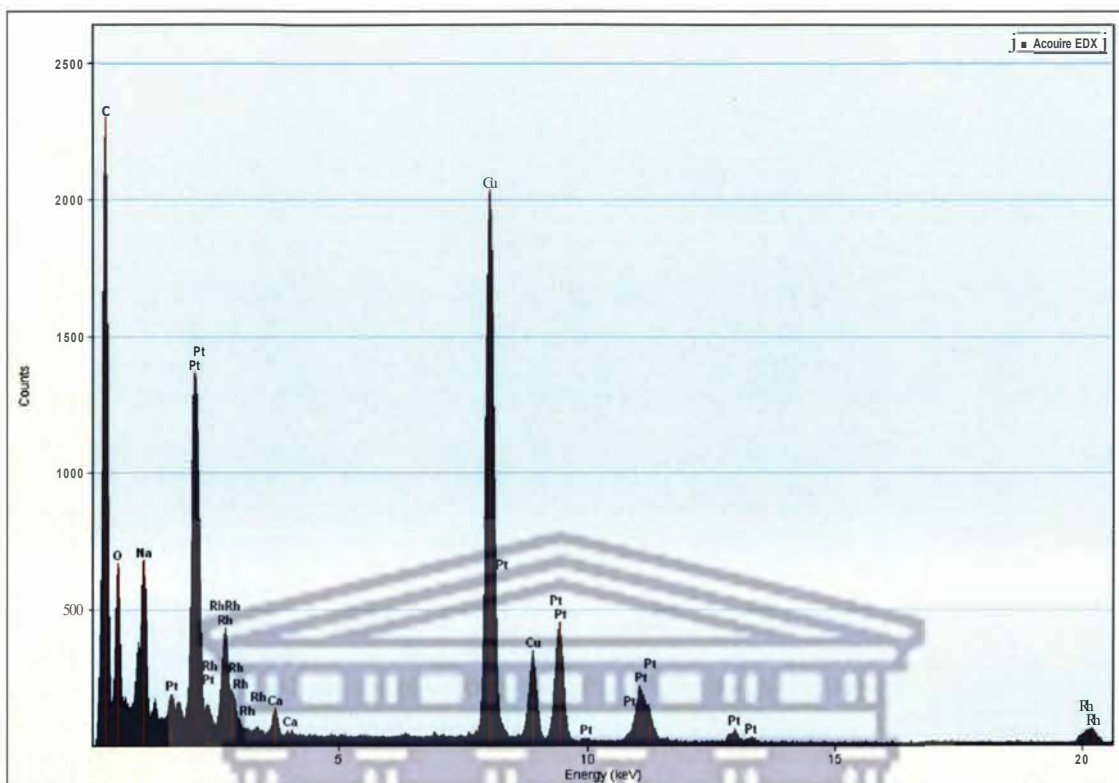


Figure 81: EDX spectrum of Pt(100)Rh nanoalloys.

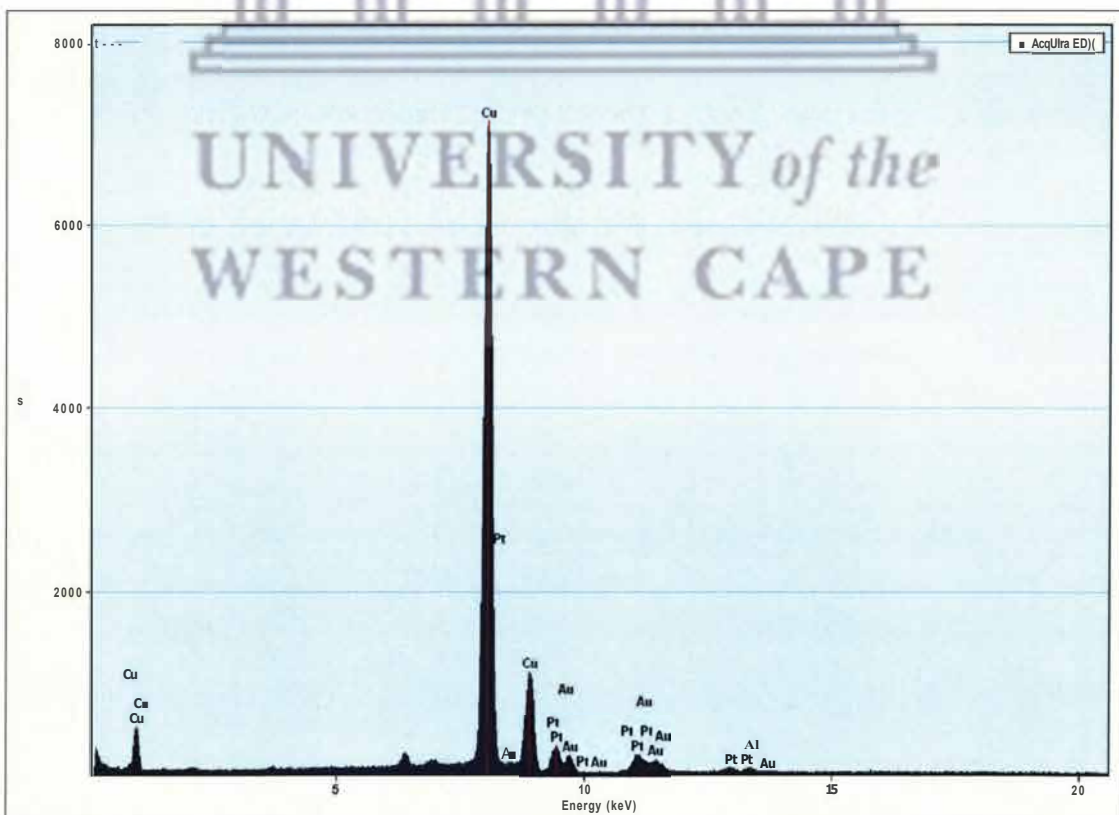
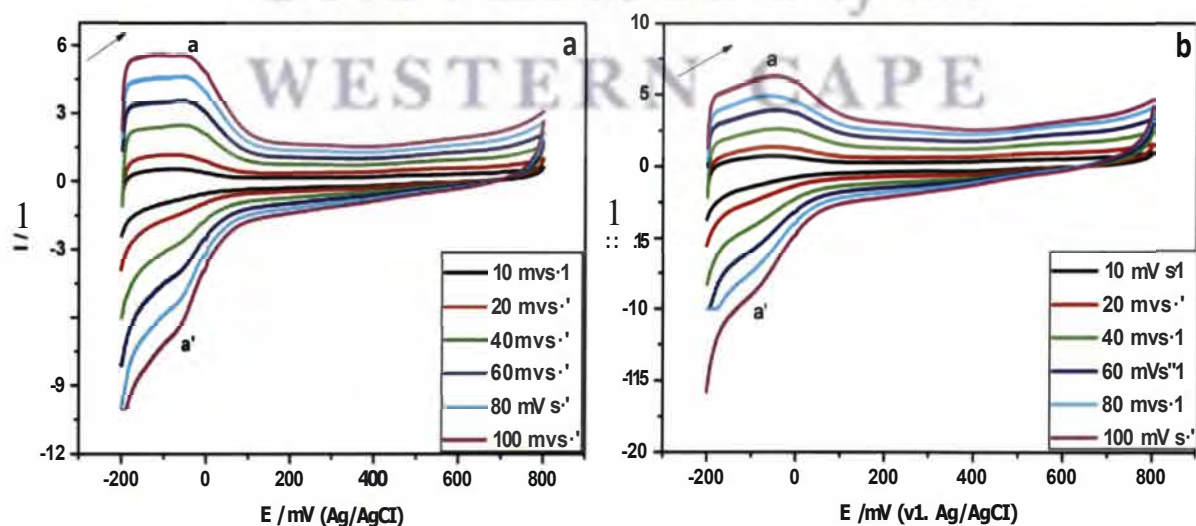


Figure 82: EDX spectrum of Pt(100)IrAu nanoalloys.

## 6.3 Electrochemical characteristics of the nanoalloys

### 6.3.1 Electrochemistry of the nanoalloys in 0.5 M H<sub>2</sub>SO<sub>4</sub> test solution

**Figure 83** shows the characteristic voltammetric profiles of the different Pt based nanoalloys in 0.5 M sulphuric acid. The symmetry of the adsorption states is indicative of the surface cleanliness. The inclusion of the adatoms to the Pt(100) system to form Pt(100)Rh, Pt(100)Ir, Pt(100)IrAu, Pt(100)PdIr and Pt(100)RhAu nanoalloys blocked the 100 domains in the Pt(100) systems as evidenced by the absence of the peak at 29 mV (see chapter 5, **section 5.4.1**). A redox peak (a/a') was observed in the nanoalloys within the range -200 and 0 mV which is attributed to the adsorption/desorption of hydrogen. This behaviour was also observed for Pt(100)Pd, Pt(100)PdAu nanoalloys discussed in chapter 5, **section 5.4.1**. The absence of two redox peaks as observed with Pt(100) nanoparticles (see **section 5.4.1**) indicated that Rh, Ir, IrAu, PdIr and RhAu adatoms were effectively incorporated into the Pt(100) system to form nanoalloys. A reduction peak was observed between 500 mV and 730 mV which can be attributed to reduction of Pt oxide formed during the anodic scanning.



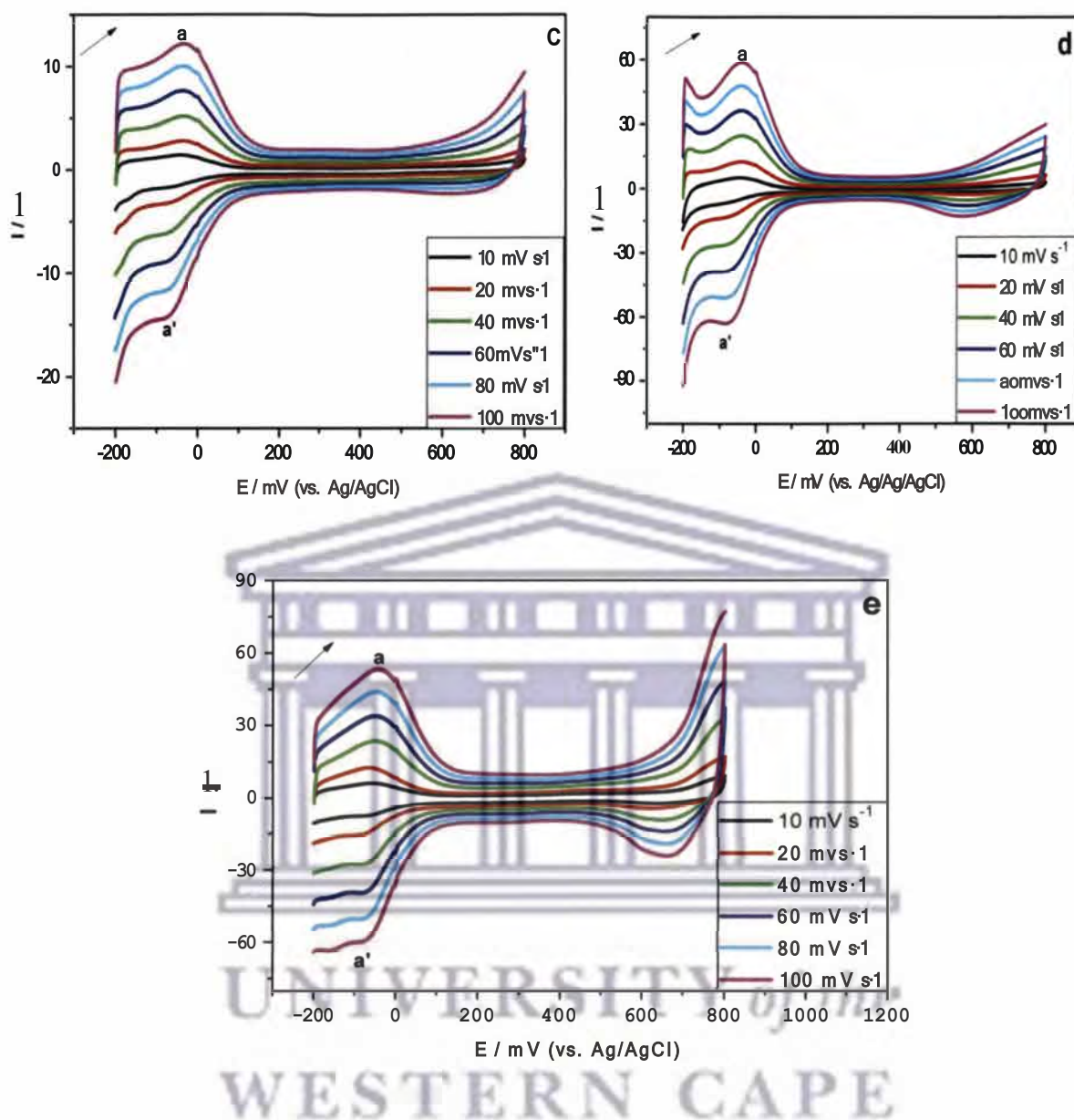
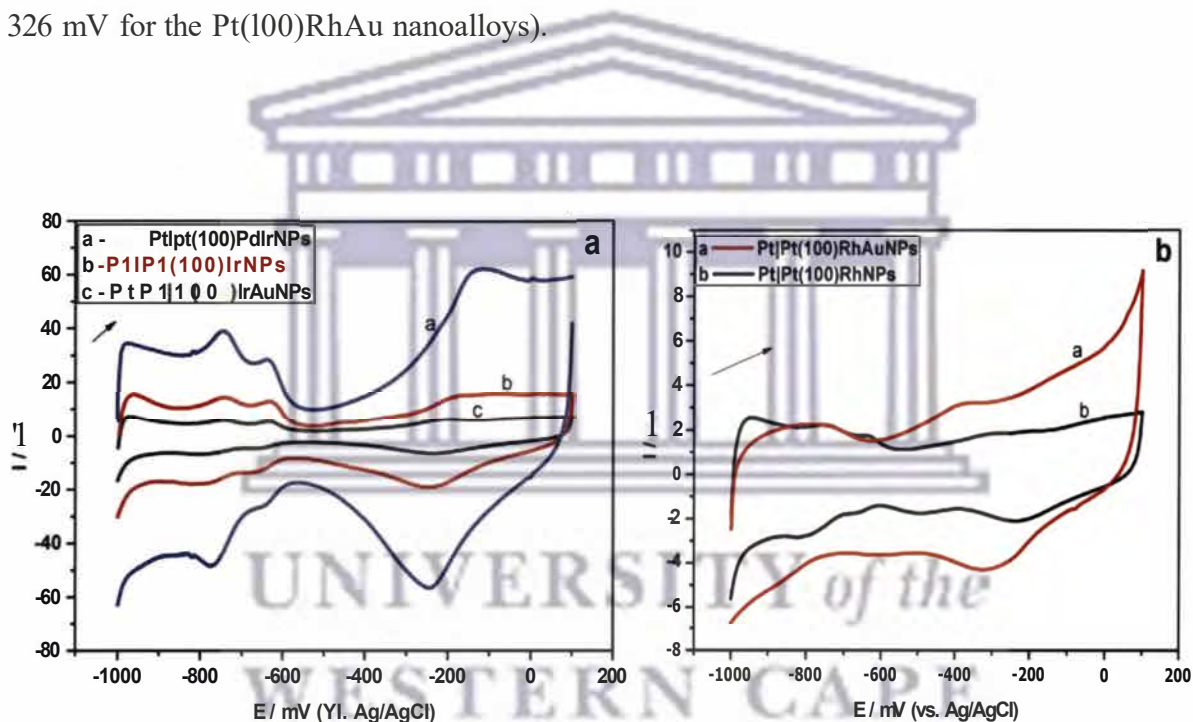


Figure 83: Cyclic voltammograms of Pt(100)Rh (a), Pt(100)Ir (b), Pt(100)IrAu (c), Pt(100)PdIr (d) and Pt(100)RhAu nanoalloys (e) modified Pt electrode in 0.5 M H<sub>2</sub>SO<sub>4</sub> at different scan rates.

### 6.3.2 Electrochemistry of the nanoalloys in 1 M KOH solution

Cyclic voltammograms of Pt(100)Rh, Pt(100)Ir, Pt(100)IrAu, Pt(100)PdIr and Pt(100)RhAu nanoalloys in 1 M KOH are presented in **Figure 84**. All nanoalloys were cycled for 4 cycles resulting in a stable and reproducible shape of CVs. For the Pt(100)PdIr, Pt(100)IrAu and Pt(100)Ir nanoalloys modified Pt electrode (**Figure 84a**), well defined hydrogen adsorption

and desorption peaks were observed in the hydrogen region (-800 to -500 mV). A redox peak in the potential range -400 mV to 0 mV was observed in Pt(100)Ir, Pt(100)IrAu and Pt(100)PdIr modified Pt electrode, respectively characteristic of Ir(IV)/Ir(III) [23]. Pt(100)Rh and Pt(100)RhAu nanoalloys showed oxidation peaks at around -400 to 100 mV depicting the formation of oxides, whereas oxide reduction was observed as a small peak at around -300 mV on the cathodic scan. Difference in surface composition of the alloys was shown by the cathodic shift of the oxygen desorption peak (from -241 mV for Pt(100)Rh nanoalloys to -326 mV for the Pt(100)RhAu nanoalloys).



**Figure 84:** Cyclic voltammograms of Pt(100)Ir, Pt(100)IrAu and Pt(100)PdIr (a) and Pt(100)RhAu and Pt(100)Rh (b) modified Pt electrode in 1 M KOH: Scan rate, 100 mV s<sup>-1</sup>.

## 6.4 Catalytic performance of the nanoalloys

### 6.4.1 Electrocatalytic oxidation of ammonia

The ability of the synthesised nanoalloys to catalyse the electro-oxidation of ammonia in strong alkaline solution (1 M KOH) was investigated with cyclic voltammetric studies. **Figure 85** shows the cyclic voltammograms of Pt(100)Ir, Pt(100)Rh, Pt(100)IrAu, Pt(100)PdIr and Pt(100)RhAu nanoalloys modified Pt electrodes in 1 M KOH aqueous solution with and without 0.1 M ammonia. All nanoalloys were cycled for 4 cycles resulting in a stable and reproducible shape of CVs in both ammonia containing and ammonia free solutions. It is apparent from **Figure 85** that the presence of ammonia has an influence on the hydrogen regions due to the possible competition between the N-containing adsorbates with  $H_{ads}$  [15]. In the presence of ammonia, Pt/Pt(100)IrNPs, (**Figure 85a**) showed a well-defined peak in the potential region of -500 and 0 mV corresponding to ammonia oxidation. Current started rising around -450 mV reached maximum at -300 mV and then decreased. The decrease in the current density was due to the surface deactivation by inert N-adsorbate species ( $N_{ads}$ ) [15]. CVs of Pt/Pt(100)RhNPs, Pt/Pt(100)IrAuNPs, Pt/Pt(100)PdIrNPs and Pt/Pt(100)RhAuNPs in 1 M KOH and 0.1 M ammonia solutions showed an ammonia oxidation peak at -301 mV, -281 mV, -299 mV and -274 mV respectively as shown in **Figure 85**. According to the comparative CVs, which are illustrated in **Figure 86**, and taking as criterion the height of the peak current observed for each nanoalloy material, the tested catalysts can be classified as: Pt/Pt(100)RhAuNPs > Pt/Pt(100)PdIrNPs > Pt/Pt(100)IrAuNPs > Pt/Pt(100)RhNPs > Pt/Pt(100)IrNPs while the overpotential of ammonia oxidation decreases as follows Pt/Pt(100)RhAuNPs > Pt/Pt(100)IrAuNPs > Pt/Pt(100)PdIrNPs > Pt/Pt(100)IrNPs > Pt/Pt(100)RhNPs. Based on the current density, the results indicate that having trimetallic catalysts has advantages for ammonia electro-oxidation. Electronic effect generated among the three metals in the trimetallic nanoparticles might be responsible for

increase in the catalytic activity of Pt-containing catalysts, causing weakening of the adsorption strength of poisonous  $\text{Nads}$  intermediate. **Table 9** show the data obtained from **Figure 86**.

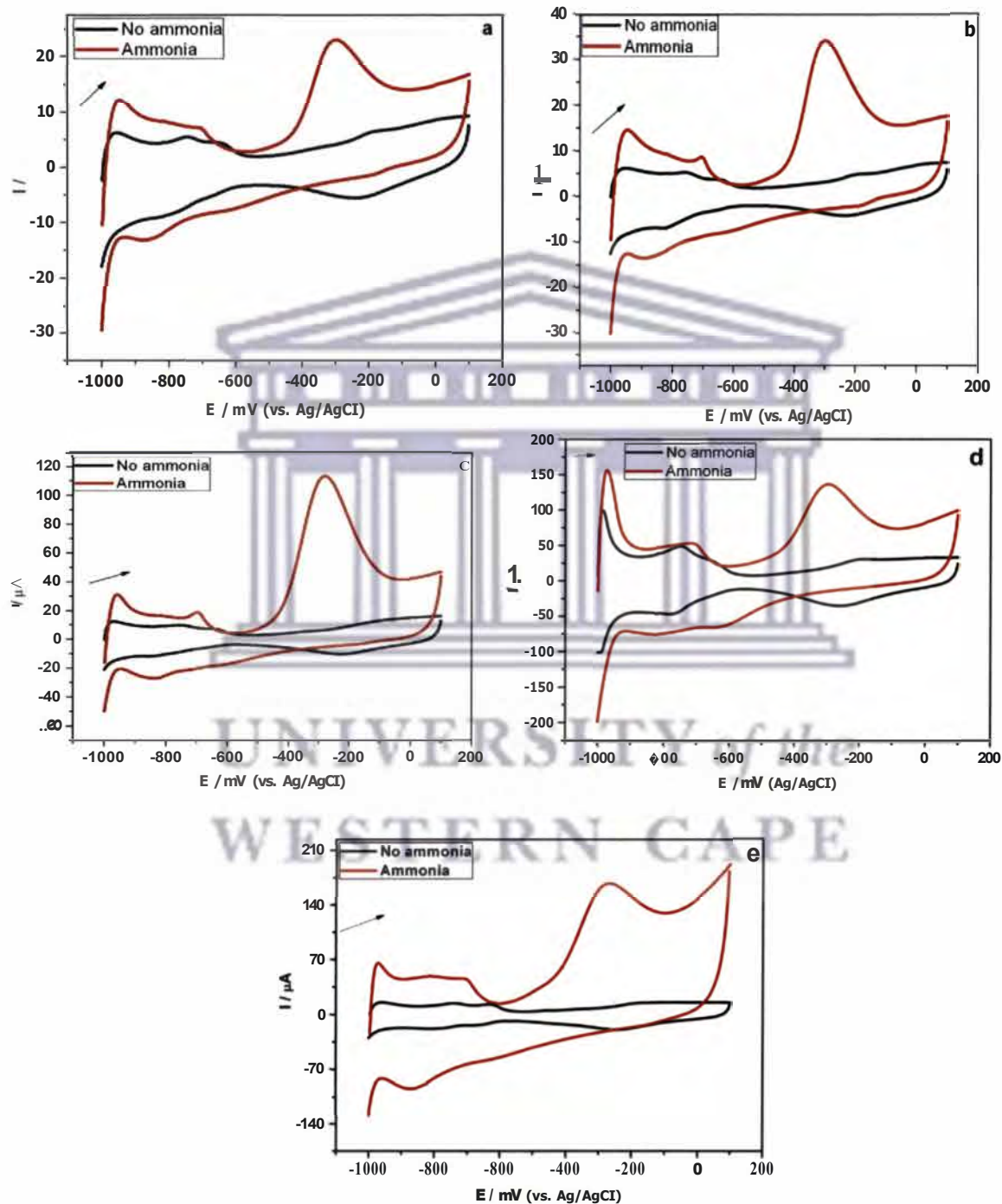


Figure 85 Cyclic voltammograms of PtPt(100)IrNPs (a), PtPt(100)RhNPs (b), PtPt(100)IrAuNPs (c), PtPt(100)PdIrNPs (d), and PtPt(100)RhAuNPs (e) in 1 M KOH and 0.1 M ammonia solution: Scan rate,  $100 \text{ mV s}^{-1}$ .

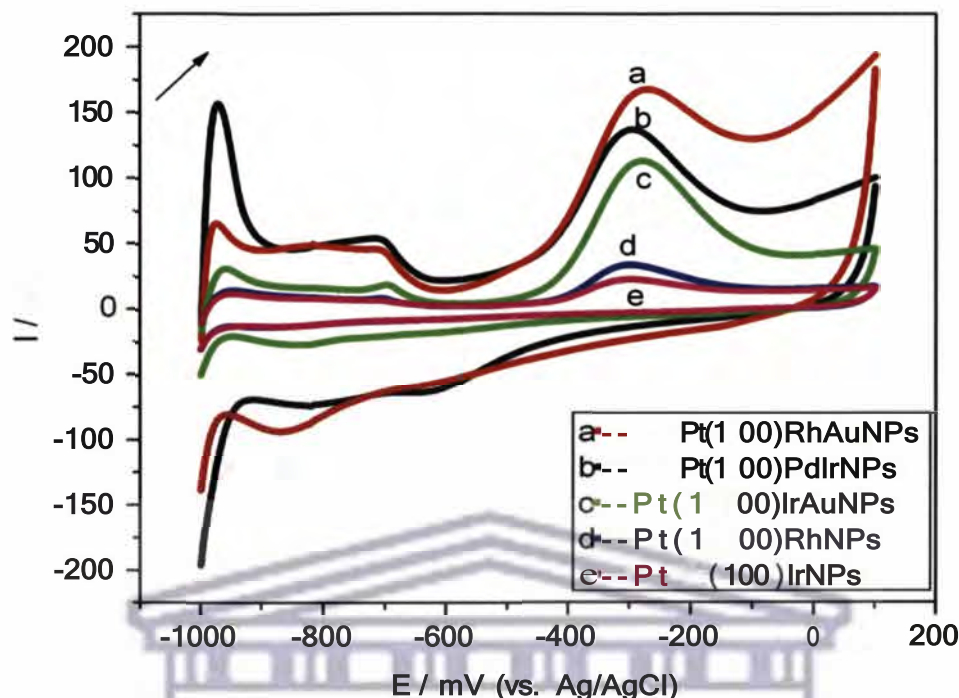


Figure 86: CVs of Pt(100)Ir, Pt(100)Rh, Pt(100)IrAu, Pt(100)PdIr and Pt(100)RhAu nanoalloys modified electrode in 0.1 M ammonia and 1 M KOH: Scan rate 100 mV s<sup>-1</sup>.

**Table 9: CV parameters of Pt(100)Ir, Pt(100)Rh, Pt(100)IrAu, Pt(100)PdIr and Pt(100)RhAu nanoalloys in 0.1 M ammonia and 1 M KOH (data extracted from Figure 86).**

Electrode	$E_{pa}$ (mV)	$I_{pa}$ (A)
PtPt(100)RhAuNPs	-274	$1.681 \times 10^{-4}$
PtPt(100)PdIrNPs	-299	$1.361 \times 10^{-4}$
PtPt(100)IrAuNPs	-281	$1.124 \times 10^{-4}$
PtPt(100)RhNPs	-301	$3.417 \times 10^{-5}$
PtPt(100)IrNPs	-300	$2.292 \times 10^{-5}$

## 6.5 Sub conclusion

Pt based nanoalloys with (100) preferentially oriented surface structures were successfully synthesised and their activities for ammonia oxidation in basic medium were studied. Among all the bimetallic and ternary samples tested, only Pt(100)PdIr and Pt(100)RhAu nanoparticles showed at low potential range and an enhancement of the oxidation density current with respect to the behaviour found for Pt(100) nanoparticles prepared by the same method.

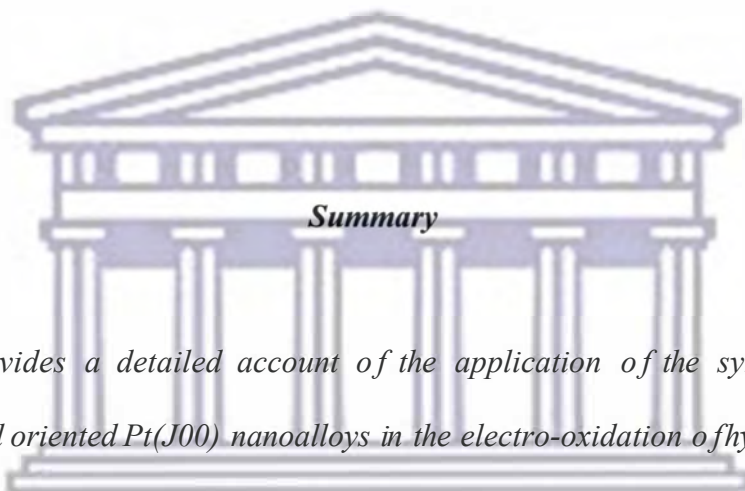




## CHAPTER SEVEN

### RESULTS AND DISCUSSION: Part 4

#### Pt(100) NANOALLOY SYSTEMS AS ELECTROCATALYSTS FOR HYDRAZINE OXIDATION



#### *Summary*

*This chapter provides a detailed account of the application of the synthesised Pt(100) nanoparticles and oriented Pt(100) nanoalloys in the electro-oxidation of hydrazine.*

UNIVERSITY of the  
WESTERN CAPE

## 7.1 Introduction

Carbon-free fuel such as hydrazine ( $\text{N}_2\text{H}_4$ ) is of particular interest since its consumption yields  $\text{N}_2$  as the main product [36, 206]. Direct electrochemical oxidation of hydrazine at ordinary solid electrodes is a slow electrode process resulting in large overpotential. A number of different catalysts have been reported for the anodic oxidation of hydrazine. Among these catalysts are Pt, Pd, Ag, Au, Hg, and Co [37]. However, the oxidation of hydrazine on these electrodes has been shown to exhibit high overpotentials and less power density. A unique class of materials called nanoparticles and nanoalloys is now emerging. Nanoparticles are clusters of atoms, ions or molecules with dimensions of less than 100 nm and frequently display unusual physical and chemical properties depending on their size, shape and stabilising agents and are known to improve the reaction rates of systems they catalyse due to their better physicochemical properties [26, 207]. Bimetallic nanoparticles in form of nanoalloys have been found to portray better catalytic properties than the monometallic nanoparticles due to their increased synergistic properties [208]. In this chapter, Pt(100) nanoparticles and oriented nanoalloy electrocatalysts deposited on glassy carbon electrodes (GCEs) for the electro-oxidation of hydrazine are presented.

## 7.2 Catalytic performance of Pt(100) nanoparticles and oriented Pt(100) nanoalloys

### 7.2.1 Electro-oxidation of hydrazine on Pt(100) nanoparticles modified GCE

The cyclic voltammograms of 10 mM hydrazine using Pt(100) nanoparticles modified GCE (Pt(100)NPs/GCE) (curve a) and bare GCE (curve b) in phosphate buffer solution (PBS, pH 7.4) at a scan rate of 50  $\text{mV s}^{-1}$  are shown in **Figure 87**. At the bare GCE, hydrazine shows a featureless voltammogram (**Figure 87** curve b). However, a well-formed profile of hydrazine oxidation for Pt(100) nanoparticles modified GCE can clearly be observed at around 20 mV (**Figure 87** curve a). In comparison with the data at the bare GCE, an increase in peak

current, a lower onset oxidation potential and a decrease in the overpotential of hydrazine was observed at the Pt(100) nanoparticles modified electrode. This result may be attributed to the high catalytic effect of the nanoparticles and the large specific surface area of the Pt(100)NPs/GCE. It is apparent from the obtained CV graph that in the absence of hydrazine, both the bare GCE and Pt(100)NPs/GCE do not show any redox peak as shown in voltammograms c and d. The electrochemical response of hydrazine on the Pt(100)NPs/GCE is irreversible as no cathodic current was observed in the reverse sweep. These observations lead to the conclusion that the synthesised Pt(100) nanoparticles are effective electrocatalysts for the electro-oxidation of hydrazine.

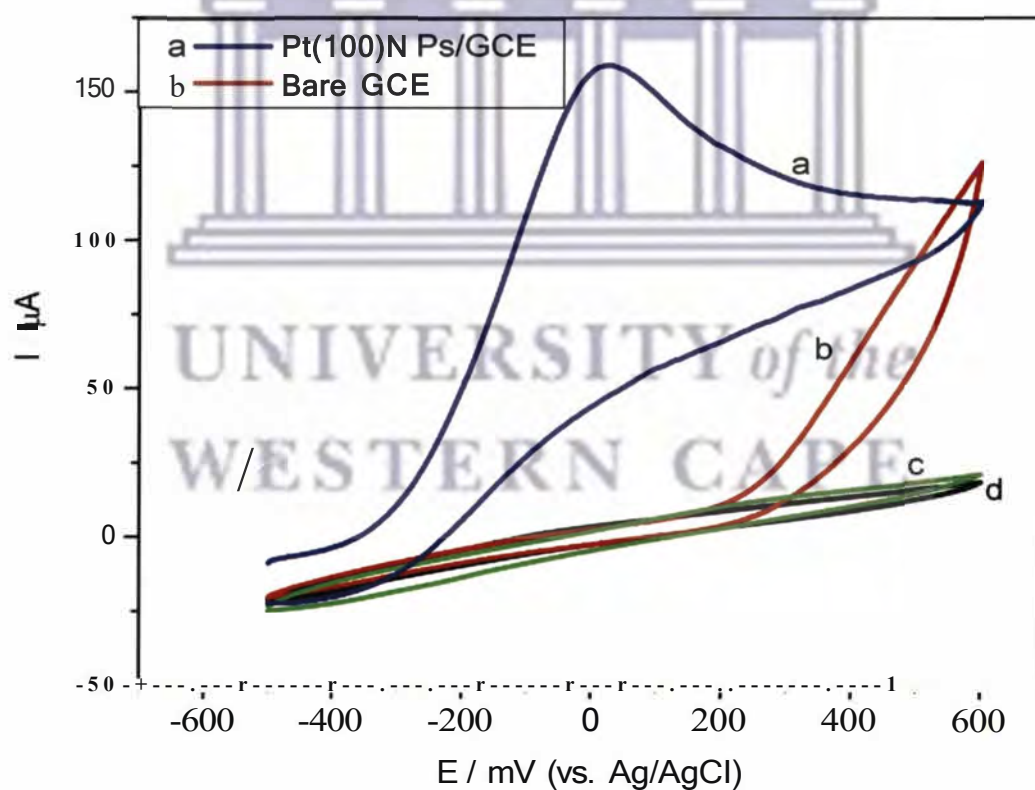
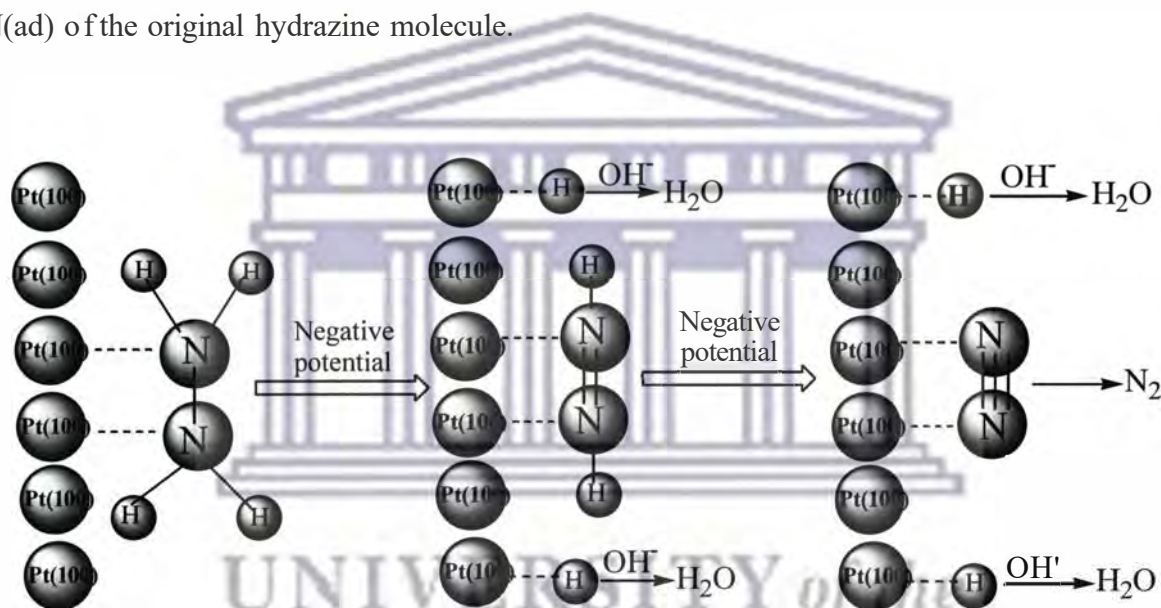


Figure 87: Cyclic voltammograms of 10 mM hydrazine at Pt(100)NPs/GCE (curve a) and bare GCE (curve b) in 0.1 M PBS (pH 7.4) at scan rate  $50 \text{ mV s}^{-1}$ . The voltammograms c and d are the backgrounds.

The reaction mechanism for the Pt(100) nanoparticles with high electrocatalytic activity towards hydrazine electro-oxidation was proposed, see **Scheme 5**. Initially, the two N atoms of  $N_2H_4$  coordinate with a Pt(100) nanoparticle to form N(ad). As the potential gradually changes from positive to negative, the surface of the Pt(100) nanoparticle becomes electron-rich, which repels nitrogen atoms and attracts hydrogen atoms. Each of the two H-N bonds breaks, so H becomes adsorbed on the metal surface, forming H(ad). Subsequently, H(ad) reacts with  $OH^-$  to form  $H_2O$  and an electron. Finally,  $N_2$  forms between the two residual N(ad) of the original hydrazine molecule.



**Scheme 5: Schematic representation of hydrazine oxidation.**

### 7.2.1.1 Effect of scan rates

The effect of different scan rates on the electrocatalytic properties of Pt(100)NPs/GCE towards hydrazine oxidation was studied and results shown in **Figure 88**. As can be seen from **Figure 88**, the increase in potential scan rate induced an increase in the electrocatalytic peak current and resulted in a shift to more positive potential values for the catalytic oxidation of hydrazine. This clear shift of the peak potential occurred as expected for irreversible electrochemical reactions [80]. This is also shown by the linear relationship

between  $E_{p,a}$  and  $\log v$  (see **Figure 90**). The obtained cyclic voltammograms were used to examine the variation of oxidation peak current versus scan rate. The oxidation current of hydrazine increased linearly with the square root of scan rate (**Figure 89**) ( $i_{pa} = -21.282 + 17.143v^{1/2}$  ( $\text{mV}^{1/2} \text{s}^{-1/2}$ ), ( $R^2 = 0.994$ ) which demonstrated a diffusion controlled redox process [209].

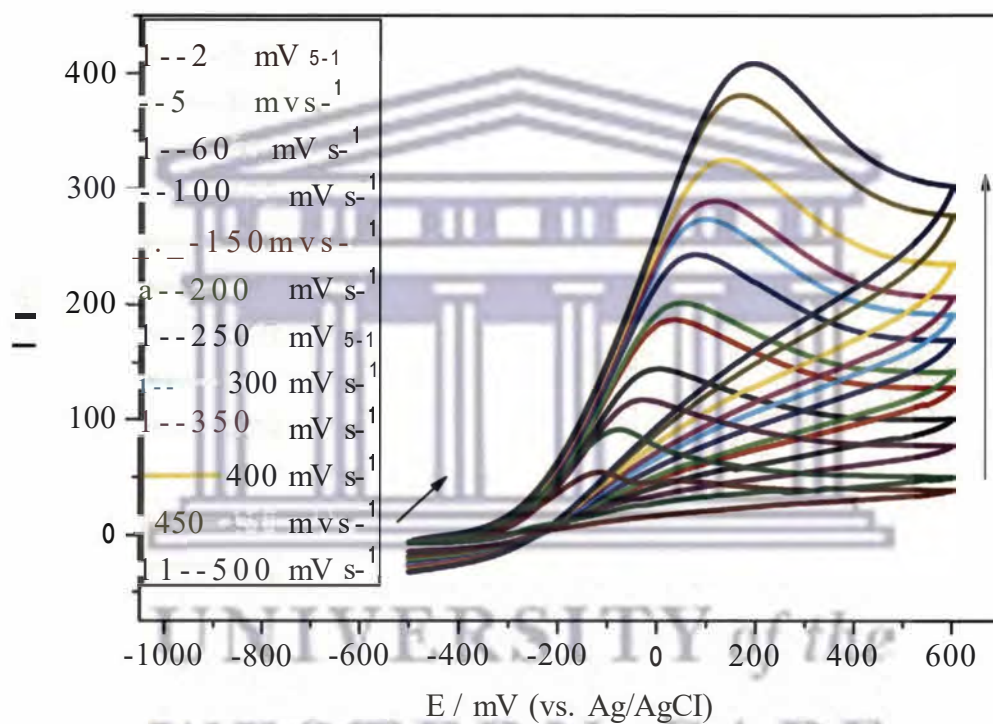


**Figure 88:** Cyclic voltammograms of Pt(100)NPs/GCE in 0.1 M PBS (pH 7.4) containing 10 mM hydrazine at various scan rates.

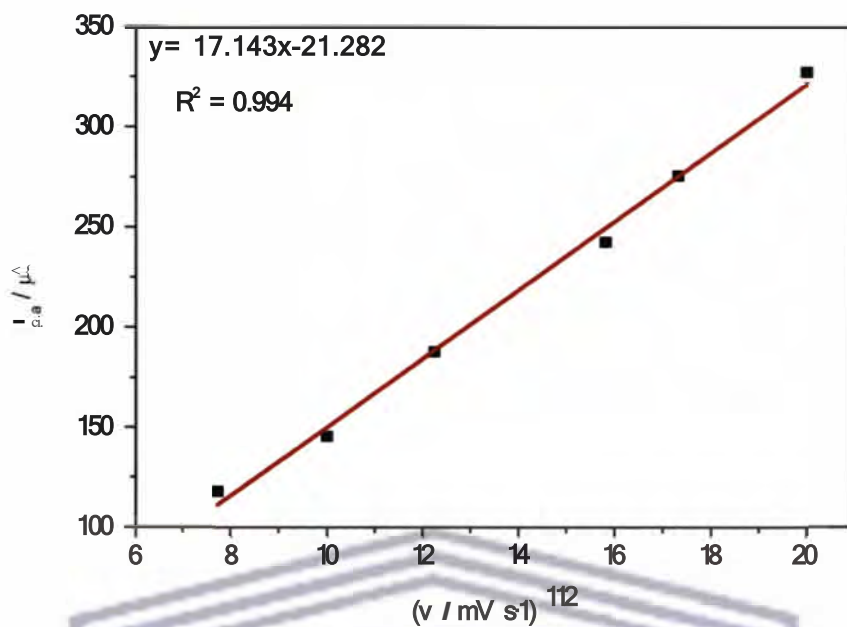


Figure 89: Randles-Sevcik plot of Pt(100)NPs/GCE in 0.1 M PBS (pH 7.4) containing 10 mM hydrazine.

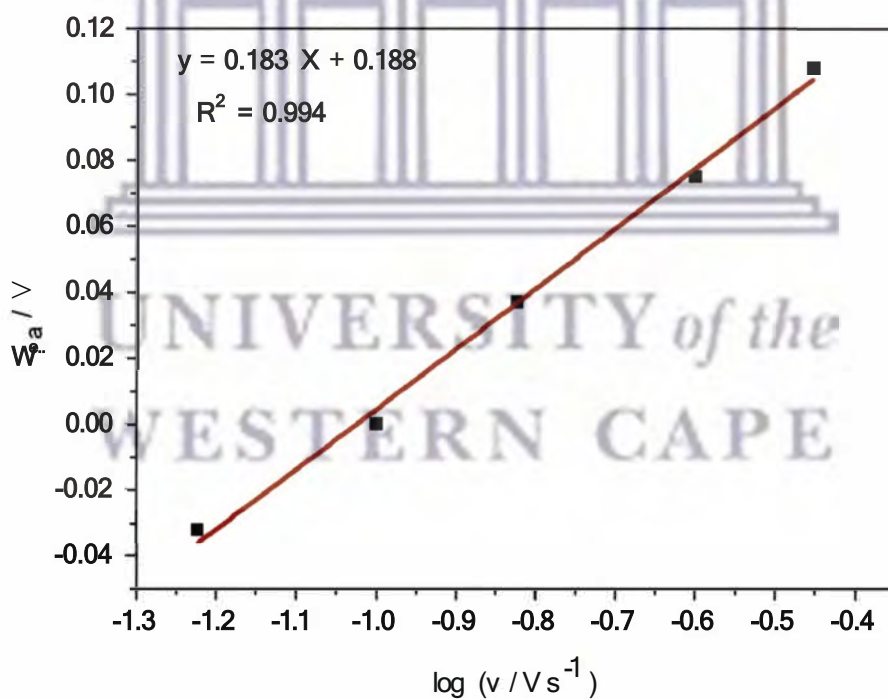


Figure 90: Relationship between the oxidation peak potential ( $E_p$ ) and log of scan rate for Pt(100)NPs/GCE in 0.1 M PBS (pH 7.4) containing 10 mM hydrazine.

## 7.2.2 Electro-oxidation of hydrazine on Pt(100)Pd nanoalloy modified GCE

Figure 91 presents the cyclic voltammograms of Pt(100)Pd nanoalloy modified GCE (Pt(100)PdNPs/GCE) (curve a) and bare GCE (curve b) in the absence and presence of 10 mM hydrazine in phosphate buffer solution (0.1 M and pH 7.4). As shown in Figure 91, curve b, no well-defined oxidation peak was observed for hydrazine at the bare GCE. A well resolved oxidation peak at 169 mV on Pt(100)PdNPs/GCE (Figure 91, curve a) was observed. This indicates the high catalytic activity of Pt(100)Pd nanoalloys towards hydrazine oxidation.

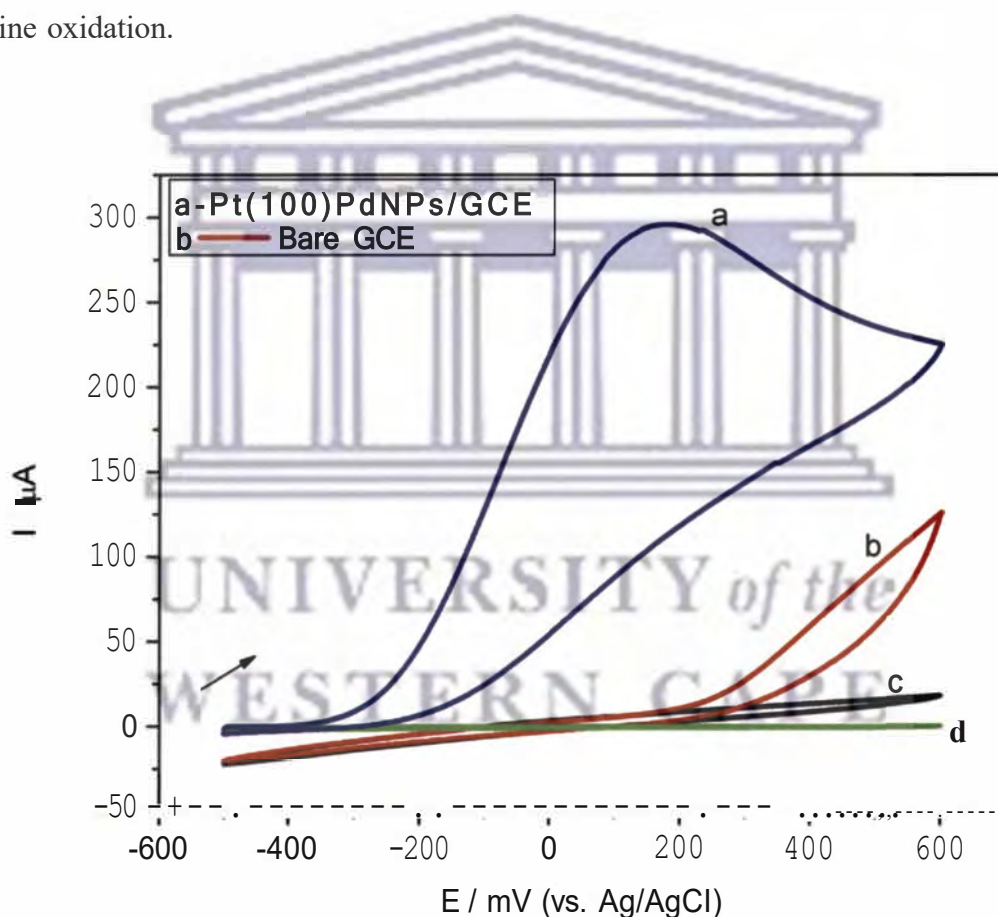


Figure 91: Cyclic voltammograms of 10 mM hydrazine at Pt(100)PdNPs/GCE (curve a) and bare GCE (curve b) in 0.1 M PBS (pH 7.4) at scan rate  $50 \text{ mV s}^{-1}$ . The voltammograms c (bare GCE) and d (Pt(100)PdNPs/GCE) are the backgrounds.

### 7.2.2.1 Effect of scan rates

Figure 92 shows the cyclic voltammograms of Pt(100)Pd nanoparticles modified GCE in 0.1 M PBS (pH 7.4) containing 10 mM hydrazine at different scan rates. It can be noted that the anodic peak currents increased and the peak potential shifted positively as the scan rate increases. The nature of the oxidation process was found to be diffusion controlled in the buffer system studied, as evidenced by the linear plots of the peak current ( $i_{p,a}$ ) versus square root of the scan rate ( $v^{1/2}$ ) (Figure 93) as depicted by the following linear relationship:

$$i_{p,a} = -112.067 + 57.966v^{1/2} \text{ (mV}^{1/2} \text{ s}^{-1/2}) \quad R^2 = 0.994 \dots \quad (56)$$

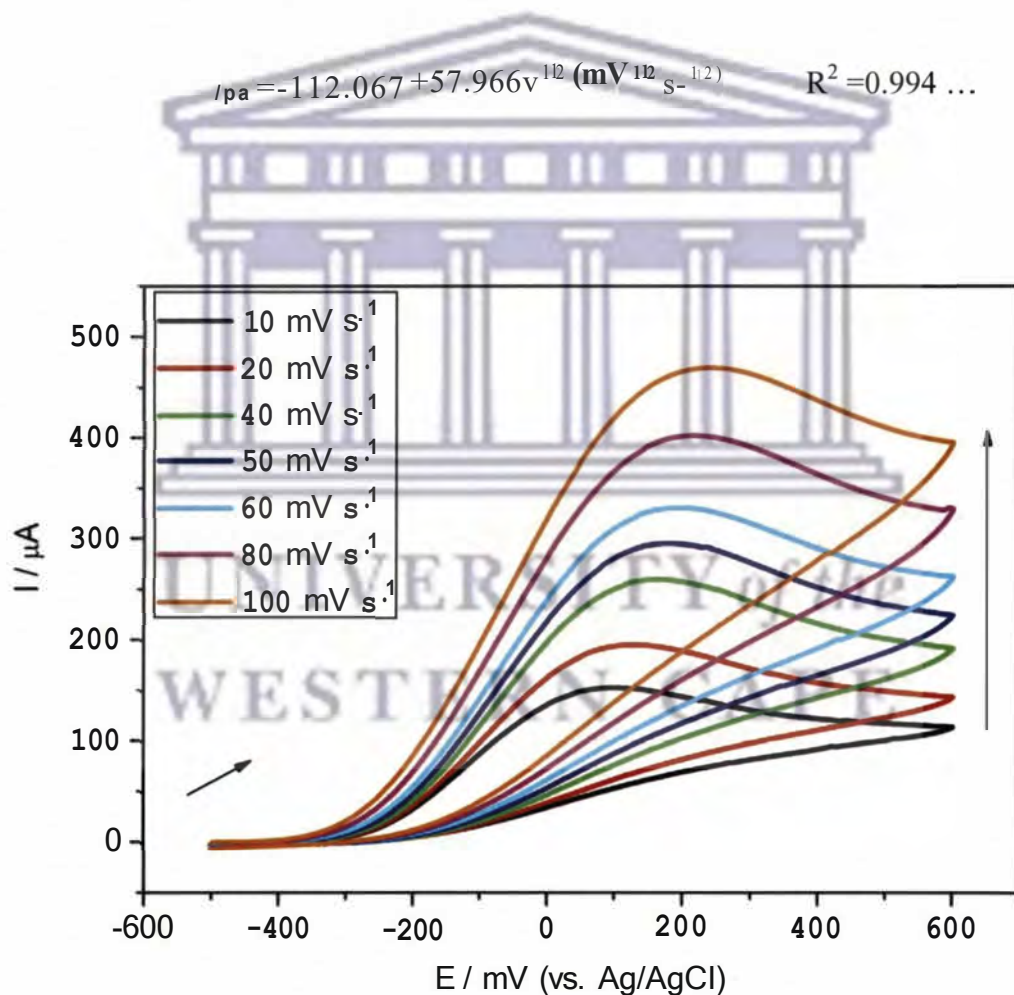
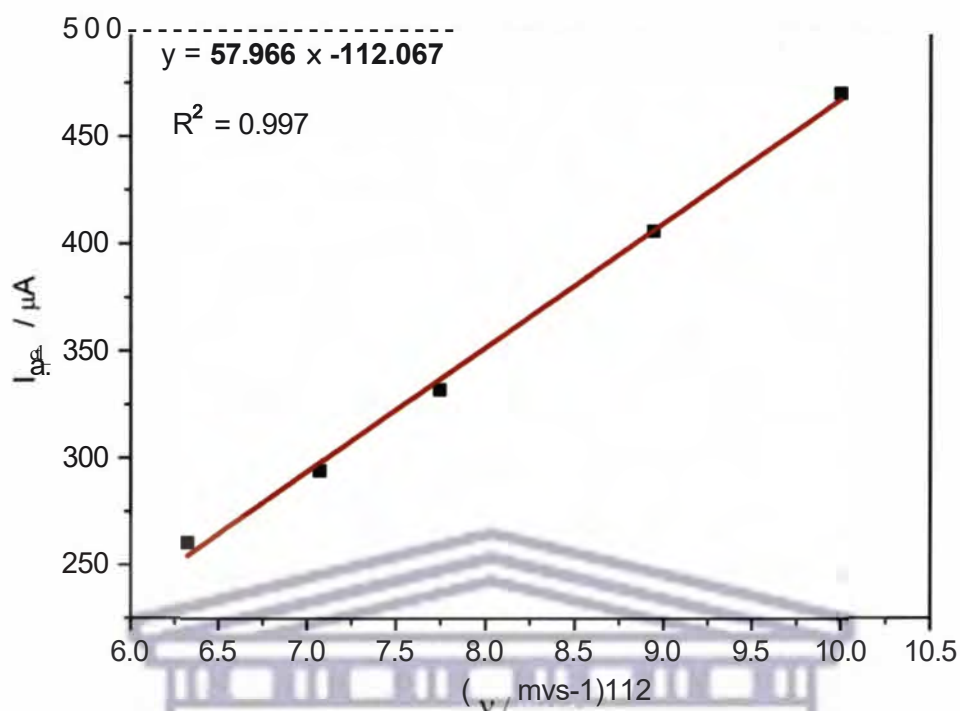


Figure 92: Cyclic voltammograms of Pt(100)PdNPs/GCE in 0.1 M PBS (pH 7.4) containing 10 mM hydrazine at various scan rates.





**Figure 93: Randles-Sevcik plot of Pt(100)PdNPs/GCE in 0.1 M PBS (pH 7.4) containing 10 mM hydrazine.**

In order to obtain the information on the rate determining step, Tafel slope,  $b$ , was determined using the following equation valid for a totally irreversible diffusion controlled process [80].

$$E_p = 0.5b \log v + \text{constant} \quad (57)$$

**Equation 57** can also be re-written as:

$$E_p = \frac{b}{2} \log v + \text{constant} \quad (58)$$

Therefore, on the basis of **equation 58**, the slope of  $E_p$  versus  $\log v$  plot is:

$$\frac{dE_p}{d \log v} = \frac{b}{2} \quad (59)$$

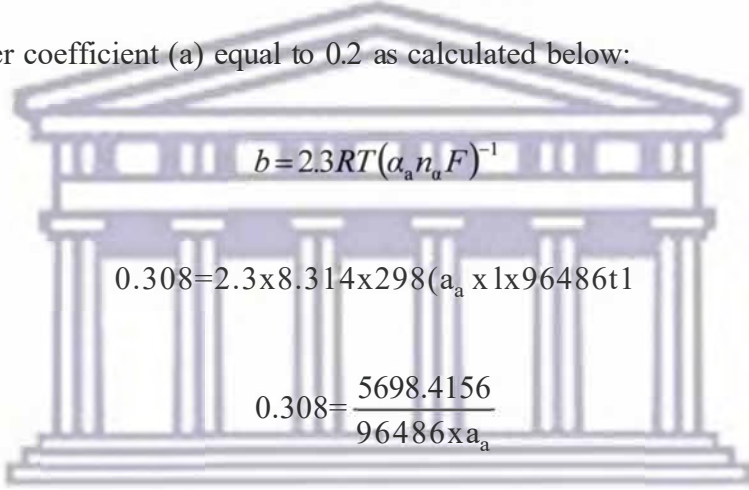
Where  $b$  is the Tafel slope and  $v$  is the scan rate. The Tafel slope can also be expressed as [80]:

$$b = 2.3RT(\alpha_a n_a F)^{-1} \quad (60)$$

When  $E_p$  values were plotted against  $\log v$  (**Figure 94**), the following linear relationship was obtained:

$$E_p = 0.373 + 0.154 \log v (\text{V s}^{-1}), \quad R^2 = 0.994 \quad (61)$$

The slope of the plots of  $E_p$  versus  $\log v$  is  $b/2$  which was found to be 0.154. So,  $b = 0.308$ . Assuming one electron transfer in the rate-determining step ( $n_a = 1$ ), this slope value indicates a transfer coefficient ( $\alpha$ ) equal to 0.2 as calculated below:



$$b = 2.3RT(\alpha_a n_a F)^{-1}$$

$$0.308 = 2.3 \times 8.314 \times 298 (\alpha_a \times 1 \times 96486)^{-1}$$

$$0.308 = \frac{5698.4156}{96486 \times \alpha_a}$$

$$\alpha_a = \frac{5698.4156}{96486 \times 0.308}$$

$$\alpha_a = 0.2$$

UNIVERSITY of the  
WESTERN CAPE

The number of electrons ( $n$ ) involved in the overall reaction was obtained from the slope of  $I_p$  versus  $v^{1/2}$  according to the following equation [80]:

$$I_p = 3.01 \times 10^5 n [(1 - \alpha) n \alpha]^{1/2} A C_s D^{1/2} v^{1/2} \quad (62)$$

where  $A$  is electrode surface area,  $C_s$  is hydrazine concentration and  $D$  is diffusion coefficient (assuming  $D = 4.1 \times 10^{-5} \text{ cm}^2 \text{ s}^{-1}$  calculated from chronoamperometric data). From the slope of  $I_p$  versus  $v^{1/2}$  plot, the total number of electrons ( $n$ ) involved in the oxidation was evaluated to be 4. This correlated well with the number of electrons involved in hydrazine oxidation as reported in literature [210].

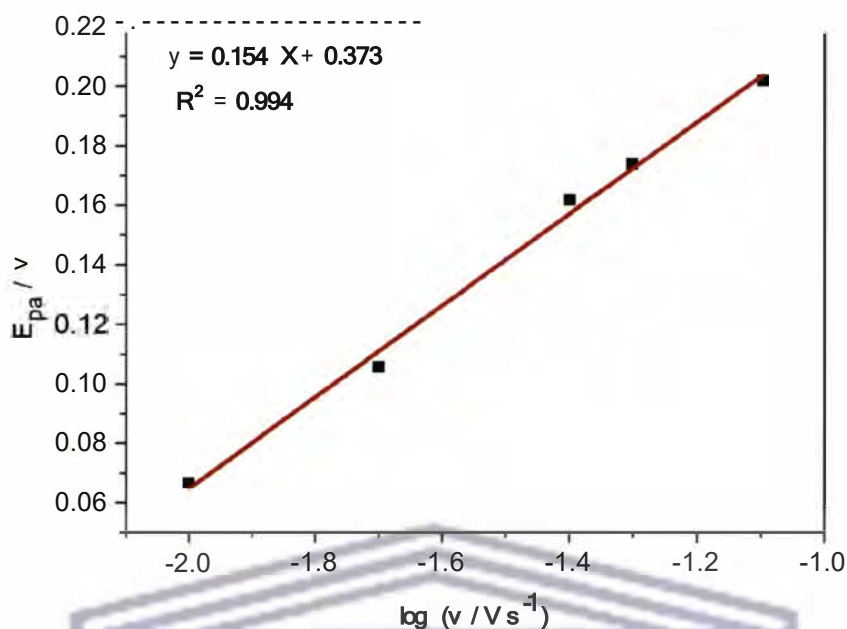
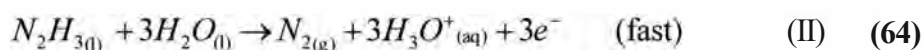
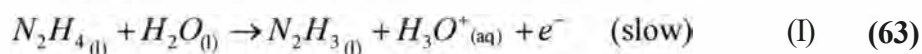
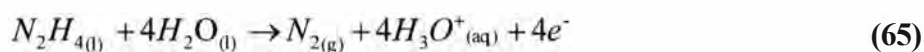


**Figure 94: Relationship between the oxidation peak potential ( $E_p$ ) and log of scan rate for Pt(100)PdNPs/GCE in 0.1 M PBS (pH 7.4) containing 10 mM hydrazine.**

The mechanism of hydrazine oxidation depends significantly on the electrolyte solution and the nature of the electrodes. Under solution conditions, hydrazine is mainly present in its unprotonated form and the protonated form is partially presented. The following mechanism could be proposed for the oxidation of hydrazine at the Pt(100)PdNPs/GCE [80, 210].



The rate-determining step is one electron transfer followed by a 3-electron process to give  $N_2$  as the final product. The overall reaction of the oxidation of hydrazine can be expressed as:



### 7.2.3 Electro-oxidation of hydrazine on Pt(100)Au nanoalloy modified GCE

In order to interrogate the catalytic effect of Pt(100)Au nanoalloys towards hydrazine electro-oxidation, Pt(100)Au nanoalloys modified GCE (Pt(100)AuNPs/GCE) was compared with bare GCE in presence of 10 mM hydrazine. The cyclic voltammetry method was used to estimate the electrocatalytic behaviour of the electrodes. **Figure 95** presents cyclic voltammograms of Pt(100)AuNPs/GCE (curve a) and bare GCE (curve b) in 0.1 M PBS (pH 7.4) at a scan rate of  $50 \text{ mV s}^{-1}$ . The bare GCE showed no catalytic effect towards hydrazine oxidation as no oxidation peak was observed. However, Pt(100)AuNPs/GCE showed a well-resolved oxidation peak with increased current density and reduced overpotential compared to the bare GCE. This result may be attributed to the large specific surface area of the Pt(100)Au nanoalloys. The electrochemical response of hydrazine on Pt(100)AuNPs/GCE was found to be irreversible as no cathodic peak was observed during the reverse sweep. Thus, Pt(100)Au nanoalloys were found to be good electrocatalysts for the oxidation of ammonia based on their ability to reduce hydrazine oxidation overpotential and increase the oxidation current density.

UNIVERSITY of the  
WESTERN CAPE

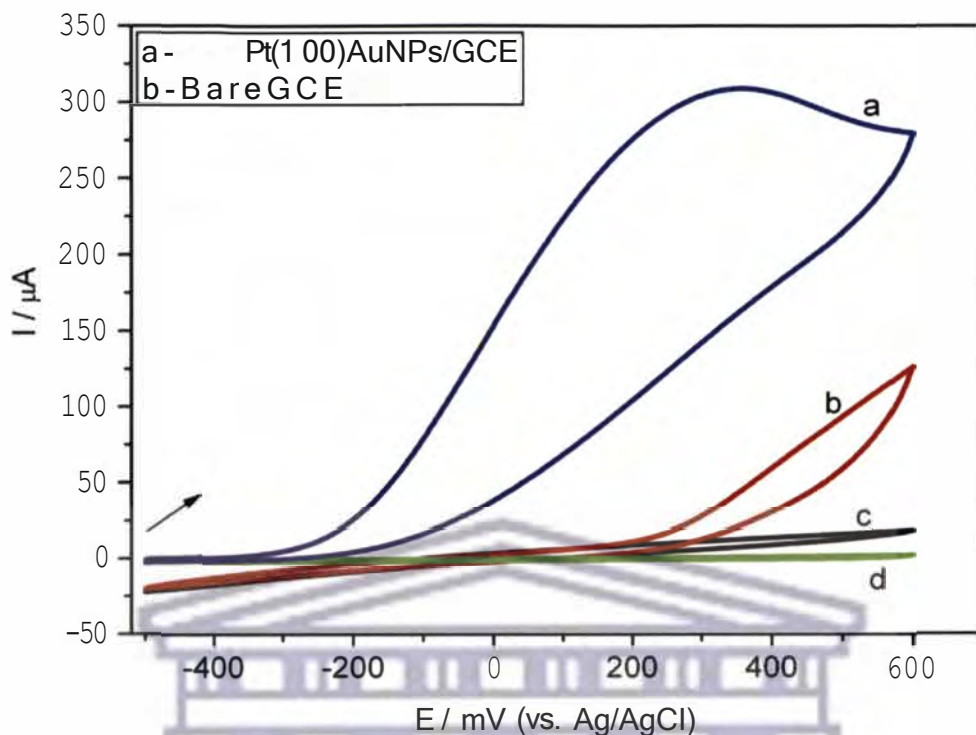


**Figure 95:** Cyclic voltammograms of 10 mM hydrazine at Pt(100)AuNPs/GCE (curve a) and bare GCE (curve b) in 0.1 M PBS (pH 7.4) at scan rate 50 mV s<sup>-1</sup>. The voltammograms c and d are the backgrounds.

### 7.2.3.1 Effect of scan rates

The effect of scan rate on hydrazine oxidation at Pt(100)AuNPs/GCE was studied and shown in **Figure 96**. It can be seen that the peak potential shifted slightly toward positive direction with increasing scan rate. The peak currents of hydrazine oxidation were linearly proportional to the square root of the scan rate ( $v^{1/2}$ ) with a correlation coefficient of 0.995 as shown in **Figure 97**. This indicates that the electrochemical reaction rate is fast and the oxidation of hydrazine on Pt(100)AuNPs/GCE is a typical diffusion-controlled process. A linear relationship between  $E_{p,a}$  and  $\log v$  was obtained, indicating the oxidation of hydrazine was an irreversible electrode process (**Figure 98**).

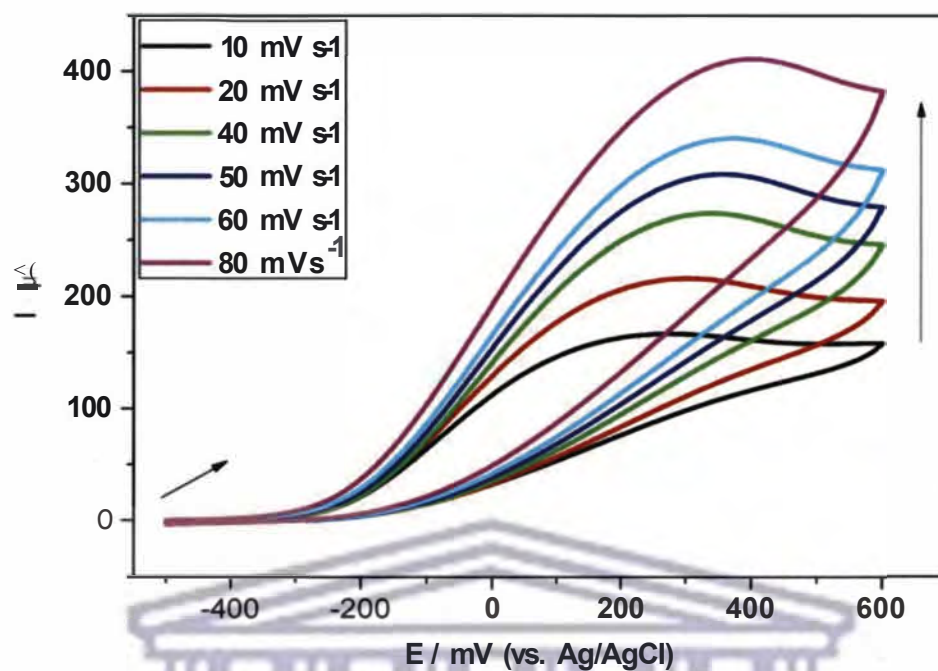


Figure 96: Cyclic voltammograms obtained for Pt(100)AuNPs/GCE in 0.1 M PBS (pH 7.4) containing 10 mM hydrazine at various scan rates.

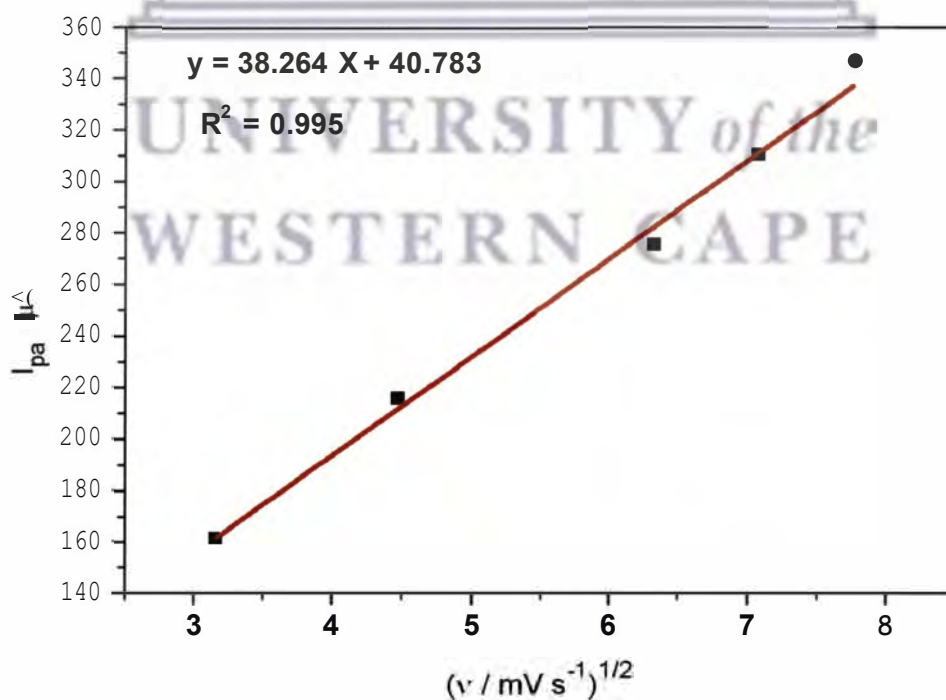
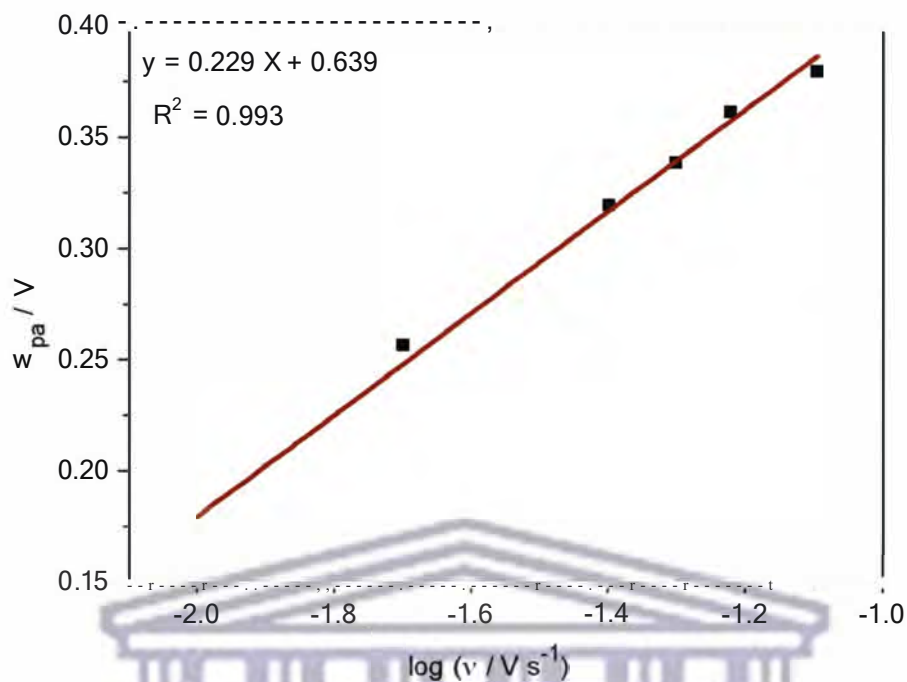


Figure 97: Randles-Sevcik plot of Pt(100)AuNPs/GCE in 0.1 M PBS (pH 7.4) containing 10 mM hydrazine.



**Figure 98: Relationship between the oxidation peak potential ( $E_p$ ) and log of scan rate for Pt(100)AuNPs/GCE in 0.1 M PBS (pH 7.4) containing 10 mM hydrazine.**

#### 7.2.4 Electro-oxidation of hydrazine on Pt(100)Ir, Pt(100)IrAu and Pt(100)PdIr nanoalloys modified GCE

In order to investigate the electrocatalytic behaviour of Pt(100)Ir, Pt(100)IrAu and Pt(100)PdIr nanoalloys modified GCE towards hydrazine oxidation, CVs were obtained in 10 mM hydrazine as shown in **Figure 99**. No defined anodic peak for hydrazine oxidation was observed on the bare GCE (curve a). Under the same experimental conditions, the CV obtained on Pt(100)IrNPs/GCE showed a remarkable increase in oxidation current and negative shift of the peak potential (curve b). The 352 mV reduction of overpotential indicated an efficiently catalytic ability of the Pt(100)Ir nanoalloys towards the oxidation of hydrazine. This large decrease in oxidation overpotential corresponds to the presence of high density arrays of Pt(100)Ir nanoalloys and their electrocatalytic behaviour. A well-defined oxidation peak appeared at 20 mV on the Pt(100)PdIr/GCE (curve c). There was an increased

peak current density and reduced overpotential as compared to the bare GCE which can be attributed to the high specific surface area of the Pt(100)PdIr nanoalloys. Pt(100)IrAuNPs/GCE (curve d) showed a stronger catalytic activity toward the oxidation of hydrazine as revealed by the increased current density and reduced overpotential.

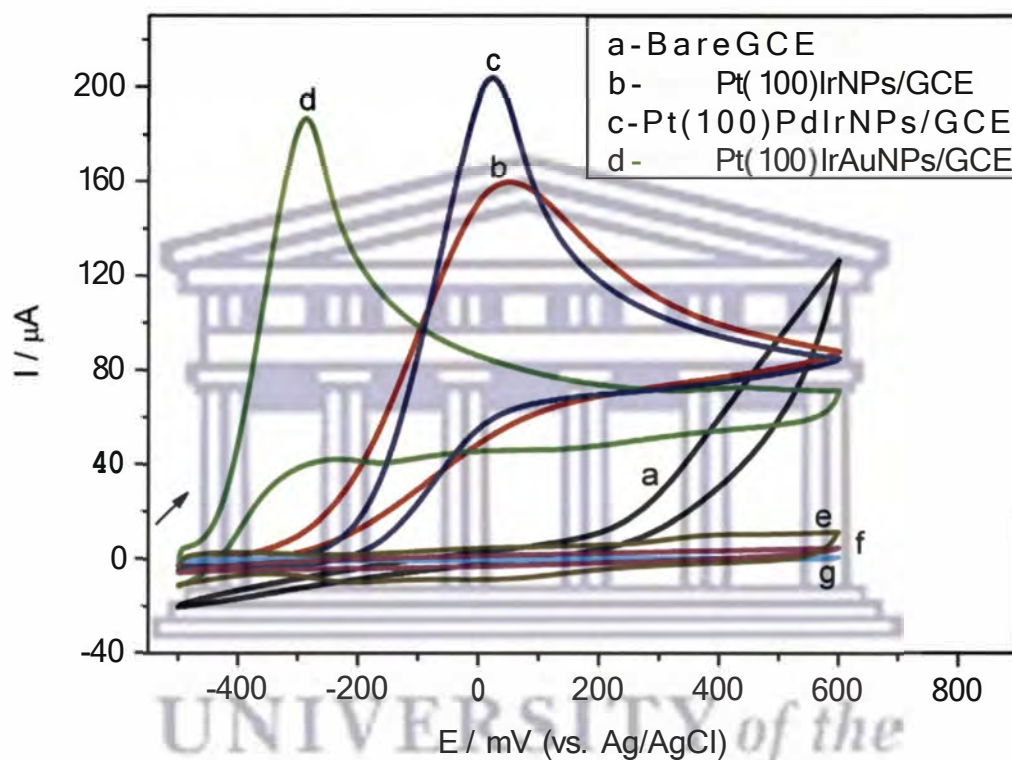


Figure 99: Cyclic voltammograms of 10 mM hydrazine at bare GCE (curve a), Pt(100)IrNPs/GCE (curve b), Pt(100)PdIrNPs/GCE (curve c), and Pt(100)IrAuNPs/GCE (curve d) in 0.1 M PBS (pH 7.4) at scan rate  $50 \text{ mV s}^{-1}$ . The voltammograms e, f and g are the backgrounds.

#### 7.2.4.1 Effect of scan rates

The scan rate effects on the oxidation of 10 mM hydrazine at Pt(100)IrNPs/GCE, Pt(100)PdIrNPs/GCE and Pt(100)IrAuNPs/GCE were investigated by CV as shown in Figures 100-102. Plots of anodic peak current versus the square root of scan rate ( $v^{1/2}$ )



yielded a straight line in the range of 20-400  $\text{mV s}^{-1}$ ,  $J_{p,a} (\mu\text{A}) = 20.316 v^{1/2} (\text{mV}^{1/2} \text{s}^{1/2}) + 9.696$  ( $R^2 = 0.997$ ) for Pt(100)IrNPs/GCE,  $10-400 \text{ mV s}^{-1}$ ,  $J_{p,a} (\mu\text{A}) = 28.270 v^{1/2} (\text{mV}^{1/2} \text{s}^{1/2}) + 17.643$  ( $R^2 = 0.994$ ) for Pt(100)PdIrNPs/GCE and  $50-400 \text{ mV s}^{-1}$ ,  $i_{p,a} (\mu\text{A}) = 35.932 v^{1/2} (\text{mV}^{1/2} \text{s}^{1/2}) - 66.761$  ( $R^2 = 0.994$ ) for Pt(100)IrAuNPs/GCE, respectively indicating that the electrocatalytic oxidation of hydrazine at the modified GCE's was typical diffusion-controlled electron transfer mechanism. The oxidation peak potentials ( $E_{p,a}$ ) of all the modified GCE's shifted positively with increase in scan rate ( $v$ ) denoting that the oxidation of hydrazine was an irreversible electrode process.

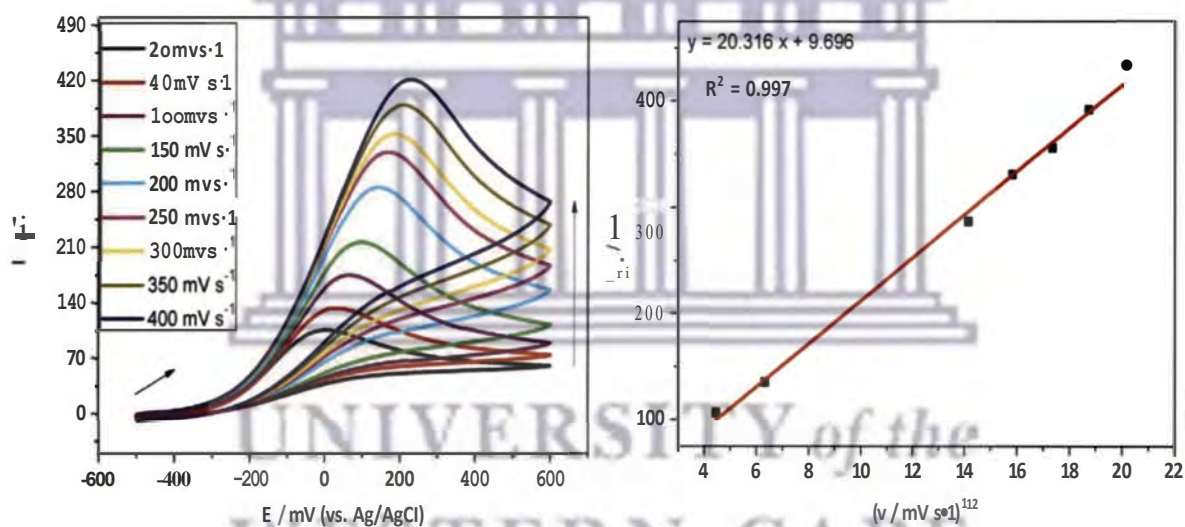


**Figure 100:** Cyclic voltammograms of Pt(100)IrNPs/GCE in 0.1 M PBS (pH 7.4) containing 10 mM hydrazine at various scan rates and a plot of peak current versus the square root of scan rate.

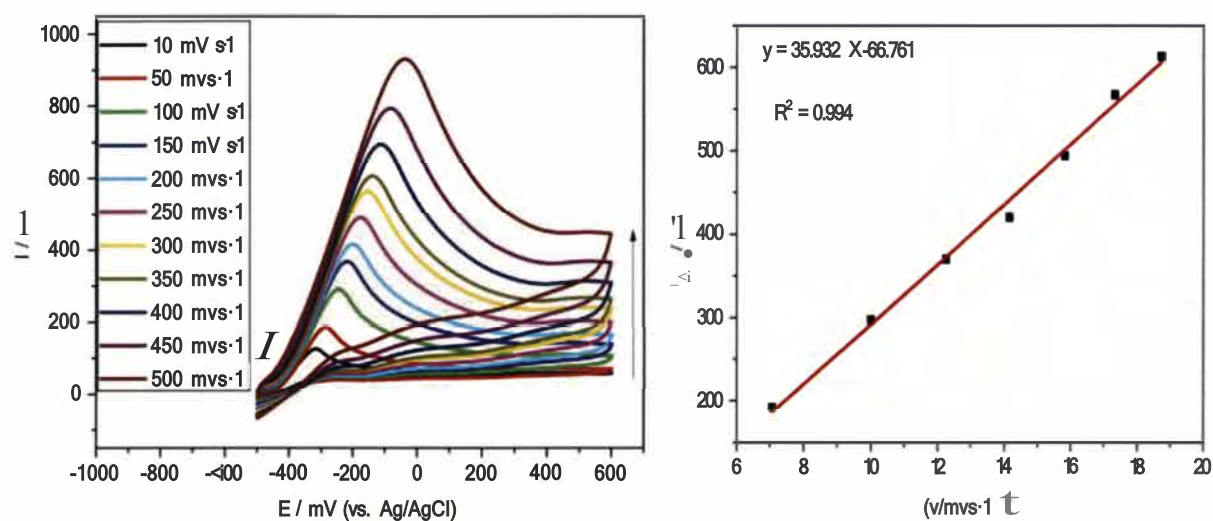


Figure 101: Cyclic voltammograms of Pt(IO0)IrAuNPs/GCE in 0.1 M PBS (pH 7.4) containing 10 mM hydrazine at various scan rates and a plot of peak current versus the square root of scan rate.

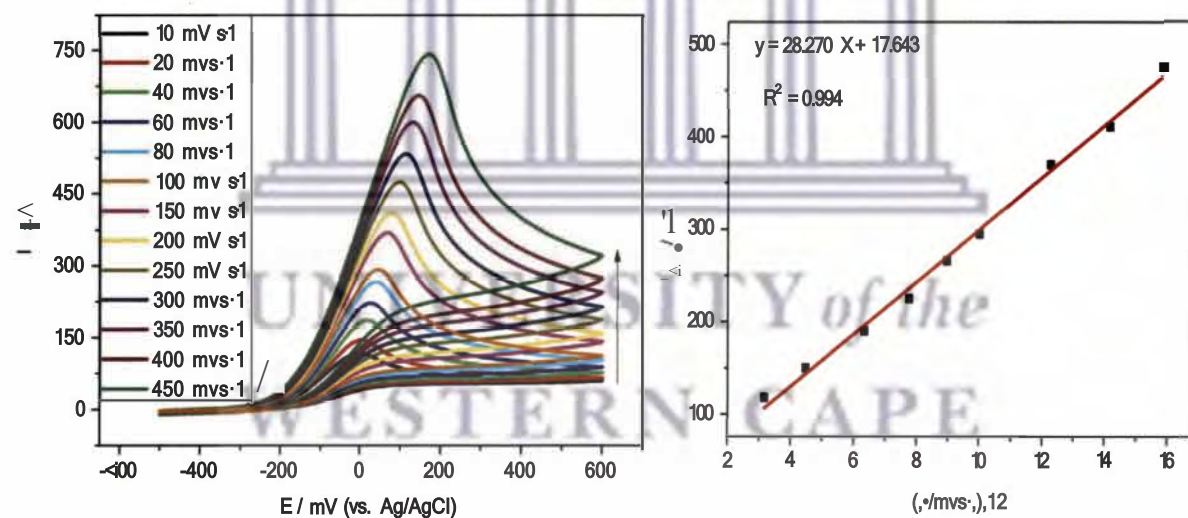


Figure 102: Cyclic voltammograms of Pt(IO0)PdIrNPs/GCE in 0.1 M PBS (pH 7.4) containing 10 mM hydrazine at various scan rates and a plot of peak current versus the square root of scan rate.

### 7.2.5 Electrocatalytic oxidation of hydrazine on Pt(100)Rh and Pt(100)RhAu nanoalloys modified GCE

In order to evaluate the electrocatalytic activity of Pt(100)RhNPs/GCE and Pt(100)RhAuNPs/GCE toward the oxidation of hydrazine, CVs were obtained in the presence of 10 mM hydrazine as shown in **Figure 103**. At bare GCE, a featureless oxidation peak current was observed at about 400 mV (curve a). The CV obtained at Pt(100)RhNPs/GCE showed a well-formed  $sh_{arp}$  catalytic oxidation peak at -82 mV (curve b). An even  $sh_{arp}$  catalytic peak appeared at -328 mV at Pt(100)RhAuNPs/GCE (curve c). There was an overall negative shift of the peak potentials which indicated that the catalytic activity of these electrodes was in the order of Pt(100)RhAuNPs/GCE > Pt(100)RhNPs/GCE > bare GCE. The increase in peak current and the reduction in peak potentials proved that Pt(100)RhAu and Pt(100)Rh nanoalloys have a strong catalytic character on hydrazine. The increase of current response can be partly attributed to the increase of reversibility of the electron transfer process, however, it may also be generated from the increased large surface area leading to a high surface accumulation of the electroactive species. The large decrease in the overpotential associated with a substantial increase in the peak height reflects a faster electron transfer reaction on the nanoalloys modified GCE's owing to the high catalytic effect of the nanoalloys. The faster electron transfer leads to sharper and better defined peaks.

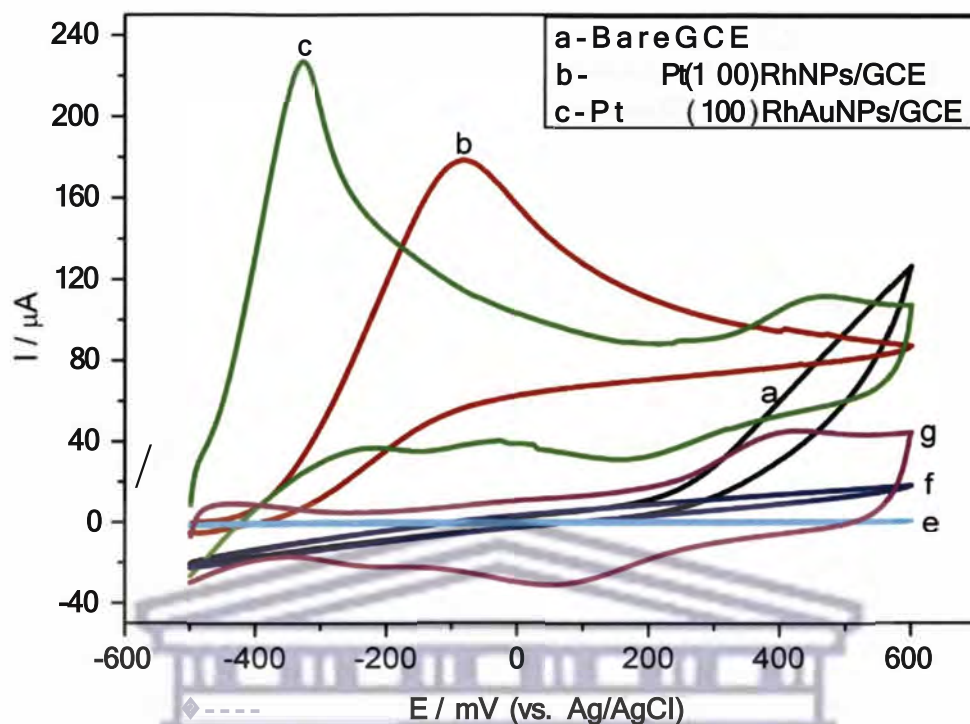


Figure 103: Cyclic voltammograms of 10 mM hydrazine at bare GCE (curve a), Pt(100)RhNPs/GCE (curve b) and Pt(100)RhAuNPs/GCE (curve c) in 0.1 M PBS (pH 7.4) at scan rate  $50 \text{ mV s}^{-1}$ . Curves e, f and g represent CVs at OM hydrazine.

### 7.2.5.1 Effect of scan rates

The scan rate effect on the cyclic voltammetric responses of Pt(100)Rh and Pt(100)RhAu nanoalloys modified electrodes in 0.1 M PBS (pH 7.4) with 10 mM hydrazine is shown in **Figures 104-105**. As the scan rate increased, the oxidation peak currents ( $i_{p,a}$ ) increased. A good linear relationship between  $i_{p,a}$  and scan rate was obtained over the range of 10 - 400  $\text{mV s}^{-1}$  for Pt(100)RhNPs/GCE and 60 - 300  $\text{mV s}^{-1}$  for Pt(100)RhAuNPs/GCE. The linear regression equation was  $i_{p,a} (\mu\text{A}) = 18.045 v^{1/2} (\text{mV}^{1/2} \text{s}^{1/2}) + 28.520$  ( $R^2 = 0.996$ ) for Pt(100)RhNPs/GCE and  $i_{p,a} (\mu\text{A}) = 30.506 v^{1/2} (\text{mV}^{1/2} \text{s}^{1/2}) - 68.414$  ( $R^2 = 0.997$ ) for Pt(100)RhAuNPs/GCE, respectively depicting that the responses of the hydrazine on the surface of Pt(100)Rh and Pt(100)RhAu nanoalloys modified electrodes were diffusion

controlled. It can be seen that the peak potential shifted slightly toward positive direction with increasing the scan rate a characteristic feature of irreversible systems.

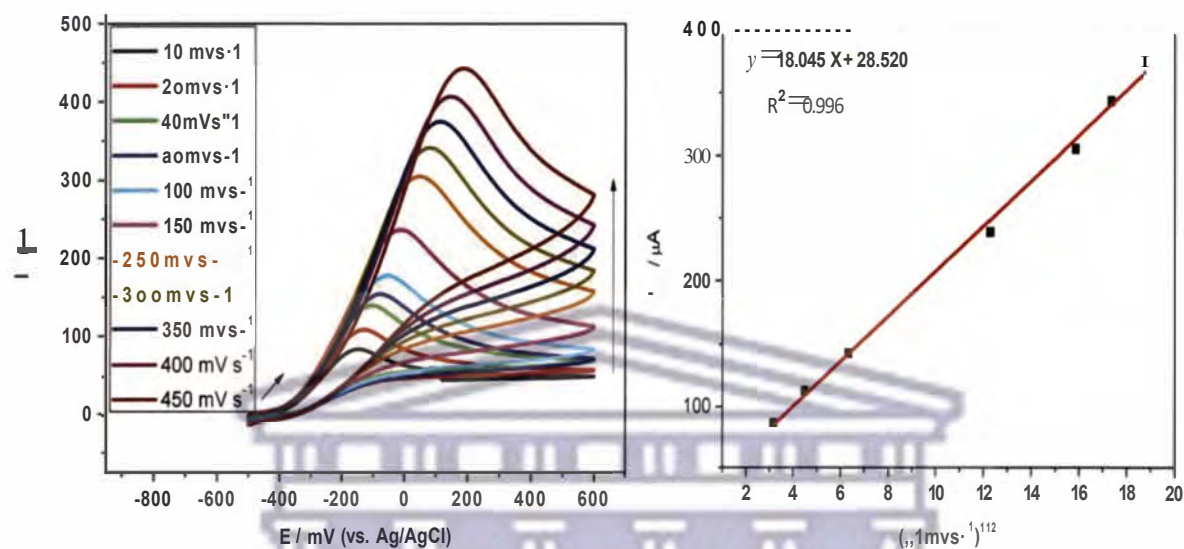


Figure 104: Cyclic voltammograms of Pt(100)RhNPs/GCE in 0.1 M PBS (pH 7.4) containing 10 mM hydrazine at various scan rates and a plot of peak current versus the square root of scan rate.

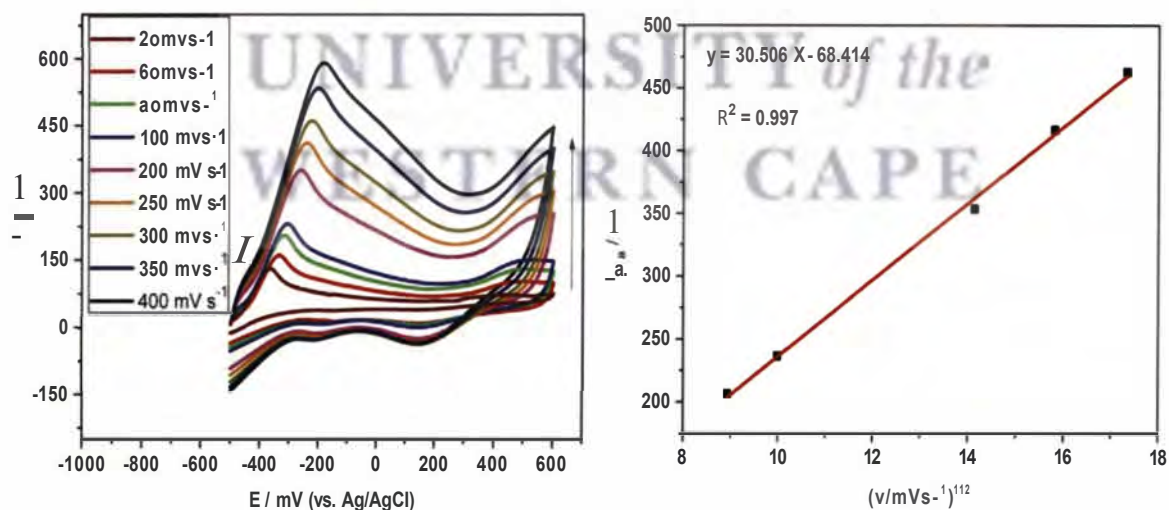


Figure 105: Cyclic voltammograms of Pt(100)RhAuNPs/GCE in 0.1 M PBS (pH 7.4) containing 10 mM hydrazine at various scan rates and a plot of peak current versus the square root of scan rate.

### 7.2.6 Comparison of the catalytic effects of the nanoalloys on hydrazine oxidation

The CVs of hydrazine oxidation on Pt(100)NPs/GCE, Pt(100)PdNPs/GCE, Pt(100)AuNPs/GCE, Pt(100)IrNPs/GCE, Pt(100)PdIrNPs/GCE, Pt(100)IrAuNPs/GCE, Pt(100)RhNPs/GCE and Pt(100)RhAuNPs/GCE were compared to that on bare GCE in the presence of 10 mM hydrazine. The catalytic activity of these electrodes with respect to reduced overpotential follows the order; Pt(100)RhAuNPs/GCE > Pt(100)IrAuNPs/GCE > Pt(100)RhNPs/GCE > Pt(100)PdIrNPs/GCE > Pt(100)NPs/GCE > Pt(100)IrNPs/GCE > Pt(100)PdNPs/GCE > Pt(100)AuNPs/GCE. Based on increased current density, the electrocatalytic activity of the nanoparticles followed the order; Pt(100)AuNPs/GCE > Pt(100)PdNPs/GCE > Pt(100)RhAuNPs/GCE > Pt(100)PdIrNPs/GCE > Pt(100)IrAuNPs/GCE > Pt(100)RhNPs/GCE > Pt(100)IrNPs/GCE > Pt(100)NPs/GCE as shown in table 10.

**Table 10: CV parameters of Pt(100) nanoalloys in 0.1 M PBS and 10 mM hydrazine**

Electrode	$E_{p,a}$ (mV)	$i_{p,a}$ ( $\mu$ A)
Bare GCE	400	11.556
Pt(100)NPs/GCE	20	159.713
Pt(100)IrNPs/GCE	48	161.039
Pt(100)RhNPs/GCE	-82	179.696
Pt(100)IrAuNPs/GCE	-288	187.581
Pt(100)PdIrNPs/GCE	20	204.406
Pt(100)RhAuNPs/GCE	-328	227.882
Pt(100)PdNPs/GCE	169	296.752
Pt(100)AuNPs/GCE	342	309.977

### 7.3 Sub conclusion

The lack of carbon atoms in hydrazine, resulting in zero emission of CO<sub>2</sub> to the atmosphere makes it a unique fuel for direct fuel cells. It is also a liquid and can be easily stored and transferred through existing supply chains. Hydrazine is a simple molecule with high theoretical power density, and can be electro-oxidized on the surface of many catalysts via mechanisms leading only to nitrogen and water. The electro-oxidation of N<sub>2</sub>H<sub>4</sub> was intensively studied using preferentially oriented Pt(100) based nanoalloys. A mechanism for electro-oxidation of hydrazine demonstrated an irreversible diffusion-controlled electrode process and a four-electron transfer involved in the overall reaction. This study has demonstrated for the first time that it is possible to catalytically oxidise hydrazine using oriented nanomaterials. This was revealed by:

- An increase oxidation current density
- Lower onset oxidation potentials
- Decrease in the oxidation overpotentials

The oriented Pt(100) nanoparticles and Pt(100) nanoalloy systems exhibited over 1000% increase in current density and 15% decrease overpotential for hydrazine electro-oxidation compared to the bare GCE. The much improved current density of the oriented nanoalloys is attributed to the increased surface area and the presence of (100) sites which favour faster hydrazine oxidation rates.

## CHAPTER EIGHT

### GENERAL CONCLUSION AND RECOMENDATIONS

#### *Summary*

*This chapter revisits the specific objectives of the study to report whether the aims of this dissertation were achieved and to give an overview of the success and shortcomings of the study. Also reported here is an indication of which areas of this study warrant further investigations in the future.*

UNIVERSITY of the  
WESTERN CAPE



## 8.1 General conclusion

### 8.1.1 Summary of findings and contributions

Highly electrocatalytic PdAuAg nanoalloys were prepared through a facile synthesis with ascorbic acid as a reductant and poly(vinyl pyrrolidone) (PVP) as a stabilising agent from aqueous solutions of PdCl<sub>2</sub>/HAuCl<sub>4</sub>·3H<sub>2</sub>O/AgNO<sub>3</sub> mixtures. High resolution transmission electron microscopy (HRTEM) revealed the formation of crystalline non-aggregated 25-35 nm sized nanoalloys. The elemental composition of the alloy nanoparticles measured using energy dispersive X-ray (EDX) showed the presence of the three elements; Pd, Au and Ag. The electrocatalytic behaviour of the PdAuAg nanoalloys for ammonia oxidation in KOH solution showed reduced overpotential properties and an increased current density compared to the bare Pt electrode thus providing a promising alternative for development of low-cost and high-performance electrocatalyst for electro-oxidation of ammonia.

Novel sodium polyacrylate-capped Pt(100)Pd, Pt(100)Au, Pt(100)PdAu, Pt(100)Rh, Pt(100)Ir, Pt(100)RhAu, Pt(100)PdIr and Pt(100)IrAu nanoalloys were also synthesised. The nanoalloys were formed in the presence of sodium polyacrylate which acted as a capping material. The electrostatic repulsion of negatively charged carboxyl groups present in the sodium polyacrylate prevented the nanoalloys from agglomeration. The shapes and the structures of the nanoalloys were studied using high resolution transmission electron microscopy (HRTEM) and cyclic voltammetry (CV). HRTEM analysis provided information about the size and the shape of the nanoalloys; the nanoalloys were found to be below 20 nm in size and having a high amount of (100) sites. The CV of the nanoparticles in the hydrogen adsorption/desorption region was used as structure sensitive reaction to obtain qualitative

information about the surface structure of the nanoparticles with the Pt(100) nanoparticles showing a voltammetric profile very similar to that of Pt(100) single crystal electrode. The results reported in this work demonstrate the importance of controlling the intrinsic structural properties of Pt nanoparticles; in terms of nature of the active sites and the effect of adding adatoms in order to understand their catalytic properties. Of all the electrocatalysts that were synthesised, Pt(100)RhAu nanoalloys were found to be the most active electrocatalyst in terms of maximising the oxidation of ammonia. In terms of minimising the ammonia oxidation overpotential, catalyst selection was ranked as follows Pt(100)Rh > Pt(100) Ir > Pt(100)PdIr > Pt(100)Pd > Pt(100)Au > Pt(100)IrAu > Pt(100)PdAu > Pt(100) > Pt(100)RhAu. With regards to maximising the exchange current density, the ranking is Pt(100)RhAu > Pt(100)PdIr > Pt(100) > Pt(100)IrAu > Pt(100)Pd > Pt(100)Rh > Pt(100)Au > Pt(100)Ir > Pt(100)PdAu as shown in **table 11**. The results indicate that having tri-metallic catalysts have advantages for ammonia electro-oxidation.



UNIVERSITY of the  
WESTERN CAPE

**Table 11. CV oxidation peak parameters Pt(100) nanoalloys in 0.1 M ammonia and 1 M KOH**

Electrode	$E_{p,a}$ (mV)	$i_{p,a}$ (A)
Bare Pt electrode	-281	$1.525 \times 10^{-5}$
Pt Pt(100)PdAuNPs	-276	$2.028 \times 10^{-5}$
Pt Pt(100)IrNPs	-300	$2.292 \times 10^{-5}$
Pt Pt(100)AuNPs	-285	$3.185 \times 10^{-5}$
Pt Pt(100)RhNPs	-301	$3.417 \times 10^{-5}$
Pt Pt(100)PdNPs	-295	$3.972 \times 10^{-5}$
Pt Pt(100)IrAuNPs	-281	$1.124 \times 10^{-4}$
Pt Pt(100)NPs	-276	$1.274 \times 10^{-4}$
Pt Pt(100)PdIrNPs	-299	$1.361 \times 10^{-4}$
Pt Pt(100)RhAuNPs	-274	$1.681 \times 10^{-4}$

The synthesised catalysts were also tested towards hydrazine oxidation. The catalytic activity of these catalysts with respect to reduced overpotential follows the order; Pt(100)Au > Pt(100)Pd > Pt(100)Ir > Pt(100)PdIr > Pt(100)Rh > Pt(100)IrAu > Pt(100)RhAu nanoalloys. Based on increased current density, the electrocatalytic activity of the nanoparticles followed the order; Pt(100)Au > Pt(100)Pd > Pt(100)RhAu > Pt(100)PdIr > Pt(100)IrAu > Pt(100)Rh > Pt(100)Ir nanoalloys. This work has shown for the first time that preferentially oriented Pt(100) nanoalloy systems possess suitable electrochemical and electrocatalytic properties

that make them applicable as electrocatalysts for the oxidation of ammonia and hydrazine. The nanoalloys film provides a promising route for the development of low-cost, high performance electrocatalysts for electro-oxidation of ammonia and hydrazine.

## 8.2 Recommendations

The following further investigations are recommended as a follow up to the research activities and results obtained in this PhD study:

- ▶ Interrogation of the electrocatalytic behaviour of the oriented Pt(100) nanoalloy systems supported on multi-walled carbon nanotubes and polymers towards the oxidation of ammonia and hydrazine.
- ▶ In-corporation of other transition metal or metal oxides into the Pt(100) nanoalloy systems to increase the activity of the electrocatalysts can also be studied.
- ▶ The Pt(100) nanoalloy systems showed excellent catalytic properties towards ammonia and hydrazine oxidation. The application of the electrocatalysts in model DAFCs and DHFCs is worth investigating.

UNIVERSITY of the  
WESTERN CAPE

## References:

1. Anghel, V. Prediction failure for PEM fuel cells. *International Journal of Advances in Engineering & Technology* **2012**, 4, 1-4.
2. Dincer, B. Hydrogen and Fuel Cell Technologies for Sustainable Future. *Jordan Journal of Mechanical and Industrial Engineering* **2008**, 2, 1-14.
3. Yin, W.X.; Li, Z.P.; Zhu, J.K.; Qin, H.Y. Effects of NaOH addition on performance of the direct hydrazine fuel cell. *Journal of Power Sources* **2008**, 182, 520-523.
4. Yamada, K.; Asazawa, K.; Yasuda, K.; Ioroi, T.; Tanaka, H.; Miyazaki, Y.; Kobayashi, T. Investigation of PEM type direct hydrazine fuel cell. *Journal of Power Sources* **2003**, 115, 236-242.
5. Dunn, S. Hydrogen futures: toward a sustainable energy system *International Journal of Hydrogen Energy* **2002**, 27, 235-264.
6. Edwards, P.P.; Kuznetsov, V.L.; David, W.I.F. Hydrogen energy. *Philosophical Transactions of the Royal Society A* **2007**, 365, 1043-1056.
7. Weissermel, K. Industrial Organic Chemistry. *Wiley-VCH*, Weinheim, Germany **2003**.
8. Jacobson, M.Z.; Colella, W.G.; Golden, D.M. Cleaning the Air and Improving Health with Hydrogen Fuel-Cell Vehicles. *Science* **2005**, 308, 1901-1905.
9. Granovskii, M.; Dincer, I.; Rosen, M.A. Exergetic life cycle assessment of hydrogen production from renewables. *Journal of Power Sources* **2007**, 167, 461-471.
10. Melaina, M.W. Initiating hydrogen infrastructures: preliminary analysis of a sufficient number of initial hydrogen stations in the US. *International Journal of Hydrogen Energy* **2003**, 28, 743 - 755.
11. Hwang, J.J.; Wang, D.Y.; Shih, N.C. Development of a lightweight fuel cell vehicle. *Journal of Power Sources* **2005**, 141, 108-115.

12. Vitse, F.; Cooper, M.; Botte, G.G. On the use of ammonia electrolysis for hydrogen production. *Journal of Power Sources* **2005**, 142, 18-26.
13. Strickland, G. Hydrogen derived from ammonia: Small-scale costs. *International Journal of Hydrogen Energy* **1984**, 9, 759-766.
14. Zhou, L.; Cheng, Y.F. Catalytic electrolysis of ammonia on platinum in alkaline solution for hydrogen generation. *International Journal of Hydrogen Energy* **2008**, 33, 5897-5904.
15. Lomocso, T.L.; Baranova, E.A. Electrochemical oxidation of ammonia on carbon-supported bi-metallic PtM (M = Ir, Pd, SnO<sub>x</sub>) nanoparticles. *Electrochimica Acta* **2011**, 56, 8551-8558.
16. Endo, K.; Nakamura, K.; Katayama, Y.; Miura, T. Pt–Me (Me = Ir, Ru, Ni) binary alloys as an ammonia oxidation anode. *Electrochimica Acta* **2004**, 49, 2503-2509.
17. Bonnin, E.P.; Biddinger, E.J.; Botte, G.G. Effect of catalyst on electrolysis of ammonia effluents. *Journal of Power Sources* **2008**, 182, 284-290.
18. Moran, E.; Cattaneo, C.; Mishima, H.; López de Mishima, B.; Silveti, S.; Rodriguez, J.; Pastor, E. Ammonia oxidation on electrodeposited Pt–Ir alloys. *Journal of Solid State Electrochemistry* **2008**, 12, 583-589.
19. Boggs, B.K.; Botte, G.G. Optimization of Pt–Ir on carbon fiber paper for the electro-oxidation of ammonia in alkaline media. *Electrochimica Acta* **2010**, 55, 5287-5293.
20. Yao, K.; Cheng, Y.F. Electrodeposited Ni–Pt binary alloys as electrocatalysts for oxidation of ammonia. *Journal of Power Sources* **2007**, 173, 96-101.
21. Kim, K.W.; Kim, Y.J.; Kim, I.T.; Park, G.I.; Lee, E.H. The electrolytic decomposition mechanism of ammonia to nitrogen at an IrO<sub>2</sub> anode. *Electrochimica Acta* **2005**, 50, 4356-4364.

22. Kapalka, A.; Fierro, S.; Frontistis, Z.; Katsaounis, A.; Neodo, S.; Frey, O.; de Rooij, N.; Udert, K.M.; Comninellis, C. Electrochemical oxidation of ammonia ( $\text{NH}_4^+/\text{NH}_3$ ) on thermally and electrochemically prepared  $\text{IrO}_2$  electrodes. *Electrochimica Acta* **2011**, *56*, 1361-1365.
23. Kapalka, A.; Fierro, S.; Frontistis, Z.; Katsaounis, A.; Frey, O.; Koudelka, M.; Comninellis, C.; Udert, K.M. Electrochemical behaviour of ammonia on electrochemically grown anodic iridium oxide film (AIROF) electrode. *Electrochemistry Communications* **2009**, *11*, 1590-1592.
24. Kapalka, A.; Katsaounis, A.; Michels, N.L.; Leonidova, A.; Souentie, S.; Comninellis, C.; Udert, K.M. Ammonia oxidation to nitrogen mediated by electrogenerated active chlorine on  $\text{Ti/PtO}_x\text{-IrO}_2$ . *Electrochemistry Communications* **2010**, *12*, 1203-1205.
25. Kapalka, A.; Cally, A.; Neodo, S.; Comninellis, C.; Wächter, M.; Udert, K.M. Electrochemical behavior of ammonia at  $\text{Ni/Ni(OH)}_2$  electrode. *Electrochemistry Communications* **2010**, *12*, 18-21.
26. Xiliang L.M.; Anthony J.K.; Malcolm R.S. Application of Nanoparticles in Electrochemical Sensors and Biosensors *Electroanalysis* **2005**, *18*, 319-326.
27. Altomare, M.; Selli, E. Effects of metal nanoparticles deposition on the photocatalytic oxidation of ammonia in  $\text{TiO}_2$  aqueous suspensions. *Catalysis Today* **2013**, *209*, 127-133.
28. Garbarino, S.; Ponrouch, A.; Pronovost, S.; Gaudet, J.; Guay, D. Synthesis and characterization of preferentially oriented (100) Pt nanowires. *Electrochemistry Communications* **2009**, *11*, 1924-1927.
29. Vidal-Iglesias, F.J.; Solla-Gullón, J.; Rodríguez, P.; Herrero, E.; Montiel, V.; Feliu, J.M.; Aldaz, A. Shape-dependent electrocatalysis: ammonia oxidation on platinum

- nanoparticles with preferential (100) surfaces. *Electrochemistry Communications* **2004**, 6, 1080-1084.
30. Vidal-Iglesias, F.J.; Solla-Gullón, J.; Montiel, V.; Feliu, J.M.; Aldaz, A. Screening of electrocatalysts for direct ammonia fuel cell: Ammonia oxidation on PtMe (Me: Ir, Rh, Pd, Ru) and preferentially oriented Pt(100) nanoparticles. *Journal of Power Sources* **2007**, 171, 448-456.
31. Zhou, M.; Chen, S.; Zhao, S.; Ma, H. One-step synthesis of Au-Ag alloy nanoparticles by a convenient electrochemical method. *Physica E* **2006** 33, 28-34.
32. Toshima, N.; Yonezawa, T. Bimetallic nanoparticles-novel materials for chemical and physical applications. *New Journal of Chemistry* **1998**, 22, 1179-1201.
33. Xiong, D.; Li, Z.; An, Y.; Ma, R.; Shi, L. Novel Au-Pd bimetallic core-shell nanocomplex and its catalytic activity modulation. *Journal of Colloid and Interface Science* **2010**, 350, 260-267.
34. Devarajan, S.; Vimalan, B.; Sampath, S. Phase transfer of Au-Ag alloy nanoparticles from aqueous medium to an organic solvent: effect of aging of surfactant on the formation of Ag-rich alloy compositions. *Journal of Colloid and Interface Science* **2004**, 278, 126-132.
35. Hung, C.M. Electrochemical properties of PtPdRh alloy catalysts for ammonia electrocatalytic oxidation. *International Journal of Hydrogen Energy* **2012**, 37, 13815-13821.
36. Yamada, K.; Yasuda, K.; Fujiwara, N.; Siroma, Z.; Tanaka, H.; Miyazaki, Y.; Kobayashi, T. Potential application of anion-exchange membrane for hydrazine fuel cell electrolyte. *Electrochemistry Communications* **2003**, 5, 892-896.
37. Martinez, U.; Asazawa, K.; Halevi, B.; Falase, A.; Kiefer, B.; Serov, A.; Padilla, M.; Olson, T.; Datye, A.; Tanaka, H.; Atanassov, P. Aerosol-derived  $Ni_{1-x}Zn_x$



- electrocatalysts for direct hydrazine fuel cells. *Physical Chemistry Chemical Physics* **2012**, 14, 5512-5517.
38. Endo, K.; Katayama, Y.; Miura, T. Pt–Ir and Pt–Cu binary alloys as the electrocatalyst for ammonia oxidation. *Electrochimica Acta* **2004**, 49, 1635–1638.
39. Endo, K.; Nakamura, K.; Katayama, Y.; Miura, T. Pt–Me (Me = Ru, Ni) binary alloys as an ammonia oxidation anode. *Electrochimica Acta* **2004**, 49, 2503–2509.
40. Endo, K.; Katayama, Y.; Miura, T. A rotating disk electrode study on the ammonia oxidation. *Electrochimica Acta* **2005**, 50, 2181–2185.
41. Rosca, V.; Koper, M.T. Electrocatalytic oxidation of ammonia on Pt(111) and Pt(100) surfaces. *Physical Chemistry Chemical Physics* **2006**, 8, 2513-2524.
42. Arana, L.R.; Schaevitz, S.B.; Franz, A.J.; Schmidt, M.A.; Jensen, K.F. A microfabricated suspended-tube chemical reactor for thermally efficient fuel processing. *Journal of Microelectromechanical Systems* **2003**, 12, 600-612.
43. Frederic, V.; Matt, C.; Gerardine, G.B. On the use of ammonia electrolysis for hydrogen production. *Journal of power sources* **2005**, 142, 18-26.
44. Kirubakaran, A.; Jain, S.; Nema, R.K. A review on fuel cell technologies and power electronic interface. *Renewable and Sustainable Energy Reviews* **2009**, 13, 2430-2440.
45. Ramakumar, R.; Chiradeja, P. Distributed generation and renewable energy systems. In: Proceedings of the 37<sup>th</sup> Intersociety Energy Conversion Engineering Conference, IECEC **2002**, 716–724.
46. Caisheng, W.; Hashem, N.M. Distributed generation applications of fuel cells. In: Power Systems Conference. *Advanced Metering, Protection, Control Communication and Distributed Resources* **2006**, 244–248.

47. Boudghene, S.A.; Traversa, E. Fuel cells, an alternative to standard sources of energy. *Renew Sustain Energy Review* **2002**, 6, 297–306.
48. "Batteries, Supercapacitors and Fuel Cells: Scope", Science Reference Services, 20 August 2007. <http://www.loc.gov/rr/scitech/tracer-bullets/batteriestb.html#scope>. Retrieved 11 February **2009**.
49. Brian, C. Introduction to fuel cells and hydrogen technology. *IEEE Proc.* **2002**, 205–216.
50. Todorovic, M.H.; Palma, L.; Prasad, E. Design of a wide input range dc–dc converter with a robust power control scheme suitable for fuel cell power conversion. In: *Proceedings of the 19<sup>th</sup> Annual IEEE Applied Power Electronics Conference and Exposition* **2004**, 374–379.
51. Huang, X.; Zhang, Z.; Jiang, J. Fuel cell technology for distributed generation: an overview. In: *IEEE Symposium on Industrial Electron* **2006**, 1613–1618.
52. Ellis, M.W.; Von, S.M.; Nelson, D.J. Fuel cell systems: efficient flexible energy conversion for the 21<sup>st</sup> century. *IEEE Proc* **2001**, 1808–1818.
53. Mozsgai, G.; Teom, J.; Flachsart, B.; Shannon, M.A. A silicon microfabricated direct formic acid fuel cell. In: *Proceedings of the 12<sup>th</sup> International Conference on Solid State Sensors, Actuators and Microsystems* **2003**, 1738–1741.
54. Farooque, M.; Maru, H.C.; Farooque, M. Fuel cells—the clean and efficient power generators. *IEEE Proc* **2001**, 89, 1819–1829.
55. U.S. Dept. of Energy. Fuel cell hand book, 7<sup>th</sup> ed., West Virginia: Office of Fossil Fuel, National Energy Technology Laboratory **2000**.
56. Garcia, B.L.; Sethuraman, V.A.; Weidner, J.W.; White, R.E.; Dougal, R. Mathematical model of a direct methanol fuel cell. *Journal of Fuel Cell Science Technol* **2004**, 43–48.

57. Zhong, C.; Hu, W.B.; Cheng, Y.F. Recent advances in electrocatalysts for electro-oxidation of ammonia. *Journal of Materials Chemistry A* **2013**, 1, 3216-3238.
58. Wynveen, R.A. *Fuel Cells*. **1963**, 2, 153-167.
59. Wasmus, S.; Vasini, E.J.; Krausa, M.; Mishima, H.T.; Vielstich, W. DEMS-cyclic voltammetry investigation of the electrochemistry of nitrogen compounds in 0.5 M potassium hydroxide. *Electrochimica Acta* **1994**, 39, 23-31.
60. Botte, G.G.; Vitse, F.; Cooper, M. Carbon fiber-electrocatalysts for the Oxidation of Ammonia, Ethanol, and Coal, and their Application to Hydrogen Production, Fuel Cells, and Purification Processes", Pending Patent **2004**.
61. Diaz, L.A.; Valenzuela-Muñiz, A.; Muthuvel, M.; Botte, G.G. Analysis of ammonia electro-oxidation kinetics using a rotating disk electrode. *Electrochimica Acta* **2013**, 89, 413-421.
62. Endo, K.; Nakamura, K.; Katayama, Y.; Miura, T. Pt-Me (Me = Ir, Ru, Ni) binary alloys as an ammonia oxidation anode. *Electrochimica Acta* **2004**, 49, 2503-2509.
63. Jisheng, G.; Dennis, C.J. Electrocatalysis of Anodic Oxygen-Transfer Reactions: Oxidation of Ammonia at Anodized Ag-Pb Eutectic Alloy Electrodes. *Journal of Electrochemical Society* **1995**, 142, 3420-3423.
64. Mikołaj, D.; Wojciech, H.; Małgorzata, C.; Zbigniew, S. Electrooxidation of ammonia and simple amines at titanium electrodes modified with a mixture of ruthenium and titanium dioxides. *Electroanalysis* **1997**, 9, 751-754.
65. Offermans, W.K.; Jansen, A.P.; Santen, V. Ammonia Dissociation on Pt{100}, Pt{111}, and Pt{211}: A Comparative Density Functional Theory Study. *American Chemical Society* **2007**, 6, 6-7.

66. Hadi, M.; Rouhollahi, A.; Yousefi, M. Nanocrystalline graphite-like pyrolytic carbon film electrode for electrochemical sensing of hydrazine. *Sensors and Actuators B: Chemical* **2011**, 160, 121-128.
67. Zare, H.R.; Shishehbore, M.R.; Nematollahi, D.; Tehrani, M.S. Electrochemical behavior of nano-composite containing 4-hydroxy-2-(triphenylphosphonio)phenolate and multi-wall carbon nanotubes spiked in carbon paste and its application for electrocatalytic oxidation of hydrazine. *Sensors and Actuators B: Chemical* **2010**, 151, 153-161.
68. Fang, B.; Feng, Y.; Liu, M.; Wang, G.; Zhang, X.; Wang, M. Electrocatalytic oxidation of hydrazine at a glassy carbon electrode modified with nickel ferrite and multi-walled carbon nanotubes. *Microchimica Acta* **2011**, 175, 145-150.
69. Zheng, L.; Song, J.F. Curcumin multi-wall carbon nanotubes modified glassy carbon electrode and its electrocatalytic activity towards oxidation of hydrazine. *Sensors and Actuators B: Chemical* **2009**, 135, 650-655.
70. Gholivand, M.B.; Azadbakht, A. A novel hydrazine electrochemical sensor based on a zirconium hexacyanoferrate film-bimetallic Au-Pt inorganic-organic hybrid nanocomposite onto glassy carbon-modified electrode. *Electrochimica Acta* **2011**, 56, 10044-10054.
71. Lin, H.; Yang, J.; Liu, J.; Huang, Y.; Xiao, J.; Zhang, X. Properties of Pd nanoparticles-embedded polyaniline multilayer film and its electrocatalytic activity for hydrazine oxidation. *Electrochimica Acta* **2013**, 90, 382-392.
72. Mehta, S.K.; Khushboo; Umar, A. Highly sensitive hydrazine chemical sensor based on mono-dispersed rapidly synthesized PEG-coated ZnS nanoparticles. *Talanta* **2011**, 85, 2411-2416.

73. Yan, X.; Meng, F.; Cui, S.; Liu, J.; Gu, J.; Zou, Z. Effective and rapid electrochemical detection of hydrazine by nanoporous gold. *Journal of Electroanalytical Chemistry* **2011**, 661, 44-48.
74. Mazloun-Ardakani, M.; Rajabi, H.; Beitollahi, H. Homogeneous and nanomolar detection of hydrazine by indigocarmine as a mediator at the surface of TiO<sub>2</sub> nanoparticles modified carbon paste electrode. *Chinese Chemical Letters* **2012**, 23, 213-216.
75. Haghghi, B.; Hamidi, H.; Bozorgzadeh, S. Sensitive and selective determination of hydrazine using glassy carbon electrode modified with Pd nanoparticles decorated multiwalled carbon nanotubes. *Analytical and Bioanalytical Chemistry* **2010**, 398, 1411-1416.
76. Kim, S.K.; Jeong, Y.N.; Ahmed, M.S.; You, J.M.; Choi, H.C.; Jeon, S. Electrocatalytic determination of hydrazine by a glassy carbon electrode modified with PEDOP/MWCNTs-Pd nanoparticles. *Sensors and Actuators B: Chemical* **2011**, 153, 246-251.
77. Liu, R.; Jiang, X.; Guo, F.; Shi, N.; Yin, J.; Wang, G.; Cao, D. Carbon fiber cloth supported micro- and nano-structured Co as the electrode for hydrazine oxidation in alkaline media. *Electrochimica Acta* **2013**, 94, 214-218.
78. Serov, A.; Kwak, C. Direct hydrazine fuel cells: A review. *Applied Catalysis B: Environmental* **2010**, 98, 1-9.
79. Blomen, L.; Mugerwa, J.; Michael, N. Fuel cell systems. *Plenum press*, New York **1993**, 614.
80. Mirghasem, H.; Mohamad, M.; Masoud, F. Electro-oxidation of hydrazine on gold nanoparticles supported on TiO<sub>2</sub> nanotube matrix as a new high active electrode. *Journal of Molecular Catalysis A: Chemical* **2011**, 335, 199-204.

81. Zhao, Y.D.; Zhang, W.D.; Chen, H.; Luo, Q.M. Anodic oxidation of hydrazine at carbon nanotube powder microelectrode and its detection. *Talanta* **2002**, 58, 529-534.
82. Wang, Y.; Yang, X.; Bai, J.; Jiang, X.; Fan, G. High sensitivity hydrogen peroxide and hydrazine sensor based on silver nanocubes with rich {100} facets as an enhanced electrochemical sensing platform. *Biosensors and Bioelectronics* **2013**, 43, 180-185.
83. Scenihr. Modified Opinion (after public consultation) on the appropriateness of existing methodologies to assess the potential risks associated with engineered and adventitious products of nanotechnologies **2006**.
84. Royal Society and Royal Academy of Engineering, UK. *Nanoscience and nanotechnologies: opportunities and uncertainties* **2004**.
85. BSI, British Standards Institution. Vocabulary – Nanoparticles, Publicly Available Specification, BSI. London **2005**.
86. Penn, S.G.; He, L.; Natan, M.J. Nanoparticles for bioanalysis. *Current Opinion in Chemical Biology* **2003**, 7, 609-615.
87. Johnston. Atomic and molecular clusters. London: Taylor and Francis **2002**.
88. Johnston, R.L. Metal Nanoparticles and Nanoalloys. *Frontiers of Nanoscience* **2012**, 3, 1-42.
89. Francesca, B.; Riccardo, F. Structural properties of nanoclusters: Energetic, thermodynamic, and kinetic effects. *Review of Modern Physics* **2005**, 77, 371-423.
90. Johnston, R.L.; Ferrando, R. Nanoalloys: from theory to application. *Faraday Discuss Faraday Discuss* **2008**, 138, 1-442.
91. Ferrando, R.; Jellinek, J.; Johnston, R. L. Nanoalloys: From theory to applications of alloy clusters and nanoparticles. *Chemical Reviews* **2008**, 108, 845-910.
92. Min, Z.; Shenhao, C.; Shiyonb, Z.; Houyi, M. One-step synthesis of Ag-Au alloy nanoparticles by convenient electrochemical method. *Physica E* **2006**, 33, 28-34.

93. Naoki, T.; Tetsu, Y. Bimetallic nanoparticles-novel materials for chemical and physical applications. *New Journal of Chemistry* **1998**, 1179-1201.
94. De'an, X.; Zhe, Z.; Yingli, A.; Rujiang, M.; Linqi, S. Novel Au-Pd bimetallic core-shell nanocomplex and its catalytic activity modulation. *Journal of Colloid and Interface Science* **2010**, 350, 260-267.
95. Devarajan, S.; Vimalan, B.; Sampath, S. Phase transfer of Au-Ag alloy nanoparticles from aqueous medium to an organic solvent: effect of aging of surfactant on the formation of Ag-rich alloy compositions. *Journal of Colloid and Interface Science* **2004**, 278, 126-132.
96. Bönemann, H.; Richards, R.M. Nanoscopic Metal Particles – Synthetic Methods and Potential Applications. *European Journal of Inorganic Chemistry* **2001**, 2001, 2455-2480.
97. Luo, X.; Morrin, A.; Killard, A.J.; Smyth, M.R. Application of Nanoparticles in Electrochemical Sensors and Biosensors. *Electroanalysis* **2006**, 18, 319-326.
98. Wang, X.; Hu, C.; Xiong, Y.; Liu, H.; Du, G.; He, X. Carbon-nanosphere-supported Pt nanoparticles for methanol and ethanol electro-oxidation in alkaline media. *Journal of Power Sources* **2011**, 196, 1904-1908.
99. Tominaga, M.; Shimazoe, T.; Nagashima, M.; Taniguchi, I. Composition-activity relationships of carbon electrode-supported bimetallic gold-silver nanoparticles in electrocatalytic oxidation of glucose. *Journal of Electroanalytical Chemistry* **2008**, 615, 51-61.
100. Liu, T.; Zhong, J.; Gan, X.; Fan, C.; Li, G.; Matsuda, N. Wiring Electrons of Cytochrome c with Silver Nanoparticles in Layered Films. *ChemPhysChem* **2003**, 4, 1364-1366.

101. Alivisatos, P. The use of nanocrystals in biological detection. *Nature Biotechnology* **2004**, 22, 47-52.
102. Jusys, Z.; Behm, R.J. Simultaneous oxygen reduction and methanol oxidation on a carbon-supported Pt catalyst and mixed potential formation-revisited. *Electrochimica Acta* **2004**, 49, 3891-3900.
103. Takasu, Y.; Sugimoto, W.; Murakami, Y. Effects of the Surface Area of Carbon Support on the Characterization of Highly-Dispersed Pt-Ru Particles as Catalysts for Methanol Oxidation. *Electrochim. Acta* **2003**, 48, 3861-3868.
104. Park, K.; Kwon, B.; Lee, S.; Sung, Y.; Ha, H.; Hong, S.; Kim, H.; Wieckowski, A. Chemical and Electronic Effects of Ni in Pt/Ni and Pt/Ru/Ni Alloy Nanoparticles in Methanol Electrooxidation. *Physical Chemistry B* **2002**, 106, 1869-1877.
105. Zhou, X., Fan, L. Pt/Pd alloy nanoparticles composed of bimetallic nanobowls: Synthesis, characterization and electrocatalytic activities. *Electrochimica Acta* **2010**, 55, 8111-8115.
106. Xu, C.; Wang, R.; Chen, M.; Zhang, Y.; Ding, Y. Dealloying to nanoporous Au/Pt alloys and their structure sensitive electrocatalytic properties. *Physical Chemistry Chemical Physics* **2010**, 12, 239-246.
107. Kang, X.; Mai, Z.; Zou X.; Cai, P.; Mo, J. A novel glucose biosensor based on immobilization of glucose oxidase in chitosan on a glassy carbon electrode modified with gold-platinum alloy nanoparticles/multiwall carbon nanotubes. *Analytical Biochemistry* **2007**, 369, 71-79.
108. Manlan, T.; Zaisheng, W.; Meng, W.; Mei, H.; Yunhui, Y. The preparation of label-free electrochemical immunosensor based on the Pt-Au alloy nanotube array for detection of human chorionic gonadotrophin. *Clinica Chimica Acta* **2011** 412 550-555.



109. Clavilier, J.; Faure, R.; Guinet, G.; Durand, R. Preparation of monocrystalline Pt microelectrodes and electrochemical study of the plane surfaces cut in the direction of the (111) and (110) planes. *Journal of Electroanalytical Chemistry* **1980**, 107, 205-209.
110. Clavilier, J.; Albalat, R. Study of the charge displacement at constant potential during CO adsorption on Pt(110) and Pt(111) electrodes in contact with a perchloric acid solution. *Journal of Electroanalytical Chemistry* **1992**, 330, 489-497.
111. Gómez, R.; Javier Gutiérrez de Dios, F.; Feliu, J.M. Carbon monoxide oxidation and nitrous oxide reduction on Rh/Pt(111) electrodes. *Electrochimica Acta* **2004**, 49, 1195-1208.
112. Gómez, R.; Feliu, J.M. Rhodium adlayers on Pt(111) monocrystalline surfaces. Electrochemical behavior and electrocatalysis. *Electrochimica Acta* **1998**, 44, 1191-1205.
113. Sinfelt, J.H. Catalysis by alloys and bimetallic clusters: Accounts of Chemical Research. *American Chemical Society* **1977**, 10, 15-20.
114. Fruéhberger, B.; Eng, J.; Chen, J.G. Observation of anomalous reactivities of Ni/Pt(111) bimetallic surfaces Catalysis Letters. *Springer Netherlands* **1997**, 45, 85-92.
115. Bauer, E. The Chemical Physics of Solid Surfaces and Heterogeneous Catalysis, *Elsevier, Amsterdam* **1984**, 3, 3.
116. Campbell, C.T. Bimetallic Surface Chemistry. *Annual Review of Physical Chemistry* **1990**, 41, 775-837.
117. Rodriguez, J. Physical and chemical properties of bimetallic surfaces. *Surface Science Reports* **1996**, 24, 223-287.

118. Ahmadi, T.S.; Wang, Z.L.; Henglein, A.; El-Sayed, M.A. "Cubic" Colloidal Platinum Nanoparticles. *Chemistry of Materials* **1996**, *8*, 1161-1163.
119. Serrano-Ruiz, J.C.; López-Cudero, A.; Solla-Gullón, J.; Sepúlveda-Escribano, A.; Aldaz, A.; Rodríguez-Reinoso, F. Hydrogenation of  $\alpha$ ,  $\beta$  unsaturated aldehydes over polycrystalline, (111) and (100) preferentially oriented Pt nanoparticles supported on carbon. *Journal of Catalysis* **2008**, *253*, 159-166.
120. Solla-Gullón, J.; Vidal-Iglesias, F.J.; Herrero, E.; Feliu, J.M.; Aldaz, A. CO monolayer oxidation on semi-spherical and preferentially oriented (100) and (111) platinum nanoparticles. *Electrochemistry Communications* **2006**, *8*, 189-194.
121. Clavilier, J.; Durand, R.; Guinet, G.; Faure, R. Electrochemical adsorption behaviour of Pt(100) in sulphuric acid solution. *Journal of Electroanalytical Chemistry and Interfacial Electrochemistry* **1981**, *127*, 281-287.
122. Zhou, S.; Jackson, G.S.; Eichhorn, B. AuPt Alloy Nanoparticles for CO-Tolerant Hydrogen Activation: Architectural Effects in Au-Pt Bimetallic Nanocatalysts. *Advanced Functional Materials* **2007**, *17*, 3099-3104.
123. Stokenius, W.; Schulam, J.H.; Prince, L.M. Mechanism of Formation and Structure of Micro Emulsions by Electron Microscopy. *Journal of Physical Chemistry* **1959**, *63*, 1677.
124. Doudna, C.M.; Bertino, M.F.; Tokuhira, A.T. Structural investigation of Ag-Pd clusters synthesized with the radiolysis method. *Langmuir* **2002**, *18*, 2434-2435.
125. Mattei, G.C; Maurizio, P.; Mazzoldi, F.; D'Acapito, G.; Battaglin, E.; Cattaruzza, C.; de Julián Fernández, C.; Sada, C. Dynamics of compositional evolution of Pd-Cu alloy nanoclusters upon heating in selected atmospheres. *Physical Review B* **2005**, *71*, 195418

126. Thomas, J.M.; Johnstone, B.; Raja, R.; Sankar, G.; Midgley, P.A. High performance nanocatalysts for single-step hydrogenations. *Accounts of Chemical Research* **2003**, 36, 20.
127. Lloyd, J.R.; Lovley, D.R. Microbial detoxification of metals and radionuclides. *Current Opinion in Biotechnology* **2001**, 12, 248.
128. Attard, G.A.; Ahmad, A.; Jenkins, D.J.; Hazzazi, O.A.; Wells, P.B.; Griffin, K.G.; Johnston, P.; Gillies, J.E. The characterisation of supported platinum nanoparticles on carbon used for enantioselective hydrogenation: a combined electrochemical-STM approach. *Chem physchem* **2003**, 4, 123-130.
129. Monk, P.M. Fundamentals of Electroanalytical Chemistry. *John Wiley & Sons Ltd.*, England **2001**.
130. Michael, J.K. Development of polyaniline nanotube electrocatalysts and sensor devices for phenolic-pollutants, in chemistry. *PhD thesis, University of the Western Cape: Cape Town, South africa* **2007**.
131. Zanello, P. Inorganic Electrochemistry. Theory, Practice and Application. *The Royal Society of Chemistry*, Cambridge, UK **2003**, 49-66.
132. Joseph, W. Analytical Electrochemistry. Second Edition, New York, NY 10158-0012, USA. *JohnWiley & Sons, Inc.* **2000**, 31-32.
133. Ndangili, P.M. Amperometric Biosensor Systems Prepared on Poly(Anilineferrocenium Hexafluorophosphate) Composites Doped with Poly(Vinyl Sulfonic Acid Sodium Salt), MSc thesis in Chemistry. *University of the Western Cape: Cape Town, South Africa* **2008**.
134. Allen, J.B.; Larry, R.F. Electrochemical methods: fundamentals and applications, New York, USA. *John Wiley & Sons, Inc.* **2001**.

135. Zhang, H.; Huang, J.; Hou, H.; You, T. Electrochemical Detection of Hydrazine Based on Electrospun Palladium Nanoparticle/Carbon Nanofibers. *Electroanalysis* **2009**, 21, 1869-1874.
136. Bard, A. J.; Faulkner, L.R. *Electrochemical methods: Fundamentals and applications*. Wiley, New York **2000**.
137. Kang, X.; Mai, Z.; Chai, P.; Mo, J. A novel glucose biosensor based on immobilization of glucose oxidase in chitosan on a glassy carbon electrode modified with gold-platinum alloy nanoparticles/multiwall carbon nanotubes. *Analytical Biochemistry* **2007**, 369, 71-79.
138. Fernández-Sánchez, C.; McNeil, C.J.; Rawson, K. Electrochemical impedance spectroscopy studies of polymer degradation: application to biosensor development. *Trends in Analytical Chemistry* **2005**, 24, 37-48.
139. Akinyenye, R.O. Nanostructured polypyrrole impedimetric sensors for anthropogenic organic pollutants, PhD Thesis in Chemistry. *University of the Western Cape: Cape Town, South Africa* **2008**.
140. Duff, D.G.; Curtis, A.C.; Edwards, P.P.; Jefferson, D.A.; Johnson B.F.; Logan, D.E. The microstructure of colloidal silver—evidence for a polytetrahedral growth sequence. *Journal of the Chemistry Society, Chemical Communications* **1987**, 16, 1264.
141. Curtis, A.C.; Duff, D.G.; Edwards, P.P.; Jefferson, D.A.; Johnson, B.F.; Kirkland, A.I.; Wallace, A.S. Preparation and structural characterization of an unprotected copper sol. *Journal of Physics Chemistry* **1988**, 92, 2270.
142. Ngece, R.F. Nanoparticulaten of silver-modified poly(8-anilino-1-naphthalene sulphonic acid) nanobiosensor systems for the determination of tuberculosis

- treatment drugs, PhD thesis in Chemistry. *University of the Western Cape: Cape Town, South Africa* **2011**, 85-90.
143. Voyles, P.M.; Muller, D.A.; Grazul, J.L.; Citrin, P.H.; Gossmann, H.J.L. Atomic-scale imaging of individual dopant atoms and clusters in highly n-type bulk Si. *Nature* **2002**, 416, 826-829.
144. Yang, L. Material characterization introduction to microscopic and spectroscopic methods. *John Wiley and sons*, Singore **2008**, 145-169.
145. Goodhen; P.J.; Humphreys, J.; Beanland.R. Electron microscopy and analysis. Taylor and Francis **2001**.
146. Samori, P. Scanning probe microscopies beyond imaging. *Journal of Material Chemistry* **2004**, 14, 1353-1366.
147. Binnig, G.; Rohrer, H.; Gerber, C.; Weibel, E. Surface studies by scanning tunneling microscopy. *Physical Review Letters* **1982**, 276, 4.
148. Blanchard, C.R. Atomic Force Microscopy *Springer-Verlag, New York, Inc. The chemical educator* **1996**, 1, 1430.
149. Binnig, G.; Quate, C.F.; Gerber, C. Atomic force microscope. *Physical Review Letters* **1986**, 56, 930-933.
150. Wang, J. Analytical Electrochemistry. *A John Willey and Sons, Inc, Publication, Newyork* **2001**, 47-49.
151. Martin, T.P. Shells of atoms. *Physics Reports* **1996**, 273, 199-241.
152. Renouprez, A.J.; Lebas, K.; Bergeret, G.; Rousset, J.L.; Delichère, P. Supported Pd-Cu catalysts prepared from bimetallic organo-metallic complexes: Relation between surface composition measured by Ion Scattering and reactivity. *Studies in Surface Science and Catalysis* **1996**, 101B, 1105-1114.

153. Russell, A.E. X-ray absorption spectroscopy of low temperature fuel cell catalysts. *Chemical Reviews* **2004**, 104, 4613-4635.
154. United Kingdom Surface Analysis Forum. URL: <http://www.uksaf.org/>.
155. Koyasu, K.; Mitsui, M.; Nakajima, A.; Kaya, K. Photoelectron spectroscopy of palladium-doped gold cluster anions; AunPd (n=1-4). *Chemical Physics Letters* **2002**, 358, 224-230.
156. Monk, P.M. Fundamentals of electroanalytical chemistry. *John Willey & Sons*, Newyork, USA **2001**, 158-159.
157. Naoki, T.; Yonezawab, T. Bimetallic nanoparticles-novel materials for chemical and physical applications. *New Journal of Chemistry* **1998**, 1179-1201.
158. Pal, A.; Shah, S.; Kulkarni, V.; Murthy R.; Devi, S. Template free synthesis of silver-gold alloy nanoparticles and cellular uptake of gold nanoparticles in Chinese Hamster Ovary cell. *Materials Chemistry and Physics* **2009**, 113, 276-282.
159. Zhu, J. Theoretical study of the optical absorption properties of Au-Ag bimetallic nanospheres. *Physica E: Low-dimensional Systems and Nanostructures* **2005**, 27, 296-301.
160. Angshuman, P.; Sunil, S.; Surekha, D. Preparation of Silver-Gold Alloy Nanoparticles at Higher Concentration Using Sodium Dodecyl Sulfate. *Journal of Chemistry* **2008**, 61, 66.
161. Sanchez-Ramirez, J.F.; Preparation and optical absorption of colloidal dispersion of Au/Cu nanoparticles. *Superficies y Vacío* **2002**, 15, 16-18.
162. Bradley, J.S. In Clusters and Colloids: From Theory to Applications; *VCH: Weinheim* **1994**, 459.

163. Renouprez, A.; Rousset, J.L.; Cadrot, A.M.; Soldo, Y.; Stievano, L. Structure and catalytic activity of palladium–platinum aggregates obtained by laser vaporisation of bulk alloys. *Journal of Alloys and Compounds* **2001**, 328, 50-56.
164. Gerischer, H.; Mauerer, A. Untersuchungen Zur anodischen Oxidation von Ammoniak an Platin-Elektroden. *Journal of Electroanalytical Chemistry and Interfacial Electrochemistry* **1970**, 25, 421-433.
165. Allagui, A.; Oudah, M.; Tuaeov, X.; Ntais, S.; Almomani, F.; Baranova, E.A. Ammonia electro-oxidation on alloyed PtIr nanoparticles of well-defined size. *International Journal of Hydrogen Energy* **2013**, 38, 2455-2463.
166. Le Vot, S.; Roué, L.; Bélanger, D. Study of the electrochemical oxidation of ammonia on platinum in alkaline solution: Effect of electrodeposition potential on the activity of platinum. *Journal of Electroanalytical Chemistry* **2013**, 691, 18-27.
167. Endo, K.; Katayama, Y.; Miura, T. Pt-Ir and Pt-Cu binary alloys as the electrocatalyst for ammonia oxidation. *Electrochimica Acta* **2004**, 49, 1635-1638
168. Vooys, A.; De, K.M.; Santen, R.A.; Veen, J. The role of adsorbates in the electrochemical oxidation of ammonia on noble and transition metal electrodes. *Journal of Electroanalytical Chemistry* **2001**, 506, 127-137.
169. Kardimi, K.; Tsoufis, T.; Tomou, A.; Kooi, B.J.; Prodromidis, M.I.; Gournis, D. Synthesis and characterization of carbon nanotubes decorated with Pt and PtRu nanoparticles and assessment of their electrocatalytic performance. *International Journal of Hydrogen Energy* **2012**, 37, 1243-1253.
170. Ahmadian, N.; Babaluo, A.A.; Bayati, B. Palladium nanoparticles synthesis using polymeric matrix: poly(ethyleneglycol) molecular weight and palladium concentration effects. *International Journal of Nanoscience and Nanotechnology* **2007**, 37-43.

171. Young, W.L.; Naam, H.K.; Kang, Y.L.; Kihyun, K.; Minjung, K.; Sang, W.H. Synthesis and characterization of flower-shaped porous of Au-Pd Alloy Nanoparticles. *Journal of Physical Chemistry C* **2008**, 112, 6717–6722.
172. Lee, Y.W.; Kim, M.; Kim, Y.; Kang, S.W.; Lee, J.H.; Han, S.W. Synthesis and Electrocatalytic Activity of Au–Pd Alloy Nanodendrites for Ethanol Oxidation. *The Journal of Physical Chemistry C* **2010**, 114, 7689-7693.
173. Teng, X.; Liang, X.; Maksimuk, S.; Yang, H. Synthesis of Porous Platinum Nanoparticles. *Small* **2006**, 2, 249-253.
174. Hoefelmeyer, J.D.; Niesz, K.; Somorjai, G.A.; Tilley, T.D. Radial anisotropic growth of rhodium nanoparticles. *Nano Letters* **2005**, 5, 435-438.
175. Kuo, C.H.; Huang, M.H. Synthesis of branched gold nanocrystals by a seeding growth approach. *Langmuir* **2005**, 21, 2012-2016.
176. Lee, H.; Habas, S.E.; Kweskin, S.; Butcher, D.; Somorjai, G.A.; Yang, P. Morphological Control of Catalytically Active Platinum Nanocrystals. *Angewandte Chemie* **2006**, 118, 7988-7992.
177. Wang, J.; Analytical Electrochemistry. *John Willey and Sons*, Inc, Publication, Newyork **2000**, 45-48.
178. Diculescu, V.; Chiorcea-Paquim, A.M.; Corduneanu, O.; Oliveira-Brett, A. Palladium nanoparticles and nanowires deposited electrochemically: AFM and electrochemical characterization. *Journal of Solid State Electrochemistry* **2007**, 11, 887-898.
179. Mailu, S.N.; Waryo, T.; Ndongili, P.M.; Ngece, F.R.; Baleg, A.A., Baker, P.G.; Iwuoha, E.I. Determination of Anthracene on Ag-Au Alloy Nanoparticles/Overoxidized-Polypyrrole Composite Modified Glassy Carbon Electrodes. *Sensors* **2010**, 10, 9449-9465.



180. Liu, T.S.; Kang, T.F.; Lu, L.P.; Zhang, Y.; Cheng, S.Y. Au-Fe(III) nanoparticle modified glassy carbon electrode for electrochemical nitrite sensor. *Journal of Electroanalytical Chemistry* **2009**, 632, 197-200.
181. Zhong, C.; Hu, W.B.; Cheng, Y.F. On the essential role of current density in electrocatalytic activity of the electrodeposited platinum for oxidation of ammonia. *Journal of Power Sources* **2011**, 196, 8064-8072.
182. Behzad, H.; Hassan, H.; Somayyeh, B. Sensitive and selective determination of hydrazine using glassy carbon electrode modified with Pd nanoparticles decorated multiwalled carbon nanotubes. *Analytical Bioanalytical Chemistry* **2010**, 398, 1411-1416.
183. Lee, Y.W.; Kim, N.H.; Lee, K.Y.; Kwon, K.; Kim, M.; Han, S.W. Synthesis and Characterization of Flower-Shaped Porous Au-Pd Alloy Nanoparticles. *The Journal of Physical Chemistry C* **2008**, 112, 6717-6722.
184. Yange, S.; I-Ming, H. Synthesis of bimetallic PdAu nanoparticles for formic acid oxidation *Electrochimica Acta* **2011**, 56, 2174-2183.
185. Gosser, D.K. Cyclic voltammetry, simulation and Analysis of Reaction Mechanisms. *VCH publishers* **1994**, 42-43.
186. Zhang, L.; Jiang, X.; Wang, E.; Dong, S. Attachment of gold nanoparticles to glassy carbon electrode and its application for the direct electrochemistry and electrocatalytic behavior of hemoglobin. *Biosensors and Bioelectronics* **2005**, 21, 337-345.
187. Laviron, E. The use of linear potential sweep voltammetry and of AC voltammetry for the study of the surface electrochemical reaction of strong adsorbed systems and of redox modified electrodes. *Journal of Electroanalytical Chemistry* **1979a**, 100, 263-270.

188. Nicholson, R.S. Theory and application of cyclic voltammetry for measurement of electrode reaction kinetics. *Analytical Chemistry* **1965**, 37, 1351-1355.
189. Katan, T.; Galiotto, R.J. Current efficiencies for the anodic oxidation of ammonia in potassium hydroxide solution. *Journal of Electrochemical Society* **1963**, 110 1022–1023.
190. Vidal-Iglesias, F.J.; Garc-Araez, N.; Montiel, V.; Feliu, J.M.; Aldaz, A. Selective electrocatalysis of ammonia oxidation on Pt(100) sites in alkaline medium. *Electrochemistry Communications* **2003**, 5, 22–26.
191. Haijiang, Z.; Jianshe, H.; Haoqing, H.; Tianyan, Y. Electrochemical Detection of Hydrazine Based on Electrospun Palladium Nanoparticle/Carbon Nanofibers. *Electroanalysis* **2009**, 21, 1869–1874.
192. Yadegari, H.; Jabbari, A.; Heli, H.; Moosavi-Movahedi, A.A.; Karimian, K.; Khodadadi, A. Electrocatalytic oxidation of deferiprone and its determination on a carbon nanotube-modified glassy carbon electrode. *Electrochimica Acta* **2008**, 53, 2907-2916.
193. Behzad, H.; Hassan, H.; Somayyeh, B. Sensitive and selective determination of hydrazine using glassy carbon electrode modified with Pd nanoparticles decorated multiwalled carbon nanotubes. *Analytical and Bioanalytical Chemistry* **2010**, 398, 1411-1416.
194. Attard, G.A.; Ye, J.Y.; Jenkins, P.; Vidal-Iglesias, F.J.; Herrero, E.; Sun, S.G. Citrate adsorption on Pt{hkl} electrodes and its role in the formation of shaped Pt nanoparticles. *Journal of Electroanalytical Chemistry* **2013**, 688, 249-256.
195. Bertin, E.; Garbarino, S.; Guay, D.; Solla-Gullón, J.; Vidal-Iglesias, F.J.; Feliu, J.M. Electrodeposited platinum thin films with preferential (100) orientation:

- Characterization and electrocatalytic properties for ammonia and formic acid oxidation. *Journal of Power Sources* **2013**, 225, 323-329.
196. Vidal-Iglesias, F.J.; Solla-Gullón, J.; Montiel, V.; Feliu, J.M.; Aldaz, A. Screening of electrocatalysts for direct ammonia fuel cell: Ammonia oxidation on PtMe (Me: Ir, Rh, Pd, Ru) and preferentially oriented Pt(100) nanoparticles. *Journal of Power Sources* **2007**, 171, 448-456.
197. Teranishi, T.; Hosoe, M.; Tanaka, T.; Miyake, M. Size Control of Monodispersed Pt Nanoparticles and Their 2D Organization by Electrophoretic Deposition. *The Journal of Physical Chemistry B* **1999**, 103, 3818-3827.
198. Figueiredo, M.C.; Solla-Gullón, J.; Vidal-Iglesias, F.J.; Climent, V.; Feliu, J.M. Nitrate reduction at Pt(100) single crystals and preferentially oriented nanoparticles in neutral media. *Catalysis Today* **2013**, 202, 2-11.
199. Ponrouch, A.; Garbarino, S.; Bertin, E.; Andrei, C.; Botton, G.A.; Guay, D. Highly Porous and Preferentially Oriented {100} Platinum Nanowires and Thin Films. *Advanced Functional Materials* **2012**, 22, 4172-4181.
200. Vidal-Iglesias, F.J.; Arán-Ais, R.M.; Solla-Gullón, J.; Herrero, E.; Feliu, J.M. Electrochemical Characterization of Shape-Controlled Pt Nanoparticles in Different Supporting Electrolytes. *ACS Catalysis* **2012**, 2, 901-910.
201. Solla-Gullon, J.; Vidal-Iglesias, F.J.; Lopez-Cudero, A.; Garnier, E.; Feliu, J.M.; Aldaz, A. Shape-dependent electrocatalysis: methanol and formic acid electrooxidation on preferentially oriented Pt nanoparticles. *Physical Chemistry Chemical Physics* **2008**, 10, 3689-3698.
202. Liu, J.; Zhong, C.; Yang, Y.; Wu, Y.T.; Jiang, A.K.; Deng, Y.D.; Zhang, Z.; Hu, W.B. Electrochemical preparation and characterization of Pt particles on ITO substrate:

- Morphological effect on ammonia oxidation. *International Journal of Hydrogen Energy* **2012**, 37, 8981-8987.
203. Liu, J.; Hu, W.; Zhong, C.; Cheng, Y.F. Surfactant-free electrochemical synthesis of hierarchical platinum particle electrocatalysts for oxidation of ammonia. *Journal of Power Sources* **2013**, 223, 165-174.
204. Ehret, R.; Baumann, W.; Brischwein, M.; Schwinde, A.; Stegbauer, K.; Wolf, B. Monitoring of cellular behaviour by impedance measurements on interdigitated electrode structures. *Biosensors and Bioelectronics* **1997**, 12, 29-41.
205. Afonin, M.V.; Simanova, S.A.; Burmistrova, N.M.; Shiryayeva, O.A.; Karpov, Y.A.; Dal'nova, Y.S.; Panina, N.S. Extraction of iridium(III) and iridium(IV) chloride complexes by a new sorbent containing sulfur and nitrogen. *Inorganic materials* **2008**, 45, 3-7.
206. Wang, J.; Dong, Z.; Huang, J.; Li, J.; Jin, X.; Niu, J.; Sun, J.; Jin, J.; Ma, J. Filling carbon nanotubes with Ni-Fe alloys via methylbenzene-oriented constant current electrodeposition for hydrazine electrocatalysis. *Applied Surface Science* **2013**, 270, 128-132.
207. Sánchez Arribas, A.; Moreno, M.; Martínez-Fernández, M.; Bermejo, E.; Zapardiel, A.; Chicharro, M. Effect of edge plane sites, oxygenated species and metallic impurities upon the electroactivity of carbon nanotube-modified electrodes toward hydrazine. *Sensors and Actuators B: Chemical* **2013**, 182, 31-39.
208. Wan, Q.; Liu, Y.; Wang, Z.; Wei, W.; Li, B.; Zou, J.; Yang, N. Graphene nanoplatelets supported metal nanoparticles for electrochemical oxidation of hydrazine. *Electrochemistry Communications* **2013**, 29, 29-32.
209. Ahmar, H.; Keshipour, S.; Hosseini, H.; Fakhari, A.R.; Shaabani, A.; Bagheri, A. Electrocatalytic oxidation of hydrazine at glassy carbon electrode modified with

- ethylenediamine cellulose immobilized palladium nanoparticles. *Journal of Electroanalytical Chemistry* **2013**, 690, 96-103.
210. Hosseini, H.; Ahmar, H.; Dehghani, A.; Bagheri, A.; Fakhari, A.R.; Amini, M.M. Au-SH-SiO<sub>2</sub> nanoparticles supported on metal-organic framework (Au-SH-SiO<sub>2</sub>@Cu-MOF) as a sensor for electrocatalytic oxidation and determination of hydrazine. *Electrochimica Acta* **2013**, 88, 301-309.



UNIVERSITY *of the*  
WESTERN CAPE